UNIVERSIDADE DA BEIRA INTERIOR
Ciências

Graphene Oxide Nanomaterials for Cancer Therapy

Duarte Miguel de Melo Diogo

Tese para obtenção do Grau de Doutor em
Bioquímica
(3º ciclo de estudos)

Orientador: Prof. Doutor Ilídio Joaquim Sobreira Correia
Co-orientador: Prof. Doutor Ricardo Saraiva Loureiro de Oliveira Louro

Covilhã, outubro de 2018

Dedicatory

To my parents, sister and grandparents.

Acknowledgments

First of all, I would like to thank my supervisors, Dr. Ilídio J. Correia and Dr. Ricardo O. Louro, for everything. Words do not make justice to all the support, guidance and knowledge that I received from both during these last years. Pursuing a PhD is not a simple path, but with your help I can say it became a lot easier.

Moreover, I would like to acknowledge the University of Beira Interior, in particular the CICS-UBI, as well as the ITQB-NOVA, for providing the equipment and the facilities required to perform this PhD thesis. Likewise, I am grateful for all the assistance and friendship from my laboratory colleagues. Your contribution to this research was invaluable.

Furthermore, I would like to thank my family, specially my parents, sister and grandparents, and also my friends, for the continuous support, love and care during these years. Thanks for forgiving my absence when my focus was required to be elsewhere. To Diana, thanks for your love, believe, and patience. Your continuous support made this journey more enjoyable.

Finally, I would like to show my gratitude to Fundação para a Ciência e a Tecnologia (FCT) for the financial support through the individual PhD fellowship (SFRH/BD/103506/2014). Furthermore, the funding from the projects POCI-01-0145-FEDER-007491 and UID/Multi/00709/2013 is also acknowledged.

List of Publications

Articles published in peer-reviewed international journals included in this Doctoral thesis

I. D-α-tocopheryl polyethylene glycol 1000 succinate functionalized nanographene oxide for cancer therapy
Duarte de Melo-Diogo, Cleide Pais-Silva, Elisabete C. Costa, Ricardo O. Louro, Ilídio J. Correia
Nanomedicine (Lond), 2017, 12(5):443-456
DOI: 10.2217/nnm-2016-0384
I.F. = 5.005; Q1 Biotechnology & Applied Microbiology (22/160)
Citations - ISI Web of Knowledge: 3, Google Scholar: 3, Scopus: 2

II. Strategies to Improve Cancer Photothermal Therapy Mediated by Nanomaterials
Duarte de Melo-Diogo, Cleide Pais-Silva, Diana R. Dias, André F. Moreira, Ilídio J. Correia
Advanced Healthcare Materials, 2017, 6(10):201700073
DOI: 10.1002/adhm.201700073
I.F. = 5.609; Q1 and TOP10 Engineering, Biomedical (6/78)
Citations - ISI Web of Knowledge: 6, Google Scholar: 15, Scopus: 12

Manuscripts submitted for publication in peer-reviewed international journals included in this Doctoral thesis

I. POxylated Graphene Oxide Nanomaterials for Combination Chemo-Phototherapy of Breast Cancer Cells
Duarte de Melo-Diogo, Elisabete C. Costa, Cátia G. Alves, Rita Lima-Sousa, Ricardo O. Louro, Ilídio J. Correia
Submitted for publication.

II. Functionalization of Graphene Family Nanomaterials for Application in Cancer Therapy
Duarte de Melo-Diogo, Rita Lima-Sousa, Cátia G. Alves, Elisabete C. Costa, Ricardo O. Louro, Ilídio J. Correia
Submitted for publication.

Articles published in peer-reviewed international journals not included in this Doctoral thesis

I. Poly(2-ethyl-2-oxazoline)-PLA-g-PEI amphiphilic triblock micelles for co-delivery of minicircle DNA and chemotherapeutics
Vítor M. Gaspar, Cristine Gonçalves, Duarte de Melo-Diogo, Elisabete C. Costa, João A. Queiroz, Chantal Pichon, Fani Sousa, Ilídio J. Correia
Journal of Controlled Release, 2014, 189:90-104
DOI: 10.1016/j.jconrel.2014.06.040
I.F. = 7.877; Q1 and TOP10 Pharmacology & Pharmacy (9/261)
Citations - ISI Web of Knowledge: 42, Google Scholar: 55, Scopus: 46

II. Preparation of end-capped pH-sensitive mesoporous silica nanocarriers for on-demand drug delivery
André F. Moreira, Vítor M. Gaspar, Elisabete C. Costa, Duarte de Melo-Diogo, Paulo Machado, Catarina M. Paquete, Ilídio J. Correia
European Journal of Pharmaceutics and Biopharmaceutics, 2014, 88(3):1012-1025
DOI: 10.1016/j.ejpb.2014.09.002
I.F. = 4.491; Q1 Pharmacology & Pharmacy (28/261)
Citations - ISI Web of Knowledge: 20, Google Scholar: 27, Scopus: 23

III. Combinatorial delivery of Crizotinib–Palbociclib–Sildenafil using TPGS-PLA micelles for improved cancer treatment
Duarte de Melo-Diogo, Vítor M. Gaspar, Elisabete C. Costa, André F. Moreira, David Oppolzer, Eugénia Gallardo, Ilídio J. Correia
European Journal of Pharmaceutics and Biopharmaceutics, 2014, 88(3):718-729
DOI: 10.1016/j.ejpb.2014.09.013
I.F. = 4.491; Q1 Pharmacology & Pharmacy (28/261)
Citations - ISI Web of Knowledge: 23, Google Scholar: 33, Scopus: 28

IV. Minicircle DNA vectors for gene therapy: advances and applications
Vítor M. Gaspar, Duarte de Melo-Diogo, Elisabete C. Costa, André F. Moreira, João A. Queiroz, Chantal Pichon, Ilídio J. Correia, Fani Sousa
Expert Opinion on Biological Therapy, 2015, 15(3):353-379
DOI: 10.1517/14712598.2015.996544
I.F. = 3.974; Q1 Biotechnology & Applied Microbiology (30/160)
Citations - ISI Web of Knowledge: 20, Google Scholar: 29, Scopus: 21

V. Bioreducible poly(2-ethyl-2-oxazoline)-PLA-PEI-SS triblock copolymer micelles for co-delivery of DNA minicircles and Doxorubicin
Vítor M. Gaspar, Patrick Baril, Elisabete C. Costa, Duarte de Melo-Diogo, Frédéric Foucher, João A. Queiroz, Fani Sousa, Chantal Pichon, Ilídio J. Correia
Journal of Controlled Release, 2015, 213:175-191
DOI: 10.1016/j.jconrel.2015.07.011
I.F. = 7.877; Q1 and TOP10 Pharmacology & Pharmacy (9/261)
Citations - ISI Web of Knowledge: 29, Google Scholar: 34, Scopus: 34

VI. 3D tumor spheroids: an overview on the tools and techniques used for their analysis
Elisabete C. Costa, André F. Moreira, Duarte de Melo-Diogo, Vítor M. Gaspar, Marco P. Carvalho, Ilídio J. Correia
Biotechnology Advances, 2016, 34(8):1427-1441
DOI: 10.1016/j.biotechadv.2016.11.002
I.F. = 11.452; Q1 and TOP10 Biotechnology & Applied Microbiology (5/160)
Citations - ISI Web of Knowledge: 17, Google Scholar: 29, Scopus: 18

VII. IR780-loaded TPGS-TOS micelles for breast cancer photodynamic therapy
Cleide Pais-Silva, Duarte de Melo-Diogo, Ilídio J. Correia
European Journal of Pharmaceutics and Biopharmaceutics, 2017, 133:108-117
DOI: 10.1016/j.ejpb.2017.01.002
I.F. = 4.491; Q1 Pharmacology & Pharmacy (28/261)
Citations - ISI Web of Knowledge: 7, Google Scholar: 13, Scopus: 7

VIII. Characterization of OmcA Mutants from *Shewanella oneidensis* MR-1 to Investigate the Molecular Mechanisms Underpinning Electron Transfer Across the Microbe-Electrode Interface
Sónia E. Neto, Duarte de Melo-Diogo, Ilídio J. Correia, Catarina M. Paquete, Ricardo O. Louro
Fuel Cells, 2017, 17(5):601-611
DOI: 10.1002/fuce.201700023
I.F. = 2.149; Q3 Energy & Fuels (54/97)
Citations - ISI Web of Knowledge: 0, Google Scholar: 0, Scopus: 1

IX. Spheroids Formation on Non-Adhesive Surfaces by Liquid Overlay Technique: Considerations and Practical Approaches
Elisabete C. Costa, Duarte de Melo-Diogo, André F. Moreira, Marco P. Carvalho, Ilídio J. Correia
Biotechnology Journal, 2018, 13(1):1700417
DOI: 10.1002/biot.201700417
I.F. = 4.515; Q2 Biochemical Research Methods (23/79)
Citations - ISI Web of Knowledge: 1, Google Scholar: 1, Scopus: 1

X. *In vitro* characterization of 3D printed scaffolds aimed at bone tissue regeneration
João C. Boga, Sónia P. Miguel, Duarte de Melo-Diogo, António G. Mendonça, Ricardo O. Louro, Ilídio J. Correia
Colloids and Surfaces B: Biointerfaces, 2018, 165(1):207-218
DOI: 10.1016/j.colsurfb.2018.02.038
I.F. = 3.997; Q1 Biophysics (13/72)
Citations - ISI Web of Knowledge: 0, Google Scholar: 0, Scopus: 0

XI. IR780 based nanomaterials for cancer imaging and photothermal, photodynamic and combinatorial therapies
Cátia G. Alves*, Rita Lima-Sousa*, Duarte de Melo-Diogo*, Ricardo O. Louro, Ilídio J. Correia
International Journal of Pharmaceutics, 2018, 542(1-2):164-175
DOI: 10.1016/j.ijpharm.2018.03.020
I.F. = 3.862; Q1 Pharmacology & Pharmacy (46/261)
Citations - ISI Web of Knowledge: 0, Google Scholar: 1, Scopus: 1
* these authors contributed equally to this article

XII. Clear^{T} immersion optical clearing method for intact 3D spheroids imaging through confocal laser scanning microscopy
Elisabete C. Costa, André F. Moreira, Duarte de Melo-Diogo, Ilídio J. Correia
Optics & Laser Technology, 2018, 106:94-99
DOI: 10.1016/j.optlastec.2018.04.002
I.F. = 2.503; Q2 Physics, Applied (51/146)
Citations - ISI Web of Knowledge: 0, Google Scholar: 0, Scopus: 0

XIII. Polyethylene glycol molecular weight influences the Clear^{T2} optical clearing method for spheroids imaging by confocal laser scanning microscopy
Elisabete C. Costa, André F. Moreira, Duarte de Melo-Diogo, Ilídio J. Correia
Journal of Biomedical Optics, 2018, 23(5):1-11
DOI: 10.1117/1.JBO.23.5.055003
I.F. = 2.367; Q2 Radiology, Nuclear Medicine & Medical Imaging (53/128)
Citations - ISI Web of Knowledge: 0, Google Scholar: 0, Scopus: 0

Book chapters in peer-reviewed scientific books published by international publishers not included in this Doctoral thesis

I. Chapter 6 - Multifunctional Nanocarriers for Codelivery of Nucleic Acids and Chemotherapeutics to Cancer Cells
Vítor M. Gaspar, André F. Moreira, Duarte de Melo-Diogo, Elisabete C. Costa, João A. Queiroz, Fani Sousa, Chantal Pichon, Ilídio J. Correia
Nanobiomaterials in Medical Imaging – Volume VIII, Edited by Alexandru M. Grumezescu, Published by Elsevier (2016)
DOI: 10.1016/B978-0-323-41736-5.00006-6
Citations - ISI Web of Knowledge: 0, Google Scholar: 1, Scopus: 1

List of Scientific Communications

Oral scientific communications related to this Doctoral thesis

I. Duarte de Melo-Diogo, Ricardo O. Louro, Ilídio J. Correia, *Functionalized Graphene-Oxide Nanomaterials for Cancer Therapy*, 3 minutes, 1 slide .... Your thesis!, Universidade da Beira Interior, 24th of November of 2017, Covilhã, Portugal.

II. Duarte de Melo-Diogo, Cleide Pais-Silva, Elisabete C. Costa, Cátia G. Alves, Rita Lima-Sousa, Ricardo O. Louro, Ilídio J. Correia, *Near infrared light responsive nanomaterials for cancer therapy*, XVI Portuguese Conference on Fracture, 23rd to 24th of April of 2018, Covilhã, Portugal.

III. Duarte de Melo-Diogo, Cleide Pais-Silva, Elisabete C. Costa, Cátia G. Alves, Rita Lima-Sousa, Ricardo O. Louro, Ilídio J. Correia, *Near infrared light responsive nanomaterials for cancer therapy*, VI Jornadas de Bioengenharia, 2nd to 3rd of May of 2018, Covilhã, Portugal (invited speaker).

Oral scientific communications not related to this Doctoral thesis

I. Vítor M. Gaspar, Cristine Gonçalves, Duarte de Melo-Diogo, Elisabete C. Costa, João A. Queiroz, Chantal Pichon, Fani Sousa, Ilídio J. Correia, *Simultaneous Delivery of Drugs and Genes by Multiblock Polymeric Nanomicelles for Synergistic Cancer Therapy*, NanoPT, 11th to 13th of February of 2015, Porto, Portugal.

II. Vítor M. Gaspar, Cristine Gonçalves, Duarte de Melo-Diogo, Elisabete C. Costa, João A. Queiroz, Chantal Pichon, Fani Sousa, Ilídio J. Correia, *Polymeric Nanocarriers for Delivery of Multiple Bioactive Molecules to Breast Cancer Cells*, Biochemistry Symposium, 6th to 7th of May of 2015, Covilhã, Portugal.

III. Duarte de Melo-Diogo, *Research in Biomedical Sciences*, I joined Biomedical Sciences! And now?, Hospital Pêro da Covilhã, 25th of November of 2015, Covilhã, Portugal (invited speaker).

IV. Elisabete C. Costa, Marco P. Carvalho, André F. Moreira, Duarte de Melo-Diogo, Ilídio J. Correia, *Agarose and Hyaluronic Acid (HA) application in 3D cell culture of breast cancer cells*, XVI Portuguese Conference on Fracture, 23rd to 24th of April of 2018, Covilhã, Portugal.

V. Sónia P. Miguel, Kevin D. De Sá, João C. Boga, Daniela R. Figueira, Duarte de Melo-Diogo, Tiago R. Correia, Abílio P. Silva, António G. Mendonça, Ricardo O. Louro, Ilídio J. Correia, *Functionalization of 3D printed scaffolds for bone tissue regeneration*, XVI Portuguese Conference on Fracture, 23rd to 24th of April of 2018, Covilhã, Portugal.

Poster presentations related to this Doctoral thesis

I. Duarte de Melo-Diogo, Cleide Pais-Silva, Elisabete C. Costa, Ricardo O. Louro, Ilídio J. Correia, *Functionalization of graphene oxide for anticancer applications*, V Ciclo de Conferências da Faculdade de Ciências, 21st of January of 2017, Covilhã, Portugal (**best poster award**).

II. Duarte de Melo-Diogo, Cleide Pais-Silva, Elisabete C. Costa, Ricardo O. Louro, Ilídio J. Correia, *PEGylated Vitamin E functionalized nanographene oxide for breast cancer therapy*, II International Congress in Health Sciences Research Towards Innovation and Entrepreneurship: Trends in Biotechnology for Biomedical Applications, 17th to 20th of May of 2017, Covilhã, Portugal.

III. Duarte de Melo-Diogo, Cleide Pais-Silva, Elisabete C. Costa, Ricardo O. Louro, Ilídio J. Correia, *Nanographene oxide functionalized with PEGylated Vitamin E for breast cancer therapy*, Encontro com a Ciência e Tecnologia 2017, 3rd to 5th of July of 2017, Lisboa, Portugal.

Poster presentations not related to this Doctoral thesis

I. David Oppolzer, João G. Marques, Duarte de Melo-Diogo, Vítor M. Gaspar, Elisabete C. Costa, Eugenia Gallardo, Ilídio J. Correia, *Simultaneos Determination of Sildenafil and Crizotinib using HPLC-DAD*, 8º Encontro Nacional de Cromatografia, 2nd of December of 2013, Covilhã, Portugal.

II. André F. Moreira, Vítor M. Gaspar, Elisabete C. Costa, Duarte de Melo-Diogo, Paulo Machado, Catarina M. Paquete and Ilídio J. Correia, *Synthesis and characterization of MCM-41 type sílica nanoparticles by a Stöber modified method*, Encontro Bienal das Divisões Técnicas da Sociedade Portuguesa de Materiais (SPM), 4th of May of 2014, Covilhã, Portugal.

III. Elisabete C. Costa, Vítor M. Gaspar, Duarte de Melo-Diogo, André F. Moreira, João F.G. Marques, Paula Coutinho, Ilídio J. Correia, *Evaluation of nanoparticles uptake in breast cancer co-cultures*, Encontro Bienal das Divisões Técnicas da Sociedade Portuguesa de Materiais (SPM), 4th of May of 2014, Covilhã, Portugal.

IV. André F. Moreira, Vítor M. Gaspar, Elisabete C. Costa, Duarte de Melo-Diogo, Paulo Machado, Catarina M. Paquete and Ilídio J. Correia, *Development of Mesoporous Silica Nanoparticles for Drug Delivery to Cancer Cells*, IX Anual CICS Symposium, 30th of June and 1st of July of 2014, Covilhã, Portugal (**best poster award**).

V. Elisabete C. Costa, Vítor M. Gaspar, Duarte de Melo-Diogo, André F. Moreira, João G. Marques, Paula Coutinho, Ilídio J. Correia, *Co-cultures for nanoparticles uptake analysis,* IX Anual CICS Symposium, 30th of June and 1st of July of 2014, Covilhã, Portugal.

VI. João G. Marques, Vítor M. Gaspar, David Markl, Elisabete C. Costa, Duarte de Melo-Diogo, André F. Moreira, Eugénia Gallardo, Ilídio J. Correia, *Co-delivery of a dual drug combination in polymeric nanovehicles for improved anticancer therapy*, IX Anual CICS Symposium, 30th of June and 1st of July of 2014, Covilhã, Portugal.

VII. André F. Moreira, Vítor M. Gaspar, Elisabete C. Costa, Duarte de Melo-Diogo, Paulo Machado, Catarina M. Paquete, Ilídio J. Correia, *pH-sensitive mesoporous silica nanoparticles for drug delivery to prostate cancer cells*, Semana da Ciência, 28th of November of 2014, Covilhã, Portugal.

VIII. Duarte de Melo-Diogo, Vítor M. Gaspar, Elisabete C. Costa, André F. Moreira, David Oppolzer, Eugénia Gallardo, Ilídio J. Correia, *Triple drug loaded polymeric micelles for improved lung cancer therapy*, Semana da Ciência, 28th of November of 2014, Covilhã, Portugal.

IX. Elisabete C. Costa, Vítor M. Gaspar, Duarte de Melo-Diogo, André F. Moreira, João G. Marques, Paula Coutinho, Ilídio J. Correia, *Liquid Overlay Technique (LOT) optimizations for spheroids 3D cell culture*, Semana da Ciência, 28th of November of 2014, Covilhã, Portugal.

X. André F. Moreira, Vítor M. Gaspar, Elisabete C. Costa, Duarte de Melo-Diogo, Paulo Machado, Catarina M. Paquete, Ilídio J. Correia, *Calcium carbonate coated nanoparticles for pH-responsive drug co-delivery to prostate cancer cells*, VIII Jornadas Nacionais sobre Tecnologia e Saúde, 17th of April of 2015, Guarda, Portugal.

XI. Duarte de Melo-Diogo, Vítor M. Gaspar, Elisabete C. Costa, André F. Moreira, David Oppolzer, Eugénia Gallardo, Ilídio J. Correia, *Triple-drug co-delivery by TPGS-PLA micelles for lung cancer therapy*, VIII Jornadas Nacionais sobre Tecnologia e Saúde, 17th of April of 2015, Guarda, Portugal.

XII. Elisabete C. Costa, Vítor M. Gaspar, Duarte de Melo-Diogo, André F. Moreira, Paula Coutinho, Ilídio J. Correia, *Optimization of Liquid Overlay Technique (LOT) to produce 3D Breast and Cervical Co-Culture Models*, VIII Jornadas Nacionais sobre Tecnologia e Saúde, 17th of April of 2015, Guarda, Portugal (**best poster award**).

XIII. André F. Moreira, Vítor M. Gaspar, Elisabete C. Costa, Duarte de Melo-Diogo, Paulo Machado, Catarina M. Paquete, Ilídio J. Correia, *Calcium carbonate coated nanoparticles for pH responsive drug co-delivery to prostate cancer cells*, Encontro com a Ciência e Tecnologia 2016, 4th to 6th of July of 2016, Lisboa, Portugal.

XIV. Cleide Pais-Silva, Duarte de Melo-Diogo, Ilídio J. Correia, *Vitamin E-based micelles for cancer cell imaging*, V Encontro Nacional de Estudantes de Materiais (ENEM), 29th of September of 2016, Covilhã, Portugal.

XV. Elisabete C. Costa, Marco P. Carvalho, Duarte de Melo-Diogo, André F. Moreira, Ilídio J. Correia, *Mimicking Breast Cancer Microenvironment with In Vitro 3D Co-culture Models*, II International Congress in Health Sciences Research Towards Innovation and Entrepreneurship: Trends in Biotechnology for Biomedical Applications, 17th to 20th of May of 2017, Covilhã, Portugal.

XVI. Elisabete C. Costa, Marco P. Carvalho, Duarte de Melo-Diogo, André F. Moreira, Ilídio J. Correia, *Mimicking breast cancer microenvironment with in vitro 3D heterotypic spheroids*, Encontro com a Ciência e Tecnologia 2017, 3rd to 5th of July of 2017, Lisboa, Portugal.

Conference Organizing Committees

Member of the organizing committee of scientific conferences

I. II International Congress in Health Sciences Research Towards innovation and entrepreneurship: Trends in Biotechnology for Biomedical Applications, Universidade da Beira Interior, 17th to 20th of May of 2017, Covilhã, Portugal.

II. XVI Portuguese Conference on Fracture, TRYP Dona Maria, 23rd to 24th of April of 2018, Covilhã, Portugal.

Resumo Alargado

A sociedade atual é profundamente afetada por diversas doenças, sendo o cancro uma das mais devastadoras. Apesar de toda a investigação desenvolvida em torno do cancro, as taxas de incidência e de mortalidade associadas a esta doença continuam muito elevadas. Esta realidade está em parte relacionada com as limitações dos tratamentos disponíveis para o cancro, que incluem cirurgia, quimioterapia e radioterapia. Estas terapias são caracterizadas por apresentarem uma baixa eficácia terapêutica e por causarem efeitos secundários nos pacientes. Para além disto, a eficácia destes tratamentos é ainda diminuída por mecanismos de resistência a fármacos/radiação desenvolvidos pelas células cancerígenas. Por outro lado, as novas terapias que estão a ser testadas em meio clínico (ex.: imunoterapia e quimioterapia direcionada) também são afetadas por mecanismos de resistência e acarretam custos superiores para o Serviço Nacional de Saúde. Desta forma, existe uma necessidade premente de desenvolver e implementar tratamentos inovadores para o cancro, que apresentem maior eficácia sem, no entanto, induzirem efeitos secundários significativos.

De entre as numerosas abordagens terapêuticas em investigação, a terapia fototérmica (PTT) mediada por nanomateriais tem demonstrado resultados promissores nos ensaios pré-clínicos. Esta abordagem explora a utilização de nanomateriais, que devido às suas propriedades físico-químicas, conseguem acumular-se preferencialmente no local do tumor. Posteriormente, a zona do tumor é irradiada com um feixe de luz, e os nanomateriais acumulados nesta zona absorvem-na e convertem-na em calor, induzindo assim danos nas células cancerígenas.

Na PTT mediada por nanomateriais é fundamental usar uma radiação com um comprimento de onda na região do infravermelho próximo (NIR; 750-1000 nm) uma vez que os principais componentes biológicos (ex.: água, hemoglobina, proteínas, melanina) têm uma absorção mínima ou insignificante nesta gama de comprimentos de onda. Devido a este facto, as nanoestruturas projetadas para utilização na PTT devem ter uma elevada absorção no NIR de modo a conseguirem produzir um efeito fototérmico, que induza citotoxicidade para as células cancerígenas. Assim, comparativamente com as terapias convencionais, a PTT mediada por nanomateriais pode induzir um efeito espácio-temporal controlado, permitindo-lhe atingir uma maior seletividade para a zona do tumor.

De entre os diferentes nanomateriais responsivos à luz, o óxido de grafeno (GO) tem revelado propriedades promissoras para aplicação na PTT do cancro. O GO é um nanomaterial composto por uma matriz de grafite, que contém diversos tipos de grupos funcionais (carboxílico, hidroxilo e epóxi). Este nanomaterial absorve na região do NIR, apresentando uma capacidade fototérmica eficiente. Para além disto, os seus grupos aromáticos permitem o encapsulamento de diversas moléculas na sua estrutura através de interações não covalentes (interações

hidrofóbicas e empilhamento π-π). Assim, o GO tem um elevado potencial para aplicações fototérmicas e de entrega de fármacos.

Porém, a aplicação direta do GO na terapia do cancro é severamente limitada pela sua baixa estabilidade coloidal, o que faz com que este nanomaterial precipite em soluções salinas e em fluídos biológicos. Este fator limita assim a sua administração intravenosa. Para além disto, a matriz aromática do GO pode adsorver moléculas do sistema complemento e este nanomaterial pode ser reconhecido por macrófagos. Estes eventos induzem a rápida eliminação do GO, diminuindo a probabilidade deste se acumular na zona do tumor. Finalmente, o GO não é seletivamente internalizado pelas células cancerígenas e, portanto, pode afetar as células saudáveis que se encontram no microambiente tumoral. As estratégias que permitam ultrapassar estas limitações irão certamente contribuir para incrementar a aplicabilidade e a capacidade terapêutica dos materiais à base de GO.

Tendo em consideração as limitações do GO, o principal objetivo do plano de trabalhos desenvolvido nesta tese foi implementar novas estratégias para melhorar a PTT mediada por nanomateriais à base de GO. Para tal, procurou-se i) implementar revestimentos com capacidade de melhorar a performance biológica do GO, ii) explorar métodos de preparação capazes de aumentar a capacidade fototérmica do GO, e iii) encapsular combinações de fármacos com atividade anticancerígena sinérgica na matriz do GO.

No primeiro estudo apresentado nesta tese, foi avaliada a capacidade terapêutica de materiais à base de GO funcionalizados com succinato de D-α-tocoferil polietilenoglicol 1000 (TPGS). Inicialmente, o óxido de grafite foi sintetizado usando uma versão modificada do método de Hummer's melhorado. Seguidamente, este material sofreu um tratamento alcalino, com o intuito de remover os detritos da oxidação (o que pode melhorar a sua capacidade para adsorver moléculas), e foi posteriormente exfoliado de forma a obter o GO com dimensões nanométricas (bwGO). De seguida, foram exploradas duas abordagens diferentes para funcionalizar o bwGO com TPGS: um processo de sonicação simples (obtendo-se TPGS/bwGO) e um tratamento hidrotérmico (obtendo-se TPGS/htGO). Os resultados obtidos demonstraram que os nanomateriais revestidos com TPGS apresentam uma maior estabilidade coloidal. Em particular, o TPGS/htGO demonstrou possuir uma estabilidade coloidal superior e cerca de 1,9 vezes maior absorção no NIR (a 808 nm), quando comparado com o TPGS/bwGO. Após a sua irradiação com luz NIR, o TPGS/htGO induziu uma variação de temperatura 1,4 a 1,6 vezes superior àquela que é induzida pelo TPGS/bwGO. Nos estudos *in vitro*, os nanomateriais funcionalizados com TPGS reduziram a viabilidade das células do cancro da mama, e não tiveram um efeito citotóxico considerável nas células saudáveis. Para além disto, a combinação da luz NIR com os derivados de GO funcionalizados com TPGS promoveu um efeito terapêutico ainda mais acentuado. Neste ensaio, o TPGS/htGO mediou uma fototerapia ligeiramente mais eficaz devido às suas propriedades óticas melhoradas.

No segundo estudo apresentado nesta tese, foi avaliado o potencial quimio-fototerapêutico do bwGO funcionalizado na sua superfície com um polímero anfifílico baseado em poli(2-etil-2-oxazolina) (bwGO POxilado) e que tinha incorporado na sua matriz a combinação de fármacos Doxorrubicina (DOX) e Succinato de D-α-tocoferol (TOS). Os resultados obtidos demonstraram que o bwGO POxilado apresenta propriedades físico-químicas, coloidais, óticas e biológicas adequadas para a sua aplicação na terapia do cancro. Para além disto, a análise da eficácia de diferentes combinações molares de DOX:TOS, de 5:1 a 1:5, revelou que o rácio molar 1:3 de DOX:TOS produz um efeito terapêutico sinérgico ótimo nas células do cancro da mama. Este rácio de fármacos demonstrou ainda um efeito cerca de 2 vezes inferior nas células saudáveis. Com base nestes resultados, a combinação molar 1:3 DOX:TOS foi selecionada para encapsulação no bwGO POxilado, com o objetivo de avaliar o potencial quimio-fototerapêutico deste. Nos estudos *in vitro*, a entrega de DOX:TOS pelo bwGO POxilado às células cancerígenas induziu um efeito terapêutico superior àquele que é obtido com a combinação dos fármacos na sua forma livre. Para além disto, a exposição do bwGO POxilado carregado com a combinação DOX:TOS à luz NIR induziu um maior efeito citotóxico nas células cancerígenas.

Em suma, os resultados obtidos nestes estudos demonstraram que a aplicabilidade dos materiais à base de GO na terapia do cancro pode ser melhorada através da funcionalização deste com polímeros anfifílicos. Para além disto, o potencial terapêutico dos derivados de GO pode ser melhorado através do uso de revestimentos com atividade anticancerígena intrínseca, ou através da co-encapsulação de fármacos com um efeito citotóxico maior para as células cancerígenas. Estudos pré-clínicos mais aprofundados destes nanomateriais poderão conduzir à sua avaliação em ensaios clínicos.

Palavras-chave

Cancro, Infravermelho Próximo, Nanomateriais, Óxido de Grafeno, Terapia Fototérmica.

Abstract

Regardless of the advancements in medicine, there are diseases that have a tremendous impact on today's society. In this context, cancer is probably the most devastating one. Despite all the intensive research on cancer, its incidence and mortality rates are still high. In fact, the classical cancer treatments (surgery, chemotherapy and radiotherapy) have a low therapeutic efficacy and induce side effects in patients that can pose a threat to their life. Furthermore, the low therapeutic index of the available treatments is further impaired by resistance mechanisms developed by cancer cells to drugs/radiation. On the other hand, the novel therapies that are under clinical investigation (*e.g.* targeted chemotherapy and immunotherapy) are also affected by resistance mechanisms and have an even higher cost to the health service providers. In this way, there is an urgent need to discover and implement innovative cancer treatments that possess a higher therapeutic efficacy and display fewer side-effects.

Among the different therapeutic approaches under investigation, photothermal therapy (PTT) mediated by nanomaterials has been showing promising results both in *in vitro* and *in vivo* assays. This therapy employs nanomaterials that, due to their physicochemical properties, can accumulate preferentially in the tumor site. Afterwards, an external light is used to irradiate the tumor zone, and the nanostructures accumulated at the tumor site absorb the radiation energy and convert it into heat, inducing damage to the cells. In nanomaterials' mediated PTT, it is crucial to use near infrared radiation (NIR; 750-1000 nm) since most of the biological components (*e.g.* water, hemoglobin, proteins, melanin) have a minimal or an insignificant absorption within this wavelength range. Consequently, nanostructures should have a high NIR absorption in order to produce an efficient photothermal effect, when they are exposed to NIR light. In this way, compared to conventional therapies, cancer PTT mediated by nanomaterials can induce a spatial-temporal controlled effect with a higher selectivity towards the tumor zone.

Among the different light-responsive nanomaterials, graphene oxide (GO) reveals promising properties to be applied in cancer PTT. GO is a 2D nanomaterial composed by a graphitic lattice that contains several types of oxygen-functional groups (carboxyl, hydroxyl and epoxy). This nanomaterial absorbs in the NIR region, displaying an efficient photothermal capacity. Furthermore, the aromatic lattice of this nanomaterial allows the loading of different types of molecules through non-covalent interactions (hydrophobic-hydrophobic interactions and π-π stacking). In this way, GO has a tremendous potential for photothermal and drug delivery applications.

However, the direct use of GO in cancer therapy is severely limited by different factors. Firstly, GO has a weak colloidal stability – it precipitates in saline solutions and in biological fluids. This factor limits its intravenous administration. Furthermore, the aromatic lattice of GO can adsorb complement proteins, leading to its recognition by macrophages, and subsequent clearance from blood circulation. This removal avoids nanomaterials' accumulation in the tumor zone. Additionally, GO is not selectively internalized by cancer cells, and thus can mediate a therapeutic effect that also affects the healthy cells found within the tumor microenvironment.

The main objective of this thesis' work plan was to address the limitations associated to GO-based materials and implement novel strategies to improve the PTT mediated by these materials. Such was pursued by i) employing coatings that can improve the biological performance of GO-based materials, ii) exploring preparation methods that can enhance GO photothermal capacity, and iii) encapsulating drug combinations with optimal synergistic anticancer activity on GO.

In the first study, the anticancer capacity of D-α-tocopheryl polyethylene glycol 1000 succinate (TPGS) functionalized GO-based materials was evaluated. Initially, graphite oxide was synthesized through a modified version of the improved Hummer's method. This material was then base-washed to remove the oxidation debris from its structure, which can improve its ability to adsorb molecules. Then, the material was exfoliated, yielding nanosized base-washed GO (bwGO). Afterwards, TPGS was explored for the functionalization of bwGO through two different approaches: a simple sonication method (yielding TPGS/bwGO) and a one-pot hydrothermal treatment (yielding TPGS/htGO). The results revelated that the TPGS coating successfully improved the stability of the GO derivatives. In particular, the TPGS/htGO displayed a greater colloidal stability and a 1.9-times higher NIR absorption (at 808 nm) in comparison to TPGS/bwGO. In *in vitro* studies, the TPGS/GO derivatives reduced the viability of breast cancer cells and had an insignificant effect on healthy cells. Furthermore, the combined application of TPGS/GO derivatives and NIR light induced an improved therapeutic effect. Particularly, the enhanced optical properties of TPGS/htGO enabled it to mediate a slightly more efficient phototherapy.

In the second part of this thesis, the chemo-phototherapeutic potential of bwGO functionalized with an amphiphilic polymer based on poly(2-ethyl-2-oxazoline) (POxylated bwGO) and loaded with Doxorubicin (DOX) and D-α-Tocopherol succinate (TOS) was assessed. The results revealed that the POxylated bwGO presents suitable physicochemical, colloidal, optical and biological properties for application in cancer therapy. In addition, the screening of different DOX:TOS molar combination ratios, ranging from 5:1 to 1:5, disclosed that the 1:3 DOX:TOS molar ratio produces an optimal synergistic therapeutic effect towards breast cancer cells (combination index of about 0.56). Furthermore, this drug ratio had a 2-times weaker effect on normal cells. POxylated bwGO was then loaded with the 1:3 DOX:TOS combination in order to evaluate its chemo-phototherapeutic potential. In *in vitro* studies, the delivery of DOX:TOS by POxylated

bwGO to cancer cells induced a stronger therapeutic effect than that attained with the free drug combination. Furthermore, an even greater cytotoxicity towards cancer cells was achieved by exposing DOX:TOS loaded POxylated bwGO to NIR radiation.

Overall, the obtained results demonstrate that the applicability of GO-based materials in cancer therapy can be improved by performing their functionalization with amphiphilic polymers. Furthermore, the therapeutic potential of GO derivatives can be enhanced by using coatings with intrinsic anticancer activity or by encapsulating drugs that display a higher effect on cancer cells. These novel strategies will further contribute for the translation of GO-based materials from the bench to the bedside.

Keywords

Cancer, Graphene Oxide, Nanomaterials, Near infrared, Photothermal Therapy.

Thesis Overview

This Doctoral thesis is organized in 6 chapters.

The first chapter comprises the general and specific aims established for the work plan of this PhD thesis.

The second and third chapters enclose the introductory section. Chapter 2 gives an overview on the cancer PTT mediated by nanomaterials, reviewing the different strategies applied so far to improve its therapeutic outcome. Chapter 3 analyses the state-of-the-art of the functionalizations used in the design of GO-based materials aimed for application in cancer therapy, disclosing their role on surpassing the critical issues related to this nanomaterial.

The fourth and fifth chapters present the results of the research works developed during this PhD thesis:

-Research Work 1: D-α-Tocopheryl polyethylene glycol 1000 succinate functionalized nanographene oxide for cancer therapy (Chapter 4)

-Research Work 2: POxylated Graphene Oxide Nanomaterials for Combination Chemo-Phototherapy of Breast Cancer Cells (Chapter 5)

Finally, the sixth chapter contains the concluding remarks, discussing the results obtained during this PhD thesis in the light of the state-of-the-art, and provides future directions regarding this research topic.

Index

List of Figures

List of Tables

List of Supplementary Tables

Abbreviations

A549	Non-small cell lung cancer cells
Akt	Protein Kinase B
ANOVA	One-way Analysis of Variance
BSA	Bovine Serum Albumin
bwGO	Base-washed GO
C_{18}-PMH-PEG	PEG grafted poly(maleic anhydride-*alt*-1-octadecene)
CI	Combination Index
CNT	Carbon nanotubes
cRGD	cyclic RGD
DLS	Dynamic Light Scattering
DMEM-F12	Dulbecco's Modified Eagle's Medium F-12
DOX	Doxorubicin
DSPE-mPEG	1,2-distearoyl-*sn*-glycero-3-phosphoethanolamine-*N*-mPEG
DSPE-PEG	1,2-distearoyl-*sn*-glycero-3-phosphoethanolamine-*N*-PEG
DSPE-PEG-CREKA	DSPE-PEG-(Cys-Arg-Glu-Lys-Ala)
DT loaded Pox-GO	DOX and TOS Loaded POx-GO
EB	Emeraldine base
EDC	1-ethyl-3-(-3-dimethylaminopropyl) carbodiimide
EDS	Energy-Dispersive X-ray Spectroscopy
EDTA	Ethylenediaminetetraacetate
EPR	Enhanced Permeability and Retention
ES	Emeraldine salt
FA	Folic Acid
Fa	Fraction affected
FBS	Fetal Bovine Serum
FSHR	Follicle Stimulating Hormone Receptor
FTIR	Fourier Transform Infrared Spectroscopy
GFN	Graphene Family Nanomaterials
GNR	Gold nanorods
GO	Graphene Oxide
GO-COOH	Carboxylated GO
GONR	Graphene oxide nanoribbons
GrO	Graphite Oxide
HA	Hyaluronic Acid
HEK 293T	Human Embryonic Kidney Cells
HeLa	Human Cervical Cancer Cells

HMDA-HA	Hexamethylenediamine-HA
hMSCs	Human Mesenchymal Stem Cells
htGO	Hydrothermal Treated GO
ID g^{-1}	Injected Dose per gram of tissue
MCF-7	Michigan Cancer Foundation-7
mPEG	methoxy-PEG
MWCNT	Multiwall carbon nanotubes
nGO	Nanographene Oxide
NHDF	Normal Human Dermal Fibroblasts
NHS	*N*-Hydroxysuccinimide
NIR	Near Infrared
P.I.	Post-injection
PAA	Poly(acrylic acid)
PANI	Polyaniline
PB	Prussian Blue
PBS	Phosphate Buffered Saline
PEDOT	Poly(3,4-ethylenedioxythiophene)
PEG	Poly(ethylene glycol)
PEI	Poly(ethyleneimine)
PEtOx	Poly(2-ethyl-2-oxazoline)
PKB	Protein Kinase B
Pluronic® F-68	Poloxamer 188
PMAO	Poly(maleic anhydride-*alt*-1-octadecene)
Pox-GO	POx-*g*-PMAO functionalized bwGO
Pox-*g*-PMAO	PEtOx grafted PMAO
PProDOS	Poly(3,4-propylenedioxyselenophene)
PPy	Polypyrrole
PTT	Photothermal Therapy
PVA	Poly(vinyl alcohol)
PVP	Poly(vinylpyrrolidone)
RBC	Red Blood Cells
RES	Reticuloendothelial system
RGD	Arginine-Glycine-Aspartic acid
rGO	Reduced GO
rGONM	Reduced graphene oxide nanomesh
rGONR	Reduced graphene oxide nanoribbons
RT	Room Temperature
$t_{1/2}$	Blood circulation half-life
$t'_{1/2}$	Second phase blood circulation half-life
TEM	Transmission Electron Microscopy

TOS	D-α-Tocopherol Succinate
TPGS	D-α-Tocopheryl Polyethylene Glycol 1000 Succinate
TPGS/bwGO	TPGS functionalized bwGO
TPGS/htGO	TPGS functionalized htGO
XRD	X-ray Diffraction

Chapter 1

Global Aims

Global Aims

GO-based materials encompass an extraordinary potential for cancer therapy due to their excellent photothermal and drug delivery capabilities. However, the intrinsic limitations of GO derivatives hinder their direct use in cancer therapy. Taking this into account, the main objective of this PhD thesis was to implement novel strategies to improve cancer PTT mediated by GO-based materials, while simultaneously addressing the core problems associated with these nanomaterials. In this way, the specific aims of this thesis were:

- Assess the suitability of the novel coatings in the improvement of the biological performance of GO-based materials;

- Evaluate formulation methods that yield GO-based materials with an improved photothermal capacity;

- Screen drug combinations with optimal synergistic anticancer activity for encapsulation in GO-based materials.

Chapter 2

Introduction (part. A)

Strategies to Improve Cancer Photothermal Therapy Mediated by Nanomaterials

This chapter is based on the publication entitled: Strategies to Improve Cancer Photothermal Therapy Mediated by Nanomaterials, Advanced Healthcare Materials, 2017, 6(10):201700073.

2.1. Abstract

The deployment of hyperthermia-based treatments for cancer therapy has captured the attention of different researchers worldwide. In particular, the application of light-responsive nanomaterials to mediate hyperthermia has revealed promising results in several pre-clinical assays. Unlike conventional therapies, these nanostructures can display a preferential tumor accumulation and thus mediate, upon irradiation with near-infrared light, a selective hyperthermic effect with temporal resolution. Different types of nanomaterials such as those based on gold, carbon, copper, molybdenum, tungsten, iron, palladium and conjugated polymers have been used for this photothermal modality. This chapter summarizes the different strategies that have been applied so far for increasing the efficacy of the photothermal therapeutic effect mediated by nanomaterials, namely those that improve the accumulation of nanomaterials in tumors (*e.g.* by changing the corona composition or through the functionalization with targeting ligands), increase nanomaterials' intrinsic capacity to generate photoinduced heat (*e.g.* by synthesizing new nanomaterials or assembling nanostructures) or by optimizing the parameters related to the laser light used in the irradiation process (*e.g.* by modulating the radiation wavelength). Overall, the development of new strategies or the optimization and combination of the existing ones will surely give a major contribution for the application of nanomaterials in cancer PTT.

Keywords: cancer treatment; hyperthermia; inorganic nanostructures; light-responsive nanomaterials; photothermal therapy.

2.2. Introduction

Cancer is a highly complex disease and it is responsible for an overwhelming number of deaths worldwide [1]. In the clinic, the mainstream therapeutic options for this disease include surgical resection of the tumor, radiotherapy, chemotherapy, or their combined application. However, in many cases, these treatment regimens are not effective and have associated notorious side effects.

Nowadays, different therapeutic modalities are under clinical evaluation to further improve the effectiveness of cancer treatment. In particular, hyperthermia-based treatments that involve a localized or an unrestricted increase of body temperature have captured the attention of clinicians [2]. However, depending on the area under treatment, the maximum temperature and the duration used vary [3]. Hyperthermia at mid-temperatures (41.8-45 °C) is capable of exerting a therapeutic effect on malignant cells in hypoxic environments, while eliciting a minimum damage on the surrounding healthy tissues (reviewed in detail in [3]). Additionally, it can also be used to improve the therapeutic outcome of radio- and chemotherapy [3]. On the other hand, hyperthermia at high-temperatures (45-90 °C) can affect both cancer and normal cells, inducing cellular changes (*e.g.* enzymatic and mitochondrial dysfunctions) and ultimately necrosis (reviewed in detail in [3, 4]). However, the equipment and techniques currently available to perform such types of hyperthermia-based treatments present some limitations and need further improvements for attaining a higher selectivity, tissue penetration, and effectiveness [5]. To accomplish that, researchers are currently developing new responsive nanomaterials that due to their small size (usually < 200 nm), can accumulate preferably in tumor and induce on-demand hyperthermia, after being subjected to an external stimulus (*e.g.* magnetic field or light), with a high efficacy and safety [6, 7-10]. Among the different nanomaterials explored, until now, to induce hyperthermia, some can mediate this effect by absorbing light, generated by a laser, and releasing its energy as heat (nanomaterials' mediated photothermal therapy (PTT)). This feature has been displayed by several types of nanostructures produced with gold, carbon, copper, molybdenum, tungsten, iron, palladium or conjugated polymers [7, 11-18]. Moreover, different strategies are currently being explored to further enhance the photothermal potential of these nanostructures. Compared to laser-induced interstitial thermotherapy (a therapeutic modality that only employs laser light to thermally ablate tumors), nanomaterials' mediated PTT is less invasive, demands radiation with a lower intensity and its therapeutic outcome is less dependent on the characteristics of the irradiated tissue (*e.g.* water or hemoglobin content) [19]. In addition, PTT mediated by nanomaterials can potentially achieve a higher selectivity towards cancer cells through the use of precisely engineered nanostructures that are specifically internalized by diseased cells [20-22]. Still, it should be noted that the clinical translation of these photothermal agents is challenging since only recently the clinical safety profile of AuroLase® therapy (PTT using AuroShell® - poly(ethylene glycol) (PEG) functionalized gold nanoshells), whose initial

pre-clinical studies started in the 1990's, was published and the clinical efficacy of this therapy is yet to be disclosed (*ClinicalTrials.gov Identifier*: NCT02680535, NCT00848042, NCT01679470) [23].

In the following sub-sections, the different strategies described in the literature to improve nanomaterials' mediated cancer PTT are highlighted. In section 2.3, an overview of the key parameters that dictate the success of PTT is given. In section 2.4, the approaches used to enhance nanomaterials tumor accumulation are described. The improvement of nanomaterials' intrinsic capacity to generate photoinduced heat and the optimization of the parameters related to the laser light are other types of procedures assessed in sections 2.5 and 2.6, respectively. Finally, an outlook about the state of the art of nanomaterials' mediated PTT will be presented (section 2.7). For the sake of simplicity, this chapter will not cover improvements based on the inclusion of other therapeutics in the nanomaterials (*e.g.* chemotherapeutic drugs), nor on the utilization of hybrid nanostructures to externally promote tumor accumulation (*e.g.* by applying magnetic fields).

2.3. Cancer photothermal therapy mediated by nanomaterials

Cancer PTT mediated by nanomaterials involves the application of nano-sized structures and laser light to irradiate the tumor zone (or metastatic sites) for inducing hyperthermia. Generally, this therapeutic approach starts with the intravenous administration of the nanomaterials, which can become accumulated within the tumor through the enhanced permeability and retention (EPR) effect, by taking advantage of the 3D architecture of blood vessels that supply the tumor, which are characterized by having fenestrae of variable sizes (ranging from 200 to 1200 nm; Figure 2.1) [24]. Moreover, the impaired lymphatic drainage prevents nanomaterials removal, leading to their retention within the tumor microenvironment [25]. Simultaneously, the accumulation of nanomaterials in off-target organs or their rapid elimination from the body (*e.g.* by renal filtration or through the reticuloendothelial system (RES)) must be avoided.

Once inside the tumor tissue, nanomaterials must be capable of migrating and also be homogeneously internalized by cancer cells [26]. However, such internalization may be hampered by tumor's high interstitial fluid pressure that results from a defective lymphatic drainage [27].

After nanomaterials successful accumulation within tumor tissue, the PTT is performed by irradiating the tumor zone with a laser light (Figure 2.1). The effectiveness of this therapeutic

modality is dependent on the capacity of nanomaterials to absorb radiation emitted by the laser. A significant or negligible interaction may occur between radiation and biological components like proteins, melanin, hemoglobin, collagen and water [28]. All these biological components have a low or residual absorption within the 750-1000 nm wavelength range (near infrared (NIR)) [28]. Therefore, the use of NIR light in cancer PTT is crucial since this radiation displays low off-target interactions and high penetration depth (up to 1-2 cm, that is dependent on the type of tissue under irradiation, the wavelength and the power density of the laser light used) [29]. The knowledge of the laser light properties is fundamental to maximize light-nanomaterials interactions in order to guarantee a selective and effective hyperthermia, that produces irreversible damages on cancer cells leading to their death by necrosis (such effect is usually attained for temperatures above 50 °C) [4]. Moreover, the laser beam is directed to the tumor zone, thus preventing any side effects resulting from nanomaterials that were accumulated in off-target organs [8, 30]. Exceptionally, nanomaterials accumulated in skin can cause off-target hyperthermia and, consequently, origin an undesired outcome since this organ is inevitably irradiated during the PTT [12].

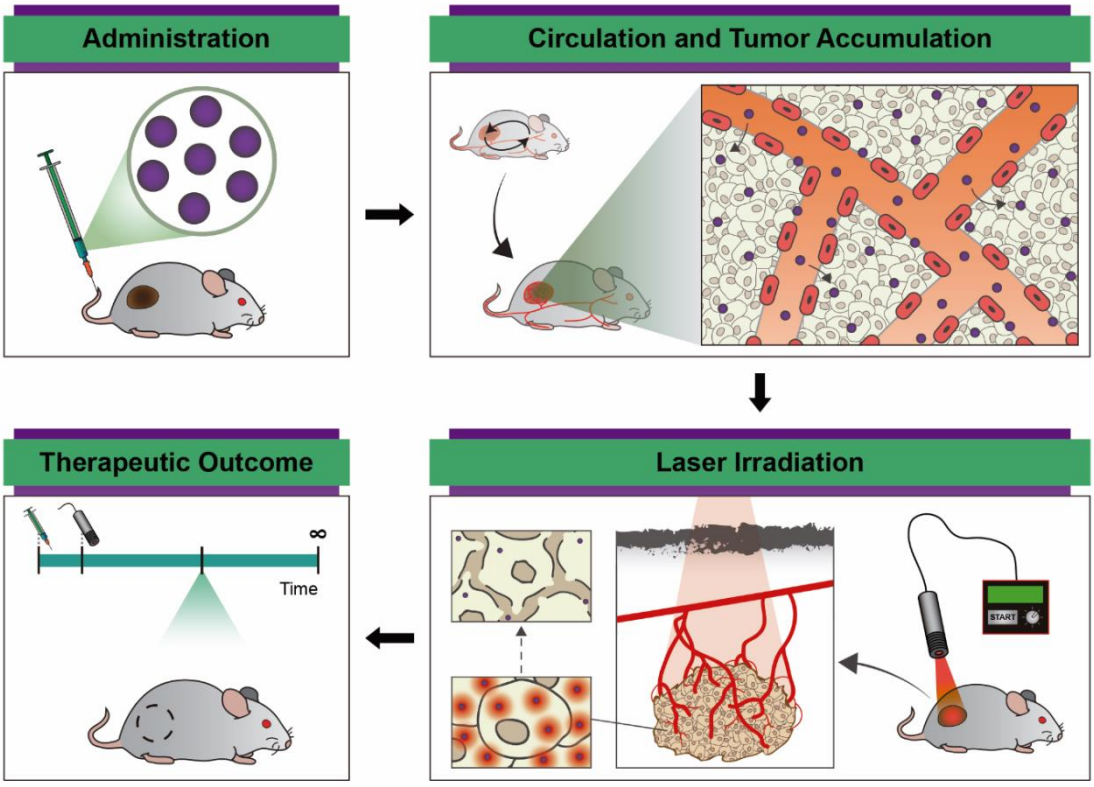

Figure 2.1. Representation of the several events that occur during the PTT mediated by nanomaterials. First nanomaterials are administered and can accumulate in the tumor through the so-called EPR effect. Afterward, the tumor zone is irradiated and nanomaterials induce hyperthermia with high spatial-temporal resolution. Finally, the therapeutic effect is monitored and may have as outcome mice's survival due to tumor elimination.

To date, different types of nanomaterials (both organic and inorganic) have been studied for cancer PTT. Among the inorganic nanomaterials, gold-based nanostructures like gold nanocages, nanohexapods, nanorods (GNR), nanoshells and nanostars have been deeply investigated for this biomedical application [31, 32, 33, 34]. More recently, researchers also began investigating the applicability of gold nanobipyramids for cancer PTT [35]. Furthermore, carbon-based nanostructures such as carbon nanotubes (CNT) and nanographene oxide (nGO) have also been explored as PTT agents [12, 13]. Currently, other inorganic nanostructures based on copper (Cu), molybdenum (Mo), tungsten (W), iron (Fe) and palladium (Pd) are being studied for tumor photoablation [7, 14-17]. The Cu-based nanostructures include copper sulfides (*e.g.* $Cu_{2-x}S$ nanodots, $Cu_{7.2}S_4$ nanocrystals or CuS nanoparticles), selenides (*e.g.* $Cu_{2-x}Se$ nanocrystals) and bismuth sulfides (*e.g.* Cu_3BiS_3 hollow nanospheres) [10, 36-39]. Regarding Mo and W-based nanomaterials, their oxides (*e.g.* MoO_{3-x} hollow nanospheres, WO_3 nanoparticles) and disulfides (MoS_2 and WS_2 nanosheets) have been the most selected for this particular biomedical application [9, 15, 26, 40]. Fe-based nanomaterials such iron oxides (*e.g.* Fe_3O_4 nanoparticles), sulfides (FeS nanoplates), diselenides ($FeSe_2$ nanoparticles) and prussian blue nanostructures ($Fe_4[Fe(CN)_6]_3$; PB) have also revealed suitable properties to act as PTT agents [17, 41-43]. Regarding Pd-based nanomaterials, researchers have been mainly focused on the applicability of Pd nanosheets for PTT [7, 44]. On the other hand, the application of organic nanomaterials for cancer PTT is not so developed as for inorganic materials. In literature, polyaniline (PANI), polypyrrole (PPy), poly(3,4-ethylenedioxythiophene) (PEDOT) and other polymeric materials have been used for cancer PTT [8, 18, 45-47].

Overall, several approaches have been followed to further improve the PTT capacity of these nanostructures (both organic and inorganic). Researchers used different strategies to (i) improve nanomaterials accumulation in tumor, (ii) augment nanomaterials' intrinsic capacity to produce photoinduced heat or (iii) optimize the parameters related to the laser light. A detailed description of the *in vivo* therapeutic outcome attained so far by adopting such strategies is summarized in Table S.2.1 (supplementary information).

2.4. Approaches used to improve nanomaterials accumulation in tumors

In order to mediate an effective and selective hyperthermia upon laser irradiation, nanomaterials must be accumulated in the tumor tissue and also be internalized by cancer cells. The fulfillment of these milestones is affected by nanomaterials' size, shape, surface charge, and corona composition, as well as by the presence of targeting ligands on their surface (Figure 2.2). Therefore, the modulation of these features is currently being explored to improve nanomaterials' mediated PTT (summarized in Table 2.1; presented after the conclusion section).

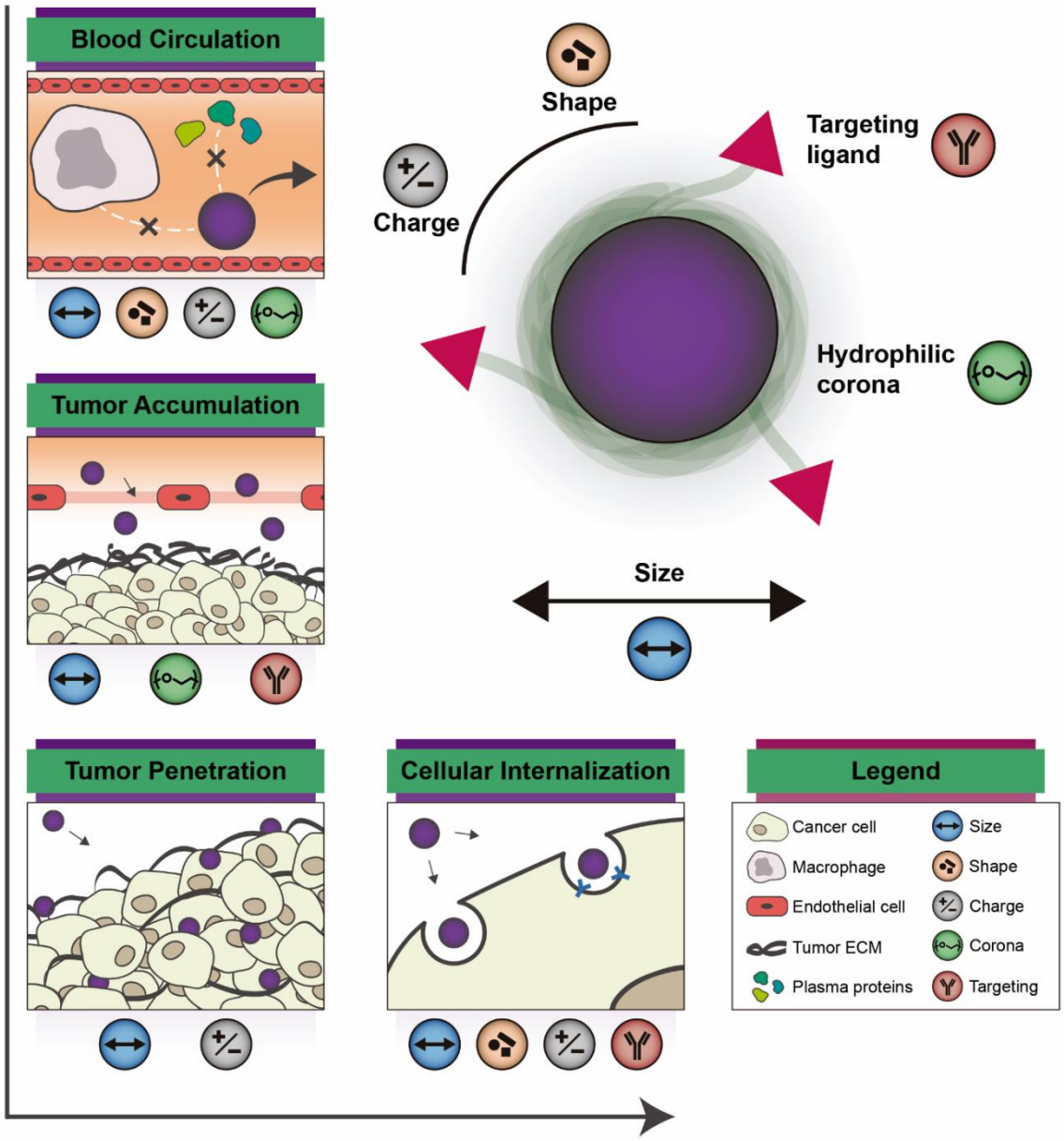

Figure 2.2. Schematic illustration of the parameters of the nanomaterials that influence their blood circulation, accumulation and penetration in the tumor, and internalization by cancer cells. The key mediators of each process are indicated below the respective panels through the use of round-shaped icons.

2.4.1. Size

The blood clearance or off-target accumulation in RES organs (liver and spleen) of nanomaterials are size dependent. In literature, it is described that nanostructures with a size bellow 3-5 nm tend to be rapidly cleared through renal filtration, which constitutes a drawback for their accumulation in the tumor tissue [48]. Moreover, nanostructures with a diameter lower than 50 nm tend to be off-target accumulated in the liver, whereas those larger than 200 nm

are more likely to become accumulated in spleen and in liver [25, 27, 49]. By taking such restrictions into account, nanomaterials aimed to be accumulated within the tumor through the EPR effect must have an appropriate size in the range between 100 and 200 nm [25]. Still, these are general considerations and the optimization of nanomaterials' size must be performed for each type of photothermal agent in order to attain a proper distribution in the body and therapeutic performance. In this context, Tang and co-workers observed that by reducing the Pd-poly(vinylpyrrolidone) (PVP) nanosheets' size from 41 to 4.4 nm, their liver uptake decreases from ≈ 45 to ≈ 35 % of the total injected dose per gram of tissue (ID g^{-1}) [7]. In another study, Akhavan and Ghaderi demonstrated that PEGylated graphene oxide (GO) derivatives with a size of ≈ 61 nm were more effective in cancer PTT than their ≈ 2 μm sized equivalents, since the smaller nanomaterials have a higher tumor-homing capacity (≈ 8.9 *vs.* ≈ 7.3 % ID g^{-1}) and their uptake by liver (≈ 17 *vs.* ≈ 26 % ID g^{-1}) and spleen (≈ 12 *vs.* ≈ 22 % ID g^{-1}) is lower [50].

In addition to the influence of nanomaterials' size in tumor accumulation, this parameter also has a direct impact on nanomaterials tumor penetration and cellular internalization [51]. Once again, the optimization of the size is decisive for improving nanomaterials therapeutic efficacy. In this context, Wang and co-workers substantiated that PEGylated gold-based capsules with a size of 207 x 105 nm can penetrate and achieve a wide distribution within the tumor mass, while those with a size of 125 x 95 nm are mainly accumulated in the tumor periphery [52]. Due to this fact, the 207 x 105 nm sized nanocapsules were able to mediate a stronger photothermal effect *in vivo*. In another work, Wang and co-workers observed that 80 and 100 nm sized PEGylated MoS_2 nanosheets are better internalized by cancer cells than those with 300 nm, rendering them as the most suitable for being applied in cancer PTT [15]. In a recent study, Zhang *et al*. adjusted the size of GO to improve its uptake by cancer cells and their results revealed that the smallest nanosheets (< 50 nm) achieve an higher internalization [53].

2.4.2. Shape

The nanomaterial's shape is another feature that has a huge impact on its blood circulation time, tumor uptake, and cellular internalization [54]. Although the shape contribution on these bioprocesses tends to be different for each type of nanostructure, the modulation of this property can be explored for improving nanomaterials' mediated PTT. Tang and co-workers verified that by coating Pd-PVP nanosheets with silica (transition from a 2D material to a nanosphere), their uptake by cancer cells is increased by ≈ 4.7-fold, leading to an enhanced photothermal effect [55]. Moreover, Wang *et al*. reported that PEGylated gold nanohexapods display a 1.2- and 3.2-fold higher internalization by cancer cells than PEGylated gold nanocages and PEGylated GNR, respectively [31]. In contrast, under *in vivo* conditions, PEGylated gold nanocages displayed a low blood circulation time and a high liver uptake (≈ 62 % ID g^{-1}), which

resulted in a low tumor accumulation (≈ 2.6 % ID g^{-1}). On the other hand, PEGylated GNR and gold nanohexapods had superior blood circulation times, that led to a greater tumor accumulation (GNR: ≈ 8.4 % ID g^{-1}; nanohexapods: ≈ 7.2 % ID g^{-1}). Based on these remarks, the application of PEGylated gold nanohexapods in cancer PTT seems to be a promising strategy due to their improved tumor accumulation and cellular uptake.

2.4.3. Surface charge

The surface charge exhibited by nanomaterials is another parameter that has to be taken into account when an augmented cellular internalization is aimed. In general, positively charged nanostructures tend to be better internalized by normal and cancer cells since these materials are able to interact with the negatively charged components of cells' membrane [56]. In particular, cancer cells have on their plasma membrane a higher number of negatively charged components (*e.g.* phosphatidylserine or sialic acid), which further promote the uptake of positively charged nanomaterials [57]. In this context, Tang and co-workers functionalized Pd-PVP nanosheets with poly(ethyleneimine) (PEI; polycation) and confirmed that this modification increases their cellular internalization by ≈ 1.9-fold [55]. Moreover, the functionalization of silica coated Pd-PVP nanosheets with amine groups also revealed an improved uptake (2.75-fold increase), which is crucial for attaining a heightened photothermal effect [55].

Nevertheless, the surface charge of nanomaterials must be properly tuned since it also mediates nanodevices interaction with RES, blood components and elements of the extracellular matrix of the tumor. Nanomaterials with a highly charged surface (positively or negatively) have a greater uptake by RES cells and liver, which has a direct impact on their capacity to reach the tumor tissue [58]. Furthermore, serum proteins can also be adsorbed on nanomaterials' charged surface, which may lead to the opsonization and clearance of these materials [59]. Moreover, nanomaterials' surface charge can impair their tumor penetration capacity by favoring interactions with the components of the extracellular matrix of the tumor, such as hyaluronic acid (HA; for positively charged nanomaterials) or collagen (for negatively charged nanomaterials) [27]. Owing to these facts, the so-called neutral nanomaterials, which have a zeta potential (ζ) between -10 and +10 mV, are considered the most appealing for cancer-related applications [27].

As discussed above, positively charged nanomaterials may display a higher internalization by cancer cells but an excessive surface charge can also impair nanomaterials accumulation in tumors. To circumvent this pitfall, Wang *et al.* prepared PEGylated gold nanostars whose charge changes according to the pH of the extracellular environment [34]. Such feature was achieved by controlling the content of amine and carboxyl groups on the surface of the nanostars. In

their study, the nanostars with a ratio of four amines to one carboxyl group showed a high differential uptake by cancer cells, *i.e.*, these presented a low internalization at pH 7.4 and an enhanced internalization at pH 6.4. These results may be explained by the surface charge of the nanostars since these are slightly negative at physiological pH (ζ ≈ -14 mV) and become neutral (ζ ≈ - 6 mV) at the pH characteristic of the tumor microenvironment. *In vivo*, these carboxyl/amine functionalized nanostars demonstrated a high tumor uptake (≈ 10 % ID g^{-1}), which was sufficient to allow tumors elimination under NIR laser irradiation. In stark contrast, nanostars functionalized only with carboxyl (ζ ≈ - 27 mV) or amine (ζ ≈ + 13 mV) groups presented a tumor accumulation of ≈ 4 and ≈ 2 % ID g^{-1}, respectively. Therefore, the PTT mediated by these nanomaterials only caused a reduction of the tumor growth. In particular, the majority of the amine functionalized nanostars became accumulated in liver (> 120 % ID g^{-1}), thus leading to a lower tumor uptake.

2.4.4. Corona composition

Nanomaterials' corona composition is another important factor that influences their biological fate. The functionalization of nanomaterials' surface with PEG is known for improving nanodevices hydrophilicity and biocompatibility, features that are fundamental for their successful biological application [60]. Moreover, PEG functionalization can increase nanomaterials' blood circulation time and also reduces their opsonization and recognition by the RES, thus leading to their improved accumulation in the tumors [12, 44, 61]. Therefore, the appropriate PEGylation of the different types of nanomaterials has been pursued in order to improve their potential for cancer PTT. Zhou *et al*. verified that PEGylated CuS nanoparticles have a higher blood residence than citrate coated CuS nanoparticles and almost 3-fold higher tumor accumulation (7.6 % ID g^{-1}) [37]. Compared to the PEGylated nanoparticles, the citrate coated nanomaterials displayed a higher uptake by the liver (≈ 44 *vs*. ≈ 23 % ID g^{-1}) and spleen (≈ 34 *vs*. ≈ 9 % ID g^{-1}), resulting in a lower tumor uptake (2.6 % ID g^{-1}). Choi *et al*. encapsulated GNR in photocrosslinked chitosan-Pluronic® F-68 conjugates and verified that this modification increases nanomaterials tumor accumulation from ≈ 12 to ≈ 117 % ID g^{-1} [11]. Due to their superior tumor-homing capacity, the PTT mediated by these nanodevices resulted in tumor eradication while when non-coated GNR were used only a slight decrease in the rate of tumor growth was noticed.

On the other hand, CNT coated with PEGylated poly(maleic anhydride-*alt*-1-octadecene) (C_{18}-PMH-mPEG) showed a blood circulation half-life ($t_{1/2}$) of ≈ 30.8 h and a tumor accumulation of ≈ 30 % ID g^{-1} [62]. In contrast, the CNT coated with 1,2-distearoyl-*sn*-glycero-3-phosphoethanolamine-*N*-(methoxy PEG) (DSPE-mPEG) had a lower tumor accumulation (4 % ID g^{-1}), resulting from their lower blood circulation time ($t_{1/2}$ ≈ 3.5 h) and higher liver uptake (≈ 69 *vs*. ≈ 28 % ID g^{-1}) [62]. In other studies, C_{18}-PMH-mPEG was also successfully used

to coat reduced nGO and Mo oxide nanosheets, conferring these nanomaterials a tumor-homing capacity that granted tumors eradication upon laser irradiation [63, 64]. PEGylation of W, Fe, Pd and conjugated polymer-based nanostructures also allowed the production of materials with a high tumor-homing capacity and that were efficiently applied for cancer PTT [8, 17, 26, 44, 65].

However, the PEGylation of nanomaterials to enhance their biologic properties is not always a straightforward process since the molecular weight and the density of the PEG immobilized on the surface of the nanostructures can affect their biodistribution [12, 66]. In this regard, Liu *et al*. thoroughly investigated the coating of CNT with C_{18}-PMH-mPEG with different PEG lengths (2 and 5 kDa) and densities (5 to 100 %) [12]. The results revealed that by increasing the PEG length and density, the CNT blood circulation time is extended, which in turn boosts their accumulation in the tumor and skin (CNT accumulation in the skin can induce an off-target heating and simultaneously decrease the amount of radiation that reaches the tumor during PTT). Furthermore, an opposite trend was noticed for CNT accumulation in RES organs. Therefore, the CNT coated with C_{18}-PMH-mPEG with a PEG density of 10 % and a molecular weight of 5 kDa were considered the most appealing for cancer PTT, since these displayed a suitable blood circulation time ($t_{1/2}$ = 12.8 h), high tumor accumulation (≈ 15 % ID g^{-1}) and scarce uptake by skin (≈ 3 % ID g^{-1}). Shi and co-workers noticed that PEGylated Pd nanosheets prepared using a thiolated mPEG to Pd-PVP nanosheet mass ratio of 1 to 1 are optimal since the incorporation of a higher PEG mass did not significantly improve the blood circulation time of the nanosheets ($t_{1/2}$ ≈ 30 h) [44]. However, the tumor accumulation of these nanosheets was further increased from ≈ 8 to ≈ 12 % ID g^{-1} by increasing the PEG molecular weight from 5 to 10 kDa, thus allowing tumor eradication upon NIR laser irradiation using a low power density.

To further improve nanomaterials accumulation in tumors, other coatings are currently being investigated. A variety of hydrophilic polymers such as poly(carboxybetaine), poly(glycerol), poly(2-ethyl-2-oxazoline), PVP and poly(N-(2-hydroxypropyl) methacrylamide) have been used for such purpose [67]. Zhou *et al.*, observed that PVP coated CuS nanodots display a higher resistance to protein adsorption than those prepared with mPEG, which is fundamental for their efficient tumor accumulation (≈ 3.6 % ID g^{-1}) and low uptake by RES organs (≈ 4.3 % ID g^{-1} of liver; ≈ 1 % ID g^{-1} of spleen) [14].

Moreover, coatings produced with red blood cells' (RBC) and macrophages' membranes have been added to nanomaterials' surface as an alternative to polymeric-based coatings since these coatings exhibit long-blood circulation times [33, 68, 69]. Piao and co-workers reported that the incorporation of PVP coated gold nanocages within vesicles derived from RBC ghosts amplifies their $t_{1/2}$ from 1 to 9.5 h [68]. Accordingly, the RBC coating was also responsible for enhancing the tumor accumulation of the nanocages from 4.37 to 8.34 % ID g^{-1} and subsequently, an improved PTT was attained. Recently, Xu *et al*. demonstrated that by coating gold nanoshells with macrophages' membranes, their blood circulation time is extended and tumor

accumulation is amended from ≈ 1.6 to ≈ 7.5 % ID g^{-1} [33]. Additionally, the modification of the nanoshells' surface also reduced their accumulation in liver and spleen, from about 27 and 14 to 14 and 9 % ID g^{-1}, respectively. *In vivo*, the PTT mediated by non-coated gold nanoshells only produced a reduction of the tumor growth, while when macrophage-based coated nanomaterials were used a potent tumor regression was obtained.

2.4.5. Targeting ligands

Nanomaterials' surface can be further tailored with targeting moieties in order to raise their specificity towards cancer cells. As previously substantiated for CNT, nGO, gold, Cu, W, Fe and PANI-based nanomaterials, the outcome of the PTT mediated by these nanostructures can be improved by targeting receptors overexpressed on the surface of cancer cells [9, 30, 70-74]. Liang *et al*. verified that by grafting anti-CD44 antibodies on PEGylated gold nanostars, their accumulation in tumor is enhanced by more than 2-fold and, simultaneously, their uptake by RES organs is reduced [72]. Due to these features, the CD44 targeted nanostars produced a greater therapeutic effect upon laser irradiation than their non-targeted equivalents [72].

Nanomaterials surface can also be simultaneously functionalized with more than one targeting ligand to further increase the therapeutic outcome achieved with the PTT [75, 76]. Jang *et al*. demonstrated that the dual functionalization of nGO with Pluronic® F-127-Folic acid (FA) and Pluronic® F-127-(arginine-glycine-aspartic acid) (RGD) conjugates (25 % density for each ligand) heightens the tumor accumulation of this nanomaterial, leading to tumor eradication upon NIR laser irradiation [76]. In contrast, nGO functionalized only with RGD (density of 25 %) or FA (density of 25%)-based conjugates promoted a similar reduction of the tumor growth, however this effect was smaller than that reached by the dual-functionalized nGO.

The targeting of the endothelial cells present in tumor vasculature has also been explored for ameliorating the accumulation of nanomaterials in the tumor zone [77]. Neves *et al*. functionalized CNT with DSPE-PEG-Annexin V to target the phosphatidylserine residues available on the membranes of tumor cells and endothelial cells found in the tumor vasculature [70]. Such approach allowed CNT to be almost 7-times more accumulated in tumor (≈ 5 % ID g^{-1}) [70]. Additionally, the targeting of angiogenic biomarkers present on tumor vasculature has also been exploited to grant nanomaterials accumulation in metastases. To accomplish that, Yang and co-workers functionalized PEGylated nGO with an anti-follicle stimulating hormone receptor (FSHR) antibody and noticed that this functionalization is able to rise the accumulation of nanomaterials in breast cancer lung metastasis from about 5 to 19.7 % ID g^{-1} [78].

Yet, the functionalization of nanomaterials is still regarded as a complex and a delicate process. In some cases, the complete functionalization of nanomaterials' surface does not guarantees

an improvement of nanomaterials accumulation in tumors [71, 79]. In fact, targeted nanomaterials demand an appropriate ligand density for accomplishing such purpose. Lee *et al*. verified that nGO coated with Pluronic® F-127-FA conjugates with FA densities of 50 and 100 % display a similar tumor-homing capacity [71]. In contrast, nanomaterials functionalized with lower FA densities (10 and 25 %) exhibited a tumor accumulation comparable to that of non-FA functionalized nGO, and, therefore, mediated a weaker photothermal effect. Furthermore, the selectivity of targeted nanostructures can also be hampered by the formation of a protein corona on their surface [80]. To circumvent this possibility some nanomaterials are engineered to only expose their targeting moieties upon reaching the tumor microenvironment [81]. Alternatively, the immobilization of targeting ligands in PEG segments with higher lengths while leaving shorter PEG segments non-functionalized can attenuate the loss of selectivity mediated by the adsorption of serum proteins on the surface of nanomaterials [82]. In addition, the length of the spacer-arm to which the targeting ligand binds is also a decisive parameter for governing the biodistribution of these nanomaterials. To address this issue, Liu and co-workers coated CNT with DSPE-PEG-RGD conjugates containing different PEG lengths (2000 or 5400 Da). Their results revealed that CNT coated with DSPE-PEG_{5400}-RGD show a superior tumor accumulation (≈ 13 % ID g^{-1}) and lower uptake by liver (≈ 20 % ID g^{-1}) than the DSPE-PEG_{2000}-RGD coated CNT (≈ 5 % ID g^{-1} of tumor; ≈ 30 % ID g^{-1} of liver) [83]. Interestingly, CNT coated with DSPE-PEG_{2000}-RGD had only a slightly higher tumor accumulation than those coated with DSPE-PEG_{5400} (≈ 4 % ID g^{-1}). Such may be attributed to the higher resistance to protein adsorption displayed by the CNT coated with DSPE-PEG_{5400}. This fact may also be the reason for the higher blood circulation time ($t_{1/2}$ ≈ 2 h) and lower liver accumulation displayed by CNT functionalized with DSPE-PEG_{5400} derivatives, thus emphasizing the importance of the PEG length on the biodistribution of targeted nanomaterials.

2.5. Strategies used to augment nanomaterials' capacity to produce photoinduced heat

The application of nanomaterials with a high NIR absorption and good photothermal conversion efficiency for cancer PTT is highly desirable since these can produce a larger temperature variation upon NIR irradiation (Figure 2.3). Therefore, researchers are currently using a variety of strategies to obtain nanomaterials with these desired properties (see Table 2.2 for further details; presented after the conclusion section).

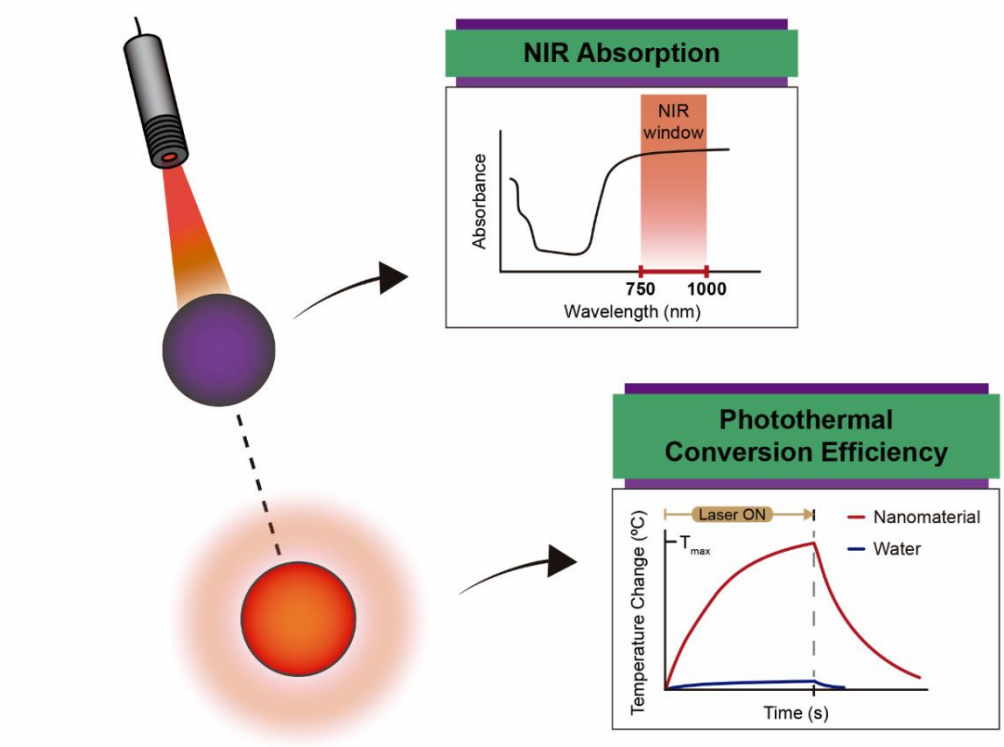

Figure 2.3. Schematic representation of the key parameters that influence nanomaterials' capacity to generate heat upon interaction with NIR light.

2.5.1. Production of new nanomaterials

Nanomaterials' capacity to produce heat under NIR laser irradiation has been enhanced through the synthesis of new materials with a higher photothermal conversion efficiency and NIR absorption [9, 40, 43, 84]. Copper sulfide nanostructures have been produced with different Cu to S stoichiometric ratios in order to obtain more efficient photothermal agents. In recent studies, nanocrystals based on Cu_9S_5 showed a photothermal conversion efficiency of ≈ 26 %, while those composed of $Cu_{7.2}S_4$ had a photothermal conversion efficiency ≈ 57 % (at 980 nm) [10, 85].

Regarding Pd and gold-based nanostructures, their photothermal capacity is influenced by their shape and this parameter has been optimized during nanostructures synthesis to obtain agents with an improved PTT capacity [31, 86]. Xiao *et al*. prepared porous Pd nanoparticles that have a higher NIR absorption than that displayed by Pd nanocubes, non-porous Pd nanoparticles, and Pd polyhedrons [86]. Such feature makes their application in cancer PTT more advantageous [86]. In addition, the photothermal conversion efficiency of gold nanomatryoshkas, nanocages, bellflowers, nanobipyramids and nanorods can be superior to 60 %, which makes them one of the most promising gold-based photothermal agents (Table 2.2) [87-91].

Moreover, nanomaterials based on Mo, W, Fe, and conjugated polymers with an upgraded photothermal capacity have also been produced for application in cancer PTT [42, 92-95]. Yang *et al*. prepared PEGylated FeS nanoplates with a ≈ 17 times higher NIR absorption than that displayed by Fe_3O_4 nanoparticles [42]. Consequently, the FeS nanoplates were able to mediate the production of a photoinduced heat to about 70 °C while, in the same conditions, the Fe_3O_4 nanoparticles only increased the temperature to ≈ 45 °C. In another work, Kim and co-workers synthesized poly(3,4-propylenedioxyselenophene) (PProDOS) nanoparticles that had a slightly superior NIR absorption than PEDOT nanoparticles and, consequently, produced a higher photoinduced heat (ΔT ≈ 10 °C *vs*. ΔT = 6 °C) [95].

Another strategy used to improve nanomaterials' mediated PTT comprises the synthesis of materials that are responsive to the pH or oxygen gradient of the tumor microenvironment. PANI-based nanoparticles in acidic media (≈ pH 3), in contact with hydroxyl radicals or in the presence of bio-dopants, change from the emeraldine base (EB) to the emeraldine salt (ES) form, that displays an augmented NIR absorption [18, 96]. Recently, Ju and co-workers polymerized a PANI shell at the surface of gold nanoparticles, enabling a heightened NIR absorption at the range of pH values found in tumor microenvironment [97]. In particular, PANI-based nanoparticles with a 16 nm gold core displayed the lowest NIR absorption at pH 7.4 while at pH 6.5 these had a high absorption. This difference led to a temperature increase under NIR laser irradiation to ≈ 40 °C and ≈ 53 °C, at pH 7.4 and 6.5, respectively. A similar responsiveness to the tumor microenvironment was also demonstrated for Mo oxide nanosheets and WO_{3-x} nanodots [64, 98].

The production of hybrid nanostructures composed by different types of photothermal agents has also been pursued to obtain materials with an improved photothermal capacity. These structures are usually obtained by combining photothermal agents with gold, PPy or polydopamine due to the ability of the latter be grown or polymerized on the surface of nanomaterials [99-104]. In this regard, Li *et al*. verified that by coating PEI-gold nanostars with polydopamine, their photothermal conversion efficiency is improved from 36.1 to 49.9 % (at 808 nm) [104]. In other works, PEGylated gold-silver star- and urchin-shaped hybrid nanostructures demonstrated a photothermal conversion efficiency of 79.01 and 80.4 % (at 808 nm), respectively, which are one of the highest efficiencies reported so far (see Table 2.2 for further details) [99, 100].

2.5.2. Optimization of nanomaterials' size

Upon irradiation, nanomaterials can scatter and absorb light, being this latter phenomenon responsible for the heat generation [105]. Smaller nanomaterials scatter less light and can display a faster heat transfer to the surrounding environment due to their large surface

area/volume ratio [106, 107]. In this way, nanomaterials with an improved photothermal capacity can be obtained by selecting nanostructures based on their size [7, 15, 107, 108]. Wang *et al*. verified that despite 100 nm sized MoS_2 nanosheets exhibiting a higher NIR absorption than their 80 nm equivalents, the latter are capable of producing a greater temperature variation under laser irradiation due to their improved photothermal efficiency ($\Delta T \approx 4.5\ ^{\circ}C$ *vs.* $\Delta T \approx 6\ ^{\circ}C$) [15]. Tang *et al*. prepared 41 and 4.4 nm sized Pd-PVP nanosheets and verified that the smallest nanomaterials show the highest photothermal conversion efficiency (52 *vs*. 27.6 % at 808 nm) [7]. Accordingly, the 4.4 nm nanosheets were able to raise the temperature to ≈ 50 °C under NIR laser irradiation, while the 41 nm nanomaterials only elevated it to ≈ 37.5 °C.

On the other hand, the absorption spectrum of some nanomaterials can be fine-tuned towards the NIR region by increasing nanomaterials' size. Peng *et al*. observed that by augmenting the size of citrate and PEG functionalized Fe_3O_4 nanoparticles from 120 to 380 nm, a red-shift in their absorption spectrum is attained [109]. Due to this phenomenon, the 380 nm sized Fe_3O_4 nanoparticles exhibited an improved NIR absorption and mediated the highest temperature increase under NIR laser irradiation when compared to their equivalents with smaller dimensions (120, 240 and 300 nm). Ye *et al*. verified that by increasing the length of gold nanotubes from 300 to 530 nm, a shift in their absorption towards the NIR region is also observed [110]. In this case, the gold nanotubes with a length of approximately 370 nm were considered optimal systems since these showed the highest absorption at 800 nm.

2.5.3. Chemical treatment of nanomaterials

The reduction of nGO is the most employed strategy to enhance its NIR absorption by restoring the aromatic lattice of this nanomaterial [50, 63]. Yang *et al*. demonstrated that the reduction of GO derivatives with hydrazine hydrate produces reduced GO (rGO)-based nanomaterials that have a 3-4 times higher NIR absorption than nGO, leading to the production of a higher photoinduced heat (≈ 58 °C *vs.* ≈ 44 °C) [63]. Akhavan and Ghaderi reported that the photodegradation and subsequent reduction of nGO yields reduced graphene oxide nanomesh (rGONM) with a NIR absorption ≈ 4.2 times higher than that of reduced nGO [50]. In this way, the rGONM induced, under NIR laser irradiation, an increase in temperature up to ≈ 57 °C, while in the same conditions the reduced nGO only elevated the temperature to ≈ 42 °C.

The photothermal capacity of PB nanostructures has been improved by doping these materials with $Mn^{2+}$and Gd^{3+} [111, 112]. PEGylated PB nanocubes doped with 15% Mn^{2+} displayed an almost 2-fold increased NIR absorption that lead to an improved temperature variation ($\Delta T \approx 10\ ^{\circ}C$), upon material irradiation [111].

2.5.4. Assembling of nanostructures

In some cases, the assembly of nanostructures into clusters or vesicles can be used to provoke a red-shift in their absorption profile towards the NIR region and, consequently, enhance their photothermal capacity [41, 113, 114]. Shen *et al*. prepared clusters of Fe_3O_4 nanoparticles that display a ≈ 3.6-fold higher NIR absorption than the individual Fe_3O_4 nanoparticles [41]. The clustered Fe_3O_4 nanoparticles elicited the highest hyperthermia (≈ 56 °C *vs.* ≈ 50 °C) and the most potent antitumoral effect upon NIR laser irradiation due to their superior NIR absorption. In another work, Huang *et al*. synthesized PEG-poly(caprolactone) functionalized gold nanoparticles, which did not display any NIR absorption, and assembled them into gold-based nanovesicles [113]. The assembled nanovesicles presented a high NIR absorption and a photothermal conversion efficiency of 37 %, which was higher than that of GNR (22 % at 808 nm). Owing to their superior photothermal efficiency, the assembled nanovesicles increased the temperature of the tumors by ≈ 18 °C and mediated their eradication under NIR laser irradiation. In the same conditions, the GNR were only able to induce a hyperthermia of ≈ 10 °C and a reduction of the tumor growth, thus revealing the advantage of the assembly of nanovesicles for the desired biomedical application.

2.5.5. Sorting of nanomaterials

The commonly available methods to produce CNT (*e.g.* high-pressure carbon monoxide conversion) yield a mixture of nanostructures with different chiralities, some of which have a low NIR absorption. For this reason, sorting CNT with defined chirality is a successful strategy for improving the photothermal performance of these materials [115, 116]. Antaris and co-workers demonstrated that PEGylated chirality sorted (6,5) CNT have a higher NIR absorption than non-sorted CNT [116]. Consequently, the sorted CNT were able to mediate under NIR laser irradiation a hyperthermia to ≈ 51 °C and tumor eradication for 3 in 4 mice. For mice treated with non-sorted CNT, tumor growth inhibition was not observed since these nanomaterials only induced a hyperthermia to ≈ 44 °C due to their inferior optical properties.

2.6. Optimization of the parameters related to the laser light for improving the PTT mediated by nanomaterials

The wavelength, power density and onset of the irradiation are important players in nanomaterials' mediated PTT since their correct modulation is crucial for avoiding off-target heating of healthy tissues and also to ensure that an appropriate hyperthermia is achieved

during the therapeutic procedure [93, 117]. Therefore, various strategies have been applied to improve the outcome of this therapeutic modality by performing the adjustment of these laser light related parameters (Figure 2.4). The exposition of multiple sites to NIR light and application of multiple irradiation sessions are other strategies that have been explored to improve nanomaterials' mediated PTT (summarized in Table 2.3; presented after the conclusion section).

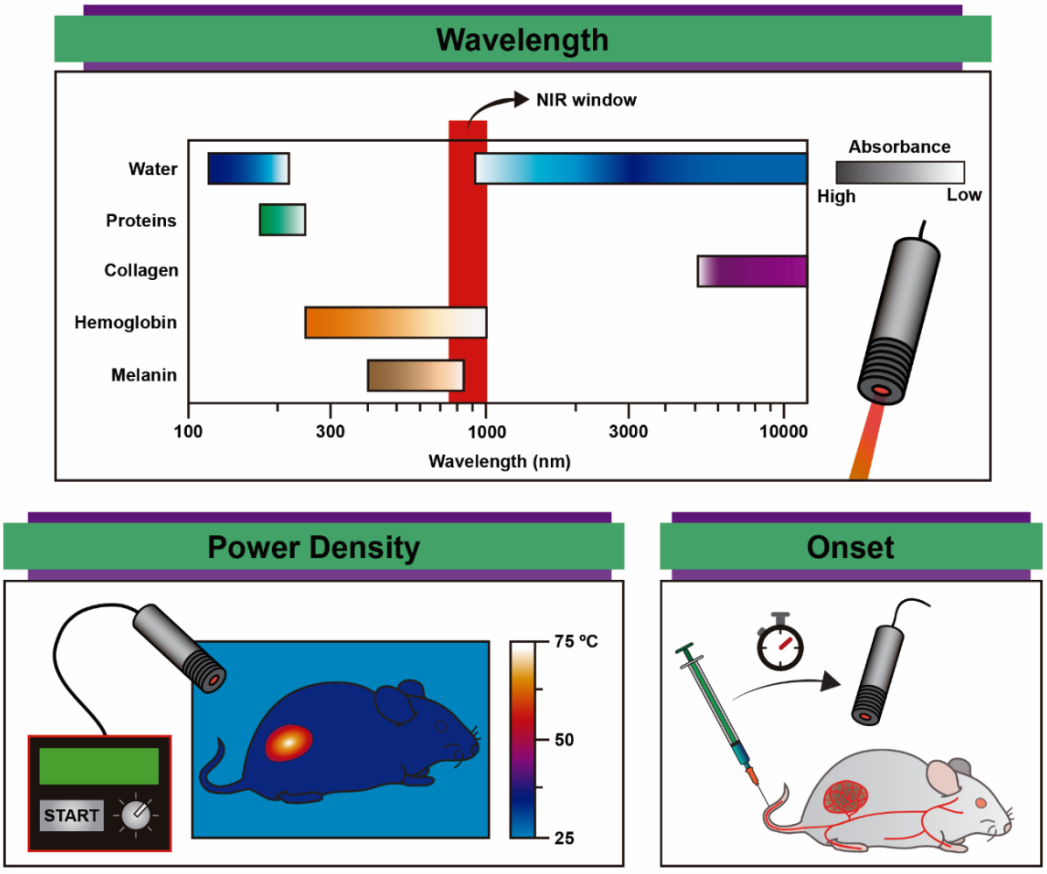

Figure 2.4. Schematic representation of the parameters related to the laser light that influence the PTT mediated by nanomaterials. In the wavelength panel, the bars represent the absorption of different bio-components and the color intensity is proportional to their absorption at that specific wavelength. The data from the wavelength panel were extrapolated from Vogel *et al.*[28].

2.6.1. Wavelength

As discussed in section 2.3, the application of NIR light is crucial in cancer PTT. However, the absorption displayed by water at wavelengths above 900 nm demands additional precautions when tissues are exposed to radiation with a wavelength superior to 900 nm in order to avoid off-target heating [28, 118, 119].

In this way, the selection of the appropriate wavelength of the NIR radiation can be pursued to improve nanomaterials' mediated PTT. Xu *et al*. verified that despite PEGylated Cs_xWO_3 nanorods having a higher absorbance at 980 nm than at 915 nm, nanostructures irradiation at 915 nm is advantageous over their irradiation at a higher wavelength, since a higher penetration and lower off-target heating are reached [119]. Tian and co-workers observed that although PVP coated $Rb_{0.27}WO_3$ nanorods display a higher absorption at 980 nm than at 808 nm, the irradiation of the nanorods with the lower wavelength light can produce a higher temperature variation, since the 980 nm light has a lower depth penetration [120].

2.6.2. Power density

The power density (total energy per second delivered into a specific area) of the NIR irradiation can be adjusted to improve the outcome of the PTT. Yang *et al*. assessed *in vivo* the PTT capacity of poly(vinyl alcohol) (PVA) coated PPy nanoparticles using different power densities [117]. When nanoparticles were irradiated at a power density of 0.1 W cm^{-2}, these mediated a hyperthermia to ≈ 42 °C that led to tumor growth reduction. In contrast, when a power density of 0.25 and 0.5 W cm^{-2} was used, a hyperthermia to about 55 and 60 °C was attained, leading to the elimination of mice's tumors. Guo *et al*. verified that $(NH_4)_xWO_3$ nanocubes mediate an increment of ≈ 45 °C in tumor's temperature when these are irradiated at a power density of 1 W cm^{-2} [93]. This hyperthermic effect was responsible for a reduction in the volume of the tumors and also for the inhibition of lung metastases. On the other hand, when PTT was performed at a power density of 0.5 W cm^{-2}, a weaker therapeutic effect was obtained, which is consistent with the lower hyperthermia attained (ΔT ≈ 33 °C).

2.6.3. Irradiation onset

The therapeutic effect achieved through nanomaterials' mediated PTT depends on the ON/OFF cycles of the radiation [9, 10]. Thereby, the hyperthermia and the therapeutic outcome can be maximized by synchronizing the onset of the laser irradiation with the maximum accumulation of the nanomaterials within the tumor. This strategy was explored by Sharker *et al.*, which verified that WO_3 nanoparticles functionalized with HA display a high tumor accumulation at 8 h post-injection (p.i.) [9]. Accordingly, these researchers noticed that the highest hyperthermia (50 °C) is obtained when the onset of the NIR laser irradiation starts on this time point (at 8 h p.i.). In another work, Zhou *et al*. verified that PVP coated CuS nanodots hit their maximum tumor accumulation (≈ 3.6 % ID g^{-1}) at 2 h p.i. and PTT performed at this time point leads to tumor eradication by using only two minutes of NIR laser irradiation [14].

2.6.4. Irradiated site

The therapeutic effect mediated by nanomaterials can also be improved by exposing simultaneously the tumor zone and metastatic sites to NIR light. This strategy was explored by Liang *et al.*, who verified that intratumorally injected PEGylated CNT remain in the tumor tissue and also become accumulated in the tumor-adjacent lymph node [121]. These zones were then exposed to NIR light and nanomaterials increased the temperature of the tumor and the lymph node to about 55 and 47 °C, respectively. Such effect was responsible for tumor eradication in 6 out of 7 mice [121]. In stark contrast, mice irradiated only in the tumor had a poor survival rate, since multiple metastases were observed in the lungs. Furthermore, it should also be highlighted that to compensate for the lower accumulation of the CNT in the lymph node (and also due to its deeper localization), this site was irradiated at a higher power density (0.8 W cm^{-2} for lymph node *vs.* 0.5 W cm^{-2} for tumor). Thus, the optimization of the irradiation site and the power density are fundamental to achieve an appropriate hyperthermia at the target sites in order for an improved photothermal effect be attained.

2.6.5. Number of irradiation sessions

The application of multiple irradiation sessions is another approach that has been used for achieving better photothermal effects. Choi and co-workers observed that chitosan-Pluronic® F-68 conjugates encapsulating GNR are able to mediate tumor eradication with two laser irradiation sessions (at 24 and 48 h p.i.) while the application of one irradiation session (at 24 h p.i.) only resulted in a reduction of the tumor growth [11]. In another work, Zhou and co-workers noticed that PEGylated $WO_{2.9}$ nanorods could mediate the elimination of mice's tumors by using a low power density (0.35 W cm^{-2}) through the application of multiple irradiation sessions (every two days during 14 days) [16]. Recently, Zhang *et al.* performed multiple irradiation sessions after administration of DSPE-PEG coated CNT (at 10 min and on day 3, 6 and 9 p.i.), and they verified that the application of NIR radiation at 10 min p.i. improves nanomaterials' tumor accumulation by about 2.6-fold, presumably due to an enhanced tumor vasculature perfusion and permeability that is promoted by the hyperthermia attained (hyperthermia enhanced EPR effect) [122]. In the same study, authors also explored DSPE-PEG-(Cys-Arg-Glu-Lys-Ala) (CREKA) functionalized CNT, which bind to fibrin, and they perceived that after administration of the targeted CNT and application of the first irradiation session (at 10 min p.i.), the hyperthermia produced greatly increases the amount of fibrin deposited in the tumor zone and such is responsible for a ≈ 3.8-fold increase in the tumor accumulation of the functionalized CNT.

2.7. Conclusion and outlook

In this chapter, the recent strategies, reported in the literature, used for improving the therapeutic outcome of the PTT mediated by gold, carbon, copper, molybdenum, tungsten, iron, palladium and conjugated polymers based nanomaterials were covered.

The application of PEG-based coatings and the inclusion of targeting ligands on nanomaterials' surface improved their tumor-homing capacity and hence their PTT capacity. Such data emphasizes the importance of pursuing the appropriate surface composition for each type of photothermal agent through the optimization of the PEG corona composition, targeting ligand density and spacer-arm length, or through the application of alternative coatings, such as those based on PVP or RCB/macrophages' membranes. Moreover, reports describing the application of targeted Mo, Pd, PPy and PEDOT based nanomaterials in cancer PTT were not found, which should motivate the development of functionalization strategies for these types of nanostructures. Nanomaterials' size, shape, and charge were not systematically optimized for each type of photothermal agent. In the particular case of the size and shape, such could be attributed to the fact that variations in these characteristics have a direct impact on nanomaterials' photothermal efficiency. Regarding nanomaterials' charge, the utilization of zwitterionic-based approaches should be further explored since it holds a great potential for improving the biodistribution of the nanostructures.

So far, several strategies have also been applied to augment the capacity of nanomaterials to generate heat under NIR laser irradiation and thus enhance their PTT potential. To accomplish that, new nanomaterials have been produced, being this the most straightforward strategy. Other approaches are currently under investigation, comprising the optimization of nanostructures' size, chemical treatment, sorting and assembling of nanostructures. However, in some of the reports describing these strategies, the photothermal efficacy of the nanostructures was only assessed *in vitro* or *in vivo* after intratumoral injection, which should motivate researchers to evaluate nanomaterials' photoablation capacity after systemic administration (*e.g.* intravenous administration) in future works. Moreover, some of these nanomaterials were not engineered to present colloidal stability, tumor-homing capacity or resistance to protein adsorption and thus, the improvement of these attributes will surely augment their PTT potential.

The optimization of the parameters related to the laser light can also improve the outcome of nanomaterials' mediated PTT. The strategies applied, until now, have been focused on the adjustment of the wavelength, power density, irradiated sites, number of irradiation sessions and on the optimization of the irradiation onset. However, these strategies were not frequently explored in the literature and were mostly applied for W-based nanostructures and to a lesser extent to others such as CNT or gold-based nanomaterials. Moreover, this type of laser-sided

optimizations does not imply modifications in the attributes of the nanomaterials and, for this reason, its implementation should be simple and further explored in cancer PTT.

Finally, excluding the influence of the differences between the tumor models (*e.g.* type and size of tumor) of the reports herein analyzed (Table S.2.1), it seems that for the bulk part of the cases and independently of the type of strategy applied to improve the PTT mediated by nanomaterials, achieving a hyperthermia to 57 °C ensures the photoablation of the tumors. Hence, the development of new strategies that endow nanomaterials with this capability or the optimization and combination of the existing ones will surely give a major contribution for their application in cancer PTT.

Table 2.1. Strategies used to improve nanomaterials' accumulation in the tumor.

Nanomaterial	Optimization	Result	Ref.
PEGylated rod-like gold nanoshell capsules	Size	PEGylated gold-based capsules with a size of 385 x 155 nm become less accumulated in the tumor zone when compared to their 125 x 95 nm and 207 x 105 nm sized equivalents; PEGylated gold-based capsules with a size of 207 x 105 nm can penetrate and achieve a wide distribution in the tumor mass, while those with a size of 125 x 95 nm become accumulated mostly in tumor periphery.	[52]
GO	Size	Small GO sheets (< 50 nm) achieve the highest internalization by cancer cells.	[53]
PEGylated MoS_2 nanosheets	Size	PEGylated MoS_2 nanosheets with a size of 80 and 100 nm are better internalized by cancer cells than those with 300 nm.	[15]
Pd-PVP nanosheets	Size	Pd-PVP nanosheets with a size of 4.4 nm have a lower uptake by the liver (≈ 35 % ID g^{-1}) than their 41 nm sized equivalents (≈ 45 % ID g^{-1}).	[7]
PEGylated GO	Size	PEGylated GO derivatives with a size of 27 nm have a lower uptake by the liver (≈ 11 % ID g^{-1}) and spleen (≈ 7 % ID g^{-1}) than their 65 nm sized equivalents (≈ 25 % ID g^{-1} of liver; ≈ 25 % ID g^{-1} of spleen).	[63]
PEGylated GO	Size	PEGylated GO derivatives with a size of ≈ 61 nm have a higher tumor-homing capacity (≈ 8.9 % ID g^{-1}) and lower uptake by the liver (≈ 17 % ID g^{-1}) and spleen (≈ 12 % ID g^{-1}) than ≈ 2 μm sized PEGylated nanomaterials (≈ 7.3 % ID g^{-1} of tumor; ≈ 26 % ID g^{-1} of liver; ≈ 22 % ID g^{-1} of spleen).	[50]
PEGylated gold nanocages, nanohexapods and nanorods	Shape	PEGylated gold nanohexapods display 1.2- and 3.2-fold higher internalization by cancer cells than PEGylated gold nanocages and nanorods, respectively; PEGylated GNR (≈ 8.4 % ID g^{-1}) and nanohexapods (≈ 7.2 % ID g^{-1}) have a higher tumor-homing capacity than nanocages (≈ 2.6 % ID g^{-1}).	[31]
Silica coated Pd-PVP nanosheets	Shape	Coating of Pd-PVP nanosheets with silica results in a ≈ 4.7-fold increase in their uptake by cancer cells.	[55]
Pd-PVP nanosheets immobilized in silica nanoparticles	Shape	Electrostatic immobilization of Pd-PVP nanosheets in amine-terminated silica nanoparticles improves their cellular uptake by ≈ 11-fold.	[123]
PEI coated Pd-PVP nanosheets	Charge	Modification of Pd-PVP nanosheets with PEI increases their cellular internalization by ≈ 1.9-fold.	[55]

Amine-terminated silica coated Pd-PVP nanosheets	Charge	Functionalization of silica coated Pd-PVP nanosheets with amine groups improves their cellular uptake by 2.75-fold.	[55]
Amine/carboxyl-terminated PEGylated gold nanostars	Charge	Amine/carboxyl-terminated nanostars have a low and enhanced internalization by cancer cells at pH 7.4 and 6.4, respectively; Amine/carboxyl-terminated nanostars display a higher tumor accumulation (≈ 10 % ID g^{-1}) than nanostars terminated with only carboxyl (≈ 4 % ID g^{-1}) or amine groups (≈ 2 % ID g^{-1}); Amine-terminated nanostars have a high liver uptake (> 120 % ID g^{-1}).	[34]
Chitosan-Pluronic® F-68 conjugates encapsulating GNR	Corona	Chitosan-Pluronic® F-68 conjugates encapsulating GNR have a superior tumor accumulation when compared to non-modified GNR (≈ 117 *vs.* ≈ 12 % ID g^{-1}).	[11]
RBC membrane coated PVP-gold nanocages	Corona	Incorporation of PVP-gold nanocages within vesicles derived from RBC membranes improves their $t_{1/2}$ from 1 to 9.5 h; RBC coating also improves the tumor accumulation of nanomaterials from 4.37 to 8.34 % ID g^{-1}.	[68]
Macrophage cell membrane coated gold nanoshells	Corona	Coating of Au nanoshells with macrophage cell membrane extends their blood circulation time and improves their tumor accumulation from ≈ 1.6 to ≈ 7.5 % ID g^{-1}; The coating also reduces the liver and spleen accumulations from about 27 and 14 to about 14 and 9 % ID g^{-1}, respectively.	[33]
C_{18}-PMH-mPEG and DSPE-mPEG coated CNT	Corona	C_{18}-PMH-mPEG coated CNT have a higher blood circulation time ($t_{1/2}$ ≈ 30.8 h) and tumor accumulation (≈ 30 % ID g^{-1}) than DSPE-mPEG coated CNT ($t_{1/2}$ ≈ 3.5 h; 4 % ID g^{-1}); C_{18}-PMH-mPEG coated CNT have a lower liver uptake than DSPE-mPEG coated CNT (≈ 28 *vs.* ≈ 69 % ID g^{-1}).	[62]
C_{18}-PMH-mPEG coated CNT	Corona	Increasing the PEG length and density of C_{18}-PMH-mPEG coated CNT enhances their blood circulation time, augments tumor and skin accumulations, and reduces uptake by RES organs; CNT coated with C_{18}-PMH-mPEG with a PEG density and molecular weight of 10 % and 5 kDa are considered optimal due to their good circulation time ($t_{1/2}$ = 12.8 h), high tumor accumulation (≈ 15 % ID g^{-1}) and low uptake by skin (≈ 3 % ID g^{-1}).	[12]

DSPE-PEG coated CNT	Corona	DSPE-PEG_{5400} coated CNT have a higher resistance to protein adsorption than those coated with DSPE-PEG_{2000}.	[83]
PEGylated rGO and reduced nGO	Corona	The blood circulation time of C_{18}-PMH-mPEG coated rGO ($t'_{1/2}$[a)] ≈ 17.5) and C_{18}-PMH-mPEG coated reduced nGO ($t'_{1/2}$ ≈ 16.7 h) is superior to that of PEGylated (6-arm branched) nGO ($t'_{1/2}$ ≈ 5.8 h); The tumor accumulation of C_{18}-PMH-mPEG coated nanomaterials (≈ 5-6 % ID g^{-1}) is 7-8 times higher than that of PEGylated nGO.	[63]
Double PEGylated reduced nGO	Corona	Conjugation of amine-terminated C_{18}-PMH-PEG_{5000} coated reduced nGO with a PEG_{5000} derivative (double PEGylation) improves its blood circulation time from $t'_{1/2}$ = 18.8 h ($t_{1/2}$ = 0.19 h) to $t'_{1/2}$ = 27.7 h ($t_{1/2}$ = 0.35 h); The tumor accumulation is also augmented from 8.8 to 15.5 % ID g^{-1}.	[124]
Citrate and mPEG coated CuS nanoparticles	Corona	mPEG coated CuS nanoparticles have a higher blood residence and almost 3-fold greater tumor accumulation (7.6 % ID g^{-1}) than citrate-CuS nanoparticles; mPEG coated CuS nanoparticles have a lower uptake by the liver (≈ 23 % ID g^{-1}) and spleen (≈ 9 % ID g^{-1}) than citrate coated nanomaterials (≈ 44 % ID g^{-1} of liver; ≈ 34 % ID g^{-1} of spleen).	[37]
Citrate, mPEG, and PVP coated CuS nanodots	Corona	PVP coated CuS nanodots display the highest resistance to protein adsorption, followed by mPEG coated nanodots and then by citrate coated nanodots.	[14]
PEGylated $Cu_{2-x}Se$ nanoparticles	Corona	PEGylated $Cu_{2-x}Se$ nanoparticles display a blood circulation time of $t'_{1/2}$ = 8.14 h ($t_{1/2}$ = 0.73 h) and a tumor accumulation of 4.4 % ID g^{-1}; Nanoparticles also have a low uptake by the liver (≈ 9 % ID g^{-1}) and spleen (≈ 8 % ID g^{-1}).	[84]
PTMP-PMAA[b)] coated WO_{3-x} nanodots	Corona	PTMP-PMAA coated WO_{3-x} nanodots have a tumor accumulation of ≈ 5 % ID g^{-1} and low uptake by the liver (≈ 15 % ID g^{-1}) and spleen (≈ 13 % ID g^{-1}).	[98]
PEGylated WS_2 nanosheets	Corona	PEGylated WS_2 nanosheets possess a high tumor-homing capacity (13 % ID g^{-1}) that allows tumor eradication using irradiation at a relatively low power density.	[26]

C_{18}-PMH-PEG coated WS_2 nanoflakes	Corona	C_{18}-PMH-PEG coated WS_2 nanoflakes possess a high tumor-homing capacity (≈ 10 % ID g^{-1}). The liver and spleen accumulations are ≈ 34 and ≈ 19 % ID g^{-1}, respectively.	[125]
PEGylated PB hollow nanocubes	Corona	Coating of hollow PB nanocubes with PEG improves their $t_{1/2}$ from 5.6 to 8.7 h.	[73]
RBC-derived membrane coated Fe_3O_4 nanoclusters	Corona	RBC coated Fe_3O_4 nanoclusters have about 2.3-fold lower uptake by macrophages than their non-coated equivalents; RBC coated Fe_3O_4 nanoclusters have a higher blood retention than their non-coated equivalents and achieve a superior tumor accumulation (≈ 4.9 *vs.* ≈ 1.3 % ID g^{-1}) and lower uptake by the liver (≈ 18 *vs.* ≈ 32 % ID g^{-1}).	[69]
GSH[c] modified Pd-PVP nanosheets	Corona	Functionalization of Pd-PVP nanosheets with GSH increases their blood circulation ($t_{1/2}$ = 1.25 h) and tumor accumulation to ≈ 4.5 % ID g^{-1}; GSH functionalization reduces the uptake of the nanosheets by the liver (from ≈ 35 to ≈ 8 % ID g^{-1}) and spleen (from ≈ 12 to ≈ 2 % ID g^{-1}).	[7]
PEGylated Pd-PVP nanosheets	Corona	PEGylated Pd-PVP nanosheets have a high blood circulation time ($t_{1/2}$ ≈ 30 h), good tumor accumulation (≈ 8 % ID g^{-1}) and low accumulation in RES organs (≈ 11 % ID g^{-1} of liver; ≈ 15 % ID g^{-1} of spleen); PEGylation using a mPEG-SH:Pd-PVP mass ratio of 1:1 is optimal for the nanosheets; Increasing the PEG molecular weight from 5 to 10 kDa improves the tumor accumulation of the nanosheets from ≈ 8 to ≈ 12 % ID g^{-1}.	[44]
PVP-PPy based nanoparticles	Corona	PVP-PPy based nanoparticles have a low blood circulation time ($t_{1/2}$ ≈ 12 min) and high uptake by the liver (≈ 49 % ID g^{-1}) but achieve a tumor accumulation of ≈ 4 % ID g^{-1}.	[45]
PEGylated PPy-based nanoparticles	Corona	Nanoparticles prepared with a Py:Py-COOH[d] molar feed ratio of 7:3 are considered as optimal since these display a good compromise between NIR absorption and carboxyl groups for PEG conjugation (inclusion of Py-COOH decreases NIR absorption); PEGylated nanoparticles have a good blood circulation time ($t_{1/2}$ ≈ 12.5 h), achieve high tumor accumulation (≈ 18 % ID g^{-1}) and demonstrate high uptake by the liver (≈ 45 % ID g^{-1}) and spleen (≈ 40 % ID g^{-1}).	[65]

PEGylated PEDOT:PSS[e)] nanoparticles	Corona	PEGylated PEDOT:PSS nanoparticles possess a high tumor-homing capacity (≈ 28 % ID g^{-1}). The liver and spleen accumulations are ≈ 32 and ≈ 17 % ID g^{-1}, respectively.	[8]
PEGylated gold-Pd nanoplates	Corona	PEGylated gold-Pd nanoplates display a blood circulation time of $t_{1/2}$ = 8 h and a tumor accumulation of ≈ 79 % ID g^{-1}; Nanoplates have a low uptake by the liver (≈ 17 % ID g^{-1}) but display a high accumulation in the spleen (≈ 33 % ID g^{-1}) and skin (≈ 16 % ID g^{-1}).	[126]
A10 and DUP-1 dual-functionalized PEGylated gold nanostars	Targeting	Dual aptamer functionalized PEGylated gold nanostars mediate a photothermal effect selective for prostate cancer cells.	[75]
CD44 targeted PEGylated gold nanostars	Targeting	Conjugation of anti-CD44 antibodies to PEGylated gold nanostars increases their tumor accumulation by more than 2-fold and reduces their uptake by RES organs.	[72]
DSPE-PEG-RGD coated CNT	Targeting	DSPE-PEG_{5400}-RGD coated CNT have a superior tumor accumulation (≈ 13 % ID g^{-1}) and lower liver uptake (≈ 20 % ID g^{-1}) than their equivalents coated with DSPE-PEG_{2000}-RGD (≈ 5 % ID g^{-1} of tumor; ≈ 30 % ID g^{-1} of liver); DSPE-PEG_{2000}-RGD and DSPE-PEG_{5400} coated CNT have similar tumor accumulations (≈ 5 *vs.* ≈ 4 % ID g^{-1}).	[83]
DSPE-PEG-Annexin V coated CNT	Targeting	Annexin V functionalization improves the tumor accumulation of CNT by almost 7-fold (≈ 5 % ID g^{-1}).	[70]
HA functionalized nGO	Targeting	HA-nGO mediates a superior PTT when compared to non-functionalized nGO.	[127]
Pluronic® F-127-FA conjugates coated nGO	Targeting	nGO functionalized with FA densities of 50 and 100% have a similar tumor accumulation; nGO with FA densities of 10 and 25 % have a tumor accumulation similar to that of non-functionalized nGO.	[71]
Pluronic® F-127-FA and Pluronic® F-127-RGD conjugates coated nGO	Targeting	Dual-targeted nGO has a higher tumor-homing capacity than single-ligand functionalized (FA or RGD) nGO.	[76]
DSPE-PEG-RGD coated rGONM and rGO	Targeting	rGONM and rGO functionalized with DSPE-PEG-RGD have a better blood circulation profile than their equivalents coated with DSPE-PEG;	[50]

		RGD functionalization improves the tumor accumulation of PEGylated rGO and rGONM from ≈ 7.3 and ≈ 8.9 to ≈ 22.7 and ≈ 31 % ID g^{-1}, respectively; RGD functionalization also reduces the uptake of these nanomaterials by the liver (values in % ID g^{-1}: ≈ 26 for rGO-PEG; ≈ 7 for rGO-PEG-RGD; ≈ 17 for rGONM-PEG; ≈ 5 for rGONM-PEG-RGD) and spleen (values in % ID g^{-1}: ≈ 22 for rGO-PEG; ≈ 6 for rGO-PEG-RGD; ≈ 12 for rGONM-PEG; ≈ 3 for rGONM-PEG-RGD).	
Anti-FSHR antibody functionalized PEGylated nGO	Targeting	Functionalization of PEGylated nGO with anti-FSHR antibody improves the accumulation of these nanomaterials in breast cancer lung metastasis from about 5 to 19.7 % ID g^{-1}.	[78]
FA and PEG coated CuS nanoparticles	Targeting	FA coated CuS nanoparticles are rapidly cleared from circulation and have high liver uptake (≈ 35 % ID g^{-1}); FA coated CuS nanoparticles have a higher tumor-homing capacity than PEGylated CuS nanoparticles (≈ 9.7 *vs.* ≈ 6.4 % ID g^{-1}).	[30]
Anti-HER-2 antibody functionalized poly(acrylic acid)-$W_{18}O_{49}$ nanoparticles	Targeting	HER-2 targeted $W_{18}O_{49}$ nanoparticles accumulate in HER-2 positive lymphatic metastases and mediate their elimination under NIR laser irradiation.	[20]
HA functionalized WO_3 nanoparticles	Targeting	HA functionalization improves the tumor accumulation of the WO_3 nanoparticles from ≈ 5 % to 34 % ID.	[9]
HER-2 affinity protein functionalized DSPE-PEG Fe_5C_2 nanoparticles	Targeting	HER-2 targeting functionalization improves the tumor accumulation of Fe_5C_2 nanoparticles, which then mediate the elimination of mice's tumors with only 3 minutes of laser irradiation.	[128]
HA-*g*-PEG coated PB hollow nanocubes	Targeting	HA-*g*-PEG coated PB nanocubes mediate a higher hyperthermia under NIR laser irradiation than PEGylated nanocubes (53 °C *vs.* 43 °C) due to their superior tumor accumulation.	[73]
HA-PANI nanoparticles	Targeting	PTT mediated by the HA-PANI nanoparticles is selective for CD44 overexpressing cells.	[21]

Cetuximab functionalized carboxymethylated PVA-PANI nanoparticles	Targeting	Cetuximab conjugation increases the tumor accumulation of PANI-based nanoparticles from ≈ 1.7 to ≈ 7.1 % ID g^{-1}.	[74]
Anti-CD44 antibody functionalized PPDS[f)] nanoparticles	Targeting	PPDS nanoparticles electrostatically complexed with anti-CD44 antibodies mediate a photothermal effect selective for cancer cells overexpressing CD44 receptors.	[22]

[a)] second phase blood circulation half-life ($t'_{1/2}$); [b)] pentaerythritol tetrakis (3-mercaptopropionate)-terminated poly(methacrylic acid) (PTMP-PMAA); [c)] reduced glutathione (GSH); [d)] pyrrole:pyrrole-1-propanoic acid (Py:Py-COOH); [e)] PEDOT:poly(styrenesulfonate) (PEDOT:PSS); [f)] poly(sodium3-((3-methyl-3,4-dihydro-2H-thieno[3,4-b][1,4]dioxepin-3-yl)methoxy)propane-1-sulfonate) (PPDS).

Table 2.2. Strategies used to improve nanomaterials' capacity to produce photoinduced heat.

Nanomaterial	Optimization	Result	Ref.
Urchinlike gold nanoparticles	New material	Photothermal conversion efficiency of 11 % (at 808 nm).	[101]
Gold nanohexapods	New material	Photothermal conversion efficiency of 29.6 % (at 808 nm).	[88]
Gold/SiO_2 nanoshells	New material	Photothermal transduction efficiency of ≈ 34 % (at 815 nm).	[90]
Gold nanoshells	New material	Photothermal transduction efficiency of 39 % (at 810 nm).	[87]
Nanoporous gold disks	New material	Photothermal conversion efficiency of ≈ 56 % (at 700-900 nm).	[129]
Gold nanomatryoshkas	New material	Photothermal transduction efficiency of 63 % (at 810 nm).	[87]
Gold nanocages	New material	Photothermal conversion efficiency of 63.6 % (at 808 nm).	[88]
Gold bellflowers	New material	Photothermal conversion efficiency of 74 % (at 808 nm).	[89]
Gold nanobipyramids	New material	Photothermal conversion efficiency depends on the radius of the nanostructures (51-≈ 90 %, at 809 nm).	[91]
GNR	New material	Photothermal conversion efficiency depends on the aspect ratio of the nanostructures (22.1-95 %).	[88, 90, 91, 130]
Gold nanocages, nanohexapods, and nanorods	New material	Gold nanocages generate a photoinduced heat similar to that of GNR and nanohexapods, but at a ≈ 3-fold lower concentration.	[31]
PEGylated Cu nanowires	New material	Photothermal conversion efficiency of 12.5 % (at 808 nm).	[131]
$Cu_{2-x}Se$ nanocrystals coated with hydrolyzed poly(isobutylene-*alt*-maleic anhydride)-oleylamine conjugates	New material	Photothermal transduction efficiency of 22 % (at 800 nm).	[38]
Cu_9S_5 nanocrystals modified with aminocaproic acid	New material	Photothermal conversion efficiency of 25.7 % (at 980 nm).	[85]
PEGylated Cu_3BiS_3 hollow nanospheres	New material	Photothermal conversion efficiency of 27.5 % (at 980 nm).	[39]
BSA-Gd:CuS nanoparticles	New material	Photothermal conversion efficiency of 32.3 % (at 980 nm).	[132]

Ferritin-CuS	New material	Photothermal conversion efficiency of ≈ 47 % (at 808 nm).	[133]
Silica coated $Cu_{1.75}S$ nanoparticles	New material	Photothermal conversion efficiency of 54.13 % (at 808 nm).	[134]
$Cu_{7.2}S_4$ nanocrystals coated with a hydrolyzed poly(maleic anhydride)-oleylamine based amphiphile	New material	Photothermal conversion efficiency of 56.7 % (at 980 nm).	[10]
PEGylated $Cu_{2-x}Se$ nanoparticles	New material	Photothermal conversion efficiency of 64.8 % (at 808 nm).	[84]
PEGylated Mo oxide nanospheres and nanoribbons	New material	Mo oxide nanorods (synthesized in the absence of PEG) have a weak NIR absorption, while Mo oxide nanospheres and nanoribbons (synthesized in the presence of PEG) have high NIR absorption.	[135]
PEGylated MoO_{3-x} hollow nanospheres	New material	MoO_{3-x} hollow nanospheres prepared in the presence of PEG have an enhanced NIR absorption and a photothermal conversion efficiency of 22.64 % (at 808 nm).	[40]
Chitosan functionalized MoS_2 nanosheets	New material	Photothermal conversion efficiency of 24.37 % (at 808 nm).	[136]
PEGylated MoS_2 nanoflakes	New material	Photothermal conversion efficiency of 27.6 % (at 808 nm).	[92]
Layered MoS_2 hollow spheres	New material	Layered MoS_2 hollow spheres have a higher NIR absorption than MoS_2 nanosheets and a photothermal conversion efficiency of 34.46 % (at 808 nm).	[137]
Pluronic® F-127 coated $MoSe_2$ nanodots	New material	Photothermal conversion efficiency of 46.5 % (at 785 nm).	[138]
Radar-like MoS_2 nanoparticles	New material	Radar-like MoS_2 nanoparticles have a higher photothermal conversion efficiency (53.3 %) than MoS_2 nanoflowers (18.2 %) and MoS_2 microspheres (15.2 %, at 808 nm).	[139]
PVP coated $MoSe_2$ nanosheets	New material	Photothermal conversion efficiency of 57.9 % (at 808 nm).	[140]
PEGylated Mo oxide nanosheets	New material	Mo oxide nanosheets display a pH dependent NIR absorption that is governed by their degradation. In healthy tissues, the nanosheets have a fast degradation rate. In the tumor microenvironment (slightly acidic) the nanosheets degrade slowly, thereby retaining their NIR absorption.	[141]
HA functionalized WO_3 nanoparticles	New material	Photothermal conversion efficiency of 11.78 % (at 808 nm).	[9]

PVP coated $Rb_{0.27}WO_3$ nanorods	New material	Photothermal conversion efficiency of 17.8 % (at 808 nm).	[120]
$(NH_4)_xWO_3$ nanocubes	New material	Photothermal conversion efficiency of 39.4 % (at 1064 nm).	[93]
WO_3 nanoparticles	New material	Photothermal conversion efficiency of 41.96 % (at 808 nm).	[9]
PTMP-PMAA coated WO_{3-x} nanodots	New material	WO_{3-x} nanodots NIR absorption is enhanced in acidic and in hypoxic environments.	[98]
Fe_3O_4 nanoparticles	New material	Photothermal conversion efficiency of 6.4 % (at 808 nm).	[103]
Fe_3O_4 nanoparticles	New material	Fe_3O_4 nanoparticles functionalized with PEG produce a higher photoinduced heat than Fe_3O_4 nanoparticles stabilized with PVP, PVA, polyglutamic acid, xalic acid, citrate, glutamic acid, and diethylene glycol.	[109]
PEGylated FeS nanoplates	New material	PEGylated FeS nanoplates have ≈ 17 times higher NIR absorption than Fe_3O_4 nanoparticles, thus producing a superior photoinduced heat (≈ 70 °C *vs.* ≈ 45 °C).	[42]
PEGylated $FeSe_2$	New material	PEGylated $FeSe_2$ nanoparticles have ≈ 9 times higher NIR absorption than Fe_3O_4-based nanoparticles, thus generating a superior photoinduced heat (≈ 65 °C *vs.* ≈ 31 °C).	[43]
Denatured BSA coated Mn^{2+} doped iron oxide nanoparticles	New material	Photothermal conversion efficiency of 26.9 % (at 808 nm).	[142]
Fe(III)-gallic acid nanoparticles	New material	Photothermal conversion efficiency of 66.8 % (at 808 nm).	[143]
Pd nanocubes, nanoparticles, porous nanoparticles, and polyhedrons	New material	Porous Pd nanoparticles have a higher NIR absorption than Pd nanocubes, Pd nanoparticles, and Pd polyhedrons.	[86]
PEG coated gold-PANI nanoparticles	New material	PANI-based nanoparticles with a 16 nm gold core display the lowest NIR absorption at physiological pH (7.4) and high NIR absorption at acidic pH (6.5). Thereby, at pH 7.4 these generate a photoinduced heat to ≈ 40 °C while at pH 6.5 the temperature reaches ≈ 53 °C.	[97]
PVP coated PPy nanoparticles	New material	Photothermal conversion efficiency of 44.7 % (at 808 nm).	[45]
Tosylate doped poly(2TMOI-OEGMA)[a]-PPy nanoparticles	New material	Photothermal transduction efficiency of 46.9 % (at 808 nm).	[94]

PEDOT nanotubes and PEDOT:PSS nanoparticles	New material	PEDOT nanotubes have almost a 2-fold higher NIR absorption than PEDOT:PSS nanoparticles and thus generate a superior photoinduced heat ($\Delta T \approx 16$ °C *vs.* $\Delta T \approx 8$ °C).	[144]
PProDOS nanoparticles	New material	PProDOS nanoparticles have a slightly superior NIR absorption than PEDOT nanoparticles, thus producing a higher photoinduced heat ($\Delta T \approx 10$ °C *vs.* $\Delta T = 6$ °C).	[95]
PCPDTBT[b)] and PCPDTBSe[c)] nanoparticles	New material	PCPDTBT nanoparticles produce a slightly higher photoinduced heat than PCPDTBSe nanoparticles ($\Delta T \approx 35$ °C *vs.* $\Delta T \approx 30$ °C).	[145]
Pluronic® F-127 coated PCPDTBSe nanoparticles	New material	Pluronic® F-127 coated PCPDTBSe nanoparticles mediate a higher photoinduced heat ($\Delta T = 47$ °C) than Pluronic® F-127 coated PCPDTBSe nanofibers ($\Delta T \approx 35$ °C) and PCPDTBSe nanoparticles ($\Delta T \approx 35$ °C).	[47]
PPDS nanoparticles	New material	Photothermal conversion efficiency of 31.4 % (at 808 nm).	[22]
Gold nanopopcorn conjugated CNT	New material	The NIR absorption of the hybrid nanostructures is enhanced by increasing the content of gold nanopopcorn immobilized on CNT.	[146]
PEG-GO/CuS nanocomposites	New material	PEG-GO/CuS nanocomposites produce a higher photoinduced heat ($\Delta T = 24.9$ °C) than GO ($\Delta T = 14$ °C) due to their superior NIR absorption.	[147]
Polydopamine coated Fe_3O_4 nanoparticles	New material	Increasing the thickness of the polydopamine shell improves the NIR absorption of the hybrid nanostructures. Photothermal conversion efficiency of 13.1 % (at 808 nm).	[103]
PEGylated Fe-Fe_3O_4 nanoparticles	New material	Photothermal conversion efficiency of 20.3 % (at 808 nm).	[148]
PPy coated GNR incorporating Fe_3O_4 nanoparticles	New material	Photothermal conversion efficiency of 23.9 % (at 808 nm).	[149]
PPy coated urchinlike gold nanoparticles	New material	Increasing the thickness of the PPy shell from 3.5 to 15.3 nm improves the photothermal conversion efficiency of the hybrid nanostructures from 18.6 to 27.5 % (at 808 nm).	[101]
PEGylated gold-Pd nanoplates	New material	Photothermal conversion efficiency of 28.6 % (at 808 nm).	[126]
Fe_3O_4 coated PPy nanoparticles	New material	Photothermal conversion efficiency of 39.15 % (at 808 nm).	[150]

PPy coated Fe_3O_4 superstructures	New material	Increasing the thickness of the PPy shell improves the NIR absorption of the hybrid nanostructures; Nanostructures with a 16 nm thick PPy shell display the highest photothermal transduction efficiency (49 % at 808 nm).	[102]
Polydopamine coated PEI-gold nanostars	New material	Polydopamine coating improves the photothermal conversion efficiency of the PEI-gold nanostars from 36.1 to 49.9 % (at 808 nm).	[104]
Gold/Au_2S nanoshells	New material	Photothermal transduction efficiency of ≈ 58 % (at 815 nm).	[90]
Gold nanopopcorn-iron oxide cluster nanoparticles	New material	Photothermal conversion efficiency of 61 % (at 808 nm).	[151]
PEGylated gold-silver nanostars	New material	Photothermal conversion efficiency of 79.01 % (at 808 nm).	[99]
PEGylated hollow gold-silver alloy urchin-shaped nanostructures	New material	Photothermal conversion efficiency of 80.4 % (at 808 nm).	[100]
PVA coated PPy nanoparticles	Size	50 nm PVA coated PPy nanoparticles produce a higher photoinduced heat (ΔT = 29.4 °C) than their 75 nm equivalents (ΔT = 26.2 °C).	[107]
PEGylated MoS_2 nanosheets	Size	80 nm MoS_2 nanosheets produce a higher photoinduced heat ($\Delta T \approx 6$ °C) than their 100 nm equivalents ($\Delta T \approx 4.5$ °C).	[15]
PEGylated WS_2 quantum dots	Size	Reduction of WS_2 particles' size increases their NIR absorption and thus improves the photoinduced heat mediated by these nanostructures; WS_2 quantum dots (3 nm) have a slightly higher photothermal conversion efficiency (44.3 %) than ≈ 28 nm WS_2 nanosheets (40.6 %, at 808 nm), and thus generate a superior photoinduced heat (ΔT = 20 °C *vs.* $\Delta T \approx 12$ °C).	[108]
Pd-PVP nanosheets	Size	4.4 nm Pd-PVP nanosheets have a higher photothermal conversion efficiency than 41 nm nanosheets (52 *vs.* 27.6 %, at 808 nm), thus producing a superior photoinduced heat (≈ 50 °C *vs.* ≈ 37.5 °C).	[7]

PEGylated hollow gold-silver alloy urchin-shaped nanostructures	Size	Reduction of the hybrid structures' size from 200 to 80 nm shifts their NIR absorption peak from 950 to 772 nm, thereby improving the photoinduced heat generated by these structures under 808 nm laser radiation.	[100]
Citrate and PEGylated Fe_3O_4 nanoparticles	Size	Increasing the size of citrate and PEG functionalized Fe_3O_4 nanoparticles from 120 to 380 nm produces a red-shift in their absorption and thus improves the photoinduced heat mediated by these materials.	[109]
Gold nanotubes	Size	Increasing the length of gold nanotubes from 300 to 530 nm produces a red-shift in their absorption; Gold nanotubes with a length of ≈ 370 nm display the highest absorption at 800 nm and thus were selected for cancer PTT using 800 nm radiation.	[110]
PEGylated rGO derivatives	Chemical treatment	rGO derivatives have about 3-4 times higher NIR absorption than non-reduced nGO and thereby generate a superior photoinduced heat (≈ 58 °C *vs.* ≈ 44 °C).	[63]
PEGylated rGONM	Chemical treatment	rGONM has about 4.2 times higher NIR absorption than reduced nGO, thus producing a superior photoinduced heat (≈ 57 °C *vs.* ≈ 42 °C).	[50]
Mn^{2+} doped PEGylated PB nanocubes	Chemical treatment	Mn^{2+} doping increases the NIR absorption of PEGylated PB nanocubes; Mn^{2+} doping of 15 % produces the highest increment in the NIR absorption of the PB nanocubes (≈ 2-fold at 808 nm).	[111]
Gd^{3+} containing mesoporous PB nanoparticles	Chemical treatment	Incorporation of Gd^{3+} in PB nanoparticles produces a red-shift in their absorption towards the NIR region.	[112]
Clustered Fe_3O_4 nanoparticles	Assembling of nanostructures	Clustered Fe_3O_4 nanoparticles have ≈ 3.6-fold higher NIR absorption than individual Fe_3O_4 nanoparticles, thus producing a superior photoinduced heat (≈ 51 °C *vs.* ≈ 42 °C).	[41]

Nanovesicles assembled using PEG-poly(caprolactone) functionalized gold nanoparticles	Assembling of nanostructures	Self-assembled gold-based nanovesicles have a higher photothermal conversion efficiency than GNR (37 % *vs.* 22 %, at 808 nm), thus producing a superior photoinduced heat ($\Delta T \approx 41$ °C *vs.* $\Delta T = 24$ °C).	[113]
Gold—attapulgite nanocomposites	Assembling of nanostructures	Electrostatic assembly of gold nanospheres on the surface of attapulgite yields a composite with a photothermal conversion efficiency of 25.6 % (at 808 nm).	[114]
PEGylated chirality sorted (6,5) CNT	Sorting of nanomaterials	Chirality sorted (6,5) CNT have an enhanced NIR absorption, thus producing a higher photoinduced heat than non-sorted CNT (≈ 53 °C *vs.* ≈ 44 °C).	[116]

[a] poly(2-(methacryloyloxy)ethylaminocarboxymethyl)thiophene-*stat*-oligo(ethylene glycol) methacrylate) (poly(2TMOI-OEGMA)); [b] poly[4,4-bis(2-ethylhexyl)-cyclopenta[2,1-b;3,4-b']dithiophene-2,6-diyl-*alt*-2,1,3-benzothiadiazole-4,7-diyl] (PCPDTBT); [c] poly[4,4-bis(2-ethylhexyl)-cyclopenta[2,1-b;3,4-b']dithiophene-2,6-diyl-*alt*-2,1,3-benzoselenadiazole-4,7-diyl] (PCPDTBSe).

Table 2.3. Strategies based on the optimization of the parameters related to the laser light.

Nanomaterial	Optimization	Result	Ref.
PEGylated Cs_xWO_3 nanorods	Wavelength	Even though PEGylated Cs_xWO_3 nanorods have a higher absorbance at 980 nm than at 915 nm, the use of 915 nm light is beneficial since the 980 nm radiation has less penetration and induces a higher off-target heating.	[119]
PVP coated $Rb_{0.27}WO_3$ nanorods	Wavelength	Even though PVP coated $Rb_{0.27}WO_3$ nanorods have a higher absorption at 980 nm than at 808 nm, the application of 808 nm light to irradiate the nanorods can produce a higher temperature variation than 980 nm radiation due to its higher penetration.	[120]
PVA coated PPy nanoparticles	Power density	Nanomaterials' mediated PTT at a power density of 0.25 and 0.5 W cm^{-2} produces a hyperthermia to about 55 and 60 °C, resulting in the elimination of mice's tumors; PTT at a power density of 0.1 W cm^{-2} mediates a hyperthermia to ≈ 42 °C, leading to a reduction of the tumor growth.	[117]
$(NH_4)_xWO_3$ nanocubes	Power density Irradiation sessions	Nanomaterials' mediated PTT at a power density of 1 W cm^{-2} (every three days during 9 days) mediates a higher hyperthermia (ΔT ≈ 45 °C) and a better therapeutic outcome than PTT at 0.5 W cm^{-2} (ΔT ≈ 33 °C).	[93]
C_{18}-PMH-mPEG coated CNT	Power density Irradiation sites	Irradiation of tumor zone and tumor-adjacent lymph node results in an improved therapeutic effect; The lymph node was irradiated at a higher power density due to its deeper location and due to CNT lower accumulation at this site (lymph node: 0.8 W cm^{-2}; tumor: 0.5 W cm^{-2}).	[121]
Chitosan-Pluronic® F-68 conjugates encapsulating GNR	Irradiation sessions	Irradiation of the tumor zone at 24 and 48 h p.i. of nanoparticles leads to tumor eradication.	[11]
RBC membrane coated PVP-gold nanocages	Irradiation sessions	Laser irradiation once a day during 19 days elicits a potent therapeutic effect.	[68]

CD44 targeted PEGylated gold nanostars	Irradiation sessions	Laser irradiation every two days during 14 days elicits a potent therapeutic effect.	[72]
PEGylated $WO_{2.9}$ nanorods	Irradiation sessions	Laser irradiation every two days during 14 days allows the elimination of mice's tumors at a low power density.	[16]
DSPE-PEG-CREKA functionalized CNT	Irradiation sessions	Irradiation of the tumor zone at 10 min after administration of DSPE-PEG-CREKA coated CNT (fibrin targeted CNT) enhances their tumor accumulation by about 3.8-fold; Irradiation of the tumor zone at 10 min after administration of DSPE-PEG coated CNT improves their tumor accumulation by about 2.6-fold; Mice administered with these materials were irradiated multiple times (at 10 min and on day 3, 6 and 9 p.i.) to take advantage of these phenomena.	[122]
HA functionalized WO_3 nanoparticles	Irradiation onset	Irradiation of the tumor zone at 8 h p.i. of HA-WO_3 nanoparticles produces the highest hyperthermia (50 °C).	[9]
PVP coated CuS nanodots	Irradiation onset	PVP coated CuS nanodots achieve their maximum tumor accumulation (≈ 3.6 % ID g^{-1}) at 2 h p.i. and PTT at this time point leads to tumor eradication with only 2 minutes of NIR laser irradiation.	[14]
HA-*g*-PEG coated PB hollow nanocubes	Irradiation onset	HA-*g*-PEG coated PB hollow nanocubes achieve their maximum tumor accumulation at 24 h p.i. and PTT at this time point leads to a hyperthermia to 53 °C.	[73]
PEGylated $Cu_{2-x}Se$ nanoparticles	Irradiation onset	PEGylated $Cu_{2-x}Se$ nanoparticles achieve their maximum tumor accumulation (4.4 % ID g^{-1}) at 12 h p.i. and PTT at this time point leads to tumor eradication.	[84]
GSH functionalized MoS_2 nanodots	Irradiation onset	GSH functionalized MoS_2 nanodots achieve their maximum tumor accumulation (≈ 5 % ID g^{-1}) at 4 h p.i. and PTT at this time point leads to tumor eradication.	[152]

2.8. References

[1] A. Jemal, F. Bray, M. M. Center, J. Ferlay, E. Ward, D. Forman, Global cancer statistics, CA: A Cancer Journal for Clinicians, 61 (2011) 69-90.

[2] N. Cihoric, A. Tsikkinis, G. van Rhoon, H. Crezee, D. M. Aebersold, S. Bodis, M. Beck, J. Nadobny, V. Budach, P. Wust, P. Ghadjar, Hyperthermia-related clinical trials on cancer treatment within the ClinicalTrials.gov registry, International Journal of Hyperthermia, 31 (2015) 609-614.

[3] C. L. K. Pang, Hyperthermia in Oncology, CRC Press, Boca Raton (2015).

[4] K. F. Chu, D. E. Dupuy, Thermal ablation of tumours: biological mechanisms and advances in therapy, Nature Reviews Cancer, 14 (2014) 199-208.

[5] G. Baronzio, M. Jackson, D. Lee, A. Szász, Conference of the International Clinical Hyperthermia Society 2012, Conference Papers in Medicine, (2013).

[6] a) S. Balivada, R. S. Rachakatla, H. Wang, T. N. Samarakoon, R. K. Dani, M. Pyle, F. O. Kroh, B. Walker, X. Leaym, O. B. Koper, A/C magnetic hyperthermia of melanoma mediated by iron (0)/iron oxide core/shell magnetic nanoparticles: a mouse study, BMC Cancer, 10 (2010) 119; b) D. P. O'Neal, L. R. Hirsch, N. J. Halas, J. D. Payne, J. L. West, Photo-thermal tumor ablation in mice using near infrared-absorbing nanoparticles, Cancer Letters, 209 (2004) 171-176.

[7] S. Tang, M. Chen, N. Zheng, Sub-10-nm Pd Nanosheets with Renal Clearance for Efficient Near-Infrared Photothermal Cancer Therapy, Small, 10 (2014) 3139-3144.

[8] L. Cheng, K. Yang, Q. Chen, Z. Liu, Organic stealth nanoparticles for highly effective in vivo near-infrared photothermal therapy of cancer, ACS Nano, 6 (2012) 5605-5613.

[9] S. M. Sharker, S. M. Kim, J. E. Lee, K. H. Choi, G. Shin, S. Lee, K. D. Lee, J. H. Jeong, H. Lee, S. Y. Park, Functionalized biocompatible WO 3 nanoparticles for triggered and targeted in vitro and in vivo photothermal therapy, Journal of Controlled Release, 217 (2015) 211-220.

[10] B. Li, Q. Wang, R. Zou, X. Liu, K. Xu, W. Li, J. Hu, Cu 7.2 S 4 nanocrystals: a novel photothermal agent with a 56.7% photothermal conversion efficiency for photothermal therapy of cancer cells, Nanoscale, 6 (2014) 3274-3282.

[11] W. I. Choi, J.-Y. Kim, C. Kang, C. C. Byeon, Y. H. Kim, G. Tae, Tumor regression in vivo by photothermal therapy based on gold-nanorod-loaded, functional nanocarriers, ACS Nano, 5 (2011) 1995-2003.

[12] X. Liu, H. Tao, K. Yang, S. Zhang, S.-T. Lee, Z. Liu, Optimization of surface chemistry on single-walled carbon nanotubes for in vivo photothermal ablation of tumors, Biomaterials, 32 (2011) 144-151.

[13] K. Yang, S. Zhang, G. Zhang, X. Sun, S.-T. Lee, Z. Liu, Graphene in mice: ultrahigh in vivo tumor uptake and efficient photothermal therapy, Nano Letters, 10 (2010) 3318-3323.

[14] M. Zhou, J. Li, S. Liang, A. K. Sood, D. Liang, C. Li, CuS Nanodots with Ultrahigh Efficient Renal Clearance for Positron Emission Tomography Imaging and Image-Guided Photothermal Therapy, ACS Nano, 9 (2015) 7085-7096.

[15] S. Wang, K. Li, Y. Chen, H. Chen, M. Ma, J. Feng, Q. Zhao, J. Shi, Biocompatible PEGylated MoS 2 nanosheets: Controllable bottom-up synthesis and highly efficient photothermal regression of tumor, Biomaterials, 39 (2015) 206-217.

[16] Z. Zhou, B. Kong, C. Yu, X. Shi, M. Wang, W. Liu, Y. Sun, Y. Zhang, H. Yang, S. Yang, Tungsten oxide nanorods: an efficient nanoplatform for tumor CT imaging and photothermal therapy, Scientific Reports, 4 (2014) 3653.

[17] L. Cheng, H. Gong, W. Zhu, J. Liu, X. Wang, G. Liu, Z. Liu, PEGylated Prussian blue nanocubes as a theranostic agent for simultaneous cancer imaging and photothermal therapy, Biomaterials, 35 (2014) 9844-9852.

[18] J. Yang, J. Choi, D. Bang, E. Kim, E. K. Lim, H. Park, J. S. Suh, K. Lee, K. H. Yoo, E. K. Kim, Convertible Organic Nanoparticles for Near-Infrared Photothermal Ablation of Cancer Cells, Angewandte Chemie International Edition, 123 (2011) 461-464.

[19] B. Mensel, C. Weigel, N. Hosten, Minimally Invasive Tumor Therapies, Springer, Heidelberg, (2006).

[20] D. Huo, J. He, H. Li, A. J. Huang, H. Y. Zhao, Y. Ding, Z. Y. Zhou, Y. Hu, X-ray CT guided fault-free photothermal ablation of metastatic lymph nodes with ultrafine HER-2 targeting W18O49 nanoparticles, Biomaterials, 35 (2014) 9155-9166.

[21] B.-P. Jiang, L. Zhang, Y. Zhu, X.-C. Shen, S.-C. Ji, X.-Y. Tan, L. Cheng, H. Liang, Water-soluble hyaluronic acid–hybridized polyaniline nanoparticles for effectively targeted photothermal therapy, Journal of Materials Chemistry B, 3 (2015) 3767-3776.

[22] J. Kim, E. Lee, Y. Hong, B. Kim, M. Ku, D. Heo, J. Choi, J. Na, J. You, S. Haam, Self-Doped Conjugated Polymeric Nanoassembly by Simplified Process for Optical Cancer Theragnosis, Advanced Functional Materials, 25 (2015) 2260-2269.

[23] J. M. Stern, V. V. K. Solomonov, E. Sazykina, J. A. Schwartz, S. C. Gad, G. P. Goodrich, Initial Evaluation of the Safety of Nanoshell-Directed Photothermal Therapy in the Treatment of Prostate Disease, International Journal of Toxicology, 35 (2016) 38-46.

[24] S. K. Hobbs, W. L. Monsky, F. Yuan, W. G. Roberts, L. Griffith, V. P. Torchilin, R. K. Jain, Regulation of transport pathways in tumor vessels: role of tumor type and microenvironment, Proceedings of the National Academy of Sciences, 95 (1998) 4607-4612.

[25] E. Blanco, H. Shen, M. Ferrari, Principles of nanoparticle design for overcoming biological barriers to drug delivery, Nature Biotechnology, 33 (2015) 941-951.

[26] L. Cheng, J. Liu, X. Gu, H. Gong, X. Shi, T. Liu, C. Wang, X. Wang, G. Liu, H. Xing, PEGylated WS2 Nanosheets as a Multifunctional Theranostic Agent for in vivo Dual-Modal CT/Photoacoustic Imaging Guided Photothermal Therapy, Advanced Materials, 26 (2014) 1886-1893.

[27] M. J. Ernsting, M. Murakami, A. Roy, S. D. Li, Factors controlling the pharmacokinetics, biodistribution and intratumoral penetration of nanoparticles, Journal of Controlled Release, 172 (2013) 782-794.

[28] A. Vogel, V. Venugopalan, Mechanisms of pulsed laser ablation of biological tissues, Chemical Reviews, 103 (2003) 577-644.

[29] a) S. Stolik, J. Delgado, A. Perez, L. Anasagasti, Measurement of the penetration depths of red and near infrared light in human “ex vivo” tissues, Journal of Photochemistry and Photobiology B, 57 (2000) 90-93; b) E. C. Dreaden, M. A. Mackey, X. Huang, B. Kang, M. A. El-Sayed, Beating cancer in multiple ways using nanogold, Chemical Society Reviews, 40 (2011) 3391-3404; c) D. E. Hudson, D. O. Hudson, J. M. Wininger, B. D. Richardson, Penetration of laser light at 808 and 980 nm in bovine tissue samples, Photomedicine and Laser Surgery, 31

(2013) 163-168; d) A. M. Smith, M. C. Mancini, S. Nie, Second window for in vivo imaging, Nature Nanotechnology, 4 (2009) 710-711.

[30] M. Zhou, S. Song, J. Zhao, M. Tian, C. Li, Theranostic CuS nanoparticles targeting folate receptors for PET image-guided photothermal therapy, Journal of Materials Chemistry B, 3 (2015) 8939-8948.

[31] Y. Wang, K. C. Black, H. Luehmann, W. Li, Y. Zhang, X. Cai, D. Wan, S.-Y. Liu, M. Li, P. Kim, Comparison study of gold nanohexapods, nanorods, and nanocages for photothermal cancer treatment, ACS Nano, 7 (2013) 2068-2077.

[32] a) D. R. Dias, A. F. Moreira, I. J. Correia, The effect of the shape of gold core-mesoporous silica shell nanoparticles on the cellular behavior and tumor spheroids penetration, Journal of Materials Chemistry B, 4 (2016) 7630-7640; b) G. von Maltzahn, J.-H. Park, A. Agrawal, N. K. Bandaru, S. K. Das, M. J. Sailor, S. N. Bhatia, Computationally guided photothermal tumor therapy using long-circulating gold nanorod antennas, Cancer Research, 69 (2009) 3892-3900.

[33] M. Xuan, J. Shao, L. Dai, J. Li, Q. He, Macrophage Cell Membrane Camouflaged Au Nanoshells for in Vivo Prolonged Circulation Life and Enhanced Cancer Photothermal Therapy, ACS Applied Materials & Interfaces, 8 (2016) 9610-9618.

[34] S. Wang, Z. Teng, P. Huang, D. Liu, Y. Liu, Y. Tian, J. Sun, Y. Li, H. Ju, X. Chen, Reversibly Extracellular pH Controlled Cellular Uptake and Photothermal Therapy by PEGylated Mixed-Charge Gold Nanostars, Small, 11 (2015) 1801-1810.

[35] a) J. Feng, L. Chen, Y. Xia, J. Xing, Z. Li, Q. Qian, Y. Wang, A. Wu, L. Zeng, Y. Zhou, Bioconjugation of Gold Nanobipyramids for SERS Detection and Targeted Photothermal Therapy in Breast Cancer, ACS Biomaterials Science & Engineering, 3 (2017) 608–618; b) X. Chen, Z. Liu, S. G. Parker, X. Zhang, J. J. Gooding, Y. Ru, Y. Liu, Y. Zhou, Light-Induced Hydrogel Based on Tumor-Targeting Mesoporous Silica Nanoparticles as a Theranostic Platform for Sustained Cancer Treatment, ACS Applied Materials & Interfaces, 8 (2016) 15857-15863.

[36] J. Mou, P. Li, C. Liu, H. Xu, L. Song, J. Wang, K. Zhang, Y. Chen, J. Shi, H. Chen, Ultrasmall Cu2-xS Nanodots for Highly Efficient Photoacoustic Imaging-Guided Photothermal Therapy, Small, 11 (2015) 2275-2283.

[37] M. Zhou, R. Zhang, M. Huang, W. Lu, S. Song, M. P. Melancon, M. Tian, D. Liang, C. Li, A chelator-free multifunctional [64Cu] CuS nanoparticle platform for simultaneous micro-PET/CT imaging and photothermal ablation therapy, Journal of the American Chemical Society, 132 (2010) 15351-15358.

[38] C. M. Hessel, V. P. Pattani, M. Rasch, M. G. Panthani, B. Koo, J. W. Tunnell, B. A. Korgel, Copper selenide nanocrystals for photothermal therapy, Nano Letters, 11 (2011) 2560-2566.

[39] S.-M. Zhou, D.-K. Ma, S.-H. Zhang, W. Wang, W. Chen, S.-M. Huang, K. Yu, PEGylated Cu3BiS3 hollow nanospheres as a new photothermal agent for 980 nm-laser-driven photothermochemotherapy and a contrast agent for X-ray computed tomography imaging, Nanoscale, 8 (2016) 1374-1382.

[40] T. Bao, W. Yin, X. Zheng, X. Zhang, J. Yu, X. Dong, Y. Yong, F. Gao, L. Yan, Z. Gu, One-pot synthesis of PEGylated plasmonic MoO 3–x hollow nanospheres for photoacoustic imaging guided chemo-photothermal combinational therapy of cancer, Biomaterials, 76 (2016) 11-24.

[41] S. Shen, S. Wang, R. Zheng, X. Zhu, X. Jiang, D. Fu, W. Yang, Magnetic nanoparticle clusters for photothermal therapy with near-infrared irradiation, Biomaterials, 39 (2015) 67-74.

[42] K. Yang, G. Yang, L. Chen, L. Cheng, L. Wang, C. Ge, Z. Liu, FeS nanoplates as a multifunctional nano-theranostic for magnetic resonance imaging guided photothermal therapy, Biomaterials, 38 (2015) 1-9.

[43] T. Fu, Y. Chen, J. Hao, X. Wang, G. Liu, Y. Li, Z. Liu, L. Cheng, Facile preparation of uniform FeSe 2 nanoparticles for PA/MR dual-modal imaging and photothermal cancer therapy, Nanoscale, 7 (2015) 20757-20768.

[44] S. Shi, Y. Huang, X. Chen, J. Weng, N. Zheng, Optimization of surface coating on small Pd nanosheets for in vivo near-infrared photothermal therapy of tumor, ACS Applied Materials & Interfaces, 7 (2015) 14369-14375.

[45] M. Chen, X. Fang, S. Tang, N. Zheng, Polypyrrole nanoparticles for high-performance in vivo near-infrared photothermal cancer therapy, Chemical Communications, 48 (2012) 8934-8936.

[46] J. Geng, C. Sun, J. Liu, L. D. Liao, Y. Yuan, N. Thakor, J. Wang, B. Liu, Biocompatible Conjugated Polymer Nanoparticles for Efficient Photothermal Tumor Therapy, Small, 11 (2015) 1603-1610.

[47] C. M. MacNeill, E. G. Graham, N. H. Levi-Polyachenko, Soft template synthesis of donor–acceptor conjugated polymer nanoparticles: Structural effects, stability, and photothermal studies, Journal of Polymer Science Part A: Polymer Chemistry, 52 (2014) 1622-1632.

[48] a) H. S. Choi, W. Liu, P. Misra, E. Tanaka, J. P. Zimmer, B. I. Ipe, M. G. Bawendi, J. V. Frangioni, Renal clearance of quantum dots, Nature Biotechnology, 25 (2007) 1165-1170; b) C. Zhou, M. Long, Y. Qin, X. Sun, J. Zheng, Luminescent gold nanoparticles with efficient renal clearance, Angewandte Chemie International Edition, 123 (2011) 3226-3230.

[49] a) D. Liu, A. Mori, L. Huang, Role of liposome size and RES blockade in controlling biodistribution and tumor uptake of GM 1-containing liposomes, Biochimica et Biophysica Acta - Biomembranes, 1104 (1992) 95-101; b) G. Sonavane, K. Tomoda, K. Makino, Biodistribution of colloidal gold nanoparticles after intravenous administration: effect of particle size, Colloids and Surfaces B: Biointerfaces, 66 (2008) 274-280.

[50] O. Akhavan, E. Ghaderi, Graphene nanomesh promises extremely efficient in vivo photothermal therapy, Small, 9 (2013) 3593-3601.

[51] a) K. Huang, H. Ma, J. Liu, S. Huo, A. Kumar, T. Wei, X. Zhang, S. Jin, Y. Gan, P. C. Wang, S. He, X. Zhang, X.-J. Liang, Size-Dependent Localization and Penetration of Ultrasmall Gold Nanoparticles in Cancer Cells, Multicellular Spheroids, and Tumors in Vivo, ACS Nano, 6 (2012) 4483-4493; b) H. Cabral, Y. Matsumoto, K. Mizuno, Q. Chen, M. Murakami, M. Kimura, Y. Terada, M. Kano, K. Miyazono, M. Uesaka, N. Nishiyama, K. Kataoka, Accumulation of sub-100 nm polymeric micelles in poorly permeable tumours depends on size, Nature Nanotechnology, 6 (2011) 815-823; c) S. D. Perrault, C. Walkey, T. Jennings, H. C. Fischer, W. C. W. Chan, Mediating Tumor Targeting Efficiency of Nanoparticles Through Design, Nano Letters, 9 (2009) 1909-1915.

[52] H. Wang, R. Zhao, Y. Li, H. Liu, F. Li, Y. Zhao, G. Nie, Aspect ratios of gold nanoshell capsules mediated melanoma ablation by synergistic photothermal therapy and chemotherapy, Nanomedicine: Nanotechnology, Biology and Medicine, 12 (2016) 439-448.

[53] H. Zhang, C. Peng, J. Yang, M. Lv, R. Liu, D. He, C. Fan, Q. Huang, Uniform ultrasmall graphene oxide nanosheets with low cytotoxicity and high cellular uptake, ACS Applied Materials & Interfaces, 5 (2013) 1761-1767.

[54] a) K. C. Black, Y. Wang, H. P. Luehmann, X. Cai, W. Xing, B. Pang, Y. Zhao, C. S. Cutler, L. V. Wang, Y. Liu, Radioactive 198Au-doped nanostructures with different shapes for in vivo analyses of their biodistribution, tumor uptake, and intratumoral distribution, ACS Nano, 8 (2014) 4385-4394; b) M. Janát-Amsbury, A. Ray, C. Peterson, H. Ghandehari, Geometry and surface characteristics of gold nanoparticles influence their biodistribution and uptake by macrophages, European Journal of Pharmaceutics and Biopharmaceutics, 77 (2011) 417-423; c) X. Huang, X. Teng, D. Chen, F. Tang, J. He, The effect of the shape of mesoporous silica nanoparticles on cellular uptake and cell function, Biomaterials, 31 (2010) 438-448.

[55] S. Tang, X. Huang, N. Zheng, Silica coating improves the efficacy of Pd nanosheets for photothermal therapy of cancer cells using near infrared laser, Chemical Communications, 47 (2011) 3948-3950.

[56] Z.-G. Yue, W. Wei, P.-P. Lv, H. Yue, L.-Y. Wang, Z.-G. Su, G.-H. Ma, Surface charge affects cellular uptake and intracellular trafficking of chitosan-based nanoparticles, Biomacromolecules, 12 (2011) 2440-2446.

[57] S. Riedl, D. Zweytick, K. Lohner, Membrane-active host defense peptides–challenges and perspectives for the development of novel anticancer drugs, Chemistry and Physics of Lipids, 164 (2011) 766-781.

[58] a) T. S. Levchenko, R. Rammohan, A. N. Lukyanov, K. R. Whiteman, V. P. Torchilin, Liposome clearance in mice: the effect of a separate and combined presence of surface charge and polymer coating, International Journal of Pharmaceutics, 240 (2002) 95-102; b) K. Xiao, Y. Li, J. Luo, J. S. Lee, W. Xiao, A. M. Gonik, R. G. Agarwal, K. S. Lam, The effect of surface charge on in vivo biodistribution of PEG-oligocholic acid based micellar nanoparticles, Biomaterials, 32 (2011) 3435-3446.

[59] a) A. Gessner, A. Lieske, B. R. Paulke, R. H. Müller, Influence of surface charge density on protein adsorption on polymeric nanoparticles: analysis by two-dimensional electrophoresis, European Journal of Pharmaceutics and Biopharmaceutics, 54 (2002) 165-170; b) A. Gessner, A. Lieske, B. R. Paulke, R. H. Müller, Functional groups on polystyrene model nanoparticles: influence on protein adsorption, Journal of Biomedical Materials Research Part A, 65 (2003) 319-326; c) S. Tenzer, D. Docter, J. Kuharev, A. Musyanovych, V. Fetz, R. Hecht, F. Schlenk, D. Fischer, K. Kiouptsi, C. Reinhardt, Rapid formation of plasma protein corona critically affects nanoparticle pathophysiology, Nature Nanotechnology, 8 (2013) 772-781.

[60] K. Knop, R. Hoogenboom, D. Fischer, U. S. Schubert, Poly (ethylene glycol) in drug delivery: pros and cons as well as potential alternatives, Angewandte Chemie International Edition, 49 (2010) 6288-6308.

[61] a) C. D. Walkey, J. B. Olsen, H. Guo, A. Emili, W. C. Chan, Nanoparticle size and surface chemistry determine serum protein adsorption and macrophage uptake, Journal of the American Chemical Society, 134 (2012) 2139-2147; b) Q. Yang, S. W. Jones, C. L. Parker, W. C. Zamboni, J. E. Bear, S. K. Lai, Evading immune cell uptake and clearance requires PEG grafting at densities substantially exceeding the minimum for brush conformation, Molecular Pharmaceutics, 11 (2014) 1250-1258.

[62] J. T. Robinson, G. Hong, Y. Liang, B. Zhang, O. K. Yaghi, H. Dai, In vivo fluorescence imaging in the second near-infrared window with long circulating carbon nanotubes capable of ultrahigh tumor uptake, Journal of the American Chemical Society, 134 (2012) 10664-10669.

[63] K. Yang, J. Wan, S. Zhang, B. Tian, Y. Zhang, Z. Liu, The influence of surface chemistry and size of nanoscale graphene oxide on photothermal therapy of cancer using ultra-low laser power, Biomaterials, 33 (2012) 2206-2214.

[64] G. Song, J. Hao, C. Liang, T. Liu, M. Gao, L. Cheng, J. Hu, Z. Liu, Degradable Molybdenum Oxide Nanosheets with Rapid Clearance and Efficient Tumor Homing Capabilities as a Therapeutic Nanoplatform, Angewandte Chemie International Edition, 55 (2015) 2122-2126.

[65] X. Liang, Y. Li, X. Li, L. Jing, Z. Deng, X. Yue, C. Li, Z. Dai, PEGylated Polypyrrole Nanoparticles Conjugating Gadolinium Chelates for Dual-Modal MRI/Photoacoustic Imaging Guided Photothermal Therapy of Cancer, Advanced Functional Materials, 25 (2015) 1451-1462.

[66] a) J. L. Perry, K. G. Reuter, M. P. Kai, K. P. Herlihy, S. W. Jones, J. C. Luft, M. Napier, J. E. Bear, J. M. DeSimone, PEGylated PRINT nanoparticles: the impact of PEG density on protein binding, macrophage association, biodistribution, and pharmacokinetics, Nano Letters, 12 (2012) 5304-5310; b) B. Pelaz, P. Del Pino, P. Maffre, R. Hartmann, M. Gallego, S. Rivera-Fernandez, J. M. de la Fuente, G. U. Nienhaus, W. J. Parak, Surface Functionalization of Nanoparticles with Polyethylene Glycol: Effects on Protein Adsorption and Cellular Uptake, ACS Nano, 9 (2015) 6996-7008.

[67] a) Y. Li, R. Liu, Y. Shi, Z. Zhang, X. Zhang, Zwitterionic poly (carboxybetaine)-based cationic liposomes for effective delivery of small interfering RNA therapeutics without accelerated blood clearance phenomenon, Theranostics, 5 (2015) 583-596; b) A. S. A. Lila, K. Nawata, T. Shimizu, T. Ishida, H. Kiwada, Use of polyglycerol (PG), instead of polyethylene glycol (PEG), prevents induction of the accelerated blood clearance phenomenon against long-circulating liposomes upon repeated administration, International Journal of Pharmaceutics, 456 (2013) 235-242; c) M. Bauer, C. Lautenschlaeger, K. Kempe, L. Tauhardt, U. S. Schubert, D. Fischer, Poly (2-ethyl-2-oxazoline) as Alternative for the Stealth Polymer Poly (ethylene glycol): Comparison of in vitro Cytotoxicity and Hemocompatibility, Macromolecular Bioscience, 12 (2012) 986-998; d) V. M. Gaspar, P. Baril, E. C. Costa, D. de Melo-Diogo, F. Foucher, J. A. Queiroz, F. Sousa, C. Pichon, I. J. Correia, Bioreducible poly (2-ethyl-2-oxazoline)–PLA–PEI-SS triblock copolymer micelles for co-delivery of DNA minicircles and Doxorubicin, Journal of Controlled Release, 213 (2015) 175-191; e) P. H. Kierstead, H. Okochi, V. J. Venditto, T. C. Chuong, S. Kivimae, J. M. Fréchet, F. C. Szoka, The effect of polymer backbone chemistry on the induction of the accelerated blood clearance in polymer modified liposomes, Journal of Controlled Release, 213 (2015) 1-9.

[68] J.-G. Piao, L. Wang, F. Gao, Y.-Z. You, Y. Xiong, L. Yang, Erythrocyte membrane is an alternative coating to polyethylene glycol for prolonging the circulation lifetime of gold nanocages for photothermal therapy, ACS Nano, 8 (2014) 10414-10425.

[69] X. Ren, R. Zheng, X. Fang, X. Wang, X. Zhang, W. Yang, X. Sha, Red blood cell membrane camouflaged magnetic nanoclusters for imaging-guided photothermal therapy, Biomaterials, 92 (2016) 13-24.

[70] L. F. Neves, J. J. Krais, B. D. Van Rite, R. Ramesh, D. E. Resasco, R. G. Harrison, Targeting single-walled carbon nanotubes for the treatment of breast cancer using photothermal therapy, Nanotechnology, 24 (2013) 375104.

[71] J. H. Lee, A. Sahu, C. Jang, G. Tae, The effect of ligand density on in vivo tumor targeting of nanographene oxide, Journal of Controlled Release, 209 (2015) 219-228.

[72] S. Liang, C. Li, C. Zhang, Y. Chen, L. Xu, C. Bao, X. Wang, CD44v6 monoclonal antibody-conjugated gold nanostars for targeted photoacoustic imaging and plasmonic photothermal therapy of gastric cancer stem-like cells, Theranostics, 5 (2015) 970-984.

[73] L. Jing, S. Shao, Y. Wang, Y. Yang, X. Yue, Z. Dai, Hyaluronic Acid Modified Hollow Prussian Blue Nanoparticles Loading 10-hydroxycamptothecin for Targeting Thermochemotherapy of Cancer, Theranostics, 6 (2016) 40-53.

[74] T. Lee, D. Bang, Y. Park, S. H. Kim, J. Choi, J. Park, D. Kim, E. Kim, J. S. Suh, Y. M. Huh, Gadolinium-Enriched Polyaniline Particles (GPAPs) for Simultaneous Diagnostic Imaging and

Localized Photothermal Therapy of Epithelial Cancer, Advanced Healthcare Materials, 3 (2014) 1408-1414.

[75] H. Jo, H. Youn, S. Lee, C. Ban, Ultra-effective photothermal therapy for prostate cancer cells using dual aptamer-modified gold nanostars, Journal of Materials Chemistry B, 2 (2014) 4862-4867.

[76] C. Jang, J. H. Lee, A. Sahu, G. Tae, The synergistic effect of folate and RGD dual ligand of nanographene oxide on tumor targeting and photothermal therapy in vivo, Nanoscale, 7 (2015) 18584-18594.

[77] D. Banerjee, R. Harfouche, S. Sengupta, Nanotechnology-mediated targeting of tumor angiogenesis, Vascular Cell, 3 (2011) 3.

[78] D. Yang, L. Feng, C. A. Dougherty, K. E. Luker, D. Chen, M. A. Cauble, M. M. B. Holl, G. D. Luker, B. D. Ross, Z. Liu, In vivo targeting of metastatic breast cancer via tumor vasculature-specific nano-graphene oxide, Biomaterials, 104 (2016) 361-371.

[79] W. Tao, J. Zhang, X. Zeng, D. Liu, G. Liu, X. Zhu, Y. Liu, Q. Yu, L. Huang, L. Mei, Blended Nanoparticle System Based on Miscible Structurally Similar Polymers: A Safe, Simple, Targeted, and Surprisingly High Efficiency Vehicle for Cancer Therapy, Advanced Healthcare Materials, 4 (2015) 1203-1214.

[80] A. Salvati, A. S. Pitek, M. P. Monopoli, K. Prapainop, F. B. Bombelli, D. R. Hristov, P. M. Kelly, C. Åberg, E. Mahon, K. A. Dawson, Transferrin-functionalized nanoparticles lose their targeting capabilities when a biomolecule corona adsorbs on the surface, Nature Nanotechnology, 8 (2013) 137-143.

[81] B.-X. Zhao, Y. Zhao, Y. Huang, L.-M. Luo, P. Song, X. Wang, S. Chen, K.-F. Yu, X. Zhang, Q. Zhang, The efficiency of tumor-specific pH-responsive peptide-modified polymeric micelles containing paclitaxel, Biomaterials, 33 (2012) 2508-2520.

[82] Q. Dai, C. Walkey, W. C. W. Chan, Polyethylene Glycol Backfilling Mitigates the Negative Impact of the Protein Corona on Nanoparticle Cell Targeting, Angewandte Chemie International Edition, 53 (2014) 5093-5096.

[83] Z. Liu, W. Cai, L. He, N. Nakayama, K. Chen, X. Sun, X. Chen, H. Dai, In vivo biodistribution and highly efficient tumour targeting of carbon nanotubes in mice, Nature Nanotechnology, 2 (2007) 47-52.

[84] S. Zhang, C. Sun, J. Zeng, Q. Sun, G. Wang, Y. Wang, Y. Wu, S. Dou, M. Gao, Z. Li, Ambient Aqueous Synthesis of Ultrasmall PEGylated Cu2− xSe Nanoparticles as a Multifunctional Theranostic Agent for Multimodal Imaging Guided Photothermal Therapy of Cancer, Advanced Materials, 28 (2016) 8927-8936.

[85] Q. Tian, F. Jiang, R. Zou, Q. Liu, Z. Chen, M. Zhu, S. Yang, J. Wang, J. Wang, J. Hu, Hydrophilic Cu9S5 nanocrystals: A photothermal agent with a 25.7% heat conversion efficiency for photothermal ablation of cancer cells in vivo, ACS Nano, 5 (2011) 9761-9771.

[86] J.-W. Xiao, S.-X. Fan, F. Wang, L.-D. Sun, X.-Y. Zheng, C.-H. Yan, Porous Pd nanoparticles with high photothermal conversion efficiency for efficient ablation of cancer cells, Nanoscale, 6 (2014) 4345-4351.

[87] C. Ayala-Orozco, C. Urban, M. W. Knight, A. S. Urban, O. Neumann, S. W. Bishnoi, S. Mukherjee, A. M. Goodman, H. Charron, T. Mitchell, M. Shea, R. Roy, S. Nanda, R. Schiff, N. J. Halas, A. Joshi, Au Nanomatryoshkas as Efficient Near-Infrared Photothermal Transducers for Cancer Treatment: Benchmarking against Nanoshells, ACS Nano, 8 (2014) 6372-6381.

[88] J. Zeng, D. Goldfeld, Y. Xia, A Plasmon-Assisted Optofluidic (PAOF) System for Measuring the Photothermal Conversion Efficiencies of Gold Nanostructures and Controlling an Electrical Switch, Angewandte Chemie International Edition, 52 (2013) 4169-4173.

[89] P. Huang, P. Rong, J. Lin, W. Li, X. Yan, M. G. Zhang, L. Nie, G. Niu, J. Lu, W. Wang, X. Chen, Triphase Interface Synthesis of Plasmonic Gold Bellflowers as Near-Infrared Light Mediated Acoustic and Thermal Theranostics, Journal of the American Chemical Society, 136 (2014) 8307-8313.

[90] J. R. Cole, N. A. Mirin, M. W. Knight, G. P. Goodrich, N. J. Halas, Photothermal Efficiencies of Nanoshells and Nanorods for Clinical Therapeutic Applications, Journal of Physical Chemistry C, 113 (2009) 12090-12094.

[91] H. Chen, L. Shao, T. Ming, Z. Sun, C. Zhao, B. Yang, J. Wang, Understanding the Photothermal Conversion Efficiency of Gold Nanocrystals, Small, 6 (2010) 2272-2280.

[92] W. Feng, L. Chen, M. Qin, X. Zhou, Q. Zhang, Y. Miao, K. Qiu, Y. Zhang, C. He, Flower-like PEGylated MoS2 nanoflakes for near-infrared photothermal cancer therapy, Scientific Reports, 5 (2015) 17422.

[93] C. Guo, H. Yu, B. Feng, W. Gao, M. Yan, Z. Zhang, Y. Li, S. Liu, Highly efficient ablation of metastatic breast cancer using ammonium-tungsten-bronze nanocube as a novel 1064 nm-laser-driven photothermal agent, Biomaterials, 52 (2015) 407-416.

[94] K. M. Au, M. Chen, S. P. Armes, N. Zheng, Near-infrared light-triggered irreversible aggregation of poly (oligo (ethylene glycol) methacrylate)-stabilised polypyrrole nanoparticles under biologically relevant conditions, Chemical Communications, 49 (2013) 10525-10527.

[95] B. Kim, J. Kim, E. Kim, Visible to Near-IR Electrochromism and photothermal effect of poly(3, 4-propylenedioxyselenophene)s, Macromolecules, 44 (2011) 8791-8797.

[96] J. Jang, J. Ha, B. Lim, Synthesis and characterization of monodisperse silica–polyaniline core–shell nanoparticles, Chemical Communications, 0 (2006) 1622-1624.

[97] E. Ju, K. Dong, Z. Liu, F. Pu, J. Ren, X. Qu, Tumor Microenvironment Activated Photothermal Strategy for Precisely Controlled Ablation of Solid Tumors upon NIR Irradiation, Advanced Functional Materials, 25 (2015) 1574-1580.

[98] L. Wen, L. Chen, S. Zheng, J. Zeng, G. Duan, Y. Wang, G. Wang, Z. Chai, Z. Li, M. Gao, Ultrasmall Biocompatible WO3− x Nanodots for Multi-Modality Imaging and Combined Therapy of Cancers, Advanced Materials, 28 (2016) 5072-5079.

[99] L. Zeng, Y. Pan, S. Wang, X. Wang, X. Zhao, W. Ren, G. Lu, A. Wu, Raman Reporter-Coupled Agcore@Aushell Nanostars for in Vivo Improved Surface Enhanced Raman Scattering Imaging and Near-infrared-Triggered Photothermal Therapy in Breast Cancers, ACS Applied Materials & Interfaces, 7 (2015) 16781-16791.

[100] Z. Liu, L. Cheng, L. Zhang, Z. Yang, Z. Liu, J. Fang, Sub-100 nm hollow Au–Ag alloy urchin-shaped nanostructure with ultrahigh density of nanotips for photothermal cancer therapy, Biomaterials, 35 (2014) 4099-4107.

[101] J. Li, J. Han, T. Xu, C. Guo, X. Bu, H. Zhang, L. Wang, H. Sun, B. Yang, Coating Urchinlike Gold Nanoparticles with Polypyrrole Thin Shells To Produce Photothermal Agents with High Stability and Photothermal Transduction Efficiency, Langmuir, 29 (2013) 7102-7110.

[102] X. Zhang, X. Xu, T. Li, M. Lin, X. Lin, H. Zhang, H. Sun, B. Yang, Composite Photothermal Platform of Polypyrrole-Enveloped Fe3O4 Nanoparticle Self-Assembled Superstructures, ACS Applied Materials & Interfaces, 6 (2014) 14552-14561.

[103] R. Zheng, S. Wang, Y. Tian, X. Jiang, D. Fu, S. Shen, W. Yang, Polydopamine-Coated Magnetic Composite Particles with an Enhanced Photothermal Effect, ACS Applied Materials & Interfaces, 7 (2015) 15876-15884.

[104] D. Li, Y. Zhang, S. Wen, Y. Song, Y. Tang, X. Zhu, M. Shen, S. Mignani, J.-P. Majoral, Q. Zhao, X. Shi, Construction of polydopamine-coated gold nanostars for CT imaging and enhanced photothermal therapy of tumors: an innovative theranostic strategy, Journal of Materials Chemistry B, 4 (2016) 4216-4226.

[105] D. Jaque, L. M. Maestro, B. Del Rosal, P. Haro-Gonzalez, A. Benayas, J. Plaza, E. M. Rodriguez, J. G. Sole, Nanoparticles for photothermal therapies, Nanoscale, 6 (2014) 9494-9530.

[106] X. Huang, M. A. El-Sayed, Gold nanoparticles: optical properties and implementations in cancer diagnosis and photothermal therapy, Journal of Advanced Research, 1 (2010) 13-28.

[107] Q. Wang, J. Wang, G. Lv, F. Wang, X. Zhou, J. Hu, Q. Wang, Facile synthesis of hydrophilic polypyrrole nanoparticles for photothermal cancer therapy, Journal of Materials Science, 49 (2014) 3484-3490.

[108] Y. Yong, X. Cheng, T. Bao, M. Zu, L. Yan, W. Yin, C. Ge, D. Wang, Z. Gu, Y. Zhao, Tungsten Sulfide Quantum Dots as Multifunctional Nanotheranostics for In Vivo Dual-Modal Image-Guided Photothermal/Radiotherapy Synergistic Therapy, ACS Nano, 9 (2015) 12451-12463.

[109] H. Peng, S. Tang, Y. Tian, R. Zheng, L. Zhou, W. Yang, Highly Ligand-Directed and Size-Dependent Photothermal Properties of Magnetite Particles, Particle & Particle Systems Characterization, 33 (2016) 332-340.

[110] S. Ye, G. Marston, J. R. McLaughlan, D. O. Sigle, N. Ingram, S. Freear, J. J. Baumberg, R. J. Bushby, A. F. Markham, K. Critchley, Engineering Gold Nanotubes with Controlled Length and Near-Infrared Absorption for Theranostic Applications, Advanced Functional Materials, 25 (2015) 2117-2127.

[111] W. Zhu, K. Liu, X. Sun, X. Wang, Y. Li, L. Cheng, Z. Liu, Mn2+-Doped Prussian Blue Nanocubes for Bimodal Imaging and Photothermal Therapy with Enhanced Performance, ACS Applied Materials & Interfaces, 7 (2015) 11575–11582.

[112] X. Cai, W. Gao, L. Zhang, M. Ma, T. Liu, W. Du, Y. Zheng, H. Chen, J. Shi, Enabling Prussian Blue with Tunable Localized Surface Plasmon Resonances: Simultaneously Enhanced Dual-Mode Imaging and Tumor Photothermal Therapy, ACS Nano, 10 (2016) 11115-11126.

[113] P. Huang, J. Lin, W. Li, P. Rong, Z. Wang, S. Wang, X. Wang, X. Sun, M. Aronova, G. Niu, Biodegradable gold nanovesicles with an ultrastrong plasmonic coupling effect for photoacoustic imaging and photothermal therapy, Angewandte Chemie International Edition, 125 (2013) 14208-14214.

[114] P. Wu, D. Deng, J. Gao, C. Cai, Tubelike Gold Sphere–Attapulgite Nanocomposites with a High Photothermal Conversion Ability in the Near-Infrared Region for Enhanced Cancer Photothermal Therapy, ACS Applied Materials & Interfaces, 8 (2016) 10243-10252.

[115] H. Liu, D. Nishide, T. Tanaka, H. Kataura, Large-scale single-chirality separation of single-wall carbon nanotubes by simple gel chromatography, Nature Communications, 2 (2011) 309.

[116] A. L. Antaris, J. T. Robinson, O. K. Yaghi, G. Hong, S. Diao, R. Luong, H. Dai, Ultra-low doses of chirality sorted (6, 5) carbon nanotubes for simultaneous tumor imaging and photothermal therapy, ACS Nano, 7 (2013) 3644-3652.

[117] K. Yang, H. Xu, L. Cheng, C. Sun, J. Wang, Z. Liu, In Vitro and In Vivo Near-Infrared Photothermal Therapy of Cancer Using Polypyrrole Organic Nanoparticles, Advanced Materials, 24 (2012) 5586-5592.

[118] Y.-F. Wang, G.-Y. Liu, L.-D. Sun, J.-W. Xiao, J.-C. Zhou, C.-H. Yan, Nd3+-sensitized upconversion nanophosphors: Efficient in vivo bioimaging probes with minimized heating effect, ACS Nano, 7 (2013) 7200-7206.

[119] W. Xu, Z. Meng, N. Yu, Z. Chen, B. Sun, X. Jiang, M. Zhu, PEGylated Cs x WO 3 nanorods as an efficient and stable 915 nm-laser-driven photothermal agent against cancer cells, RSC Advances, 5 (2015) 7074-7082.

[120] G. Tian, X. Zhang, X. Zheng, W. Yin, L. Ruan, X. Liu, L. Zhou, L. Yan, S. Li, Z. Gu, Multifunctional RbxWO3 Nanorods for Simultaneous Combined Chemo-photothermal Therapy and Photoacoustic/CT Imaging, Small, 10 (2014) 4160-4170.

[121] C. Liang, S. Diao, C. Wang, H. Gong, T. Liu, G. Hong, X. Shi, H. Dai, Z. Liu, Tumor Metastasis Inhibition by Imaging-Guided Photothermal Therapy with Single-Walled Carbon Nanotubes, Advanced Materials, 26 (2014) 5646-5652.

[122] B. Zhang, H. Wang, S. Shen, X. She, W. Shi, J. Chen, Q. Zhang, Y. Hu, Z. Pang, X. Jiang, Fibrin-targeting peptide CREKA-conjugated multi-walled carbon nanotubes for self-amplified photothermal therapy of tumor, Biomaterials, 79 (2016) 46-55.

[123] W. Fang, S. Tang, P. Liu, X. Fang, J. Gong, N. Zheng, Pd Nanosheet-Covered Hollow Mesoporous Silica Nanoparticles as a Platform for the Chemo-Photothermal Treatment of Cancer Cells, Small, 8 (2012) 3816-3822.

[124] C. Xu, S. Shi, L. Feng, F. Chen, S. A. Graves, E. B. Ehlerding, S. Goel, H. Sun, C. G. England, R. J. Nickles, Z. Liu, T. Wang, W. Cai, Long circulating reduced graphene oxide–iron oxide nanoparticles for efficient tumor targeting and multimodality imaging, Nanoscale, 8 (2016) 12683-12692.

[125] Y. Chao, G. Wang, C. Liang, X. Yi, X. Zhong, J. Liu, M. Gao, K. Yang, L. Cheng, Z. Liu, Rhenium-188 Labeled Tungsten Disulfide Nanoflakes for Self-Sensitized, Near-Infrared Enhanced Radioisotope Therapy, Small, 12 (2016) 3967-3975.

[126] M. Chen, S. Tang, Z. Guo, X. Wang, S. Mo, X. Huang, G. Liu, N. Zheng, Core–Shell Pd@Au Nanoplates as Theranostic Agents for In-Vivo Photoacoustic Imaging, CT Imaging, and Photothermal Therapy, Advanced Materials, 26 (2014) 8210-8216.

[127] H. S. Jung, W. H. Kong, D. K. Sung, M.-Y. Lee, S. E. Beack, D. H. Keum, K. S. Kim, S. H. Yun, S. K. Hahn, Nanographene oxide–hyaluronic acid conjugate for photothermal ablation therapy of skin cancer, ACS Nano, 8 (2014) 260-268.

[128] J. Yu, C. Yang, J. Li, Y. Ding, L. Zhang, M. Z. Yousaf, J. Lin, R. Pang, L. Wei, L. Xu, Multifunctional Fe5C2 Nanoparticles: A Targeted Theranostic Platform for Magnetic Resonance Imaging and Photoacoustic Tomography-Guided Photothermal Therapy, Advanced Materials, 26 (2014) 4114-4120.

[129] G. M. Santos, F. Zhao, J. Zeng, W.-C. Shih, Characterization of nanoporous gold disks for photothermal light harvesting and light-gated molecular release, Nanoscale, 6 (2014) 5718-5724.

[130] V. P. Pattani, J. W. Tunnell, Nanoparticle-mediated photothermal therapy: A comparative study of heating for different particle types, Lasers in Surgery and Medicine, 44 (2012) 675-684.

[131] K.-C. Li, H.-C. Chu, Y. Lin, H.-Y. Tuan, Y.-C. Hu, PEGylated Copper Nanowires as a Novel Photothermal Therapy Agent, ACS Applied Materials & Interfaces, 8 (2016) 12082–12090.

[132] W. Yang, W. Guo, W. Le, G. Lv, F. Zhang, L. Shi, X. Wang, J. Wang, S. Wang, J. Chang, B. Zhang, Albumin-Bioinspired Gd:CuS Nanotheranostic Agent for In Vivo Photoacoustic/Magnetic Resonance Imaging-Guided Tumor-Targeted Photothermal Therapy, ACS Nano, 10 (2016) 10245-10257.

[133] Z. Wang, P. Huang, O. Jacobson, Z. Wang, Y. Liu, L. Lin, J. Lin, N. Lu, H. Zhang, R. Tian, Biomineralization-Inspired Synthesis of Copper Sulfide–Ferritin Nanocages as Cancer Theranostics, ACS Nano, 10 (2016) 3453-3460.

[134] H. Chen, M. Song, J. Tang, G. Hu, S. Xu, Z. Guo, N. Li, J. Cui, X. Zhang, X. Chen, Ultrahigh 19F Loaded Cu1. 75S Nanoprobes for Simultaneous 19F Magnetic Resonance Imaging and Photothermal Therapy, ACS Nano, 10 (2016) 1355-1362.

[135] G. Song, J. Shen, F. Jiang, R. Hu, W. Li, L. An, R. Zou, Z. Chen, Z. Qin, J. Hu, Hydrophilic Molybdenum Oxide Nanomaterials with Controlled Morphology and Strong Plasmonic Absorption for Photothermal Ablation of Cancer Cells, ACS Applied Materials & Interfaces, 6 (2014) 3915-3922.

[136] W. Yin, L. Yan, J. Yu, G. Tian, L. Zhou, X. Zheng, X. Zhang, Y. Yong, J. Li, Z. Gu, High-throughput synthesis of single-layer MoS2 nanosheets as a near-infrared photothermal-triggered drug delivery for effective cancer therapy, ACS Nano, 8 (2014) 6922-6933.

[137] L. Tan, S. Wang, K. Xu, T. Liu, P. Liang, M. Niu, C. Fu, H. Shao, J. Yu, T. Ma, Layered MoS2 Hollow Spheres for Highly-Efficient Photothermal Therapy of Rabbit Liver Orthotopic Transplantation Tumors, Small, 12 (2016) 2046-2055.

[138] L. Yuwen, J. Zhou, Y. Zhang, Q. Zhang, J. Shan, Z. Luo, L. Weng, Z. Teng, L. Wang, Aqueous phase preparation of ultrasmall MoSe 2 nanodots for efficient photothermal therapy of cancer cells, Nanoscale, 8 (2016) 2720-2726.

[139] Z. Huang, Y. Qi, D. Yu, J. Zhan, Radar-like MoS 2 nanoparticles as a highly efficient 808 nm laser-induced photothermal agent for cancer therapy, RSC Advances, 6 (2016) 31031-31036.

[140] Z. Lei, W. Zhu, S. Xu, J. Ding, J. Wan, P. Wu, Hydrophilic MoSe2 Nanosheets as Effective Photothermal Therapy Agents and Their Application in Smart Devices, ACS Applied Materials & Interfaces, 8 (2016) 20900-20908.

[141] G. Song, J. Hao, C. Liang, T. Liu, M. Gao, L. Cheng, J. Hu, Z. Liu, Degradable Molybdenum Oxide Nanosheets with Rapid Clearance and Efficient Tumor Homing Capabilities as a Therapeutic Nanoplatform, Angewandte Chemie International Edition, 55 (2015) 2122-2126.

[142] M. Zhang, Y. Cao, L. Wang, Y. Ma, X. Tu, Z. Zhang, Manganese Doped Iron Oxide Theranostic Nanoparticles for Combined T 1 Magnetic Resonance Imaging and Photothermal Therapy, ACS Applied Materials & Interfaces, 7 (2015) 4650-4658.

[143] J. Zeng, M. Cheng, Y. Wang, L. Wen, L. Chen, Z. Li, Y. Wu, M. Gao, Z. Chai, pH-Responsive Fe(III)–Gallic Acid Nanoparticles for In Vivo Photoacoustic-Imaging-Guided Photothermal Therapy, Advanced Healthcare Materials, 5 (2016) 772-780.

[144] C. M. MacNeill, E. M. Wailes, N. H. Levi-Polyachenko, A Comparative Study of the Photothermal Efficiency of Electrically Conducting Poly (3, 4-ethylenedioxythiophene)-Based

Nanomaterials with Cancer Cells, Journal of Nanoscience and Nanotechnology, 13 (2013) 3784-3791.

[145] C. M. MacNeill, R. C. Coffin, D. L. Carroll, N. H. Levi-Polyachenko, Low Band Gap Donor-Acceptor Conjugated Polymer Nanoparticles and their NIR-mediated Thermal Ablation of Cancer Cells, Macromolecular Bioscience, 13 (2013) 28-34.

[146] L. Beqa, Z. Fan, A. K. Singh, D. Senapati, P. C. Ray, Gold Nano-Popcorn Attached SWCNT Hybrid Nanomaterial for Targeted Diagnosis and Photothermal Therapy of Human Breast Cancer Cells, ACS Applied Materials & Interfaces, 3 (2011) 3316-3324.

[147] J. Bai, Y. Liu, X. Jiang, Multifunctional PEG-GO/CuS nanocomposites for near-infrared chemo-photothermal therapy, Biomaterials, 35 (2014) 5805-5813.

[148] Z. Zhou, Y. Sun, J. Shen, J. Wei, C. Yu, B. Kong, W. Liu, H. Yang, S. Yang, W. Wang, Iron/iron oxide core/shell nanoparticles for magnetic targeting MRI and near-infrared photothermal therapy, Biomaterials, 35 (2014) 7470-7478.

[149] W. Feng, X. Zhou, W. Nie, L. Chen, K. Qiu, Y. Zhang, C. He, Au/Polypyrrole@Fe3O4 Nanocomposites for MR/CT Dual-Modal Imaging Guided-Photothermal Therapy: An in Vitro Study, ACS Applied Materials & Interfaces, 7 (2015) 4354-4367.

[150] Q. Tian, Q. Wang, K. X. Yao, B. Teng, J. Zhang, S. Yang, Y. Han, Multifunctional Polypyrrole@Fe3O4 Nanoparticles for Dual-Modal Imaging and In Vivo Photothermal Cancer Therapy, Small, 10 (2014) 1063-1068.

[151] S. Bhana, G. Lin, L. Wang, H. Starring, S. R. Mishra, G. Liu, X. Huang, Near-Infrared-Absorbing Gold Nanopopcorns with Iron Oxide Cluster Core for Magnetically Amplified Photothermal and Photodynamic Cancer Therapy, ACS Applied Materials & Interfaces, 7 (2015) 11637-11647.

[152] T. Liu, Y. Chao, M. Gao, C. Liang, Q. Chen, G. Song, L. Cheng, Z. Liu, Ultra-small MoS2 nanodots with rapid body clearance for photothermal cancer therapy, Nano Research, 9 (2016) 3003–3017.

2.9. Supplementary Information

Table S.2.1. *In vivo* assays data of some nanomaterials used in cancer PTT.

Type of nanomaterial	Tumor model	Administration route	Dose	Laser settings	Tumor temperature	Therapeutic effect	Ref.
PEGylated GNR	MDA-MB-435 tumor-bearing mice	i.v.	20 mg kg^{-1}	810 nm, 2 W cm^{-2}, 5 min	≈ 70 °C	Tumor eradication	[1]
PEGylated rod-like gold nanoshell capsules	B16F10 tumor-bearing mice	i.v.	10 mg kg^{-1}	800 nm, 0.4 W cm^{-2}, 3 min	N.A.	Tumor growth reduced	[2]
PEGylated gold nanohexapods	MDA-MB-435 tumor-bearing mice	i.v.	800 µg	808 nm, 1.2 W cm^{-2}, 10 min	≈ 56 °C	Tumor eradication	[3]
PEGylated gold nanomatryoshkas	MDA-MB-231-LM2 tumor-bearing mice	i.v.	300 µg	808 nm, 2 W cm^{-2}, 5 min	ΔT ≈ 34 °C	Tumor eradication (for 5 in 6 mice)	[4]
PEGylated gold bellflowers	4T1 tumor-bearing mice	i.t.	20 µg	808 nm, 0.5 W cm^{-2}, 5 min	≈ 52 °C	Tumor eradication	[5]
Folic acid functionalized PEGylated gold nanobipyramids	MCF-7 tumor-bearing mice	i.v.	75 µg	808 nm, 1.6 W cm^{-2}, 5 min	≈ 70 °C	Tumor eradication	[6]

Chitosan-Pluronic® F-68 conjugates loaded with GNR	SCC7 tumor-bearing mice	i.v.	100 μg	808 nm, 4 W cm^{-2}, 4 min, at 24 and 48 h p.i.	N.A.	Tumor eradication	[7]
RBC-derived membrane coated PVP-gold nanocages	4T1 tumor-bearing mice	i.v.	250 μg	850 nm, 1 W cm^{-2}, 10 min, once a day during 19 days	≈ 47 °C	Tumor regression	[8]
Macrophage cell membrane coated gold nanoshells	4T1 tumor-bearing mice	i.v.	450 μg	808 nm, 1 W cm^{-2}, 5 min	N.A.	Tumor regression	[9]
Nanovesicles assembled using PEG-PCL functionalized gold nanoparticles	MDA-MB-435 tumor-bearing mice	i.t.	20 μg	808 nm, 0.5 W cm^{-2}, 5 min	ΔT ≈ 18 °C	Tumor eradication	[10]
Au–attapulgite nanocomposites	A549 tumor-bearing mice	i.t.	100 μg	808 nm, 0.5 W cm^{-2}, 15 min	≈ 48 °C	Tumor regression	[11]
PEGylated gold nanostars functionalized with anti-CD44v6 antibody	MKN-45 tumor- bearing mice	i.v.	130 μg	790 nm, 0.8 W cm^{-2}, 5 min, every two days during 14 days	≈ 61 °C[a)]	Tumor regression	[12]
Amine/carboxyl-terminated PEGylated gold nanostars	4T1 tumor-bearing mice	i.v.	≈ 2×10^{-7} M (100 μL)	808 nm, 1 W cm^{-2}, 5 min	≈ 56 °C	Tumor eradication	[13]
C_{18}-PMH-mPEG coated CNT	4T1 tumor-bearing mice	i.v.	100 μg	808 nm, 1 W cm^{-2}, 5 min	≈ 50 °C	Tumor regression	[14]

DSPE-PEG-Annexin V functionalized CNT	4T1 tumor-bearing mice	i.v.	≈ 16.35 μg 0.8 mg kg^{-1}	980 nm, 1 W cm^{-2}, 175 sec	N.A.	Tumor eradication (for 4 in 6 mice)	[15]
DSPE-PEG-CREKA functionalized CNT	A549 tumor-bearing mice	i.v.	4 mg kg^{-1}	808 nm, 3.5 W cm^{-2}, 90 sec, on day 0, 3, 6 and 9	≈ 55 °C	Tumor regression	[16]
C_{18}-PMH-mPEG coated CNT	4T1 tumor-bearing mice	i.t.	4.25 μg 0.2 mg kg^{-1}	Tumor: 808 nm, 0.5 W cm^{-2}, 10 min Lymph node: 808 nm, 0.8 W cm^{-2}, 10 min	Tumor: ≈ 55 °C Lymph node: ≈ 47 °C	Tumor eradication (for 6 in 7 mice)	[17]
C_{18}-PMH-mPEG coated (6,5) CNT	4T1 tumor-bearing mice	i.v.	≈ 4 μg 0.254 mg kg^{-1}	980 nm, 0.6 W cm^{-2}, 5 min	≈ 51 °C	Tumor eradication (for 3 in 4 mice)	[18]
PEGylated nGO	4T1 tumor-bearing mice	i.v.	400 μg 20 mg kg^{-1}	808 nm, 2 W cm^{-2}, 5 min	≈ 50 °C	Tumor eradication	[19]
C_{18}-PMH-mPEG coated reduced nGO	4T1 tumor-bearing mice	i.v.	400 μg 20 mg kg^{-1}	808 nm, 0.15 W cm^{-2}, 5 min	≈ 48 °C	Tumor eradication	[20]
HA conjugated nGO	B16F1 tumor-bearing mice	topical	100 μg	808 nm, 2 W cm^{-2}, 10 min	N.A.	Tumor eradication	[21]

Pluronic® F-127-FA coated nGO	KB tumor-bearing mice	i.v.	10 mg kg^{-1}	808 nm, 2 W cm^{-2}, 10 min	≈ 60 °C	Tumor eradication (for 2 in 3 mice)	[22]
Pluronic® F-127-FA and Pluronic® F-127-RGD coated nGO	KB tumor-bearing mice	i.v.	7.5 mg kg^{-1}	808 nm, 2 W cm^{-2}, 10 min	≈ 57 °C	Tumor eradication	[23]
DSPE-PEG-RGD functionalized rGONM	U87MG tumor-bearing mice	i.v.	2 μg	808 nm, 0.1 W cm^{-2}, 7 min	N.A.	Tumor eradication	[24]
DSPE-PEG coated $Cu_{2-x}S$ nanodots	HeLa tumor-bearing mice	i.v.	≈ 200 μg 10 mg kg^{-1}	980 nm, 1.41 W cm^{-2}, 5 min	≈ 69 °C	Tumor eradication	[25]
Silica coated $Cu_{1.75}S$	4T1 tumor-bearing mice	i.t.	1.1 mg	808 nm, 1 W cm^{-2}, 10 min	≈ 57 °C	Tumor eradication	[26]
Hydrolyzed poly(isobutylene-*alt*-maleic anhydride)-oleylamine coated $Cu_{7.2}S_4$ nanocrystals	K7M2 tumor-bearing mice	i.t.	40 ppm (100 μL)	980 nm, 0.72 W cm^{-2}, 7 min	≈ 46 °C	N.A.	[27]
PVP coated CuS nanodots	4T1 tumor-bearing mice	i.v.	100 μg 4 mg kg^{-1}	808 nm, 2 W cm^{-2}, 2 min	≈ 46 °C	Tumor eradication	[28]
FA coated CuS nanoaparticles	KB tumor-bearing mice	i.v.	40 μg	808 nm, 1.5 W cm^{-2}, 2 min	≈ 57 °C	N.A.	[29]

Ferritin-CuS nanocages	U87MG tumor-bearing mice	i.v.	N.A.	808 nm, 0.8 W cm^{-2}, 5 min	≈ 65 °C	Tumor eradication	[30]
PEGylated Cu nanowires	CT26 tumor-bearing mice	i.t.	125 – 150 μg	808 nm, 1.5 W cm^{-2}, 6 min	≈ 56 °C	Tumor growth reduced	[31]
PEGylated $Cu_{2-x}Se$ nanoparticles	4T1 tumor-bearing mice	i.v.	100 μg	808 nm, 1.5 W cm^{-2}, 6 min	≈ 58 °C	Tumor eradication	[32]
BSA-Gd:CuS nanoparticles	SK-OV-3 tumor-bearing mice	i.v.	10 mg kg^{-1}	980 nm, 0.8 W cm^{-2}, 5 min	≈ 51 °C	Tumor eradication	[33]
PEGylated MoS_2 nanosheets	4T1 tumor-bearing mice	i.v.	200 μg	808 nm, 1 W cm^{-2}, 5 min	N.A.	Tumor growth inhibition	[34]
PEGylated MoO_{3-x} hollow nanospheres	PANC-1 tumor-bearing mice	i.v.	10 mg kg^{-1}	808 nm, 1 W cm^{-2}, 10 min	≈ 48 °C	Tumor regression	[35]
Chitosan coated MoS_2 nanosheets	PANC-1 tumor-bearing mice	i.t.	2 mg kg^{-1}	808 nm, 0.9 W cm^{-2}, 7 min	≈ 50 °C	Tumor growth reduced	[36]

C_{18}-PMH-mPEG coated Mo oxide nanosheets	4T1 tumor-bearing mice	i.t. i.v.	i.t.: 1.25 mg kg^{-1} i.v.: 20 mg kg^{-1}	808 nm, 0.7 W cm^{-2}, 10 min	≈ 55 °C (i.v.)	Tumor eradication	[37]
Layered MoS_2 hollow spheres	VX2 tumor-bearing rabbit	intra-arterial injection	1 mg kg^{-1}	808 nm, 1 W cm^{-2}, 3 min	≈ 55 °C	Tumor eradication	[38]
Radar-like MoS_2 nanoparticles	4T1 tumor-bearing mice	i.t.	100 ppm (100 μL)	808 nm, 0.5 W cm^{-2}, 10 min	N.A.	Tumor growth reduced	[39]
GSH functionalized MoS_2 nanodots	4T1 tumor-bearing mice	i.v.	≈ 100 μg	808 nm, 1 W cm^{-2}, 5 min	≈ 52 °C	Tumor eradication	[40]
$(NH_4)_xWO_3$ nanocubes	4T1 tumor-bearing mice	i.t.	≈ 500 μg 5 mg kg^{-1}	1064 nm, 1 W cm^{-2}, 2 min, every three days during 9 days	ΔT ≈ 45 °C	Tumor regression	[41]
PEGylated $WO_{2.9}$ nanorods	HeLa tumor-bearing mice	i.t.	20 mg kg^{-1}	980 nm, 0.35 W cm^{-2}, 5 min, every two days during 14 days	ΔT = 20 °C	Tumor eradication	[42]
PEGylated Cs_xWO_3 nanorods	MAD-MB-231 tumor-bearing mice	i.t.	25 μg	915 nm, 0.72 W cm^{-2}, 10 min	≈ 48 °C	N.A.	[43]

Anti-HER-2 antibody functionalized PAA-$W_{18}O_{49}$ nanoparticles	MM435 metastasis-bearing mice	subcutaneous injection	15 mg	1064 nm, 0.75 W cm^{-2}, 10 min	≈ 54 °C (lymph node)	Metastasis elimination	[44]
HA coated WO_3 nanoparticles	MAD-MB-231 tumor-bearing mice	i.v.	≈ 750 μg 30 mg kg^{-1}	808 nm, 2 W cm^{-2}, 5 min	50 °C	Tumor regression	[45]
PEGylated WS_2 nanosheets	4T1 tumor-bearing mice	i.t. i.v.	i.t.: 40 μg, 2 mg kg^{-1} i.v.: 400 μg, 20 mg kg^{-1}	808 nm, 0.8 W cm^{-2}, 5 min	≈ 65 °C (i.t. and i.v.)	Tumor eradication	[46]
C_{18}-PMH-PEG coated WS_2 nanoflakes	4T1 tumor-bearing mice	i.v.	20 mg kg^{-1}	808 nm, ≈ 0.3 W cm^{-2}, 20 min	≈ 45 °C	Tumor growth reduced	[47]
PVP-coated $Rb_{0.27}WO_3$ nanorods	PANC-1 tumor-bearing mice	i.t.	N.A.	808 nm, 1 W cm^{-2}, 10 min	≈ 50 °C	Tumor growth reduced	[48]
PTMP-PMAA coated WO_{3-x} nanodots	4T1 tumor-bearing mice	i.v.	400 μg	808 nm, 0.75 W cm^{-2}, 10 min	ΔT = 25 °C	Tumor growth reduced	[49]
PEGylated WS_2 quantum dots	BEL-7402 tumor-bearing mice	i.t.	40 μg	808 nm, 1 W cm^{-2}, 10 min	≈ 45 °C	Tumor growth reduced	[50]

Mn^{2+} doped PEGylated PB nanocubes	4T1 tumor-bearing mice	i.v.	20 mg kg^{-1}	808 nm, 0.8 W cm^{-2}, 5 min	≈ 55 °C	Tumor eradication	[51]
Gd^{3+} containing hollow mesoporous PB nanoparticles	4T1 tumor-bearing mice	i.t.	50 ppm (30 μL)	808 nm, 0.58 W cm^{-2}, 10 min	ΔT ≈ 16 °C	Tumor eradication	[52]
PEGylated PB nanocubes	4T1 tumor-bearing mice	i.v.	200 μg 10 mg kg^{-1}	808 nm, 0.8 W cm^{-2}, 5 min	≈ 62 °C	Tumor eradication	[53]
HA-grafted-PEG coated hollow PB nanocubes	HeLa tumor-bearing mice	i.v.	10 mg kg^{-1}	808 nm, 1 W cm^{-2}, 10 min	≈ 53 °C[b)]	Tumor growth inhibition	[54]
Clustered Fe_3O_4 nanoparticles	A549 tumor-bearing mice	i.t.	50 μg	808 nm, 5 W cm^{-2}, 3 min	≈ 56 °C	Tumor growth reduced	[55]
RBC-derived membrane coated Fe_3O_4 nanoclusters	MCF-7 tumor-bearing mice	i.v.	2.5 mg kg^{-1}	808 nm, 5 W cm^{-2}, 5 min	≈ 53 °C	Tumor regression	[56]
PEGylated Fe-Fe_3O_4 nanoparticles	HeLa tumor-bearing mice	i.v.	1.46 g kg^{-1}	808 nm, 0.31 W cm^{-2}, 10 min, once a day during 14 days	ΔT ≈ 7 °C	Tumor growth reduced	[57]
Denatured BSA coated Mn^{2+} doped iron oxide nanoparticles	4T1 tumor-bearing mice	i.t.	40 mg kg^{-1}	808 nm, 1.5 W cm^{-2}, 5 min	≈ 70 °C	Tumor eradication	[58]

Fe(III)-gallic acid nanoparticles	4T1 tumor-bearing mice	i.v.	4 x 10^{-3} M (200 µL)	808 nm, 1 W cm^{-2}, 10 min	ΔT ≈ 20 °C	Tumor eradication	[59]
PEGylated FeS nanoplates	4T1 tumor-bearing mice	i.v.	20 mg kg^{-1}	808 nm, 1 W cm^{-2}, 5 min	≈ 60 °C	Tumor eradication	[60]
PEGylated $FeSe_2$ nanoparticles	4T1 tumor-bearing mice	i.t.	80 µg 4 mg kg^{-1}	808 nm, 0.8 W cm^{-2}, 5 min	≈ 63 °C	Tumor eradication	[61]
DSPE-PEG-$Z_{HER2:342}$ coated Fe_5C_2 nanoparticles	SK-OV-3 tumor-bearing mice	i.v.	18 mg kg^{-1}	808 nm, 2 W cm^{-2}, 3 min	≈ 47 °C	Tumor eradication	[62]
GSH functionalized Pd nanosheets	4T1 tumor-bearing mice	i.v.	400 µg	808 nm, 1 W cm^{-2}, 5 min	≈ 56 °C	Tumor eradication	[63]
PEG-SH functionalized Pd nanosheets	S180 tumor-bearing mice	i.v.	300 µg	808 nm, 0.4 W cm^{-2}, 5 min	≈ 52 °C	Tumor eradication	[64]
PEG coated gold-PANI nanoparticles	H22 tumor-bearing mice	i.t.	100 µg mL^{-1}	808 nm, 2 W cm^{-2}, 5 min	≈ 50 °C	Tumor eradication	[65]
Cetuximab functionalized carboxymethylated PVA-PANI nanoparticles	A-431 tumor-bearing mice	i.v.	300 µg	808 nm, 1.5 W cm^{-2}, 10 min	N.A.	Tumor eradication	[66]

HA-PANI nanoparticles	HeLa tumor-bearing mice	i.t.	200 μg	808 nm, 0.64 W cm^{-2}, 5 min	N.A.	Tumor eradication	[67]
PVP-PPy nanoparticles	4T1 tumor-bearing mice	i.v.	200 μg 10 mg kg^{-1}	808 nm, 1 W cm^{-2}, 5 min	≈ 65 °C	Tumor eradication	[68]
PVA-PPy nanoparticles	4T1 tumor-bearing mice	i.t.	40 μg 2 mg kg^{-1}	808 nm, 0.25 W cm^{-2}, 5 min	≈ 55 °C	Tumor eradication	[69]
PEGylated PPy nanoparticles	U87MG tumor-bearing mice	i.t. i.v.	i.t.: 200 μg i.v.: 500 μg	808 nm, 1.5 W cm^{-2}, 10 min	i.t.: ≈ 55 °C i.v.: ≈ 53 °C	Tumor growth reduced	[70]
PEGylated PEDOT:PSS nanoparticles	4T1 tumor-bearing mice	i.v.	200 μg 10 mg kg^{-1}	808 nm, 0.5 W cm^{-2}, 5 min	≈ 51 °C	Tumor eradication	[71]
DSPE-mPEG coated PFTTQ nanoparticles	HeLa tumor-bearing mice	i.t.	40 μg	808 nm, 0.75 W cm^{-2}, 10 min	≈ 45 °C	Tumor eradication	[72]
PEGylated gold-Pd nanoplates	4T1 tumor-bearing mice	i.v.	15 mg kg^{-1}	808 nm, 0.5 W cm^{-2}, 4 min	≈ 60 °C	Tumor eradication	[73]

PEG-GO/CuS nanocomposites	HeLa tumor-bearing mice	i.t.	50 µg	980 nm, 1 W cm^{-2}, 10 min	N.A.	Tumor growth reduced	[74]
Polydopamine coated Fe_3O_4 nanoparticles	A549 tumor-bearing mice	i.t.	50 µg	808 nm, 6.6 W cm^{-2}, 3 min	≈ 60 °C	Tumor regression	[75]
Fe_3O_4 coated PPy nanoparticles	SW-1990 tumor-bearing mice	i.t.	25 µg	808 nm, 0.25 W cm^{-2}, 5 min	≈ 49 °C	N.A.	[76]
PEGylated hollow gold-silver alloy urchin-shaped nanostructures	4T1 tumor-bearing mice	i.t.	3 µg	808 nm, 1 W cm^{-2}, 5 min	≈ 70 °C	Tumor eradication	[77]
Polydopamine coated PEI-gold nanostars	HeLa tumor-bearing mice	i.t.	5.6 mM (100 µL)	808 nm, 1.3 W cm^{-2}, 10 min	≈ 59 °C	Tumor eradication	[78]
PEGylated gold-silver nanostars	MCF-7 tumor-bearing mice	i.t.	4 µg	808 nm, 2 W cm^{-2}, 5 min	N.A.	Tumor regression	[79]

[a] laser parameters were different for this assay (790 nm, 1.5 W cm^{-2}, 3 min). [b] laser parameters were different for this assay (808 nm, 0.8 W cm^{-2}, 10 min).
Intratumoral injection (i.t.); intravenous injection (i.v.); not available (N.A.).
1,2-distearoyl-*sn*-glycero-3-phosphoethanolamine-N-(methoxy PEG) (DSPE-mPEG); PEGylated poly(maleic anhydride-*alt*-1-octadecene) (C_{18}-PMH-mPEG); pentaerythritol tetrakis (3-mercaptopropionate)-terminated poly(methacrylic acid) (PTMP-PMAA); poly(3,4-ethylenedioxythiophene):poly(styrenesulfonate) (PEDOT:PSS); poly(9,9-bis(4-(2-ethylhexyl)phenyl)fluorene-*alt*-*co*-6,7-bis(4-(hexyloxy)phenyl)-4,9-di(thiophen-2-yl)-thiadiazoloquinoxaline) (PFTTQ); poly(acrylic acid) (PAA); polyaniline (PANI); poly(caprolactone) (PCL); poly(ethyleneimine) (PEI); poly(ethylene glycol) (PEG); polypyrrole (PPy); poly(vinyl alcohol) (PVA); poly(vinylpyrrolidone) (PVP); red blood cell (RBC); reduced glutathione (GSH).

2.9.1. Supplementary References

[1] G. von Maltzahn, J.-H. Park, A. Agrawal, N. K. Bandaru, S. K. Das, M. J. Sailor, S. N. Bhatia, Computationally guided photothermal tumor therapy using long-circulating gold nanorod antennas, Cancer Research, 69 (2009) 3892-3900.

[2] H. Wang, R. Zhao, Y. Li, H. Liu, F. Li, Y. Zhao, G. Nie, Aspect ratios of gold nanoshell capsules mediated melanoma ablation by synergistic photothermal therapy and chemotherapy, Nanomedicine: Nanotechnology, Biology and Medicine, 12 (2016) 439-448.

[3] Y. Wang, K. C. Black, H. Luehmann, W. Li, Y. Zhang, X. Cai, D. Wan, S.-Y. Liu, M. Li, P. Kim, Comparison study of gold nanohexapods, nanorods, and nanocages for photothermal cancer treatment, ACS Nano, 7 (2013) 2068-2077.

[4] C. Ayala-Orozco, C. Urban, M. W. Knight, A. S. Urban, O. Neumann, S. W. Bishnoi, S. Mukherjee, A. M. Goodman, H. Charron, T. Mitchell, M. Shea, R. Roy, S. Nanda, R. Schiff, N. J. Halas, A. Joshi, Au Nanomatryoshkas as Efficient Near-Infrared Photothermal Transducers for Cancer Treatment: Benchmarking against Nanoshells, ACS Nano, 8 (2014) 6372-6381.

[5] P. Huang, P. Rong, J. Lin, W. Li, X. Yan, M. G. Zhang, L. Nie, G. Niu, J. Lu, W. Wang, X. Chen, Triphase Interface Synthesis of Plasmonic Gold Bellflowers as Near-Infrared Light Mediated Acoustic and Thermal Theranostics, Journal of the American Chemical Society, 136 (2014) 8307-8313.

[6] J. Feng, L. Chen, Y. Xia, J. Xing, Z. Li, Q. Qian, Y. Wang, A. Wu, L. Zeng, Y. Zhou, Bioconjugation of Gold Nanobipyramids for SERS Detection and Targeted Photothermal Therapy in Breast Cancer, ACS Biomaterials Science & Engineering, 3 (2017) 608–618.

[7] W. I. Choi, J.-Y. Kim, C. Kang, C. C. Byeon, Y. H. Kim, G. Tae, Tumor regression in vivo by photothermal therapy based on gold-nanorod-loaded, functional nanocarriers, ACS Nano, 5 (2011) 1995-2003.

[8] J.-G. Piao, L. Wang, F. Gao, Y.-Z. You, Y. Xiong, L. Yang, Erythrocyte membrane is an alternative coating to polyethylene glycol for prolonging the circulation lifetime of gold nanocages for photothermal therapy, ACS Nano, 8 (2014) 10414-10425.

[9] M. Xuan, J. Shao, L. Dai, J. Li, Q. He, Macrophage Cell Membrane Camouflaged Au Nanoshells for in Vivo Prolonged Circulation Life and Enhanced Cancer Photothermal Therapy, ACS Applied Materials & Interfaces, 8 (2016) 9610-9618.

[10] P. Huang, J. Lin, W. Li, P. Rong, Z. Wang, S. Wang, X. Wang, X. Sun, M. Aronova, G. Niu, Biodegradable gold nanovesicles with an ultrastrong plasmonic coupling effect for photoacoustic imaging and photothermal therapy, Angewandte Chemie International Edition, 125 (2013) 14208-14214.

[11] P. Wu, D. Deng, J. Gao, C. Cai, Tubelike Gold Sphere–Attapulgite Nanocomposites with a High Photothermal Conversion Ability in the Near-Infrared Region for Enhanced Cancer Photothermal Therapy, ACS Applied Materials & Interfaces, 8 (2016) 10243-10252.

[12] S. Liang, C. Li, C. Zhang, Y. Chen, L. Xu, C. Bao, X. Wang, CD44v6 monoclonal antibody-conjugated gold nanostars for targeted photoacoustic imaging and plasmonic photothermal therapy of gastric cancer stem-like cells, Theranostics, 5 (2015) 970-984.

[13] S. Wang, Z. Teng, P. Huang, D. Liu, Y. Liu, Y. Tian, J. Sun, Y. Li, H. Ju, X. Chen, Reversibly Extracellular pH Controlled Cellular Uptake and Photothermal Therapy by PEGylated Mixed-Charge Gold Nanostars, Small, 11 (2015) 1801-1810.

[14] X. Liu, H. Tao, K. Yang, S. Zhang, S.-T. Lee, Z. Liu, Optimization of surface chemistry on single-walled carbon nanotubes for in vivo photothermal ablation of tumors, Biomaterials, 32 (2011) 144-151.

[15] L. F. Neves, J. J. Krais, B. D. Van Rite, R. Ramesh, D. E. Resasco, R. G. Harrison, Targeting single-walled carbon nanotubes for the treatment of breast cancer using photothermal therapy, Nanotechnology, 24 (2013) 375104.

[16] B. Zhang, H. Wang, S. Shen, X. She, W. Shi, J. Chen, Q. Zhang, Y. Hu, Z. Pang, X. Jiang, Fibrin-targeting peptide CREKA-conjugated multi-walled carbon nanotubes for self-amplified photothermal therapy of tumor, Biomaterials, 79 (2016) 46-55.

[17] C. Liang, S. Diao, C. Wang, H. Gong, T. Liu, G. Hong, X. Shi, H. Dai, Z. Liu, Tumor Metastasis Inhibition by Imaging-Guided Photothermal Therapy with Single-Walled Carbon Nanotubes, Advanced Materials, 26 (2014) 5646-5652.

[18] A. L. Antaris, J. T. Robinson, O. K. Yaghi, G. Hong, S. Diao, R. Luong, H. Dai, Ultra-low doses of chirality sorted (6, 5) carbon nanotubes for simultaneous tumor imaging and photothermal therapy, ACS Nano, 7 (2013) 3644-3652.

[19] K. Yang, S. Zhang, G. Zhang, X. Sun, S.-T. Lee, Z. Liu, Graphene in mice: ultrahigh in vivo tumor uptake and efficient photothermal therapy, Nano Letters, 10 (2010) 3318-3323.

[20] K. Yang, J. Wan, S. Zhang, B. Tian, Y. Zhang, Z. Liu, The influence of surface chemistry and size of nanoscale graphene oxide on photothermal therapy of cancer using ultra-low laser power, Biomaterials, 33 (2012) 2206-2214.

[21] H. S. Jung, W. H. Kong, D. K. Sung, M.-Y. Lee, S. E. Beack, D. H. Keum, K. S. Kim, S. H. Yun, S. K. Hahn, Nanographene oxide–hyaluronic acid conjugate for photothermal ablation therapy of skin cancer, ACS Nano, 8 (2014) 260-268.

[22] J. H. Lee, A. Sahu, C. Jang, G. Tae, The effect of ligand density on in vivo tumor targeting of nanographene oxide, Journal of Controlled Release, 209 (2015) 219-228.

[23] C. Jang, J. H. Lee, A. Sahu, G. Tae, The synergistic effect of folate and RGD dual ligand of nanographene oxide on tumor targeting and photothermal therapy in vivo, Nanoscale, 7 (2015) 18584-18594.

[24] O. Akhavan, E. Ghaderi, Graphene nanomesh promises extremely efficient in vivo photothermal therapy, Small, 9 (2013) 3593-3601.

[25] J. Mou, P. Li, C. Liu, H. Xu, L. Song, J. Wang, K. Zhang, Y. Chen, J. Shi, H. Chen, Ultrasmall Cu2-xS Nanodots for Highly Efficient Photoacoustic Imaging-Guided Photothermal Therapy, Small, 11 (2015) 2275-2283.

[26] H. Chen, M. Song, J. Tang, G. Hu, S. Xu, Z. Guo, N. Li, J. Cui, X. Zhang, X. Chen, Ultrahigh 19F Loaded Cu1.75S Nanoprobes for Simultaneous 19F Magnetic Resonance Imaging and Photothermal Therapy, ACS Nano, 10 (2016) 1355–1362.

[27] B. Li, Q. Wang, R. Zou, X. Liu, K. Xu, W. Li, J. Hu, Cu7.2S4 nanocrystals: a novel photothermal agent with a 56.7% photothermal conversion efficiency for photothermal therapy of cancer cells, Nanoscale, 6 (2014) 3274-3282.

[28] M. Zhou, J. Li, S. Liang, A. K. Sood, D. Liang, C. Li, CuS Nanodots with Ultrahigh Efficient Renal Clearance for Positron Emission Tomography Imaging and Image-Guided Photothermal Therapy, ACS Nano, 9 (2015) 7085-7096.

[29] M. Zhou, S. Song, J. Zhao, M. Tian, C. Li, Theranostic CuS nanoparticles targeting folate receptors for PET image-guided photothermal therapy, Journal of Materials Chemistry B, 3 (2015) 8939-8948.

[30] Z. Wang, P. Huang, O. Jacobson, Z. Wang, Y. Liu, L. Lin, J. Lin, N. Lu, H. Zhang, R. Tian, Biomineralization-Inspired Synthesis of Copper Sulfide–Ferritin Nanocages as Cancer Theranostics, ACS Nano, 10 (2016) 3453-3460.

[31] K.-C. Li, H.-C. Chu, Y. Lin, H.-Y. Tuan, Y.-C. Hu, PEGylated Copper Nanowires as a Novel Photothermal Therapy Agent, ACS Applied Materials & Interfaces, 8 (2016) 12082–12090.

[32] S. Zhang, C. Sun, J. Zeng, Q. Sun, G. Wang, Y. Wang, Y. Wu, S. Dou, M. Gao, Z. Li, Ambient Aqueous Synthesis of Ultrasmall PEGylated Cu2−xSe Nanoparticles as a Multifunctional Theranostic Agent for Multimodal Imaging Guided Photothermal Therapy of Cancer, Advanced Materials, 28 (2016) 8927-8936.

[33] W. Yang, W. Guo, W. Le, G. Lv, F. Zhang, L. Shi, X. Wang, J. Wang, S. Wang, J. Chang, B. Zhang, Albumin-Bioinspired Gd:CuS Nanotheranostic Agent for In Vivo Photoacoustic/Magnetic Resonance Imaging-Guided Tumor-Targeted Photothermal Therapy, ACS Nano, 10 (2016) 10245-10257.

[34] S. Wang, K. Li, Y. Chen, H. Chen, M. Ma, J. Feng, Q. Zhao, J. Shi, Biocompatible PEGylated MoS 2 nanosheets: Controllable bottom-up synthesis and highly efficient photothermal regression of tumor, Biomaterials, 39 (2015) 206-217.

[35] T. Bao, W. Yin, X. Zheng, X. Zhang, J. Yu, X. Dong, Y. Yong, F. Gao, L. Yan, Z. Gu, One-pot synthesis of PEGylated plasmonic MoO 3–x hollow nanospheres for photoacoustic imaging guided chemo-photothermal combinational therapy of cancer, Biomaterials, 76 (2016) 11-24.

[36] W. Yin, L. Yan, J. Yu, G. Tian, L. Zhou, X. Zheng, X. Zhang, Y. Yong, J. Li, Z. Gu, High-throughput synthesis of single-layer MoS2 nanosheets as a near-infrared photothermal-triggered drug delivery for effective cancer therapy, ACS Nano, 8 (2014) 6922-6933.

[37] G. Song, J. Hao, C. Liang, T. Liu, M. Gao, L. Cheng, J. Hu, Z. Liu, Degradable Molybdenum Oxide Nanosheets with Rapid Clearance and Efficient Tumor Homing Capabilities as a Therapeutic Nanoplatform, Angewandte Chemie International Edition, 55 (2015) 2122-2126.

[38] L. Tan, S. Wang, K. Xu, T. Liu, P. Liang, M. Niu, C. Fu, H. Shao, J. Yu, T. Ma, Layered MoS2 Hollow Spheres for Highly-Efficient Photothermal Therapy of Rabbit Liver Orthotopic Transplantation Tumors, Small, 12 (2016) 2046-2055.

[39] Z. Huang, Y. Qi, D. Yu, J. Zhan, Radar-like MoS 2 nanoparticles as a highly efficient 808 nm laser-induced photothermal agent for cancer therapy, RSC Advances, 6 (2016) 31031-31036.

[40] T. Liu, Y. Chao, M. Gao, C. Liang, Q. Chen, G. Song, L. Cheng, Z. Liu, Ultra-small MoS2 nanodots with rapid body clearance for photothermal cancer therapy, Nano Research, 9 (2016) 3003–3017.

[41] C. Guo, H. Yu, B. Feng, W. Gao, M. Yan, Z. Zhang, Y. Li, S. Liu, Highly efficient ablation of metastatic breast cancer using ammonium-tungsten-bronze nanocube as a novel 1064 nm-laser-driven photothermal agent, Biomaterials, 52 (2015) 407-416.

[42] Z. Zhou, B. Kong, C. Yu, X. Shi, M. Wang, W. Liu, Y. Sun, Y. Zhang, H. Yang, S. Yang, Tungsten oxide nanorods: an efficient nanoplatform for tumor CT imaging and photothermal therapy, Scientific Reports, 4 (2014) 3653.

[43] W. Xu, Z. Meng, N. Yu, Z. Chen, B. Sun, X. Jiang, M. Zhu, PEGylated Cs x WO 3 nanorods as an efficient and stable 915 nm-laser-driven photothermal agent against cancer cells, RSC Advances, 5 (2015) 7074-7082.

[44] D. Huo, J. He, H. Li, A. J. Huang, H. Y. Zhao, Y. Ding, Z. Y. Zhou, Y. Hu, X-ray CT guided fault-free photothermal ablation of metastatic lymph nodes with ultrafine HER-2 targeting W18O49 nanoparticles, Biomaterials, 35 (2014) 9155-9166.

[45] S. M. Sharker, S. M. Kim, J. E. Lee, K. H. Choi, G. Shin, S. Lee, K. D. Lee, J. H. Jeong, H. Lee, S. Y. Park, Functionalized biocompatible WO 3 nanoparticles for triggered and targeted in vitro and in vivo photothermal therapy, Journal of Controlled Release, 217 (2015) 211-220.

[46] L. Cheng, J. Liu, X. Gu, H. Gong, X. Shi, T. Liu, C. Wang, X. Wang, G. Liu, H. Xing, PEGylated WS2 Nanosheets as a Multifunctional Theranostic Agent for in vivo Dual-Modal CT/Photoacoustic Imaging Guided Photothermal Therapy, Advanced Materials, 26 (2014) 1886-1893.

[47] Y. Chao, G. Wang, C. Liang, X. Yi, X. Zhong, J. Liu, M. Gao, K. Yang, L. Cheng, Z. Liu, Rhenium-188 Labeled Tungsten Disulfide Nanoflakes for Self-Sensitized, Near-Infrared Enhanced Radioisotope Therapy, Small, 12 (2016) 3967-3975.

[48] G. Tian, X. Zhang, X. Zheng, W. Yin, L. Ruan, X. Liu, L. Zhou, L. Yan, S. Li, Z. Gu, Multifunctional RbxWO3 Nanorods for Simultaneous Combined Chemo-photothermal Therapy and Photoacoustic/CT Imaging, Small, 10 (2014) 4160-4170.

[49] L. Wen, L. Chen, S. Zheng, J. Zeng, G. Duan, Y. Wang, G. Wang, Z. Chai, Z. Li, M. Gao, Ultrasmall Biocompatible WO3−x Nanodots for Multi-Modality Imaging and Combined Therapy of Cancers, Advanced Materials, 28 (2016) 5072-5079.

[50] Y. Yong, X. Cheng, T. Bao, M. Zu, L. Yan, W. Yin, C. Ge, D. Wang, Z. Gu, Y. Zhao, Tungsten Sulfide Quantum Dots as Multifunctional Nanotheranostics for In Vivo Dual-Modal Image-Guided Photothermal/Radiotherapy Synergistic Therapy, ACS Nano, 9 (2015) 12451-12463.

[51] W. Zhu, K. Liu, X. Sun, X. Wang, Y. Li, L. Cheng, Z. Liu, Mn2+-Doped Prussian Blue Nanocubes for Bimodal Imaging and Photothermal Therapy with Enhanced Performance, ACS Applied Materials & Interfaces, 7 (2015) 11575-11582.

[52] X. Cai, W. Gao, L. Zhang, M. Ma, T. Liu, W. Du, Y. Zheng, H. Chen, J. Shi, Enabling Prussian Blue with Tunable Localized Surface Plasmon Resonances: Simultaneously Enhanced Dual-Mode Imaging and Tumor Photothermal Therapy, ACS Nano, 10 (2016) 11115-11126.

[53] L. Cheng, H. Gong, W. Zhu, J. Liu, X. Wang, G. Liu, Z. Liu, PEGylated Prussian blue nanocubes as a theranostic agent for simultaneous cancer imaging and photothermal therapy, Biomaterials, 35 (2014) 9844-9852.

[54] L. Jing, S. Shao, Y. Wang, Y. Yang, X. Yue, Z. Dai, Hyaluronic Acid Modified Hollow Prussian Blue Nanoparticles Loading 10-hydroxycamptothecin for Targeting Thermochemotherapy of Cancer, Theranostics, 6 (2016) 40-53.

[55] S. Shen, S. Wang, R. Zheng, X. Zhu, X. Jiang, D. Fu, W. Yang, Magnetic nanoparticle clusters for photothermal therapy with near-infrared irradiation, Biomaterials, 39 (2015) 67-74.

[56] X. Ren, R. Zheng, X. Fang, X. Wang, X. Zhang, W. Yang, X. Sha, Red blood cell membrane camouflaged magnetic nanoclusters for imaging-guided photothermal therapy, Biomaterials, 92 (2016) 13-24.

[57] Z. Zhou, Y. Sun, J. Shen, J. Wei, C. Yu, B. Kong, W. Liu, H. Yang, S. Yang, W. Wang, Iron/iron oxide core/shell nanoparticles for magnetic targeting MRI and near-infrared photothermal therapy, Biomaterials, 35 (2014) 7470-7478.

[58] M. Zhang, Y. Cao, L. Wang, Y. Ma, X. Tu, Z. Zhang, Manganese Doped Iron Oxide Theranostic Nanoparticles for Combined T 1 Magnetic Resonance Imaging and Photothermal Therapy, ACS Applied Materials & Interfaces, 7 (2015) 4650-4658.

[59] J. Zeng, M. Cheng, Y. Wang, L. Wen, L. Chen, Z. Li, Y. Wu, M. Gao, Z. Chai, pH-Responsive Fe(III)–Gallic Acid Nanoparticles for In Vivo Photoacoustic-Imaging-Guided Photothermal Therapy, Advanced Healthcare Materials, 5 (2016) 772-780.

[60] K. Yang, G. Yang, L. Chen, L. Cheng, L. Wang, C. Ge, Z. Liu, FeS nanoplates as a multifunctional nano-theranostic for magnetic resonance imaging guided photothermal therapy, Biomaterials, 38 (2015) 1-9.

[61] T. Fu, Y. Chen, J. Hao, X. Wang, G. Liu, Y. Li, Z. Liu, L. Cheng, Facile preparation of uniform FeSe 2 nanoparticles for PA/MR dual-modal imaging and photothermal cancer therapy, Nanoscale, 7 (2015) 20757-20768.

[62] J. Yu, C. Yang, J. Li, Y. Ding, L. Zhang, M. Z. Yousaf, J. Lin, R. Pang, L. Wei, L. Xu, Multifunctional Fe5C2 Nanoparticles: A Targeted Theranostic Platform for Magnetic Resonance Imaging and Photoacoustic Tomography-Guided Photothermal Therapy, Advanced Materials, 26 (2014) 4114-4120.

[63] S. Tang, M. Chen, N. Zheng, Sub-10-nm Pd Nanosheets with Renal Clearance for Efficient Near-Infrared Photothermal Cancer Therapy, Small, 10 (2014) 3139-3144.

[64] S. Shi, Y. Huang, X. Chen, J. Weng, N. Zheng, Optimization of surface coating on small Pd nanosheets for in vivo near-infrared photothermal therapy of tumor, ACS Applied Materials & Interfaces, 7 (2015) 14369-14375.

[65] E. Ju, K. Dong, Z. Liu, F. Pu, J. Ren, X. Qu, Tumor Microenvironment Activated Photothermal Strategy for Precisely Controlled Ablation of Solid Tumors upon NIR Irradiation, Advanced Functional Materials, 25 (2015) 1574-1580.

[66] T. Lee, D. Bang, Y. Park, S. H. Kim, J. Choi, J. Park, D. Kim, E. Kim, J. S. Suh, Y. M. Huh, Gadolinium-Enriched Polyaniline Particles (GPAPs) for Simultaneous Diagnostic Imaging and Localized Photothermal Therapy of Epithelial Cancer, Advanced Healthcare Materials, 3 (2014) 1408-1414.

[67] B.-P. Jiang, L. Zhang, Y. Zhu, X.-C. Shen, S.-C. Ji, X.-Y. Tan, L. Cheng, H. Liang, Water-soluble hyaluronic acid–hybridized polyaniline nanoparticles for effectively targeted photothermal therapy, Journal of Materials Chemistry B, 3 (2015) 3767-3776.

[68] M. Chen, X. Fang, S. Tang, N. Zheng, Polypyrrole nanoparticles for high-performance in vivo near-infrared photothermal cancer therapy, Chemical Communications, 48 (2012) 8934-8936.

[69] K. Yang, H. Xu, L. Cheng, C. Sun, J. Wang, Z. Liu, In Vitro and In Vivo Near-Infrared Photothermal Therapy of Cancer Using Polypyrrole Organic Nanoparticles, Advanced Materials, 24 (2012) 5586-5592.

[70] X. Liang, Y. Li, X. Li, L. Jing, Z. Deng, X. Yue, C. Li, Z. Dai, PEGylated Polypyrrole Nanoparticles Conjugating Gadolinium Chelates for Dual-Modal MRI/Photoacoustic Imaging Guided Photothermal Therapy of Cancer, Advanced Functional Materials, 25 (2015) 1451-1462.

[71] L. Cheng, K. Yang, Q. Chen, Z. Liu, Organic stealth nanoparticles for highly effective in vivo near-infrared photothermal therapy of cancer, ACS Nano, 6 (2012) 5605-5613.

[72] J. Geng, C. Sun, J. Liu, L. D. Liao, Y. Yuan, N. Thakor, J. Wang, B. Liu, Biocompatible Conjugated Polymer Nanoparticles for Efficient Photothermal Tumor Therapy, Small, 11 (2015) 1603-1610.

[73] M. Chen, S. Tang, Z. Guo, X. Wang, S. Mo, X. Huang, G. Liu, N. Zheng, Core–Shell Pd@Au Nanoplates as Theranostic Agents for In-Vivo Photoacoustic Imaging, CT Imaging, and Photothermal Therapy, Advanced Materials, 26 (2014) 8210-8216.

[74] J. Bai, Y. Liu, X. Jiang, Multifunctional PEG-GO/CuS nanocomposites for near-infrared chemo-photothermal therapy, Biomaterials, 35 (2014) 5805-5813.

[75] R. Zheng, S. Wang, Y. Tian, X. Jiang, D. Fu, S. Shen, W. Yang, Polydopamine-Coated Magnetic Composite Particles with an Enhanced Photothermal Effect, ACS Applied Materials & Interfaces, 7 (2015) 15876-15884.

[76] Q. Tian, Q. Wang, K. X. Yao, B. Teng, J. Zhang, S. Yang, Y. Han, Multifunctional Polypyrrole@Fe3O4 Nanoparticles for Dual-Modal Imaging and In Vivo Photothermal Cancer Therapy, Small, 10 (2014) 1063-1068.

[77] Z. Liu, L. Cheng, L. Zhang, Z. Yang, Z. Liu, J. Fang, Sub-100 nm hollow Au–Ag alloy urchin-shaped nanostructure with ultrahigh density of nanotips for photothermal cancer therapy, Biomaterials, 35 (2014) 4099-4107.

[78] D. Li, Y. Zhang, S. Wen, Y. Song, Y. Tang, X. Zhu, M. Shen, S. Mignani, J.-P. Majoral, Q. Zhao, X. Shi, Construction of polydopamine-coated gold nanostars for CT imaging and enhanced photothermal therapy of tumors: an innovative theranostic strategy, Journal of Materials Chemistry B, 4 (2016) 4216-4226.

[79] L. Zeng, Y. Pan, S. Wang, X. Wang, X. Zhao, W. Ren, G. Lu, A. Wu, Raman Reporter-Coupled Agcore@Aushell Nanostars for in Vivo Improved Surface Enhanced Raman Scattering Imaging and Near-infrared-Triggered Photothermal Therapy in Breast Cancers, ACS Applied Materials & Interfaces, 7 (2015) 16781-16791.

Chapter 3

Introduction (part. B)

Functionalization of Graphene Family Nanomaterials for Application in Cancer Therapy

This chapter is based on a manuscript submitted for publication entitled: Functionalization of Graphene Family Nanomaterials for Application in Cancer Therapy.

3.1. Abstract

Graphene family nanomaterials' (GFN) ability to interact with near-infrared light has propelled their application in cancer PTT. Furthermore, the graphitic lattice of GFN can adsorb different types of molecules, which has motivated their use in cancer drug delivery. However, the direct application of GFN in cancer therapy is severely hindered by their poor colloidal stability, sub-optimal safety, inefficient tumor uptake and non-selectivity towards cancer cells. To overcome these limitations, GFN have been functionalized with different types of materials. This chapter is focused on the different functionalizations used in the design of GFN aimed for cancer therapy, disclosing their role on surpassing the critical issues related to GFN-based therapies.

Keywords: cancer therapy; graphene oxide; nanostructures; photothermal therapy; tumors

3.2. Introduction

GFN have been receiving a growing attention in various fields, including cancer therapy [1-6]. In this context, GFN have been mostly explored as photothermal agents due to their NIR absorption and as delivery vehicles due to their ability to adsorb drugs (and other molecules) on their surface [7, 8].

Despite the enormous potential of GFN, the poor water solubility and weak stability of these materials limit their use in cancer therapy [9, 10]. Moreover, as-synthesized GFN are not suited to become passively accumulated in the tumor site nor tailored to be selectively internalized by cancer cells [11-14]. Furthermore, depending on the surface chemistry, size or impurities content, some GFN have shown to be cytotoxic [15-18]. To overcome these limitations, researchers have been modifying the surface of GFN with a variety of materials.

In the following sub-sections, the different functionalizations performed to allow an efficient application of GFN in cancer therapy and enhance their therapeutic performance and safety are discussed. Firstly, the physicochemical properties of GFN as well as the most convenient routes for functionalizing these materials are analyzed (section 3.3). Afterward, the functionalization of GFN for application in cancer therapy and its implications are discussed (section 3.4). The functionalizations performed to improve GFN hydrophilicity and colloidal stability are discussed in section 3.4.1., and those that aim to improve their biocompatibility and hemocompatibility are analyzed in section 3.4.2. The approaches employed to enhance the blood circulation time and tumor uptake of GFN are reviewed in section 3.4.3. The functionalizations that improve GFN cellular uptake and selectivity towards cancer cells are discussed in section 3.4.4. Finally, an overview about the future directions are presented in section 3.5. For the sake of brevity, this chapter does not cover modifications that aim to improve GFN tumor accumulation by means of external forces (*e.g.* by using magnetic fields), nor those that enhance GFN therapeutic performance through the incorporation of other nanostructures (*e.g.* gold nanostructures).

3.3. GFN: physicochemical properties and functionalization routes

GO is probably the most applied GFN for cancer therapy and it is also used as the precursor for the synthesis of other graphene-based nanomaterials. GO is composed by a monolayer of graphite containing several types of oxygen functional groups such as carboxyl, hydroxyl or epoxy groups (Figure 3.1). This material is generally produced through the chemical oxidation of graphite and exfoliation of the resulting material (graphite oxide), into a single layer

material (GO). Over the years, several methods have been developed to synthesize GO, being the Hummer's and the improved Hummer's (also known as Tour method) methods the most commonly employed [19, 20].

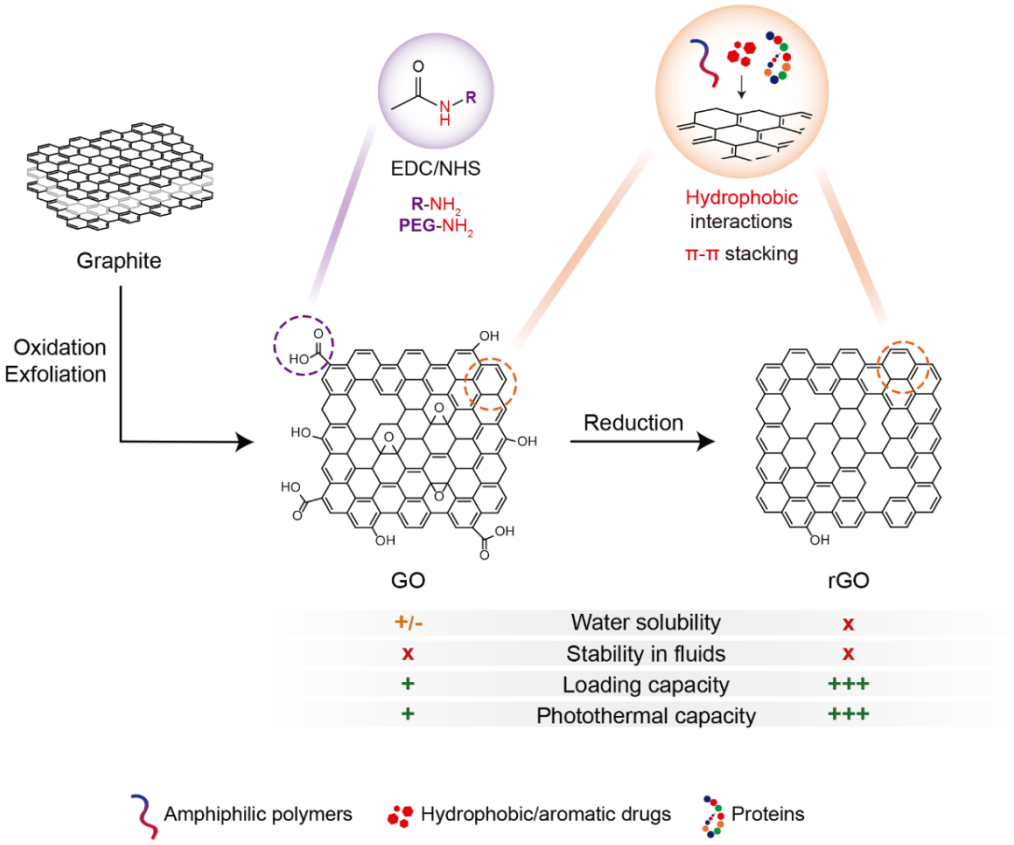

Figure 3.1. Schematic representation of the synthesis of GO and rGO. The reduction of GO provokes alterations on physicochemical properties of the materials, which impact on their application in cancer therapy. The most commonly used routes for functionalizing GO and rGO are also represented. *N*-Hydroxysuccinimide (NHS).

GO aromatic lattice can adsorb several types of molecules through hydrophobic interactions or π-π stacking. A variety of cancer-relevant molecules such as chemotherapeutic drugs or proteins can be loaded on GO by exploring these non-covalent interactions [7]. Although therapeutic agents may also be conjugated to the carboxyl-groups of GO, such approach is not usually pursued since these groups may be required for the functionalization of GO. Furthermore, the NIR absorption of GO also allows its application as a photothermal agent or as a light-responsive delivery vehicle in cancer therapy [21, 22].

However, the direct applicability of GO in cancer therapy is limited by its poor colloidal stability since it promptly precipitates in biological fluids [9]. Moreover, GO has a sub-optimal biocompatibility and hemocompatibility, as well as inefficient tumor uptake and non-selectivity towards cancer cells (discussed in detail in section 3.4). These limitations can be surpassed by functionalizing GO with different types of materials (discussed in section 3.4). Based on its structure, GO is generally functionalized through the formation of amide bonds established between the carboxyl groups of GO and primary amines of other materials using 1-ethyl-3-(-3-dimethylaminopropyl) carbodiimide (EDC; a water soluble carbodiimide crosslinker) chemistry [23]. These oxygen functional groups may also be conjugated with polymerization initiators, allowing the direct growth of polymers on GO surface [24, 25]. Alternatively, the aromatic lattice of GO allows its functionalization with amphiphilic materials by exploring hydrophobic interactions or π-π stacking [26].

GO derivatives such as base treated GO and carboxylated GO (GO-COOH) have also been explored in cancer therapy due to their improved properties [27-29]. Base treated GO is obtained by washing GO with sodium hydroxide, a process that removes the oxidation debris from GO lattice, improving its loading capacity [30, 31]. GO-COOH is produced by reacting GO with chloroacetic acid or sodium chloroacetate [32-34]. This modification introduces additional carboxyl groups for chemical conjugation and improves GO NIR absorption [32-34]. However, these GO derivatives suffer from the same stability, biocompatibility, tumor uptake and selectivity problems that affect GO, which impose their functionalization.

rGO is another GFN applied in cancer therapy. rGO is generally obtained by treating GO with reducing agents such as hydrazine hydrate (for the sake of clarity, *rGO* will refer to rGO attained using hydrazine hydrate) [10, 35]. Other reducing agents such as ascorbic acid or dopamine have also been successfully applied in the reduction of GO [12, 36-38]. The reduction of GO aims to restore its graphitic lattice by removing the oxygen functional groups, and such procedure drastically changes the properties of the materials (Figure 3.1). In fact, when compared to GO and its derivatives, rGO displays a higher NIR absorption and loading capacity, conferring an improved photothermal and drug delivery potential to this material [10, 39]. However, rGO has a weak water solubility (and stability) and its application in cancer therapy is also hindered by the same factors that affect GO, thus demanding its functionalization (discussed in detail in section 3.4). As rGO has limited (or close to none) oxygen functional groups available for conjugation, this material is generally functionalized with amphiphilic polymers through non-covalent interactions (hydrophobic interactions or π-π stacking) [23, 40-42]. Exceptionally, GO reduced by dopamine can be covalently functionalized with materials containing amine or thiol groups through catechol chemistry (reaction of the oxidized catechol groups with amine/thiol groups through Michael addition or Schiff base reactions) [37, 43].

Graphene oxide nanoribbons (GONR) and reduced graphene oxide nanoribbons (rGONR) are other GFN explored in cancer therapy. GONR are obtained by unzipping multiwall carbon

nanotubes (MWCNT) through means of oxidation and can be functionalized by the same procedures described for GO [44]. GONR can also be reduced to rGONR, a modification that also improves their NIR absorption and photothermal capacity but reduces their solubility [45]. Similar to rGO, rGONR are also usually functionalized with amphiphilic materials [45].

Overall, these functionalization routes are widely applied when preparing GFN aimed for cancer therapy due to their simplicity, ability to be performed in aqueous solutions and compatibility with the compounds to be bonded to GFN. Other functionalization approaches that are not within the scope of this chapter are thoroughly described elsewhere [46-48].

3.4. Functionalization of GFN for application in cancer therapy

The functionalization of GFN enables a safer administration of these nanomaterials and ensures that these are able to overcome the different biological barriers required for an efficient and selective accumulation in the tumor cells (Figure 3.2). The different functionalizations performed to improve GFN properties and their implications are reviewed in the next sub-sections.

3.4.1. Functionalizations used to improve the hydrophilicity and colloidal stability of GFN

GFN should be soluble in aqueous solutions and must remain stable (*i.e.* preserve their physicochemical properties) in the medium used for their administration (usually phosphate buffered saline (PBS) or NaCl solutions) and in biological fluids (usually simulated using fetal bovine serum (FBS) supplemented cell culture medium) - Figure 3.2. Although GO has adequate solubility in water (due to its oxygen-functional groups), it precipitates in saline solutions and in physiological media [9]. To overcome this limitation, GO is usually covalently functionalized with hydrophilic polymers containing amine groups through the formation of amide bonds. In this regard, branched amine terminated PEG or amine terminated Dextran have been widely explored by researchers since these polymers are capable of entailing onto GO materials a lasting stability across several fluids [9, 10, 23]. Alternatively, amphiphilic PEGylated polymers such as Pluronic® F-127, Poloxamer 188 (Pluronic® F-68) or D-α-Tocopheryl polyethylene glycol 1000 succinate (TPGS) can also be used for improving the colloidal stability of GO derivatives [26, 28, 49]. Other materials capable of improving the stability of GO-based nanomaterials are described in Table 3.1 (presented after the conclusion section).

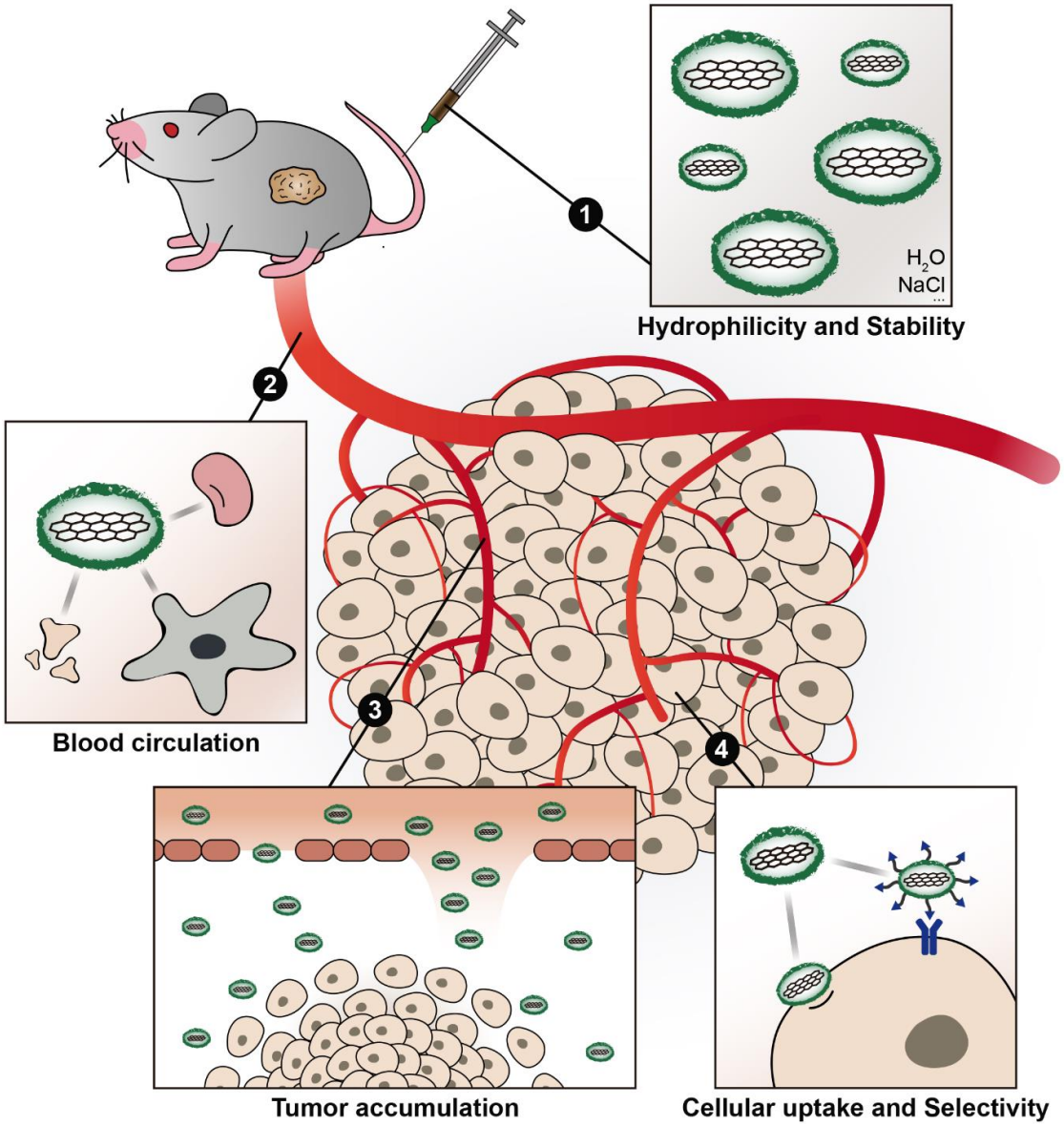

Figure 3.2. Schematic representation of the different barriers that functionalized GFN must overcome in order to become accumulated in the tumor and internalized by cancer cells.

The reduced forms of GO-based materials have a poor solubility in aqueous solutions [10]. Similar to GO, rGO derivatives also precipitate in saline and physiological media [10]. To address these limitations, rGO has been non-covalently functionalized with PEG-based amphiphilic polymers such as C_{18}-PMH-PEG and with amphiphilic polymers based on Dextran and HA [23, 40-42]. rGO coated with bovine serum albumin (BSA) also displays an improved solubility and colloidal stability [23, 50]. Alternatively, some synthetic routes allow the simultaneous reduction and functionalization of GO derivatives with hydrophilic polymers, which is a convenient approach to produce functionalized rGO-based materials with aqueous solubility and improved colloidal stability [28, 51-53]. Other types of coatings used for improving the solubility and colloidal stability of rGO-based nanostructures are also described in Table 3.1.

3.4.2. Functionalizations used to improve the biocompatibility and hemocompatibility of GFN

The biocompatibility of GFN is a topic under intense investigation, since it is affected by the intrinsic properties of the materials (*e.g.* surface chemistry, size, stability, purity/impurities) and by factors related to the assays conditions (*e.g.* culture conditions/presence of serum, cell line, type of assay used to evaluate the cytotoxicity) - extensively reviewed elsewhere [15-18, 54]. In general, GO-based nanomaterials tend to display a better cytocompatibility than their reduced equivalents [37, 52]. Part of the cytotoxicity induced by rGO derivatives can be explained by the poor solubility of rGO and by the high toxicity of hydrazine hydrate, which is used in the majority of the reduction processes [37, 52]. For instance, GO reduced by hydrazine hydrate and GO reduced by hydrothermal treatment with glucose have very distinct effects on cells, being the latter less cytotoxic [52].

To diminish the safety issues associated with the use of GFN, these materials have been functionalized with different types of hydrophilic and biocompatible materials (please see Table 3.2 for further details; presented after the conclusion section). For instance, the coating of GO and rGO with BSA or PEG (branched amine terminated PEG for GO; C_{18}-PMH-PEG for rGO) greatly improves the cytocompatibility of these materials towards macrophage, fibroblast and liver cell lines [23]. In *in vivo* studies, the administration of GO conjugated with branched amine terminated PEG by intravenous (i.v.; 20 mg kg^{-1}) and intraperitoneal (i.p.; 50 mg kg^{-1}) injections did not induce toxicity, even after 90 days of p.i. [55, 56]. An excellent *in vivo* biocompatibility was also reported for rGO coated with C_{18}-PMH-PEG [40, 56]. BSA coated rGO and GO conjugated with amine modified Dextran did also not elicit any noticeable alterations on mice organs [50, 57].

Despite the excellent *in vivo* biocompatibility displayed by some functionalized GFN, their long-term toxicity is a major concern since these materials are regarded as non-biodegradable. Zhuang Liu group unveiled that GO conjugated with PEG-SS-NH_2 can suffer oxidative-biodegradation catalyzed by peroxidases after the removal of the detachable PEG coating under reductive conditions (like those found intracellularly), leading to their fast clearance from mice body [23]. In contrast, authors found that GO and rGO functionalized with non-detachable PEG- and BSA-based coatings did not suffer oxidative-biodegradation presumably due to the inability of the enzymes to reach GFN surface [23].

On the other hand, in recent studies it was demonstrated that PEGylated GFN can induce immunologic reactions [58, 59]. Im *et al.* reported that rGO coated with a C_{18}-PMH-PEG based polymer suffers fast blood clearance at the time of its re-injection [58]. This phenomenon is known as accelerated blood clearance, and it has been associated to several PEGylated materials [60]. In this case, authors verified that the production of anti-PEG IgM by mice at the time of the first injection of the PEG coated rGO mediated the clearance of the materials in

the subsequent injections [58]. In another study, GO conjugated with amine terminated methoxy-PEG (mPEG) induced cytokine secretion by macrophages despite not being internalized by these cells [59]. Recently, it was unveiled that poly(acrylic acid) (PAA) functionalized GO displays a superior biocompatibility under *in vivo* conditions in comparison to PEGylated GO, which should motivate the continuous pursuit for the optimal surface coatings for GFN [11].

Although the hemolytic potential of GFN depends on multiple factors (*e.g.* materials size, oxygen content, surface charge), both GO and rGO based materials can induce the lysis of RBC [16]. In this regard, GO is generally a stronger inducer of RBC hemolysis than rGO [61]. For instance, a concentration as low as 12.5 μg mL^{-1} of GO can induce a hemolysis of ≈ 12 %, while 100 μg mL^{-1} of rGO induces ≈ 13 % of hemolysis [61]. On the other hand, rGO may also induce blood clumping due to its poor solubility [16]. In this way, the functionalization of GFN surface is also crucial to address their blood compatibility problems. In this regard, the modification of GO surface with heparin or bovine α-lactalbumin can suppress *in vitro* the hemolysis of RBC (see Table 3.2 for further details) [62, 63]. Regarding rGO based materials, their functionalization with PVA, BSA or heparin also reduces the *in vitro* hemolytic potential of these materials [37, 62, 64]. The good *in vivo* biocompatibility displayed by GFN coated with PAA [11], PEG [55, 56], and Dextran [65] based materials further confirms that these materials can mitigate the blood compatibility problems associated with GFN, as attested by hematological analysis (Table 3.2).

3.4.3. Functionalizations used to improve the blood circulation time and tumor accumulation of GFN

GFN are not suited to overcome the biological barriers required to achieve a suitable tumor accumulation. Upon introduction in the blood stream, GFN adsorb proteins (including opsonins) [11] and suffer internalization by macrophages [12], leading to their clearance. In this regard, the functionalization of GFN with non-fouling and *stealth* materials such as Dextran [66], PEG [11, 59], PVP [12], or PAA [11] can greatly reduce these interactions, and thus may improve materials' blood circulation time.

During circulation, nanomaterials may extravasate through the 200-1200 nm fenestrae present on the tumor vasculature and may become retained at the tumor site due to the ineffective lymphatic drainage present on this zone [8, 67, 68]. This process is known as tumor accumulation through the EPR effect and it is often regarded as a process that is strongly influenced by nanomaterials' size [8, 68]. Besides the extravasation through the static pores present on the tumor vasculature, recently it was unveiled that nanomaterials may reach the tumor zone by taking advantage from the dynamic and short-lived bursts (also termed

eruptions) that occur in tumor-associated vessels, which drive the blood flow into the tumor interstitial space [69] – Figure 3.2. Thus, the functionalization of GFN surface to achieve higher blood circulation times can lead to an improved tumor accumulation since it will increase the likelihood of the materials to benefit from the EPR effect and from the dynamic vents that may occur on tumor vasculature. In this regard, the functionalization of GFN with PEG based coatings can greatly improve their blood circulation time and thus their tumor accumulation (Table 3.3; presented after the conclusion section). Yang *et al*. observed that GO covalently functionalized with branched amine terminated PEG displays a $t_{1/2}$ of ≈ 1.5 h, being able to achieve a high tumor uptake [21]. Due to its good tumor-homing capacity, the PTT mediated by PEGylated GO led to the eradication of mice's tumor (20 mg kg^{-1}, 808 nm, 2 W cm^{-2}, 5 min) [21].

In a subsequent work, authors investigated the biodistribution in tumor bearing mice of PEGylated GO (covalently functionalized with branched amine terminated PEG) and C_{18}-PMH-PEG coated rGO [10]. In this case, PEGylated GO demonstrated a second phase blood circulation half-life ($t'_{1/2}$) of about 5.8 h ($t_{1/2}$ ≈ 0.29 h), resulting in a tumor accumulation lower than 1 % ID g^{-1} [10]. In contrast, C_{18}-PMH-PEG coated rGO displayed a up to ≈ 2.9-fold longer blood circulation time ($t'_{1/2}$ ≈ 16.7 h; $t_{1/2}$ ≈ 0.51 h), leading to a tumor accumulation of ≈ 6 % ID g^{-1}, a profile that may be attributed to a denser surface functionalization conferred by the C_{18}-PMH-PEG coating [10]. Due to its higher tumor accumulation and superior photothermal capacity, C_{18}-PMH-PEG coated rGO was able to induce tumor eradication at a power density of only 0.15 W cm^{-2} (808 nm, 5 min, 20 mg kg^{-1}), while PEGylated GO only mediated a slight reduction of the tumor growth (808 nm, 0.15 W cm^{-2}, 5 min, 20 mg kg^{-1}) [10]. Later, Xu *et al*. conjugated an additional PEG segment to C_{18}-PMH-PEG coated rGO (double PEGylation), which increased the blood circulation time of this nanomaterial from $t_{1/2}$ = 0.19 h ($t'_{1/2}$ = 18.8 h) to $t_{1/2}$ = 0.35 h ($t'_{1/2}$ = 27.7 h) [70]. This improvement on nanomaterials' blood circulation time led to a ≈ 1.8-fold increase on their tumor-homing capacity (C_{18}-PMH-PEG coated rGO: 8.8 % ID g^{-1}; C_{18}-PMH-PEG-PEG coated rGO: 15.5 % ID g^{-1}) [70]. These results are in line with other literature reports that highlight that the optimization of the PEG density and PEG molecular weight present on nanomaterials' surface is crucial to achieve an enhanced tumor accumulation [71, 72].

The ability of functionalized GFN to become accumulated in the tumor zone can also be explored to improve the accumulation of therapeutics (*e.g.* drugs) in the tumor mass, through their loading on the aromatic matrix of GFN or covalent conjugation to the nanomaterials [22, 27]. For instance, the delivery of a platinum-based drug by branched PEG-Platin-GO conjugates results in a ≈ 2.4-fold higher platinum tumor uptake than that achieved through the administration of cisplatin (≈ 9.6 *vs.* 4 μg g^{-1}) [22]. In another work, the accumulation of Photochlor® in 4T1 tumors was also enhanced when delivered by linear PEG-GO (≈ 1.3 *vs.* 3.1 % ID g^{-1}) [27]. Furthermore, drug-loaded functionalized GFN can display a lower

accumulation in off-target organs (*e.g.* liver or spleen) than free drugs, and thus reduce drugs' side-effects [22, 27] (Table 3.3).

3.4.4. Functionalizations used to improve the cellular uptake and selectivity of GFN

After reaching the tumor site, GFN must be internalized by cancer cells (Figure 3.2). In this regard, the functionalization of GFN can improve their cellular internalization, leading to an improved therapeutic effect. For instance, the delivery of therapeutics to cancer cells by PEG or Dextran functionalized GFN can be more efficient than that mediated by non-functionalized GFN or attained through the diffusion of free drugs (please see Table 3.4 for more details; presented after the conclusion section) [22, 27, 41, 73].

Furthermore, GFN can also be decorated with ligands that are recognized by the overexpressed receptors available on cancer cells' membranes, thus enhancing their tumor uptake and selectivity towards cancer cells, while reducing their off-target accumulation. In this regard, GFN have been mostly decorated with FA (folate receptor targeted) [13], RGD peptide (integrin $\alpha_v\beta_3$ targeted) [74], transferrin (transferrin receptor targeted) [75] and HA (CD44 receptor targeted) [29]. For this purpose, targeted GO based materials can be prepared by covalent interactions (Table 3.4). Jung *et al.* covalently functionalized GO-COOH with hexamethylenediamine-HA (HMDA-HA; amine terminated HA), and they noticed that the photothermal effect mediated by HA-GO leads to the eradication of mice's melanoma tumors due to the ability of these nanostructures to reach the tumor mass upon topical administration [29]. The attachment of thiol terminated antibodies to GO covalently functionalized with branched amine and maleimide (thiol reactive) terminated PEG can also be explored to prepare targeted PEGylated GO materials with a higher tumor-homing capacity than their non-targeted equivalents [76, 77].

To prepare targeted rGO-based nanostructures, this material is generally functionalized with amphiphilic polymers containing the targeting ligands (please note that this approach may also be applied to produce targeted GO derivatives) (Table 3.4). In this regard, Akhavan and Ghaderi compared the biodistribution of rGO nanomesh coated with 1,2-distearoyl-*sn*-glycero-3-phosphoethanolamine-*N*-PEG (DSPE-PEG) and DSPE-PEG-RGD amphiphilic polymers, verifying that the RGD functionalization improved the nanomaterials' tumor uptake from about 8.9 to 31 % ID g^{-1} [74]. The RGD functionalization also reduced the nanomaterials' liver and spleen accumulations from about 17 and 12 to 5 and 3 % ID g^{-1}, respectively [74]. Due to its remarkably high tumor uptake, the photothermal effect mediated by DSPE-PEG-RGD coated rGO nanomesh induced the eradication of mice's tumors using a low injected dose and at a very low power

density (2 μg, 808 nm, 0.1 W cm^{-2}, 7 min) [74]. Other routes to prepare targeted rGO-based materials are summarized in Table 3.4.

Furthermore, the decoration of GFN with more than one targeting ligand is also a promising approach to improve their tumor-homing capacity and therapeutic capacity [78, 79]. Jang and co-workers observed that GO dual-functionalized with cyclic RGD (cRGD) and FA (using Pluronic® F-127-cRGD and Pluronic® F-127-FA conjugates) has a tumor accumulation superior to that of their equivalents only decorated with one targeting ligand (cRGD or FA) [78]. *In vivo*, the photothermal effect mediated by the dual-ligand functionalized GO induced tumor eradication, while that mediated by single-ligand functionalized GO only promoted a reduction of the tumor growth (7.5 mg kg^{-1}, 808 nm, 2 W cm^{-2}, 10 min) [78].

Still, the therapeutic capacity of targeted GFN is also influenced by the density of the ligand immobilized on the materials' surface [80]. In this regard, Lee *et al*. prepared GO coated with Pluronic® F-127-FA conjugates with different FA densities [80]. *In vitro*, authors verified that increasing the FA density on GO surface augments the internalization of these materials by cancer cells [80]. However, *in vivo*, GO decorated with FA densities of 0, 10 and 25 % had a similar tumor accumulation [80]. In contrast, GO functionalized with FA densities of 50 and 100 % had a similar performance, displaying the highest tumor uptake [80]. In agreement with these findings, the photothermal effect (10 mg kg^{-1}, 808 nm, 2 W cm^{-2}, 10 min) mediated by GO with 50 % FA decoration produced a hyperthermia to 60 °C and tumor eradication in 2 mice (out of 3) [80]. On the other hand, GO with 0 and 25 % FA densities only caused a reduction of the tumors' growth upon irradiation, since these only produced hyperthermia to 47 and 50 °C, respectively [80].

3.5. Conclusion and outlook

In this chapter, the different strategies used to functionalize GFN aimed for application in cancer therapy have been presented, disclosing their impact on overcoming the limitations associated with GFN based therapies.

GFN are promising materials for application in cancer therapy due to their photothermal and drug delivery capabilities. However, the direct application of these materials for cancer therapy is severely limited by their poor colloidal stability, sub-optimal safety, inefficient tumor uptake and non-selectivity towards cancer cells. These critical limitations have been surpassed through the functionalization of GFN with different materials. In particular, GO derivatives were mostly functionalized by conjugating them with amine terminated polymers while rGO-based materials were largely non-covalently modified with amphiphilic polymers.

In general, the passivation of GFN surface with PEG-based materials was the most explored approach by researchers. In fact, PEGylated GFN demonstrated an excellent colloidal stability and biocompatibility both *in vitro* and *in vivo*. PEG coatings also improved the blood circulation time of GFN. In some cases, the high tumor uptake of PEGylated GFN enabled the eradication of mice's tumors upon NIR laser irradiation. Moreover, the decoration of GFN with targeting ligands could further improve their tumor-homing capacity and selectivity towards cancer cells, which permitted the complete photoablation of tumors, using a low injected dose of nanostructures and power density, as well as a reduction in the off-target toxicity of the delivered drugs.

The therapeutic potential of passive and active-targeted PEGylated GFN is only challenged by the recent reports that disclose the immunogenicity of some PEG-based coatings. Considering the vast research on the immunogenicity of PEGylated liposomes, the PEGylated GFN-immune system interactions are likely to be influenced by multiple factors and thus further research is needed on this topic. Moreover, this phenomenon should motivate researchers to investigate alternative coatings that i) have a good safety profile, ii) are able to functionalize both GO and rGO derivatives, iii) display long blood circulation times, to promote a higher tumor uptake, and iv) offer versatility to be conjugated with targeting ligands, allowing a cancer-cell selective therapy. Moreover, coatings that detach from GFN surface in response to tumor-microenvironment or intracellular stimuli should be further investigated due to their possible impact on the clearance of GFN.

Overall, the continuous interdisciplinary efforts for developing new routes or materials to functionalize GFN will surely have a major impact on their application in cancer therapy.

Table 3.1. Different functionalizations used to improve the hydrophilicity and colloidal stability of GFN.

GFN	Material	Type of functionalization	Observations	Ref.
GO	Branched amine terminated PEG	Covalent	Stable in water, PBS and 10 % FBS supplemented cell culture medium (for at least 7 days)	[23]
GO	Branched amine terminated PEG	Covalent	Stable in water, 9 % NaCl and FBS	[10]
GO	Amine terminated mPEG with a bio-reducible linkage	Covalent	Stable in water and PBS	[23]
GO	Amine terminated Dextran	Covalent	Stable in water, PBS and 20 % BSA solution (up to 1 month)	[81]
GO	Amine modified Dextran	Covalent	Stable in water, 9 % NaCl, serum and cell culture medium	[57]
GO	Chitosan	Covalent	Stable in water and cell culture medium (for at least 48 h)	[82]
GO	HA-ADH	Covalent	Stable in water, PBS and cell culture medium	[83]
GO	Branched PEI	Covalent	Stable in water and saline solution	[84]
GO	Heparin modified with dopamine	Covalent	Stable in water and PBS (for at least 1 month)	[62]
GO	Branched amine terminated PEG, Branched PEI	Covalent	Stable in water, saline and FBS supplemented cell culture medium	[84]
GO	Branched amine terminated PEG, PAH	Covalent	Stable in water and 10 % FBS supplemented cell culture medium (for at least 12 h)	[73]
GO	Amine terminated branched PEG, PAH modified with Succinic anhydride or 2,3-Dimethylmaleic anhydride	Covalent	Stable in water and 10 % FBS supplemented cell culture medium (for at least 12 h)	[73]
GO	PEGylated alginate with a bio-reducible linkage containing amine groups	Covalent	Stable in water and PBS (for at least 48 h)	[85]

GO	Amine terminated PEG (conjugation), PMAA (polymerization), Crosslinked with cystamine	Covalent	Stable in water and PBS (for at least 24 h)	[86]
GO	Amine terminated PEG (conjugation), or PAA (polymerization) or PAM (polymerization)	Covalent	Stable in water, PBS and FBS supplemented cell culture medium (for at least 24 h)	[11]
GO	BSA	Non-covalent	Stable in water, PBS and 10 % FBS supplemented cell culture medium (for at least 7 days)	[23]
GO	Pluronic® F-127	Non-covalent	Stable in water, 75 mM NaCl, PBS, 10 % FBS supplemented cell culture medium and FBS (for at least 24 h)	[26]
GO	Poloxamer 188	Non-covalent	Stable in water, PBS and cell culture medium	[49]
GO (base treated)	Amine terminated mPEG	Covalent	Stable in water, PBS, FBS and cell culture medium (for at least 24 h)	[27]
GO (base treated)	Branched amine terminated PEG	Covalent	Stable in water, PBS, cell culture medium and serum	[9]
GO (base treated)	TPGS	Non-covalent	Stable in NaCl (during 12 h) and water and 10 % FBS supplemented cell culture medium (for at least 5 days)	[28]
GO-COOH	Amine terminated PEG with a bio-reducible linkage	Covalent	Stable in water, PBS and cell culture medium	[87]
GO-COOH	FA-PEG-NH_2	Covalent	Stable in PBS (for at least 48 h)	[88]
GO-COOH	HMDA-HA	Covalent	Stable in water and 100 mM NaCl	[29]
GO-COOH	FA	Covalent	Stable in water and D-Hanks buffer (for at least 24 h)	[34]
GO-COOH	Octaarginine	Covalent	Stable in water and 10 % FBS supplemented cell culture medium (for at least 2 days)	[89]
GO-COOH	Amine terminated mPEG, amine terminated PEG-FA conjugate	Covalent	Stable in cell culture medium	[90]

GO (modified with amines)	HA	Covalent	Stable in water and saline	[91]
rGO	Glucose	Covalent	Stable in FBS and 10 % FBS supplemented cell culture medium (for at least 1 month)	[53]
rGO	Heparin modified with dopamine	Covalent	Stable in water and PBS (for at least 1 month)	[62]
rGO	C_{18}-PMH-PEG	Non-covalent	Stable in water, PBS and 10 % FBS supplemented cell culture medium (for at least 7 days)	[23]
rGO	C_{18}-PMH-PEG	Non-covalent	Stable in water, 9 % NaCl, PBS, FBS and cell culture medium (for at least 1 week)	[40]
rGO	Pluronic® F-127	Non-covalent	Stable in water and cell culture medium	[92]
rGO	BSA	Non-covalent	Stable in water, PBS and 10 % FBS supplemented cell culture medium (for at least 7 days)	[23]
rGO	BSA	Non-covalent	Stable in water, 9 % NaCl, PBS, 10 % FBS solution and cell culture medium (for at least 1 month)	[50]
rGO	Hematin-terminated Dextran	Non-covalent	Stable in water, PBS and 10 % FBS supplemented cell culture medium	[41]
rGO	Cholesteryl HA	Non-covalent	Stable in water, PBS and 10 % FBS supplemented cell culture medium (for at least 7 days)	[42]
rGO	Low molecular weight heparin-taurocholate conjugate	Non-covalent	Stable in PBS (up to 3 days) and 10, 50 and 90 % FBS supplemented cell culture medium (up to 4 h).	[93]
rGO	Poly(glycerol)-naphthol conjugate	Non-covalent	Stable in PBS (up to several weeks)	[94]
rGO	Dextran, Chitosan; FA-NHS	Non-covalent; Covalent	Stable in water, PBS, FBS and cell culture medium	[14]

rGO	Gelatin	Non-covalent	Stable in water, PBS, FBS and cell culture medium (for at least 24 h)	[95]
rGO (hydrothermal treated)	TPGS	Non-covalent	Stable in water, NaCl and 10 % FBS supplemented cell culture medium (at least for 5 days)	[28]
rGO (hydrothermal treated)	Starch	Non-covalent	Stable in water (for at least 2 months, 4 ºC)	[96]
rGO (reduced by dopamine)	Poly(dopamine), BSA	Covalent	Stable in water (for at least 2 weeks) and PBS (2 weeks)	[37]
rGO (reduced by dopamine)	Poly(dopamine), Heparin	Covalent	Stable in water (for at least 1 month) and PBS (2 weeks)	[37]
rGO (ascorbic acid reduced)	1,2-Dimyristoyl-*sn*-glycero-3-phospho-(1-*rac*-glycerol) sodium salt	Non-covalent	Stable in water	[97]
rGO (octadeylamine modified)	Lactoferrin	Non-covalent	Stable in PBS and FBS supplemented cell culture medium (for at least 1 month)	[98]
rGO-PEI	mPEG	Covalent	Stable in water (for at least 6 h)	[39]
rGO-Alkynyl	PNIPAM-N_3	Covalent	Stable in water and PBS	[99]
rGO nanoplatelets	Dextran	Non-covalent	Stable in water and biological fluids	[65]
Graphene	Pluronic® F38, F68, F77, F87, F88, F98, F108, F127, L62, L64 P84, P103, P104 or P123	Non-covalent	Pluronic® F68, F77 and F87 are the most effective in the production of aqueous graphene suspensions	[100]
Graphene	Tetronic® 304, 904, 908, 1107 or 1307	Non-covalent	Tetronic® 1107 and 1307 are the most effective in the production of aqueous graphene suspensions	[100]

Adipic dihydrazide (ADH), poly(acrylamide) (PAM), poly(acrylic acid) (PAA), poly(allylamine hydrochloride) (PAH), poly(ethyleneimine) (PEI), poly(*N*-isopropylacrylamide) (PNIPAM), poly(methacrylic acid) (PMAA).

Table 3.2. Different functionalizations used to improve the biocompatibility and hemocompatibility of GFN.

GFN	Material	Type of functionalization	Observations	Ref.
GO	Branched amine terminated PEG	Covalent	PEG-GO (20 mg kg^{-1}; i.v. injection) did not induce abnormalities on the major organs of tumor bearing mice after 40 days p.i.; Blood related parameters of healthy mice injected with PEG-GO (20 mg kg^{-1}) after 3 months were similar to those of the control.	[21]
GO	Branched amine terminated PEG	Covalent	PEG-GO is eliminated from mice body through feces and urine; PEG-GO (20 mg kg^{-1}; i.v. injection) did not induce appreciable toxic effects on mice after 90 days p.i.; PEG-GO did not change mice's hepatic and kidney functions nor blood biochemistry and hematological related parameters.	[55]
GO	Branched amine terminated PEG	Covalent	PEG-GO (50 mg kg^{-1}; i.p. injection) did not induce appreciable toxic effects on mice after 90 days p.i.; PEG-GO did not induce physiologically significant changes on mice's hepatic and kidney functions nor on blood biochemistry and hematological related parameters.	[56]
GO	Branched amine terminated PEG	Covalent	Coating GO with PEG improves the cytocompatibility of the materials in 7792, MRC-5 and U937 cell lines.	[23]
GO	Amine terminated PEG with a bio-reducible linkage	Covalent	PEG-SS-GO has an improved cytocompatibility in U937 cells when compared to GO; After the detachment of the reducible coating, materials can be oxidized by horseradish peroxidase, leading to their degradation.	[23]

GO	Amine terminated mPEG	Covalent	PEG-GO induces cytokine secretion by macrophages despite not being internalized.	[59]
GO	Amine modified Dextran	Covalent	Dextran-GO has a lower effect on the HeLa cells proliferation than GO; Dextran-GO (20 mg kg^{-1}; i.v. injection) did not induce abnormalities in mice after 1 and 7 days p.i. (histological analysis).	[57]
GO	Amine terminated PEG (conjugation), or PAA (polymerization) or PAM (polymerization)	Covalent	The protein corona formed on the surface of GO-PEG and GO-PAA is lower than that present on GO and GO-PAM surfaces; GO-PEG and GO-PAA adsorb less IgG than GO and GO-PAM; GO-PEG and GO-PAA do not induce meaningful cytotoxicity to J774.A1 cells up to 10 μg mL^{-1} (24 h of incubation) when incubated in serum-free and serum-supplemented medium; GO-PAA presents the lowest uptake by macrophages; The survival rate of mice injected with GO-PEG and GO-PAA (1 mg kg^{-1}; i.v. injection) was 100 %; Mice injected with GO and GO-PAM (1 mg kg^{-1}) had a survival rate of 80 and 90 %, respectively; GO-PAA has the best *in vivo* biocompatibility profile since it had the lowest effect on mice's liver and lungs (histological analysis) and all the assessed blood biochemistry markers were non-significantly different from those of the control (at 1 mg kg^{-1} for 14 days).	[11]
GO	Heparin modified with dopamine	Covalent	At 200 μg mL^{-1}, Heparin-GO induces ≈ 1.2 % of hemolysis while GO induces 78.5 %; Heparin-GO has a better cytocompatible profile in HUVECs than GO (viability of ≈ 95 *vs.* ≈ 68 %; at 100 μg mL^{-1}; 24 h of incubation).	[62]

GO	PEG	Non-covalent	PEG-GO reduces the invasion and migration of breast cancer cells (*in vitro* and *in vivo*); PEG-GO can disturb the assembly of cytoskeletal F-actin through the downregulation of the expression of energy metabolism-related genes, reduction of mitochondrial oxidative phosphorylation, and inhibition of the synthesis of ATP.	[101]
GO	BSA	Non-covalent	Coating GO with BSA improves the cytocompatibility of the materials in 7792, MRC-5 and U937 cell lines.	[23]
GO	BSA, transferrin, fibrinogen, immunoglobulin or FBS proteins	Non-covalent	A549 cells incubated with GO (in FBS free medium) display a viability of about 55 % (at 200 μg mL^{-1}); GO coated with several proteins does not induce considerable cytotoxicity to A549 cells (at 200 μg mL^{-1}).	[102]
GO	PEG, DOC or Pluronic® P123	Non-covalent	PEG coated GO has a better cytocompatible profile in L929 cells than DOC coated GO and Pluronic® P123 coated GO (48 h incubation period).	[103]
GO	Bovine α-lactalbumin; Glutaraldehyde	Non-covalent; Covalent	GO induces a hemolysis of about 27 % at the concentration of 30 μg mL^{-1}; Bovine α-lactalbumin/GO induces a hemolysis of about 3 % at the concentration of 333.33 μg mL^{-1}.	[63]
GO (modified with amines)	HA	Covalent	HA-GO does not induce considerable alterations in HeLa and L929 cells' viability up to 200 μg mL^{-1} (24 h of incubation; viability > 80 %); At 400 μg mL^{-1}, HA-GO induces 0.7 % of hemolysis while GO induces 1.5 %; No toxicity at the tested dose of HA-GO (10 mg kg^{-1}; i.v. injection) was found *in vivo* 10 days p.i. (blood biochemistry and histological analysis).	[91]
GO-COOH	L-Cysteine	Covalent	GO has a stronger effect on the hatching rate of zebrafish embryos than Cysteine-GO;	[104]

			Cysteine-GO does not induce considerable tissue abnormalities, malformations or death in the embryos at the tested doses (up to 10 μg mL^{-1}).	
rGO	Chitosan	Covalent	Chitosan-rGO does not induce meaningful alterations on CEM cells viability up to 400 μg mL^{-1} (5 days of incubation).	[105]
rGO	C_{18}-PMH-PEG	Non-covalent	Coating rGO with PEG-based amphiphile improves the cytocompatibility of the materials in 7792, MRC-5 and U937 cell lines.	[23]
rGO [a)]	C_{18}-PMH-PEG	Non-covalent	PEG-rGO (50 mg kg^{-1}; i.p. injection) did not induce appreciable toxic effects on mice after 90 days p.i.; PEG-rGO did not induce physiologically significant changes on mice's hepatic and kidney functions nor on blood biochemistry and hematological related parameters.	[56]
rGO [b)]	C_{18}-PMH-PEG	Non-covalent	PEG-rGO (50 mg kg^{-1}; i.p. injection) did not induce appreciable toxic effects on mice after 90 days p.i.; PEG-rGO did not induce physiologically significant changes on mice's hepatic and kidney functions nor on blood biochemistry and hematological related parameters.	[56]
rGO	C_{18}-PMH-PEG	Non-covalent	Mice injected with PEG-rGO (10 mg kg^{-1}; i.v. injection) did not display signs of toxicity after 50 days p.i. (histological, blood and biochemistry analysis).	[40]
rGO	DSPE-PEG-NH_2	Non-covalent	DSPE-PEG-NH_2 coated rGO induces cytotoxic effects on glioblastoma cells at concentrations above 10 μg mL^{-1}.	[45]
rGO	BSA	Non-covalent	Coating rGO with BSA improves the cytocompatibility of the materials in 7792, MRC-5 and U937 cell lines.	[23]
rGO	BSA	Non-covalent	BSA-rGO (20 mg kg^{-1}) did not induce appreciable alterations on mice's major organs after 30 days p.i..	[50]

rGO	Cholesteryl HA	Non-covalent	HA-rGO and rGO have a similar cytocompatibility *in vitro* (24 h of incubation); 1 day p.i., rGO reduces mice survival rate to 40 % (dose of 20 mg kg^{-1}; i.v. injection); 1 day p.i., HA-rGO treated mice have a 100 % survival rate (40 mg kg^{-1}).	[42]
rGO	Hematin terminated Dextran	Non-covalent	Dextran-rGO has a better cytocompatible profile in MCF-7/ADR cells than GO (viability of ≈ 85 *vs.* ≈ 53 %; at 100 µg mL^{-1}; 48 h of incubation).	[41]
rGO	Poly(glycerol)-naphthol conjugate	Non-covalent	Poly(glycerol)-rGO does not induce considerable cytotoxicity to MCF-7 cells (at 100 µg mL^{-1}; 48 h of incubation)	[94]
rGO (reduced by dopamine)	Heparin modified with dopamine	Covalent	At 200 µg mL^{-1}, Heparin-rGO induces ≈ 0.6 % of hemolysis while GO induces 78.5 %; Heparin-rGO has a better cytocompatible profile in HUVECs than GO (viability of ≈ 100 *vs.* ≈ 68 %; at 100 µg mL^{-1}; 24 h of incubation).	[62]
rGO (reduced by dopamine)	Poly(dopamine), BSA	Covalent	BSA-poly(dopamine)-rGO induces an insignificant hemolysis (≈ 1.8 %; at 200 µg mL^{-1}); At 100 µg mL^{-1}, BSA-poly(dopamine)-rGO has a better cytocompatibility than rGO (≈ 73 *vs.* ≈ 39 %).	[37]
rGO (reduced by dopamine)	Poly(dopamine), Heparin	Covalent	Heparin-poly(dopamine)-rGO induces an insignificant hemolysis (≈ 0.2 %; at 200 µg mL^{-1}); At 100 µg mL^{-1}, Heparin-poly(dopamine)-rGO has a better cytocompatibility than rGO (≈ 95 *vs.* ≈ 39 %; HUVECs; 24 h of incubation).	[37]
rGO (ascorbic acid treated)	PVP	Covalent	PVP-rGO is less immunogenic than GO (induces less maturation of dendritic cells); PVP-rGO only induces IL-6 secretion by dendritic cells while GO induces higher IL-6 secretion as well as IL-1ß and TNF-α secretions; PVP-rGO induces less apoptosis of T lymphocytes than GO;	[12]

			PVP-rGO suffered no appreciable phagocytosis by macrophages and enhanced their activity (GO was susceptible to phagocytosis).	
rGO (glucose reduced)	PEG, DOC or Pluronic® P123	Non-covalent	PEG coated rGO has a better cytocompatible profile in L929 cells than DOC coated rGO and Pluronic® P123 coated rGO (48 h incubation period).	[103]
rGO (hydrothermal treatment)	Starch	Non-covalent	Starch-rGO does not induce meaningful alterations on SW-620 cells' viability up to 200 μg mL^{-1} (viability > 90 %; 48 h of incubation).	[96]
rGONR	DSPE-PEG-NH_2	Non-covalent	DSPE-PEG-NH_2 coated rGONR induce cytotoxic and genotoxic effects on glioblastoma cells at concentrations above 1 μg mL^{-1}.	[45]
rGO nanoplatelets	Dextran	Non-covalent	Dextran-rGO nanoplatelets do not adsorb human serum albumin.	[66]
rGO nanoplatelets	Dextran	Non-covalent	The maximum tolerable dose of Dextran-rGO nanoplatelets is between 50 and 125 mg kg^{-1} (i.v. injection); 30 days p.i., Dextran-rGO nanoplatelets demonstrate an excellent biocompatibility at injected doses of 50 mg kg^{-1} and bellow (histology, respiratory, cardiovascular and hematological factors analysis); Materials are excreted mostly through feces; Materials are almost completely eliminated from the body after 24 h p.i.	[65]
Graphene nanoplatelets	PVA, HEC, PEG, PVP, CON, GLU or HA	Non-covalent	Graphene nanoplatelets coated with PVA or HEC present the lowest hemolytic effect (hemolysis ≤ 0.05 % at 500 μg mL^{-1}); PVA coated graphene nanoplatelets are cytocompatible towards HFF-1 cells at 50 (24 h of incubation) or 100 μg mL^{-1} (48 and 72 h of incubation).	[64]
Hydroxyl-functionalized graphene	PLA (polymerization), PEG (conjugation)	Covalent	PEG-PLA-graphene has a better cytocompatibility than graphene.	[106]

[a)] after PEGylation the size was estimated to be 50 nm; [b)] after PEGylation the size was estimated to be 27 nm; chondroitin sulfate potassium (CON), D-glucosamine sulfate potassium (GLU), hydroxyethyl cellulose (HEC), poly(lactide) (PLA), sodium deoxycholate (DOC).

Table 3.3. Different functionalizations used to improve the blood circulation time and tumor accumulation of GFN.

GFN	Material	Type of functionalization	Observations	Ref.
GO	Branched amine terminated PEG	Covalent	PEG-GO has a $t_{1/2}$ of about 1.5 h; PEG-GO achieves a high tumor uptake in 4T1, KB and U87 tumor bearing mice; Photothermal effect mediated by PEG-GO leads to tumor eradication (20 mg kg^{-1}, 808 nm, 2 W cm^{-2}, 5 min).	[21]
GO	Branched amine terminated PEG	Covalent	PEG-GO displays a $t_{1/2}$ = 0.29 h ($t'_{1/2}$ = 5.8 h) but achieves a tumor accumulation lower than 1 % ID g^{-1}; PTT mediated by PEG-GO induces a slight reduction of the tumor growth (20 mg kg^{-1}, 808 nm, 0.15 W cm^{-2}, 5 min).	[10]
GO	Branched amine terminated PEG-Oxoplatin-COOH conjugate	Covalent	Accumulation of platinum in 4T1 tumors is enhanced when delivered by Platin-PEG-GO (≈ 4 *vs.* 9.6 μg g^{-1}); Platinum tumor uptake of mice treated with Platin-PEG-GO and NIR radiation was ≈ 13.3 μg g^{-1}, presumably due to hyperthermia enhanced EPR effect; The chemo-photothermal effect mediated by Platin-PEG-GO led to tumor eradication (twice: 10 mg kg^{-1}, 785 nm, 1.5 W cm^{-2}, 3 min); No obvious signs of toxicity were found on the off-target organs of mice treated with Platin-PEG-GO + NIR; Accumulation of platinum in the liver of mice treated with cisplatin, Platin-PEG-GO and Platin-PEG-GO in combination with NIR radiation were ≈ 9.0, 7.2 and 6.6 μg g^{-1}, respectively.	[22]
GO	Amine modified Dextran	Covalent	Dextran-GO has $t_{1/2}$ = 0.19 h ($t'_{1/2}$ = 1.81 h);	[57]

			The liver and spleen accumulations reduce from about 16 and 10 % ID g^{-1} (at 4 h p.i.) to lower than 2 % ID g^{-1} at 7 days p.i.; Dextran-GO is mainly excreted in feces.	
GO (base treated)	Amine terminated mPEG	Covalent	Accumulation of Photochlor® in 4T1 tumors is enhanced when delivered by PEG-GO (≈ 1.3 *vs.* 3.1 % ID g^{-1}); The liver accumulation of Photochlor® is also reduced when delivered by PEG-GO (≈ 37 *vs.* 27 % ID g^{-1}).	[27]
rGO	C_{18}-PMH-PEG	Non-covalent	PEG-rGO has a $t_{1/2}$ = 0.65 h ($t'_{1/2}$ ≈ 18 h), achieving a tumor accumulation of ≈ 4 % ID g^{-1} (at 48 h p.i.); The liver and spleen accumulations are about 15 and 21 % ID g^{-1}, respectively.	[40]
rGO [a)]	C_{18}-PMH-PEG	Non-covalent	C_{18}-PMH-PEG coated rGO displays a $t_{1/2}$ = 0.22 h ($t'_{1/2}$ = 17.5 h) and achieves a tumor accumulation of ≈ 5 % ID g^{-1}.	[10]
rGO [b)]	C_{18}-PMH-PEG	Non-covalent	C_{18}-PMH-PEG coated rGO displays a $t_{1/2}$ = 0.51 h ($t'_{1/2}$ = 16.7 h) and achieves a tumor accumulation of ≈ 6 % ID g^{-1}; PTT mediated by C_{18}-PMH-PEG coated rGO leads to tumor eradication (20 mg kg^{-1}, 808 nm, 0.15 W cm^{-2}, 5 min).	[10]
rGO	C_{18}-PMH-PEG-NH_2; Succinimidyl carboxyl methyl ester-PEG-Maleimide	Non-covalent; Covalent	Conjugation of additional PEG to C_{18}-PMH-PEG coated rGO improves materials' blood circulation time from $t_{1/2}$ = 0.19 h ($t'_{1/2}$ = 18.8 h) to $t_{1/2}$ = 0.35 h ($t'_{1/2}$ = 27.7 h); This modification also improves materials' tumor accumulation from 8.8 to 15.5 % ID g^{-1}.	[70]

[a)] after PEGylation the size was estimated to be 65 nm; [b)] after PEGylation the size was estimated to be 27 nm.

Table 3.4. Different functionalizations used to improve the cellular uptake and selectivity of GFN.

GFN	Material	Type of functionalization	Observations	Ref.
GO	Branched amine terminated PEG, PAH modified with 2,3-Dimethylmaleic anhydride	Covalent	Delivery of DOX to MCF-7/ADR cells by the polymer functionalized GO produces a stronger therapeutic effect than that achieved using free DOX; The chemo-photothermal effect mediated by the polymer functionalized GO produces an even higher reduction on cancer cells' viability.	[73]
GO	Branched amine terminated PEG-Oxoplatin-COOH conjugate	Covalent	Delivery of platinum to 4T1 cancer cells by Platin-PEG-GO can produce a stronger therapeutic effect than that achieved using free cisplatin.	[22]
GO	Branched amine and maleimide terminated PEG, TRC105-SH	Covalent	TRC105-PEG-GO targets tumor vasculature by binding to CD105; TRC105-PEG-GO can achieve a 2.9-fold higher accumulation in the tumor zone than PEG-GO (5.8 *vs.* 2.0 % ID g^{-1}; at 0.5 h p.i.).	[76]
GO	Branched amine and maleimide terminated PEG, TRC105-SH	Covalent	TRC105-PEG-GO targets tumor vasculature by binding to CD105; TRC105-PEG-GO can achieve a ≈ 1.6-fold higher accumulation in the tumor zone than PEG-GO (5.8 *vs.* 3.6 % ID g^{-1}; at 7 h p.i.).	[77]
GO	FA-PEG-NH_2	Covalent	Camptothecin loaded FA-PEG-GO produces a slightly higher reduction on HeLa cells' viability than free Camptothecin; Drug loaded FA-PEG-GO therapeutic effect appears to be selective for folate receptor expressing cell lines; The homing capacity of camptothecin loaded FA-PEG-GO to HeLa tumors is superior to that of Camptothecin loaded PEG-GO.	[13]
GO	Anti-MUC1 Antibody, PEG	Covalent	Antibody-PEG-GO achieves a higher uptake by $MUC1^+$ cancer cells than PEG-GO;	[107]

			Antibody-PEG-GO internalization by $MUC1^-$ cancer cells is inferior to that occurring in $MUC1^+$ cells.	
GO	HA-ADH	Covalent	Delivery of Ce6 by HA-GO to HeLa cells is faster than the diffusion of free Ce6; HA-GO delivers its payload more effectively to CD44 overexpressing cells.	[83]
GO	Carboxymethyl chitosan, HA	Covalent	HA-Carboxymethyl chitosan-GO delivers a higher DOX dose to CD44 overexpressing cancer cells (HeLa) than to normal cells (L929).	[108]
GO	A1 aptamer	Covalent	A1-GO achieves a higher binding to A549 cells' membrane than GO; Binding of A1-GO seems to be highly selective for A549 cells; Decitabine loaded A1-GO produces a stronger therapeutic effect than decitabine loaded GO and free decitabine.	[109]
GO	Amine terminated Dextran, AS1411 aptamer	Covalent	Curcumin loaded AS1411-Dextran-GO delivers a higher drug dose to MCF-7 and 4T1 cells than curcumin loaded Dextran-GO and free curcumin, leading to an improved therapeutic effect.	[81]
GO	Carboxymethyl chitosan, Lactobionic acid	Covalent	DOX loaded Lactobionic acid functionalized GO produces a stronger therapeutic effect on cancer cells that express asialoglycoprotein receptors.	[110]
GO	HA-ADH, APMA, RGD	Covalent	RGD-HA-GO delivers a higher DOX dose to SKOV-3 cancer cells than HA-GO and GO, thus producing a superior therapeutic effect; Nanomaterials deliver an inferior DOX dose to normal cells.	[79]
GO	Amine terminated HA; Pluronic® F68	Covalent; Non-covalent	Pluronic® F68/HA-GO mediates the delivery of a higher mitoxantrone dose to MCF-7 and MCF-7/ADR cells than Pluronic® F68/GO and free mitoxantrone; The uptake of mitoxantrone in MCF-7 and MCF-7/ADR tumors is higher in the group treated with mitoxantrone loaded Pluronic® F68/HA-GO than in those treated with mitoxantrone loaded Pluronic® F68/GO or free mitoxantrone.	[111]

GO	Bovine α-lactalbumin; Glutaraldehyde	Non-covalent; Covalent	GO induces cytotoxic effects at low concentrations on normal and breast cancer cells; Bovine α-lactalbumin/GO induces cytotoxicity to breast cancer cells and it is cytocompatible to normal cells.	[63]
GO	PEI; Transferrin	Non-covalent; Covalent	Platinum loaded Transferrin-PEI functionalized GO can enhance the cytotoxicity of platinum towards cancer cells, while maintaining its low cytotoxicity towards normal cells.	[112]
GO	cRGD-chitosan conjugate	Non-covalent	cRGD-chitosan functionalized GO internalization by $\alpha_v\beta_3$ overexpressing cells is higher than that of chitosan functionalized GO; DOX loaded cRGD-chitosan functionalized GO produces a stronger reduction on cancer cells' viability than DOX loaded chitosan/GO and free DOX.	[113]
GO	Transferrin-PAH conjugate	Non-covalent	Docetaxel loaded transferrin-PAH coated GO can induce a stronger reduction of MCF-7 cells' viability than Docetaxel loaded PAH coated GO and free Docetaxel.	[75]
GO	Pluronic® F-127-FA conjugate	Non-covalent	Increasing the FA density on GO from 0 to 100 % augments the internalization of these materials by KB cells; *In vivo*, GO functionalized with FA densities of 50 and 100 % have a similar and the highest tumor-homing capacity; GO decorated with 0, 10 and 25 % of FA have a similar tumor accumulation; The photothermal effect mediated by GO with 50 % folate decoration led to the eradication of tumors in 2 out of 3 mice (10 mg kg^{-1}, 808 nm, 2 W cm^{-2}, 10 min).	[80]
GO	Pluronic® F-127-FA, Pluronic® F-127-cRGD	Non-covalent	GO dual-functionalized with cRGD and FA has a tumor accumulation superior to that of their equivalents only functionalized with one ligand (cRGD or FA); Photothermal effect mediated by dual-ligand functionalized GO induces tumor eradication, while that mediated by single-ligand functionalized GO only promotes a reduction of the tumor growth (7.5 mg kg^{-1}, 808 nm, 2 W cm^{-2}, 10 min).	[78]

GO (base treated)	Amine terminated mPEG	Covalent	Delivery of Photochlor® by PEG-GO to 4T1 cells is more efficient than the diffusion of free Photochlor®.	[27]
GO (base treated)	TPGS	Non-covalent	TPGS functionalized GO induces a strong reduction on MCF-7 cells' viability but has a very low effect on fibroblasts' viability.	[28]
GO (modified with amines)	HA	Covalent	HA-GO delivers a high DOX dose to cancer cells overexpressing CD44 receptors and has an unappreciable internalization in normal cells (low CD44 expression).	[91]
GO-COOH	Chlorotoxin	Covalent	Chlorotoxin-GO delivers a higher DOX dose to C6 glioma cells than GO; DOX loaded Chlorotoxin-GO can produce a higher reduction on cancer cells' viability than DOX loaded GO and free DOX.	[114]
GO-COOH	HMDA-HA	Covalent	HA-GO achieves a higher uptake in melanoma cells than in fibroblasts, and thus its photothermal effect only affects the melanoma cells; HA-GO applied on normal skin remains in the top of the skin; HA-GO can diffuse through cancerous skin, reaching the tumor mass; Photothermal effect mediated by HA-GO leads to tumor eradication.	[29]
GO-COOH	FA	Covalent	FA functionalized GO achieves a higher internalization in cancer cells overexpressing FA receptors; DOX loaded FA functionalized GO and free DOX can produce a similar reduction of MCF-7 cells' viability.	[34]
GO-COOH	PEI, Anti-integrin $\alpha_v\beta_3$ Antibody; DOX-(PAH-Cit) conjugate	Covalent; Non-covalent	Delivery of DOX to U87 MG cancer cells by antibody functionalized GO produces a more potent therapeutic effect than that obtained using non-targeted GO and free DOX; Antibody functionalized GO promotes a DOX tumor accumulation of ≈ 3 % ID g^{-1} while free DOX has a tumor uptake of ≈ 1.4 % ID g^{-1}.	[115]

GO-COOH	PVP; FA	Non-covalent; Covalent	FA functionalized GO achieves a higher internalization in cancer cells overexpressing FA receptors; Chemo-photothermal therapy mediated by DOX loaded FA functionalized GO leads to an improved therapeutic effect.	[116]
rGO	Hematin terminated Dextran	Non-covalent	Delivery of DOX by Dextran-rGO to MCF-7/ADR cells is more efficient than the diffusion of free DOX, leading to an improved therapeutic effect.	[41]
rGO	Maleimide terminated C_{18}-PMH-PEG; TRC105-SH	Non-covalent; Covalent	TRC105-PEG-rGO can achieve ≈ 2.1-fold higher accumulation in the tumor zone than PEG-rGO (5.6 *vs.* 2.7 % ID g^{-1}; at 3 h p.i.).	[117]
rGO	Cholesteryl HA	Non-covalent	HA-rGO can deliver a higher DOX dose to CD44 overexpressing cells than rGO.	[42]
rGO	Cholesteryl HA, DSPE-PEG	Non-covalent	Dox loaded PEG-HA-rGO tumor and liver accumulations are superior to that of DOX loaded PEG-rGO.	[42]
rGO	DSPE-PEG-RGD	Non-covalent	rGO coated with DSPE-PEG-RGD has a higher tumor accumulation than DSPE-PEG coated rGO (≈ 22.7 *vs.* ≈ 7.3 % ID g^{-1}); Target functionalization also reduces nanomaterials' liver and spleen uptakes from about 26 and 22 to 7 and 6 % ID g^{-1}, respectively.	[74]
rGO	DSPE-PEG-RGD, C_{18}-PMH-PEG	Non-covalent	DSPE-PEG-RGD/C_{18}-PMH-PEG functionalized rGO achieves a higher internalization in U87MG cells than its equivalent functionalized with DSPE-PEG-RAD/C_{18}-PMH-PEG.	[118]
rGO	Low molecular weight heparin-taurocholate conjugate	Non-covalent	DOX loaded heparin functionalized rGO produces a stronger *in vitro* and *in vivo* therapeutic effect than free DOX (the heparin conjugate has also anticancer activity).	[93]
rGO	Dextran, Chitosan; FA-NHS	Non-covalent; Covalent	FA-polymer functionalized rGO achieves a selective and higher internalization in HeLa cells than polymer-rGO;	[14]

			DOX loaded FA-polymer-rGO produces a stronger reduction on HeLa cells' viability than free DOX.	
rGO (hydrothermal treated)	TPGS	Non-covalent	TPGS functionalized rGO induces a strong reduction on MCF-7 cells' viability but has a very low effect on fibroblasts' viability.	[28]
rGO (reduced by dopamine)	AAP10	Covalent	The photothermal effect mediated by AAP10 functionalized rGO leads to tumor eradication, while that mediated by rGO only induces tumor regression (intratumoral injection, 808 nm, 1.5 W cm^{-2}, 5 min).	[43]
rGO (octadeylamine modified)	Lactoferrin	Non-covalent	Lactoferrin-rGO capsules display a greater internalization in lactoferrin receptor overexpressing cells than PVA-rGO capsules; Lactoferrin-rGO capsules display an improved tumor accumulation when compared to their PVA coated equivalents.	[98]
rGO nanomesh	DSPE-PEG-RGD	Non-covalent	rGO nanomesh coated with DSPE-PEG-RGD has a higher tumor accumulation than DSPE-PEG coated rGO nanomesh (≈ 31 *vs.* ≈ 8.9 % ID g^{-1}); Target functionalization also reduces nanomaterials' liver and spleen uptakes from about 17 and 12 to 5 and 3 % ID g^{-1}, respectively; Photothermal effect mediated by DSPE-PEG-RGD coated rGO nanomesh leads to tumor eradication (2 μg, 808 nm, 0.1 W cm^{-2}, 7 min).	[74]
rGONR	DSPE-PEG-RGD	Non-covalent	DSPE-PEG-RGD functionalized rGONR achieve a higher internalization in glioblastoma cells than their equivalents functionalized with DSPE-PEG-RAD, leading to an enhanced photothermal effect.	[45]

N-(3-aminopropyl)methacrylamide hydrochloride (APMA), arginine-alanine-aspartate (RAD), chlorin e6 (Ce6), doxorubicin (DOX), PAH functionalized with citraconic anhydride (PAH-Cit).

3.6. References

[1] H. Shen, L. Zhang, M. Liu, Z. Zhang, Biomedical Applications of Graphene, Theranostics, 2 (2012) 283-294.

[2] C. Chung, Y.-K. Kim, D. Shin, S.-R. Ryoo, B.H. Hong, D.-H. Min, Biomedical Applications of Graphene and Graphene Oxide, Accounts of Chemical Research, 46 (2013) 2211-2224.

[3] G. Gonçalves, M. Vila, M.T. Portolés, M. Vallet-Regi, J. Gracio, P.A.A.P. Marques, Nano-Graphene Oxide: A Potential Multifunctional Platform for Cancer Therapy, Advanced Healthcare Materials, 2 (2013) 1072-1090.

[4] D. Bitounis, H. Ali-Boucetta, B.H. Hong, D.H. Min, K. Kostarelos, Prospects and Challenges of Graphene in Biomedical Applications, Advanced Materials, 25 (2013) 2258-2268.

[5] M. Orecchioni, R. Cabizza, A. Bianco, L.G. Delogu, Graphene as Cancer Theranostic Tool: Progress and Future Challenges, Theranostics, 5 (2015) 710-723.

[6] C. Cheng, S. Li, A. Thomas, N.A. Kotov, R. Haag, Functional Graphene Nanomaterials Based Architectures: Biointeractions, Fabrications, and Emerging Biological Applications, Chemical Reviews, 117 (2017) 1826-1914.

[7] J. Liu, L. Cui, D. Losic, Graphene and graphene oxide as new nanocarriers for drug delivery applications, Acta Biomaterialia, 9 (2013) 9243-9257.

[8] D. de Melo-Diogo, C. Pais-Silva, D.R. Dias, A.F. Moreira, I.J. Correia, Strategies to Improve Cancer Photothermal Therapy Mediated by Nanomaterials, Advanced Healthcare Materials, 6 (2017) 1700073.

[9] Z. Liu, J.T. Robinson, X. Sun, H. Dai, PEGylated Nanographene Oxide for Delivery of Water-Insoluble Cancer Drugs, Journal of the American Chemical Society, 130 (2008) 10876-10877.

[10] K. Yang, J. Wan, S. Zhang, B. Tian, Y. Zhang, Z. Liu, The influence of surface chemistry and size of nanoscale graphene oxide on photothermal therapy of cancer using ultra-low laser power, Biomaterials, 33 (2012) 2206-2214.

[11] M. Xu, J. Zhu, F. Wang, Y. Xiong, Y. Wu, Q. Wang, J. Weng, Z. Zhang, W. Chen, S. Liu, Improved In Vitro and In Vivo Biocompatibility of Graphene Oxide through Surface Modification: Poly(Acrylic Acid)-Functionalization is Superior to PEGylation, ACS Nano, 10 (2016) 3267-3281.

[12] X. Zhi, H. Fang, C. Bao, G. Shen, J. Zhang, K. Wang, S. Guo, T. Wan, D. Cui, The immunotoxicity of graphene oxides and the effect of PVP-coating, Biomaterials, 34 (2013) 5254-5261.

[13] J. Tian, Y. Luo, L. Huang, Y. Feng, H. Ju, B.-Y. Yu, Pegylated folate and peptide-decorated graphene oxide nanovehicle for in vivo targeted delivery of anticancer drugs and therapeutic self-monitoring, Biosensors and Bioelectronics, 80 (2016) 519-524.

[14] A.R. Maity, A. Chakraborty, A. Mondal, N.R. Jana, Carbohydrate coated, folate functionalized colloidal graphene as a nanocarrier for both hydrophobic and hydrophilic drugs, Nanoscale, 6 (2014) 2752-2758.

[15] S.F. Kiew, L.V. Kiew, H.B. Lee, T. Imae, L.Y. Chung, Assessing biocompatibility of graphene oxide-based nanocarriers: A review, Journal of Controlled Release, 226 (2016) 217-228.

[16] S. Syama, P.V. Mohanan, Safety and biocompatibility of graphene: A new generation nanomaterial for biomedical application, International Journal of Biological Macromolecules, 86 (2016) 546-555.

[17] A. Bianco, Graphene: Safe or Toxic? The Two Faces of the Medal, Angewandte Chemie International Edition, 52 (2013) 4986-4997.

[18] A. Bianco, Graphen: sicher oder toxisch?, Angewandte Chemie, 125 (2013) 5086-5098.

[19] W.S. Hummers Jr, R.E. Offeman, Preparation of graphitic oxide, Journal of the American Chemical Society, 80 (1958) 1339-1339.

[20] D.C. Marcano, D.V. Kosynkin, J.M. Berlin, A. Sinitskii, Z. Sun, A. Slesarev, L.B. Alemany, W. Lu, J.M. Tour, Improved synthesis of graphene oxide, ACS Nano, 4 (2010) 4806-4814.

[21] K. Yang, S. Zhang, G. Zhang, X. Sun, S.-T. Lee, Z. Liu, Graphene in Mice: Ultrahigh In Vivo Tumor Uptake and Efficient Photothermal Therapy, Nano Letters, 10 (2010) 3318-3323.

[22] J. Li, Z. Lyv, Y. Li, H. Liu, J. Wang, W. Zhan, H. Chen, H. Chen, X. Li, A theranostic prodrug delivery system based on Pt(IV) conjugated nano-graphene oxide with synergistic effect to enhance the therapeutic efficacy of Pt drug, Biomaterials, 51 (2015) 12-21.

[23] Y. Li, L. Feng, X. Shi, X. Wang, Y. Yang, K. Yang, T. Liu, G. Yang, Z. Liu, Surface Coating-Dependent Cytotoxicity and Degradation of Graphene Derivatives: Towards the Design of Non-Toxic, Degradable Nano-Graphene, Small, 10 (2014) 1544-1554.

[24] N. Yeole, S.N.R. Kutcherlapati, T. Jana, Polystyrene–graphene oxide (GO) nanocomposite synthesized by interfacial interactions between RAFT modified GO and core–shell polymeric nanoparticles, Journal of Colloid and Interface Science, 443 (2015) 137-142.

[25] S.H. Lee, D.R. Dreyer, J. An, A. Velamakanni, R.D. Piner, S. Park, Y. Zhu, S.O. Kim, C.W. Bielawski, R.S. Ruoff, Polymer Brushes via Controlled, Surface-Initiated Atom Transfer Radical Polymerization (ATRP) from Graphene Oxide, Macromolecular Rapid Communications, 31 (2010) 281-288.

[26] B.J. Hong, O.C. Compton, Z. An, I. Eryazici, S.T. Nguyen, Successful Stabilization of Graphene Oxide in Electrolyte Solutions: Enhancement of Biofunctionalization and Cellular Uptake, ACS Nano, 6 (2012) 63-73.

[27] P. Rong, K. Yang, A. Srivastan, D.O. Kiesewetter, X. Yue, F. Wang, L. Nie, A. Bhirde, Z. Wang, Z. Liu, G. Niu, W. Wang, X. Chen, Photosensitizer Loaded Nano-Graphene for Multimodality Imaging Guided Tumor Photodynamic Therapy, Theranostics, 4 (2014) 229-239.

[28] D. de Melo-Diogo, C. Pais-Silva, E.C. Costa, R.O. Louro, I.J. Correia, D-α-tocopheryl polyethylene glycol 1000 succinate functionalized nanographene oxide for cancer therapy, Nanomedicine, 12 (2017) 443-456.

[29] H.S. Jung, W.H. Kong, D.K. Sung, M.-Y. Lee, S.E. Beack, D.H. Keum, K.S. Kim, S.H. Yun, S.K. Hahn, Nanographene Oxide–Hyaluronic Acid Conjugate for Photothermal Ablation Therapy of Skin Cancer, ACS Nano, 8 (2014) 260-268.

[30] J.P. Rourke, P.A. Pandey, J.J. Moore, M. Bates, I.A. Kinloch, R.J. Young, N.R. Wilson, The Real Graphene Oxide Revealed: Stripping the Oxidative Debris from the Graphene-like Sheets, Angewandte Chemie, 123 (2011) 3231-3235.

[31] D. Ma, L. Dong, M. Zhou, L. Zhu, The influence of oxidation debris containing in graphene oxide on the adsorption and electrochemical properties of 1,10-phenanthroline-5,6-dione, Analyst, 141 (2016) 2761-2766.

[32] X. Sun, Z. Liu, K. Welsher, J.T. Robinson, A. Goodwin, S. Zaric, H. Dai, Nano-graphene oxide for cellular imaging and drug delivery, Nano Research, 1 (2008) 203-212.

[33] W. Zhang, Z. Guo, D. Huang, Z. Liu, X. Guo, H. Zhong, Synergistic effect of chemo-photothermal therapy using PEGylated graphene oxide, Biomaterials, 32 (2011) 8555-8561.

[34] L. Zhang, J. Xia, Q. Zhao, L. Liu, Z. Zhang, Functional Graphene Oxide as a Nanocarrier for Controlled Loading and Targeted Delivery of Mixed Anticancer Drugs, Small, 6 (2010) 537-544.

[35] P.-G. Ren, D.-X. Yan, X. Ji, T. Chen, Z.-M. Li, Temperature dependence of graphene oxide reduced by hydrazine hydrate, Nanotechnology, 22 (2010) 055705.

[36] M.J. Fernández-Merino, L. Guardia, J. Paredes, S. Villar-Rodil, P. Solís-Fernández, A. Martínez-Alonso, J. Tascon, Vitamin C is an ideal substitute for hydrazine in the reduction of graphene oxide suspensions, Journal of Physical Chemistry C, 114 (2010) 6426-6432.

[37] C. Cheng, S. Nie, S. Li, H. Peng, H. Yang, L. Ma, S. Sun, C. Zhao, Biopolymer functionalized reduced graphene oxide with enhanced biocompatibility via mussel inspired coatings/anchors, Journal of Materials Chemistry B, 1 (2013) 265-275.

[38] M. Agharkar, S. Kochrekar, S. Hidouri, M.A. Azeez, Trends in green reduction of graphene oxides, issues and challenges: A review, Materials Research Bulletin, 59 (2014) 323-328.

[39] H. Kim, D. Lee, J. Kim, T.-i. Kim, W.J. Kim, Photothermally Triggered Cytosolic Drug Delivery via Endosome Disruption Using a Functionalized Reduced Graphene Oxide, ACS Nano, 7 (2013) 6735-6746.

[40] L. Chen, X. Zhong, X. Yi, M. Huang, P. Ning, T. Liu, C. Ge, Z. Chai, Z. Liu, K. Yang, Radionuclide 131I labeled reduced graphene oxide for nuclear imaging guided combined radio- and photothermal therapy of cancer, Biomaterials, 66 (2015) 21-28.

[41] R. Jin, X. Ji, Y. Yang, H. Wang, A. Cao, Self-Assembled Graphene–Dextran Nanohybrid for Killing Drug-Resistant Cancer Cells, ACS Applied Materials & Interfaces, 5 (2013) 7181-7189.

[42] W. Miao, G. Shim, C.M. Kang, S. Lee, Y.S. Choe, H.-G. Choi, Y.-K. Oh, Cholesteryl hyaluronic acid-coated, reduced graphene oxide nanosheets for anti-cancer drug delivery, Biomaterials, 34 (2013) 9638-9647.

[43] J. Yu, Y.-H. Lin, L. Yang, C.-C. Huang, L. Chen, W.-C. Wang, G.-W. Chen, J. Yan, S. Sawettanun, C.-H. Lin, Improved Anticancer Photothermal Therapy Using the Bystander Effect Enhanced by Antiarrhythmic Peptide Conjugated Dopamine-Modified Reduced Graphene Oxide Nanocomposite, Advanced Healthcare Materials, 6 (2017) 1600804.

[44] Y.-J. Lu, C.-W. Lin, H.-W. Yang, K.-J. Lin, S.-P. Wey, C.-L. Sun, K.-C. Wei, T.-C. Yen, C.-I. Lin, C.-C.M. Ma, J.-P. Chen, Biodistribution of PEGylated graphene oxide nanoribbons and their application in cancer chemo-photothermal therapy, Carbon, 74 (2014) 83-95.

[45] O. Akhavan, E. Ghaderi, H. Emamy, Nontoxic concentrations of PEGylated graphene nanoribbons for selective cancer cell imaging and photothermal therapy, Journal of Materials Chemistry, 22 (2012) 20626-20633.

[46] V. Georgakilas, M. Otyepka, A.B. Bourlinos, V. Chandra, N. Kim, K.C. Kemp, P. Hobza, R. Zboril, K.S. Kim, Functionalization of Graphene: Covalent and Non-Covalent Approaches, Derivatives and Applications, Chemical Reviews, 112 (2012) 6156-6214.

[47] Q. Tang, Z. Zhou, Z. Chen, Graphene-related nanomaterials: tuning properties by functionalization, Nanoscale, 5 (2013) 4541-4583.

[48] T. Kuila, S. Bose, A.K. Mishra, P. Khanra, N.H. Kim, J.H. Lee, Chemical functionalization of graphene and its applications, Progress in Materials Science, 57 (2012) 1061-1105.

[49] T.H. Tran, H.T. Nguyen, T.T. Pham, J.Y. Choi, H.-G. Choi, C.S. Yong, J.O. Kim, Development of a Graphene Oxide Nanocarrier for Dual-Drug Chemo-phototherapy to Overcome Drug Resistance in Cancer, ACS Applied Materials & Interfaces, 7 (2015) 28647-28655.

[50] Z. Sheng, L. Song, J. Zheng, D. Hu, M. He, M. Zheng, G. Gao, P. Gong, P. Zhang, Y. Ma, L. Cai, Protein-assisted fabrication of nano-reduced graphene oxide for combined in vivo photoacoustic imaging and photothermal therapy, Biomaterials, 34 (2013) 5236-5243.

[51] J. Chen, H. Liu, C. Zhao, G. Qin, G. Xi, T. Li, X. Wang, T. Chen, One-step reduction and PEGylation of graphene oxide for photothermally controlled drug delivery, Biomaterials, 35 (2014) 4986-4995.

[52] O. Akhavan, E. Ghaderi, S. Aghayee, Y. Fereydooni, A. Talebi, The use of a glucose-reduced graphene oxide suspension for photothermal cancer therapy, Journal of Materials Chemistry, 22 (2012) 13773-13781.

[53] H. Liu, T. Li, Y. Liu, G. Qin, X. Wang, T. Chen, Glucose-Reduced Graphene Oxide with Excellent Biocompatibility and Photothermal Efficiency as well as Drug Loading, Nanoscale Research Letters, 11 (2016) 211.

[54] C. Bussy, H. Ali-Boucetta, K. Kostarelos, Safety Considerations for Graphene: Lessons Learnt from Carbon Nanotubes, Accounts of Chemical Research, 46 (2013) 692-701.

[55] K. Yang, J. Wan, S. Zhang, Y. Zhang, S.-T. Lee, Z. Liu, In Vivo Pharmacokinetics, Long-Term Biodistribution, and Toxicology of PEGylated Graphene in Mice, ACS Nano, 5 (2011) 516-522.

[56] K. Yang, H. Gong, X. Shi, J. Wan, Y. Zhang, Z. Liu, In vivo biodistribution and toxicology of functionalized nano-graphene oxide in mice after oral and intraperitoneal administration, Biomaterials, 34 (2013) 2787-2795.

[57] S. Zhang, K. Yang, L. Feng, Z. Liu, In vitro and in vivo behaviors of dextran functionalized graphene, Carbon, 49 (2011) 4040-4049.

[58] H.-J. Im, C.G. England, L. Feng, S.A. Graves, R. Hernandez, R.J. Nickles, Z. Liu, D.S. Lee, S.Y. Cho, W. Cai, Accelerated Blood Clearance Phenomenon Reduces the Passive Targeting of PEGylated Nanoparticles in Peripheral Arterial Disease, ACS Applied Materials & Interfaces, 8 (2016) 17955-17963.

[59] N. Luo, J.K. Weber, S. Wang, B. Luan, H. Yue, X. Xi, J. Du, Z. Yang, W. Wei, R. Zhou, G. Ma, PEGylated graphene oxide elicits strong immunological responses despite surface passivation, Nature Communications, 8 (2017) 14537.

[60] A.S. Abu Lila, H. Kiwada, T. Ishida, The accelerated blood clearance (ABC) phenomenon: Clinical challenge and approaches to manage, Journal of Controlled Release, 172 (2013) 38-47.

[61] K.-H. Liao, Y.-S. Lin, C.W. Macosko, C.L. Haynes, Cytotoxicity of Graphene Oxide and Graphene in Human Erythrocytes and Skin Fibroblasts, ACS Applied Materials & Interfaces, 3 (2011) 2607-2615.

[62] C. Cheng, S. Li, S. Nie, W. Zhao, H. Yang, S. Sun, C. Zhao, General and Biomimetic Approach to Biopolymer-Functionalized Graphene Oxide Nanosheet through Adhesive Dopamine, Biomacromolecules, 13 (2012) 4236-4246.

[63] S. Mahanta, S. Paul, Bovine α-lactalbumin functionalized graphene oxide nano-sheet exhibits enhanced biocompatibility: A rational strategy for graphene-based targeted cancer therapy, Colloids and Surfaces B: Biointerfaces, 134 (2015) 178-187.

[64] A.M. Pinto, J.A. Moreira, F.D. Magalhães, I.C. Gonçalves, Polymer surface adsorption as a strategy to improve the biocompatibility of graphene nanoplatelets, Colloids and Surfaces B: Biointerfaces, 146 (2016) 818-824.

[65] S. Kanakia, J.D. Toussaint, S. Mullick Chowdhury, T. Tembulkar, S. Lee, Y.-P. Jiang, R.Z. Lin, K.R. Shroyer, W. Moore, B. Sitharaman, Dose ranging, expanded acute toxicity and safety pharmacology studies for intravenously administered functionalized graphene nanoparticle formulations, Biomaterials, 35 (2014) 7022-7031.

[66] S. Kanakia, J.D. Toussaint, S.M. Chowdhury, G. Lalwani, T. Tembulkar, T. Button, K.R. Shroyer, W. Moore, B. Sitharaman, Physicochemical characterization of a novel graphene-based magnetic resonance imaging contrast agent, International Journal of Nanomedicine, 8 (2013) 2821-2833.

[67] S.K. Hobbs, W.L. Monsky, F. Yuan, W.G. Roberts, L. Griffith, V.P. Torchilin, R.K. Jain, Regulation of transport pathways in tumor vessels: role of tumor type and microenvironment, Proceedings of the National Academy of Sciences, 95 (1998) 4607-4612.

[68] E. Blanco, H. Shen, M. Ferrari, Principles of nanoparticle design for overcoming biological barriers to drug delivery, Nature Biotechnology, 33 (2015) 941-951.

[69] Y. Matsumoto, J.W. Nichols, K. Toh, T. Nomoto, H. Cabral, Y. Miura, R.J. Christie, N. Yamada, T. Ogura, M.R. Kano, Y. Matsumura, N. Nishiyama, T. Yamasoba, Y.H. Bae, K. Kataoka, Vascular bursts enhance permeability of tumour blood vessels and improve nanoparticle delivery, Nature Nanotechnology, 11 (2016) 533-538.

[70] C. Xu, S. Shi, L. Feng, F. Chen, S.A. Graves, E.B. Ehlerding, S. Goel, H. Sun, C.G. England, R.J. Nickles, Z. Liu, T. Wang, W. Cai, Long circulating reduced graphene oxide-iron oxide nanoparticles for efficient tumor targeting and multimodality imaging, Nanoscale, 8 (2016) 12683-12692.

[71] J.T. Robinson, G. Hong, Y. Liang, B. Zhang, O.K. Yaghi, H. Dai, In vivo fluorescence imaging in the second near-infrared window with long circulating carbon nanotubes capable of ultrahigh tumor uptake, Journal of the American Chemical Society, 134 (2012) 10664-10669.

[72] X. Liu, H. Tao, K. Yang, S. Zhang, S.T. Lee, Z. Liu, Optimization of surface chemistry on single-walled carbon nanotubes for in vivo photothermal ablation of tumors, Biomaterials, 32 (2011) 144-151.

[73] L. Feng, K. Li, X. Shi, M. Gao, J. Liu, Z. Liu, Smart pH-Responsive Nanocarriers Based on Nano-Graphene Oxide for Combined Chemo- and Photothermal Therapy Overcoming Drug Resistance, Advanced Healthcare Materials, 3 (2014) 1261-1271.

[74] O. Akhavan, E. Ghaderi, Graphene Nanomesh Promises Extremely Efficient In Vivo Photothermal Therapy, Small, 9 (2013) 3593-3601.

[75] F. Nasrollahi, J. Varshosaz, A.A. Khodadadi, S. Lim, A. Jahanian-Najafabadi, Targeted delivery of docetaxel by use of transferrin/poly (allylamine hydrochloride)-functionalized graphene oxide nanocarrier, ACS Applied Materials & Interfaces, 8 (2016) 13282-13293.

[76] H. Hong, K. Yang, Y. Zhang, J.W. Engle, L. Feng, Y. Yang, T.R. Nayak, S. Goel, J. Bean, C.P. Theuer, T.E. Barnhart, Z. Liu, W. Cai, In Vivo Targeting and Imaging of Tumor Vasculature with Radiolabeled, Antibody-Conjugated Nanographene, ACS Nano, 6 (2012) 2361-2370.

[77] H. Hong, Y. Zhang, J.W. Engle, T.R. Nayak, C.P. Theuer, R.J. Nickles, T.E. Barnhart, W. Cai, In vivo targeting and positron emission tomography imaging of tumor vasculature with 66Ga-labeled nano-graphene, Biomaterials, 33 (2012) 4147-4156.

[78] C. Jang, J.H. Lee, A. Sahu, G. Tae, The synergistic effect of folate and RGD dual ligand of nanographene oxide on tumor targeting and photothermal therapy in vivo, Nanoscale, 7 (2015) 18584-18594.

[79] Y. Guo, H. Xu, Y. Li, F. Wu, Y. Li, Y. Bao, X. Yan, Z. Huang, P. Xu, Hyaluronic acid and Arg-Gly-Asp peptide modified Graphene oxide with dual receptor-targeting function for cancer therapy, Journal of Biomaterials Applications, 32 (2017) 54-65.

[80] J.H. Lee, A. Sahu, C. Jang, G. Tae, The effect of ligand density on in vivo tumor targeting of nanographene oxide, Journal of Controlled Release, 209 (2015) 219-228.

[81] M. Alibolandi, M. Mohammadi, S.M. Taghdisi, M. Ramezani, K. Abnous, Fabrication of aptamer decorated dextran coated nano-graphene oxide for targeted drug delivery, Carbohydrate Polymers, 155 (2017) 218-229.

[82] H. Bao, Y. Pan, Y. Ping, N.G. Sahoo, T. Wu, L. Li, J. Li, L.H. Gan, Chitosan-Functionalized Graphene Oxide as a Nanocarrier for Drug and Gene Delivery, Small, 7 (2011) 1569-1578.

[83] F. Li, S.-J. Park, D. Ling, W. Park, J.Y. Han, K. Na, K. Char, Hyaluronic acid-conjugated graphene oxide/photosensitizer nanohybrids for cancer targeted photodynamic therapy, Journal of Materials Chemistry B, 1 (2013) 1678-1686.

[84] Y. Tao, E. Ju, J. Ren, X. Qu, Immunostimulatory oligonucleotides-loaded cationic graphene oxide with photothermally enhanced immunogenicity for photothermal/immune cancer therapy, Biomaterials, 35 (2014) 9963-9971.

[85] X. Zhao, L. Liu, X. Li, J. Zeng, X. Jia, P. Liu, Biocompatible Graphene Oxide Nanoparticle-Based Drug Delivery Platform for Tumor Microenvironment-Responsive Triggered Release of Doxorubicin, Langmuir, 30 (2014) 10419-10429.

[86] X. Zhao, L. Yang, X. Li, X. Jia, L. Liu, J. Zeng, J. Guo, P. Liu, Functionalized Graphene Oxide Nanoparticles for Cancer Cell-Specific Delivery of Antitumor Drug, Bioconjugate Chemistry, 26 (2015) 128-136.

[87] H. Wen, C. Dong, H. Dong, A. Shen, W. Xia, X. Cai, Y. Song, X. Li, Y. Li, D. Shi, Engineered Redox-Responsive PEG Detachment Mechanism in PEGylated Nano-Graphene Oxide for Intracellular Drug Delivery, Small, 8 (2012) 760-769.

[88] X. Zhao, P. Liu, Biocompatible graphene oxide as a folate receptor-targeting drug delivery system for the controlled release of anti-cancer drugs, RSC Advances, 4 (2014) 24232-24239.

[89] R. Imani, S.H. Emami, S. Faghihi, Synthesis and characterization of an octaarginine functionalized graphene oxide nano-carrier for gene delivery applications, Physical Chemistry Chemical Physics, 17 (2015) 6328-6339.

[90] A.-J. Shen, D.-L. Li, X.-J. Cai, C.-Y. Dong, H.-Q. Dong, H.-Y. Wen, G.-H. Dai, P.-J. Wang, Y.-Y. Li, Multifunctional nanocomposite based on graphene oxide for in vitro hepatocarcinoma diagnosis and treatment, Journal of Biomedical Materials Research Part A, 100 (2012) 2499-2506.

[91] H. Wu, H. Shi, Y. Wang, X. Jia, C. Tang, J. Zhang, S. Yang, Hyaluronic acid conjugated graphene oxide for targeted drug delivery, Carbon, 69 (2014) 379-389.

[92] H. Hu, J. Yu, Y. Li, J. Zhao, H. Dong, Engineering of a novel pluronic F127/graphene nanohybrid for pH responsive drug delivery, Journal of Biomedical Materials Research Part A, 100 (2012) 141-148.

[93] G. Shim, J.-Y. Kim, J. Han, S.W. Chung, S. Lee, Y. Byun, Y.-K. Oh, Reduced graphene oxide nanosheets coated with an anti-angiogenic anticancer low-molecular-weight heparin derivative for delivery of anticancer drugs, Journal of Controlled Release, 189 (2014) 80-89.

[94] F. Bani, M. Adeli, S. Movahedi, M. Sadeghizadeh, Graphene-polyglycerol-curcumin hybrid as a near-infrared (NIR) laser stimuli-responsive system for chemo-photothermal cancer therapy, RSC Advances, 6 (2016) 61141-61149.

[95] K. Liu, J.-J. Zhang, F.-F. Cheng, T.-T. Zheng, C. Wang, J.-J. Zhu, Green and facile synthesis of highly biocompatible graphene nanosheets and its application for cellular imaging and drug delivery, Journal of Materials Chemistry, 21 (2011) 12034-12040.

[96] K. Liu, Y. Wang, H. Li, Y. Duan, A facile one-pot synthesis of starch functionalized graphene as nano-carrier for pH sensitive and starch-mediated drug delivery, Colloids and Surfaces B: Biointerfaces, 128 (2015) 86-93.

[97] J. Liu, S. Guo, L. Han, T. Wang, W. Hong, Y. Liu, E. Wang, Synthesis of phospholipid monolayer membrane functionalized graphene for drug delivery, Journal of Materials Chemistry, 22 (2012) 20634-20640.

[98] S.-H. Hu, R.-H. Fang, Y.-W. Chen, B.-J. Liao, I.W. Chen, S.-Y. Chen, Photoresponsive Protein–Graphene–Protein Hybrid Capsules with Dual Targeted Heat-Triggered Drug Delivery Approach for Enhanced Tumor Therapy, Advanced Functional Materials, 24 (2014) 4144-4155.

[99] Y. Pan, H. Bao, N.G. Sahoo, T. Wu, L. Li, Water-Soluble Poly(N-isopropylacrylamide)–Graphene Sheets Synthesized via Click Chemistry for Drug Delivery, Advanced Functional Materials, 21 (2011) 2754-2763.

[100] J.-W.T. Seo, A.A. Green, A.L. Antaris, M.C. Hersam, High-Concentration Aqueous Dispersions of Graphene Using Nonionic, Biocompatible Block Copolymers, Journal of Physical Chemistry Letters, 2 (2011) 1004-1008.

[101] T. Zhou, B. Zhang, P. Wei, Y. Du, H. Zhou, M. Yu, L. Yan, W. Zhang, G. Nie, C. Chen, Y. Tu, T. Wei, Energy metabolism analysis reveals the mechanism of inhibition of breast cancer cell metastasis by PEG-modified graphene oxide nanosheets, Biomaterials, 35 (2014) 9833-9843.

[102] Y. Chong, C. Ge, Z. Yang, J.A. Garate, Z. Gu, J.K. Weber, J. Liu, R. Zhou, Reduced Cytotoxicity of Graphene Nanosheets Mediated by Blood-Protein Coating, ACS Nano, 9 (2015) 5713-5724.

[103] M. Wojtoniszak, X. Chen, R.J. Kalenczuk, A. Wajda, J. Łapczuk, M. Kurzewski, M. Drozdzik, P.K. Chu, E. Borowiak-Palen, Synthesis, dispersion, and cytocompatibility of graphene oxide and reduced graphene oxide, Colloids and Surfaces B: Biointerfaces, 89 (2012) 79-85.

[104] L. Mu, Y. Gao, X. Hu, l-Cysteine: A biocompatible, breathable and beneficial coating for graphene oxide, Biomaterials, 52 (2015) 301-311.

[105] V.K. Rana, M.-C. Choi, J.-Y. Kong, G.Y. Kim, M.J. Kim, S.-H. Kim, S. Mishra, R.P. Singh, C.-S. Ha, Synthesis and Drug-Delivery Behavior of Chitosan-Functionalized Graphene Oxide Hybrid Nanosheets, Macromolecular Materials and Engineering, 296 (2011) 131-140.

[106] T.L. Moore, R. Podilakrishna, A. Rao, F. Alexis, Systemic Administration of Polymer-Coated Nano-Graphene to Deliver Drugs to Glioblastoma, Particle & Particle Systems Characterization, 31 (2014) 886-894.

[107] N. Rubio, K.-C. Mei, R. Klippstein, P.M. Costa, N. Hodgins, J.T.-W. Wang, F. Festy, V. Abbate, R.C. Hider, K.L.A. Chan, K.T. Al-Jamal, Solvent-Free Click-Mechanochemistry for the Preparation of Cancer Cell Targeting Graphene Oxide, ACS Applied Materials & Interfaces, 7 (2015) 18920-18923.

[108] H. Yang, D.H. Bremner, L. Tao, H. Li, J. Hu, L. Zhu, Carboxymethyl chitosan-mediated synthesis of hyaluronic acid-targeted graphene oxide for cancer drug delivery, Carbohydrate Polymers, 135 (2016) 72-78.

[109] Y. Lu, P. Wu, Y. Yin, H. Zhang, C. Cai, Aptamer-functionalized graphene oxide for highly efficient loading and cancer cell-specific delivery of antitumor drug, Journal of Materials Chemistry B, 2 (2014) 3849-3859.

[110] Q. Pan, Y. Lv, G.R. Williams, L. Tao, H. Yang, H. Li, L. Zhu, Lactobionic acid and carboxymethyl chitosan functionalized graphene oxide nanocomposites as targeted anticancer drug delivery systems, Carbohydrate Polymers, 151 (2016) 812-820.

[111] L. Hou, Q. Feng, Y. Wang, X. Yang, J. Ren, Y. Shi, X. Shan, Y. Yuan, Y. Wang, Z. Zhang, Multifunctional hyaluronic acid modified graphene oxide loaded with mitoxantrone for overcoming drug resistance in cancer, Nanotechnology, 27 (2015) 015701.

[112] H. Zhu, B. Zhou, L. Chan, Y. Du, T. Chen, Transferrin-functionalized nanographene oxide for delivery of platinum complexes to enhance cancer-cell selectivity and apoptosis-inducing efficacy, International Journal of Nanomedicine, 12 (2017) 5023-5038.

[113] C. Wang, B. Chen, M. Zou, G. Cheng, Cyclic RGD-modified chitosan/graphene oxide polymers for drug delivery and cellular imaging, Colloids and Surfaces B: Biointerfaces, 122 (2014) 332-340.

[114] H. Wang, W. Gu, N. Xiao, L. Ye, Q. Xu, Chlorotoxin-conjugated graphene oxide for targeted delivery of an anticancer drug, International Journal of Nanomedicine, 9 (2014) 1433-1442.

[115] T. Zhou, X. Zhou, D. Xing, Controlled release of doxorubicin from graphene oxide based charge-reversal nanocarrier, Biomaterials, 35 (2014) 4185-4194.

[116] X.C. Qin, Z.Y. Guo, Z.M. Liu, W. Zhang, M.M. Wan, B.W. Yang, Folic acid-conjugated graphene oxide for cancer targeted chemo-photothermal therapy, Journal of Photochemistry and Photobiology B: Biology, 120 (2013) 156-162.

[117] S. Shi, K. Yang, H. Hong, H.F. Valdovinos, T.R. Nayak, Y. Zhang, C.P. Theuer, T.E. Barnhart, Z. Liu, W. Cai, Tumor vasculature targeting and imaging in living mice with reduced graphene oxide, Biomaterials, 34 (2013) 3002-3009.

[118] J.T. Robinson, S.M. Tabakman, Y. Liang, H. Wang, H. Sanchez Casalongue, D. Vinh, H. Dai, Ultrasmall Reduced Graphene Oxide with High Near-Infrared Absorbance for Photothermal Therapy, Journal of the American Chemical Society, 133 (2011) 6825-6831.

Chapter 4

Research Work 1

D-α-tocopheryl polyethylene glycol 1000 succinate functionalized nanographene oxide for cancer therapy

This chapter is based on the publication entitled: D-α-tocopheryl polyethylene glycol 1000 succinate functionalized nanographene oxide for cancer therapy, Nanomedicine (Lond), 2017, 12(5):443-456.

4.1. Abstract

Aim: Evaluate the therapeutic capacity of TPGS functionalized nGO in breast cancer cells. **Methods:** TPGS functionalized nGO-based materials were obtained through two different approaches: a simple sonication method and a one-pot hydrothermal treatment. **Results:** TPGS coating successfully improved the stability of the nGO-based materials. The nanomaterials that underwent the hydrothermal procedure generated a 1.4 – 1.6 fold higher temperature variation under NIR laser irradiation than those prepared only by sonication. *In vitro*, the TPGS/nGO derivatives reduced breast cancer cells' viability and had an insignificant effect on healthy cells. Furthermore, the combined application of TPGS/nGO derivatives and NIR light generated an improved therapeutic effect. **Conclusion:** TPGS/nGO derivatives are promising materials for breast cancer phototherapy.

Keywords: breast cancer; nanographene oxide; PEGylated vitamin E; phototherapy; TPGS.

4.2. Introduction

Cancer ablation mediated by nanosized photothermal agents is currently showing promising results in *in vitro* and *in vivo* assays [1]. This therapeutic approach takes advantage of the ability of nanomaterials to accumulate at the tumor site, through passive (using the EPR effect) or active (involving the grafting of targeting ligands) transport, and from the capacity of some nanostructures to mediate a hyperthermic effect by converting optical energy, like NIR light (750-1000 nm), into heat [1]. For therapeutic applications, NIR light is fundamental since it has a good tissue penetration and major biological components (*e.g.* collagen, melanin or water) have minimal absorption within this wavelength range [2], thus assuring limited off-target interactions with this type of radiation [3, 4]. Therefore, nanomaterials designed to be applied in PTT must produce a photothermal effect upon NIR light irradiation. So far, different types of nanostructures such as GNR, CNT, tungsten-based nanomaterials, copper sulfide nanocrystals or GO have revealed this ability [5-10].

nGO is a 2D carbon nanomaterial with oxygen functional groups (carboxyl, hydroxyl and epoxy groups) that possesses NIR absorption [11, 12]. Due to this fact, nGO has been investigated for application in cancer PTT [13, 14]. Moreover, the high versatility of nGO, that is associated with its ability to adsorb different molecules through hydrophobic interactions or π-π stacking, has instigated its use in other cancer-related applications such as drug or protein delivery [15-17]. Independently of the type of biomedical application, nGO must be functionalized with hydrophilic polymers since it has a low colloidal stability, especially in solutions with a high concentration of salts like biological fluids [18]. To overcome such drawback, nGO is often functionalized with PEG through covalent bonds, that are established between the amine groups of amine-terminated PEG and the carboxyl groups of GO [13, 18]. This type of functionalization improves the stability of nGO and is also fundamental to extend the blood circulation time of this nanomaterial, which in turn favors its tumor accumulation [18, 19]. Alternatively, nGO can also be non-covalently PEGylated using amphiphilic molecules such as Pluronic® F-127 [20]. This type of functionalization exploits the hydrophobic interactions that are established between the hydrophobic blocks of the amphiphilic molecules and the aromatic regions of nGO. In the particular case of reduced nGO (usually obtained by treating GO with hydrazine hydrate) and graphene-based materials (*e.g.* obtained through the oxidation and chemical reduction of MWCNT), due to their lack of oxygen functional groups available for conjugation, they have been mostly functionalized with amphiphilic molecules such as C_{18}-PMH-PEG or DSPE-PEG [18, 21, 22]. Moreover, the PEGylation of these two types of materials is also pursued for improving their biocompatibility [22-24]. The application of reduced nGO derivatives and graphene-based materials for cancer PTT is appealing since these materials have a higher NIR absorption than nGO, and consequently produce a higher hyperthermia and an improved therapeutic effect when irradiated with NIR light [18, 22, 24, 25].

From the different and unexplored amphiphilic molecules that can be used to non-covalently functionalize nGO and its reduced derivatives, TPGS (PEGylated Vitamin E) appears to be a promising candidate for heightening the colloidal stability of these nanomaterials. TPGS is a FDA and EMA approved molecule with a broad application in cancer-related topics [26-31]. Due to its amphiphilic character, TPGS has been used in the formulation of amphiphilic micelles or for coating polymeric and inorganic nanomaterials [32-36]. Moreover, TPGS has intrinsic anticancer activity, which renders it with very appealing features for improving the stability of nGO derivatives and to endow them with anticancer activity similar to that of a chemotherapeutic drug [37, 38].

In this work, TPGS was employed to functionalize nGO-based materials using two different approaches: a simple sonication method and a one-pot hydrothermal treatment. The results revealed that the TPGS coating successfully improved the stability of nGO-based materials. Moreover, the nGO materials that underwent the hydrothermal procedure demonstrated an improved NIR absorption, which in turn enhanced their capacity to generate heat under NIR laser irradiation. *In vitro*, the TPGS/nGO derivatives diminished breast cancer cells' viability and had an insignificant effect on healthy cells. This preferential effect towards breast cancer cells can be attributed to TPGS intrinsic anticancer activity. Furthermore, the combined application of TPGS/nGO derivatives and NIR light produced an enhanced therapeutic effect, thereby confirming the potential of these materials for breast cancer phototherapy.

4.3. Materials and Methods

4.3.1. Materials

Dulbecco's Modified Eagle's Medium F-12 (DMEM-F12), ethylenediaminetetraacetate (EDTA), graphite, resazurin, TPGS, and trypsin were acquired from Sigma–Aldrich (Sintra, Portugal). Potassium permanganate was obtained from Acros Organics (Geel, Belgium). Sulfuric acid (H_2SO_4, 96 %) was purchased from Panreac (Darmstadt, Germany). Phosphoric acid (H_3PO_4, 85 %) was acquired from VWR (Carnaxide, Portugal). Michigan Cancer Foundation-7 (MCF-7) cell line was purchased from ATCC (Middlesex, UK). Normal Human Dermal Fibroblasts (NHDF) were obtained from PromoCell (Heidelberg, Germany). FBS was obtained from Biochrom AG (Berlin, Germany). Cell culture plates and T-flasks were acquired from Thermo Fisher Scientific (Porto, Portugal). Water used in all experiments was double deionized (0.22 μm filtered, 18.2 MΩ·cm).

4.3.2. Methods

4.3.2.1. Synthesis of bwGO

Graphite oxide (GrO) was synthesized using a modified version of the improved Hummer's method [39]. In brief, a solution of H_2SO_4/H_3PO_4 (9:1 v/v, 67 mL) was slowly added to a mixture of $KMnO_4$ (3.10 g) and graphite (0.51 g) in an ice bath. This solution was then left to react for 4 days at room temperature (RT) under stirring. Afterward, the reaction was poured into 67 mL of frozen water followed by the addition of H_2O_2 until a yellow colored solution was attained. The product was purified by performing several centrifugations with HCl (3.7 %) and then with water. The gathered material was finally dialyzed against water for 5 days, yielding GrO. Afterward, nanosized base-washed graphene oxide (bwGO) was obtained by washing GrO with a NaOH solution, following a protocol described by Thomas *et al*. [40], and by subjecting the materials to ultrasonication (Vibra-Cell VC600-2, Sonics & Materials, Newtown, USA).

4.3.2.2. Synthesis of TPGS/bwGO

bwGO was non-covalently functionalized with TPGS by sonication, according to methodologies previously described in the literature [18, 41]. In brief, an aqueous solution of bwGO (0.2 mg mL^{-1}; 1 mL) was mixed with TPGS (3 mg) and sonicated for 1 h (Branson 5800, Branson Ultrasonics, Danbury, USA). Afterward, the solution was dialyzed using a dialysis membrane (14 kDa molecular weight cut-off) against water for 3.5 h to remove non-bound TPGS. The solution was then centrifuged and the supernatant was recovered to remove any aggregates, yielding TPGS functionalized bwGO (TPGS/bwGO). The concentration of bwGO in TPGS/bwGO was determined by using a mass extinction coefficient of 3.01 L g^{-1} cm^{-1} at 808 nm. The amount of TPGS incorporated in TPGS/bwGO was calculated by analyzing the UV-Vis-NIR absorption spectrum of this compound and by using the following equation:

$$Abs_{TPGS/bwGO\ at\ 285\ nm} = Abs_{bwGO\ at\ 285\ nm} + Abs_{TPGS\ at\ 285\ nm}$$

First, the concentration of bwGO in the TPGS/bwGO solution was determined by performing a standard curve of bwGO at 808 nm (please note that TPGS does not absorb at this wavelength). Afterwards, the determined concentration of bwGO and the standard curve of bwGO at 285 nm were employed to find the absorbance of bwGO at this wavelength. Subsequently, the determined absorbance of bwGO was subtracted to that of TPGS/bwGO, yielding the absorbance of TPGS (at 285 nm). Finally, the absorbance of TPGS at 285 nm was used to determine its concentration using a standard curve of TPGS (at 285 nm). The gathered data revealed that 15.8 ± 1.0 µg of TPGS were incorporated per each µg of bwGO.

4.3.2.3. Synthesis of TPGS/htGO

bwGO was also reduced and functionalized with TPGS through a one-pot hydrothermal treatment according to a methodology previously described in the literature [42]. In brief, an aqueous solution of bwGO (0.2 mg mL^{-1}; 1 mL) was mixed with TPGS (3 mg) and placed in an oil-bath at 80 °C, for 24 h. Afterward, the solution was left to cool at RT and then dialyzed and centrifuged using the procedure described above for TPGS/bwGO. The supernatant was then recovered yielding TPGS functionalized hydrothermal treated GO (TPGS/htGO). The concentration of htGO in TPGS/htGO was determined by using a mass extinction coefficient of 5.64 L g^{-1} cm^{-1} at 808 nm. Non-coated htGO was produced using a similar procedure, but without adding TPGS.

The presence of TPGS in the hydrothermal procedure affects the extent of the reduction of htGO. Due to that, a standard curve of htGO can not be used for determining the concentration of TPGS in TPGS/htGO since the obtained values would be underestimated. To accomplish that, solutions of as-prepared TPGS/htGO (*i.e.*, that were not subject to dialysis or centrifugation) at different concentrations were used to obtain the standard curve of this material at 285 nm (please note that in this case the exact amount of TPGS and htGO are known since the samples were not purified). Afterwards, the absorbance of TPGS at 285 nm was subtracted to that of as-prepared TPGS/htGO (at 285 nm), yielding the absorbance of htGO. Subsequently, the standard curve of htGO (referred from now on as htGO*) at this wavelength was performed. The amount of TPGS incorporated in TPGS/htGO was then calculated by analyzing the UV-Vis-NIR absorption spectrum of this compound and through the following equation:

$$Abs_{TPGS/htGO\ at\ 285\ nm} = Abs_{htGO\ at\ 285\ nm} + Abs_{TPGS\ at\ 285\ nm}$$

To do so, the concentration of htGO in the TPGS/htGO solution was determined by using a standard curve of as-prepared TPGS/htGO at 808 nm (please note that TPGS does not have absorption at this wavelength). The determined concentration of htGO and the standard curve of htGO* at 285 nm were employed to find the absorbance of htGO at 285 nm. Subsequently, the determined absorbance of htGO at 285 nm was subtracted to that of TPGS/htGO, yielding the absorbance of TPGS. Finally, the absorbance of TPGS at 285 nm was used to determine its concentration using a standard curve of TPGS. The gathered data revealed that 26.8 ± 0.7 μg of TPGS were incorporated per each μg of htGO.

4.3.2.4. Characterization of GrO and nGO-based materials

The interlayer spacing of GrO and graphite was characterized by X-ray Diffraction (XRD) analysis in a Rigaku Geigger Flex D-max III/c diffractometer (Rigaku Americas Corporations, Woodlands, USA), equipped with a copper tube, over the range of 2θ from 5 to 90 °. The carbon to oxygen ratio of GrO, bwGO and htGO was characterized by Energy-dispersive X-ray spectroscopy (EDS) using a XFlash Detector 5010 (Bruker, Karlsruhe, Germany). The different chemical bonds present in GrO, bwGO and htGO were identified by Fourier transform infrared spectroscopy (FTIR) using a Nicolet iS10 spectrometer (Thermo Scientific Inc., Waltham, USA) with a spectral width ranging from 4000 to 600 cm^{-1}. FTIR characterization was also employed to confirm the TPGS functionalization through the analysis of the chemical bonds present in the spectra of TPGS/nGO derivatives. The suitability and efficacy of the TPGS functionalization were also confirmed by dynamic light scattering (DLS) using a Zetasizer Nano ZS (Malvern Instruments, Worcestershire, UK) at a scattering angle of 173 °. The nanosized dimensions of TPGS/nGO derivatives were assessed by transmission electron microscopy (TEM, HT7700, Hitachi, Japan) using an accelerating voltage of 100 kV, after staining the samples with phosphotungstic acid (2 %, w/v). To determine the potential of the different nGO-derivatives to be applied in cancer PTT, their UV-Vis-NIR absorption spectra were acquired on an Evolution 201 spectrophotometer (Thermo Scientific Inc., Waltham, USA) over the wavelength range from 200 to 1000 nm. Moreover, the photothermal efficiency of TPGS/bwGO and TPGS/htGO derivatives was determined by exposing these nanomaterials to NIR laser irradiation (808 nm, 1.7 W cm^{-2}) over 5 min and recording the temperature variations using a thermocouple thermometer.

4.3.2.5. Evaluation of the cytotoxic profile of non-functionalized nGO derivatives

The biocompatibility of the non-functionalized nGO derivatives was evaluated by the resazurin assay as previously described [43]. To do so, NHDF or MCF-7 cells (1 x 10^4 cells/well) were seeded on 96-well plates and cultured in DMEM-F12 medium supplemented with 10 % of FBS and 1 % of penicillin/streptomycin in a humidified incubator (37 °C, 5 % CO_2) [44]. After 24 h, the medium was removed and cells were incubated with medium containing bwGO or htGO at different concentrations (1 – 100 μg mL^{-1} of GO equivalents) for 24 and 48 h. After incubation, the medium was replaced with fresh medium containing resazurin (10 % v/v) and then cells were incubated for 4 h in the dark (37 °C, 5 % CO_2). Cells incubated only with medium (without nGO derivatives) and cells treated with ethanol (70 %) were used as negative (K^-) and positive (K^+) controls, respectively. Cells' viability was determined by analyzing the fluorescence of resorufin (λ_{ex} = 560 nm; λ_{em} = 590 nm) in a Spectramax Gemini EM spectrofluorometer (Molecular Devices LLC, Sunnyvale, USA).

4.3.2.6. Evaluation of the cytotoxic effect of TPGS/nGO derivatives

The cytotoxic effect of TPGS and TPGS/nGO derivatives to NHDF and MCF-7 cells was evaluated using the resazurin assay [44]. In brief, NHDF or MCF-7 cells were seeded in 96-well plates at a density of 1 x 10^4 cells/well. After 24 h, the medium was exchanged and cells were incubated with fresh medium containing TPGS, TPGS/bwGO or TPGS/htGO at different concentrations (TPGS: 0.1 – 40 μM; TPGS/bwGO and TPGS/htGO: 0.1 – 10 μg mL^{-1} of GO equivalents) for 24 and 48 h. Cells' viability was then determined by the resazurin assay as described above.

4.3.2.7. Evaluation of the phototherapeutic effect mediated by TPGS/nGO derivatives

The phototherapeutic capacity of TPGS/nGO derivatives was determined as previously described in the literature [45]. In brief, MCF-7 cells were sub-cultured in 96-well plates at a density of 1 x 10^4 cells/well. After 24 h, the medium was exchanged and cells were incubated with fresh medium containing bwGO, htGO, TPGS/bwGO or TPGS/htGO at different concentrations (6.25 and 10 μg mL^{-1} of GO equivalents) for 24 h. Afterward, cells were irradiated with NIR light (808 nm, 1.7 W cm^{-2}) during 5 min. Cancer cells' viability was determined by following the resazurin protocol described above.

4.3.2.8. Calcein-AM and trypan blue stainings

Calcein-AM (labels live cells) staining was performed to confirm the phototherapeutic efficacy of TPGS/nGO derivatives. In brief, 3 x 10^4 MCF-7 cells/well were seeded in μ-slide 8-well imaging plates (Ibidi GmbH, Munich, Germany). On the following day, the medium was exchanged and cells were incubated with fresh medium containing bwGO, htGO, TPGS/bwGO or TPGS/htGO for 24 h. Afterward, cells were irradiated with NIR light (808 nm, 1.7 W cm^{-2}) during 5 min. Then, the medium was removed, cells were rinsed with PBS and incubated with Calcein-AM (2 μM). Subsequently, cells were rinsed with PBS and fixed in paraformaldehyde 4 % (15 min, RT). Imaging experiments were performed in a Zeiss Axio Observer Z1 (Carl Zeiss AG, Oberkochen, Germany) under a 10x objective using an excitation λ of 470 ± 20 nm and an emission λ of 525 ± 25 nm.

Trypan blue (labels dead cells) staining was also performed to assess the phototherapeutic capacity of TPGS/nGO derivatives. Briefly, after the laser irradiation step, cells were rinsed with PBS and then incubated with trypan blue (0.2 % (w/v)). Afterward, cells were rinsed, fixed and images were collected in an Olympus CX41 inverted optical microscope equipped with an Olympus SP-500 UZ digital camera.

4.3.2.9. Statistical analysis

One-way analysis of variance (ANOVA) with the Student-Newman-Keuls test was used for multiple groups comparison. A *p* value lower than 0.05 ($p < 0.05$) was considered statistically significant. GraphPad Prism v6.0 (Trial version, GraphPad Software, San Diego, USA) was used for data analysis.

4.4. Results and discussion

4.4.1. Preparation and characterization of GrO

The successful synthesis of GrO was confirmed by XRD, FTIR, UV-Vis and EDS analysis (Figure 4.1).

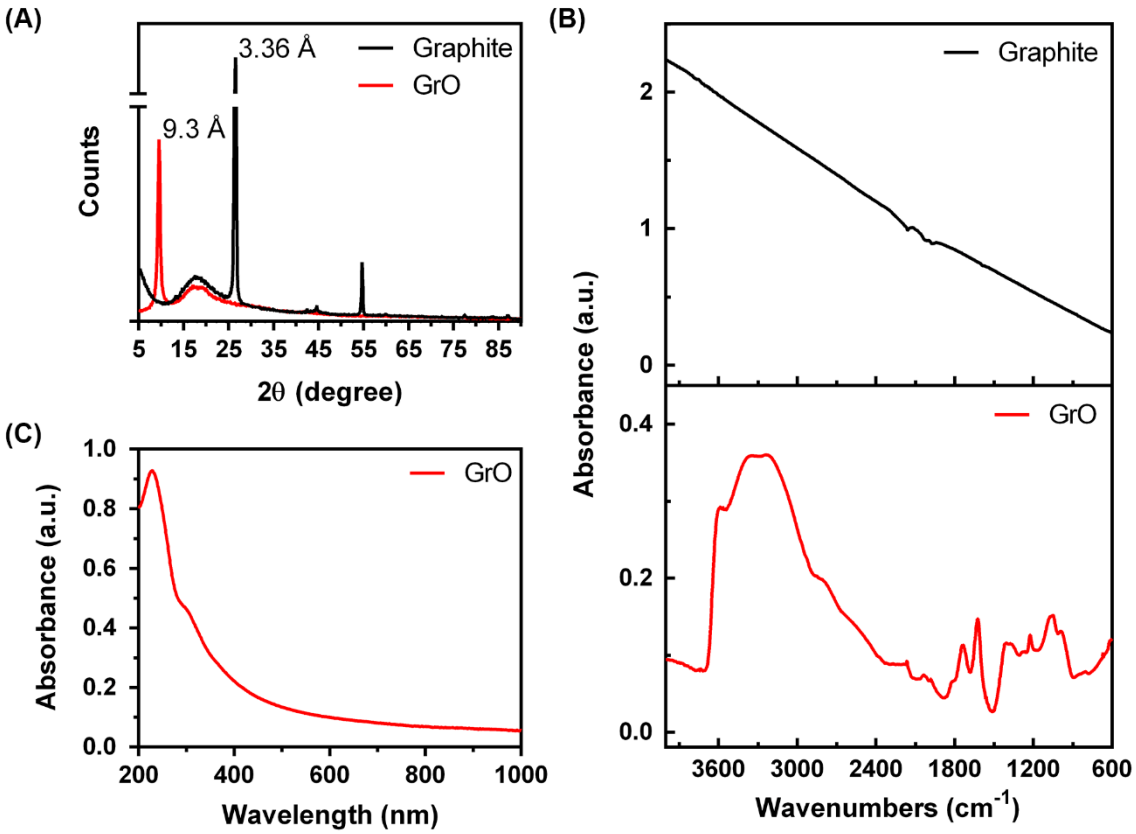

Figure 4.1. Characterization of GrO. XRD (A) and FTIR (B) spectra of GrO and graphite. UV-Vis-NIR absorption spectrum of GrO (C).

XRD spectrum of graphite (GrO precursor) showed its characteristic peak at 2Θ = 26.5 ° (Figure 4.1A). After the chemical oxidation, a product with a diffraction peak of 2Θ = 9.55 ° was obtained (Figure 4.1A). This result demonstrates the introduction of oxygen groups in graphite since the interlayer space increased to approx. 9.3 Å. As importantly, the absence of graphite diffraction peaks in GrO spectrum indicates that the final product does not have un-oxidized graphite. FTIR analysis demonstrated that GrO has different types of oxygen functional groups (hydroxyl, carboxyl and epoxy), further corroborating the successful oxidation of graphite (Figure 4.1B). EDS analysis of GrO revealed that this material has a carbon:oxygen (C:O) ratio of 61:39. Finally, the characteristic absorbance peak of GrO was also present in the absorption spectrum of GrO (λ_{max}= 229 nm) (Figure 4.1C). These results are in agreement with literature reports and together these confirm the successful synthesis of GrO [39].

4.4.2. Preparation and characterization of TPGS/nGO derivatives

Subsequently, GrO was base-washed in order to remove the oxidation debris since it can improve the adsorption of molecules, like TPGS, on the surface of GO [40, 46, 47]. Then, the obtained material was subjected to ultrasonication, yielding nanosized bwGO.

Two different approaches were used to produce bwGO derivatives functionalized with TPGS (Figure 4.2A). In the first approach, bwGO was functionalized with TPGS using a simple sonication method (TPGS/bwGO) (Figure 4.2A). The binding of TPGS to bwGO was confirmed through FTIR analysis. Prior to functionalization, the bwGO FTIR spectrum shows various peaks at ≈ 3270 cm^{-1} (O-H stretch), 1730 cm^{-1} (C=O stretch), and 1041 cm^{-1} (C-O stretch) that belong to the different oxygen functional groups present on this material (see Figure 4.2B for further details). In turn, the FTIR spectrum of TPGS/bwGO displayed peaks with an increased intensity at 2884 cm^{-1} (C-H stretch), 1737 cm^{-1} (C=O stretch) and 1105 cm^{-1} (C-O stretch) (Figure 4.2B). Such peaks can be attributed to the chemical bonds present in TPGS (Figure 4.3A) and also confirm that bwGO was functionalized with TPGS.

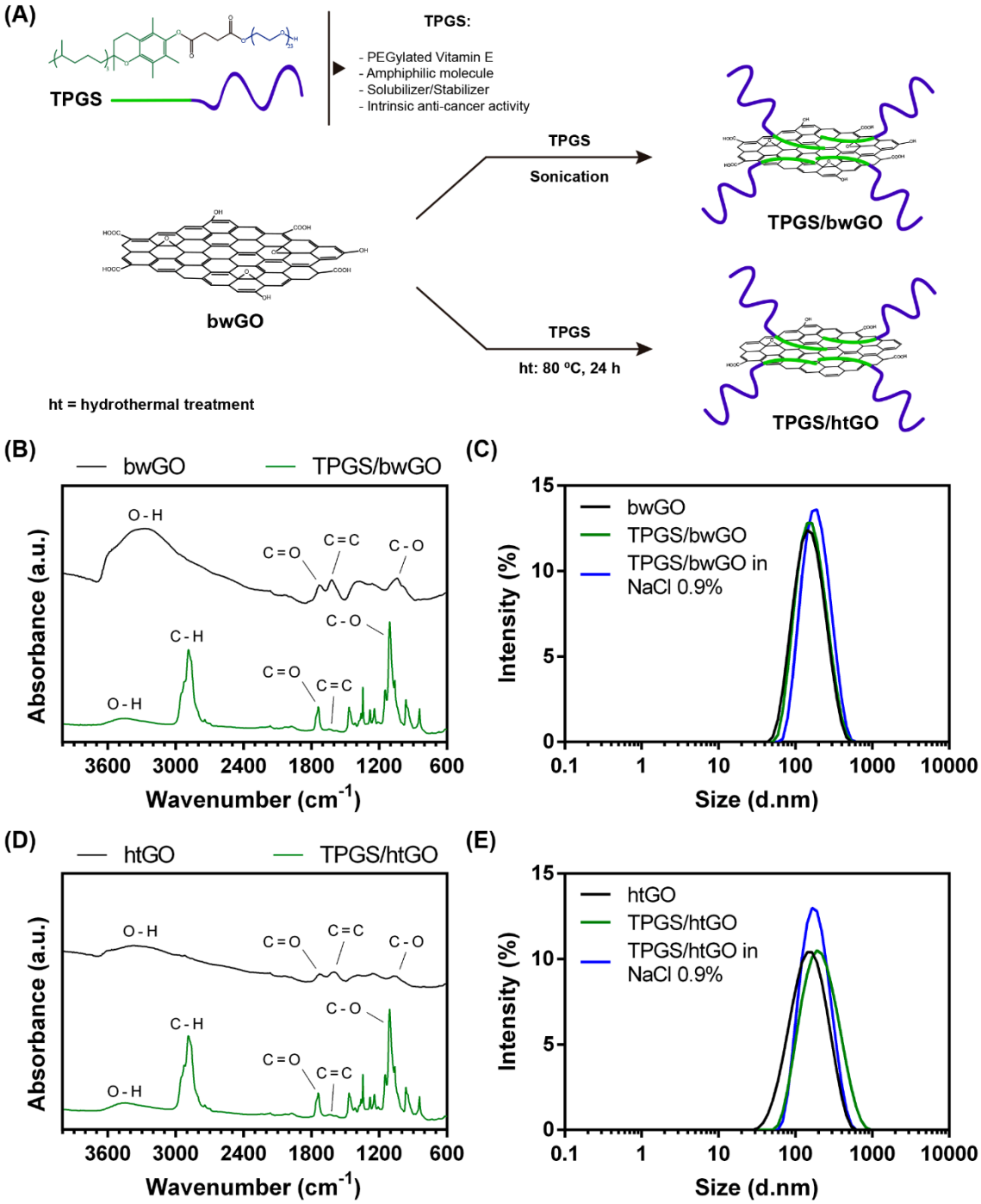

Figure 4.2. Preparation and characterization of TPGS/nGO derivatives. Schematic illustration of the method used for preparing TPGS/bwGO and TPGS/htGO (A). FTIR spectra of bwGO and TPGS/bwGO (B). DLS size distribution of bwGO, TPGS/bwGO, and TPGS/bwGO in saline solution (NaCl 0.9 %) (C). FTIR spectra of htGO and TPGS/htGO (D). DLS size distribution of htGO, TPGS/htGO, and TPGS/htGO in saline solution (NaCl 0.9 %) (E).

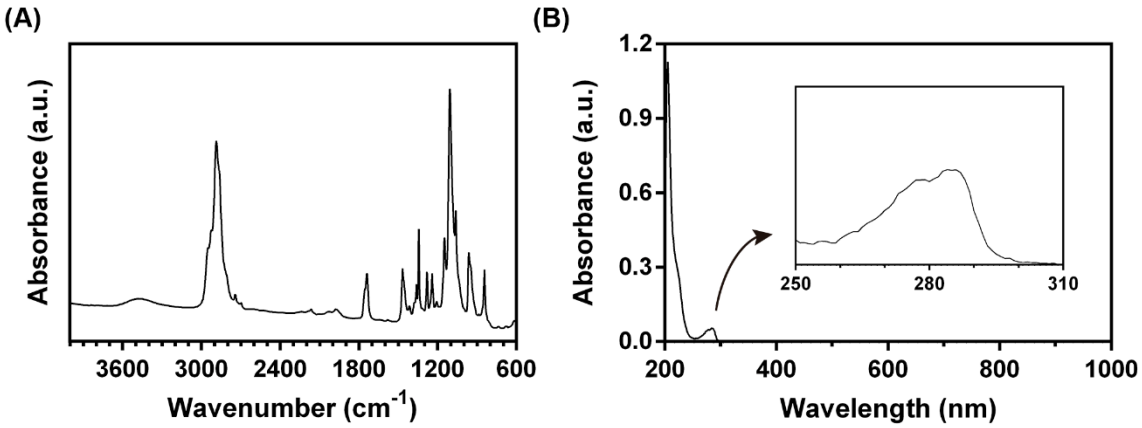

Figure 4.3. TPGS characterization. FTIR spectra of TPGS (A). Peaks observed at 2884, 1737 and 1105 cm^{-1} are attributed to C-H, C=O and C-O stretches, respectively. Absorption spectra of TPGS (B). An absorption peak at 260 – 300 nm is observed (inset).

DLS results indicate that the TPGS functionalization did not affect the size of the nanostructures since bwGO and TPGS/bwGO reveal a similar size distribution (Figure 4.2C). To further assess the suitability of the TPGS coating, DLS analysis of bwGO and TPGS/bwGO in NaCl 0.9 % (that was used as a model saline solution) was also performed. As expected, bwGO promptly precipitated in NaCl 0.9 % (Figure 4.4), which is in agreement with the poor colloidal stability of nGO derivatives in saline solutions [18].

Figure 4.4. Macroscopic images of bwGO, htGO, TPGS/bwGO, and TPGS/htGO in water, NaCl 0.9 % and serum supplemented medium (DMEM-F12 supplemented with FBS (10 %, (v/v)) taken over the course of 5 days (end-point of the study). bwGO and htGO promptly precipitated in NaCl 0.9 %. TPGS/bwGO precipitated in NaCl 0.9 % after an incubation period of 12 h.

In contrast, TPGS/bwGO demonstrated a similar size distribution, without any signs of aggregation, when immersed in NaCl 0.9 % or in water (Figures 4.2C and 4.4). TPGS/bwGO remained stable in NaCl 0.9 % during 12 h and maintained its stability in water and in serum supplemented medium up to 5 days (Figure 4.4). Such findings also attest the successful functionalization of bwGO with TPGS and ensure the applicability of TPGS/bwGO in subsequent experiments. TEM characterization was then performed to confirm the lateral dimensions of TPGS/bwGO since DLS analysis cannot be used to estimate with confidence the precise dimensions of non-spherical materials. The results revealed that TPGS/bwGO has an average lateral size of 53 nm, which is crucial for its application in cancer-related topics (Figure 4.5A-5B). Moreover, bwGO and TPGS/bwGO displayed a zeta potential of -56.2 ± 1.1 and -22.5 ± 1.1 mV, respectively. The zeta potential value obtained for TPGS/bwGO is in agreement with those previously published in the literature for TPGS-based nanomedicines [32, 48].

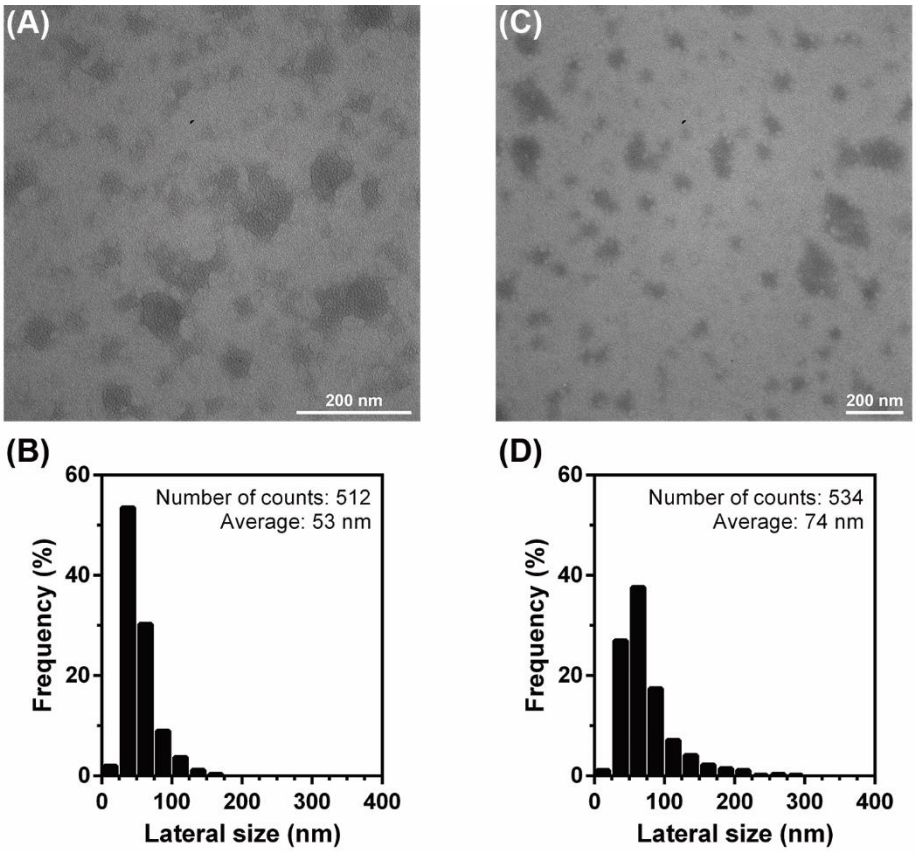

Figure 4.5. Size distribution of TPGS/nGO derivatives. TEM images of TPGS/bwGO (A) and TPGS/htGO (C). Prior to the analysis samples were stained with phosphotungstic acid (2 %, w/v). More than 500 nanostructures were measured for each sample in TEM images. Lateral size distribution of TPGS/bwGO (B) and TPGS/htGO (D).

Finally, the 260 – 300 nm peak observed in the UV-Vis-NIR spectrum of TPGS/bwGO also supports the presence of TPGS in this material (Figures 4.6A and 4.3B). Moreover, the UV-Vis-NIR absorption spectra of TPGS/bwGO and bwGO were similar for higher wavelengths (Figure 4.6A), indicating that bwGO functionalization with TPGS did not affect its NIR absorption, which is crucial for its application in cancer PTT.

To improve the NIR absorption of bwGO, this nanomaterial was reduced by a hydrothermal treatment (24 h at 80 °C), yielding hydrothermal treated GO (htGO). The hydrothermal treatment produced a prominent decrease in the intensity of the oxygen functional groups of htGO when compared to bwGO (Figure 4.2D) and also increased the zeta potential of the nanosheets to -44.7 ± 2.1 mV. The EDS analysis revealed that bwGO and htGO have a carbon to oxygen ratio of 65:35 and 68:32, respectively. Together these results confirm the reductive capacity of the hydrothermal treatment. Moreover, htGO displayed a higher UV-Vis-NIR absorption than bwGO (on average a 2.4-fold higher absorption at 808 nm), thus confirming the suitability of this method to improve the NIR absorption of bwGO (Figures 4.6A), as previously described by Chen and co-workers [42].

Furthermore, the hydrothermal treatment was also applied to reduce bwGO and non-covalently functionalize it with TPGS (TPGS/htGO) by a one-pot approach (Figure 4.2A). Similar to TPGS/bwGO, the FTIR (Figures 4.2D and 4.3A), DLS (Figure 4.2E), and UV-Vis-NIR (Figures 4.6A and 4.3B) analysis of TPGS/htGO also confirmed the suitability and the efficacy of the TPGS functionalization. Interestingly, TPGS/htGO maintained its stability in water, NaCl 0.9 % and serum supplemented medium during 5 days, which may be correlated with the higher capacity of htGO to adsorb TPGS (Figure 4.4). Moreover, the TEM characterization revealed that TPGS/htGO has an average lateral size of 74 nm, rendering it suitable to be applied in cancer therapy (Figure 4.5C-5D). The zeta potential of TPGS/htGO (-23.0 ± 2.7 mV) was also similar to that of TPGS/bwGO. However, the NIR absorption displayed by TPGS/htGO was lower than that of htGO, which implies that the inclusion of TPGS in the hydrothermal treatment affects the reduction process of bwGO (Figure 4.6A). Nevertheless, TPGS/htGO demonstrated on average a 1.9-fold higher absorption at 808 nm than TPGS/bwGO (Figure 4.6B). Since a 808 nm laser light will be employed in photothermal studies to irradiate the TPGS/nGO derivatives, TPGS/htGO may produce an enhanced temperature variation under NIR irradiation and consequently an improved therapeutic outcome due to its higher NIR absorption.

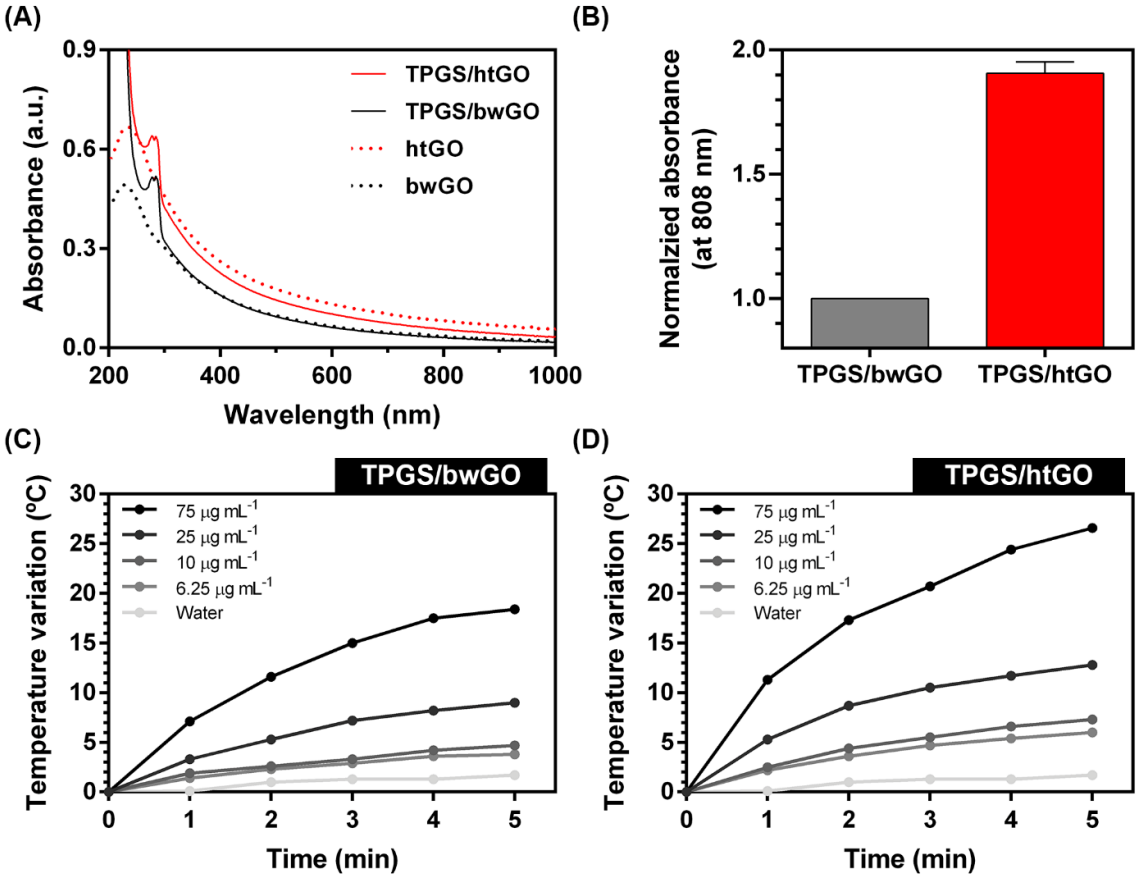

Figure 4.6. Photothermal capacity of TPGS/nGO derivatives. UV-Vis-NIR absorption spectra of bwGO, htGO, TPGS/bwGO, and TPGS/htGO at a concentration of 10 μg mL^{-1} (of GO equivalents) (A). Absorbance of TPGS/htGO at 808 nm normalized to that of TPGS/bwGO at the same wavelength (data represent mean ± SD, n = 4) (B). Temperature variation curves of TPGS/bwGO solutions at different concentrations (of bwGO) during 5 min of NIR irradiation (808 nm, 1.7 W cm^{-2}) (n = 1) (C). Temperature variation curves of TPGS/htGO solutions at different concentrations (of htGO) during 5 min of NIR irradiation (808 nm, 1.7 W cm^{-2}) (n = 1) (D).

4.4.3. Evaluation of the photothermal capacity of TPGS/nGO derivatives

After confirming the NIR absorption of TPGS/bwGO and TPGS/htGO, the photothermal ability of these materials was investigated by recording the temperature changes upon NIR laser irradiation. Both TPGS/nGO derivatives produced a dose-dependent temperature variation under NIR laser irradiation (Figures 4.6C-6D). At the highest concentration tested (75 μg mL^{-1} of GO equivalents) and after 5 min of laser irradiation, TPGS/bwGO and TPGS/htGO produced a temperature variation of about 18 and 27 °C, respectively (Figures 4.6C-6D). Such temperature increase can lead to cancer cells death through diverse mechanisms including dysfunction of mitochondrial and enzymatic functions, protein denaturation and disruption of

cells' membrane [49]. In turn, at the lowest concentration (6.25 μg mL^{-1} of GO equivalents) the photoinduced heat produced by both TPGS/nGO derivatives (ΔT ≈ 4 – 6 °C) can still damage cancer cells by compromising DNA repair mechanisms, altering cellular metabolism and increasing the sensitivity of cancer cells to anticancer agents (Figures 4.6C-6D) [49]. In these experiments, water was used as the control and it demonstrated a negligible response to NIR light during the irradiation period (Figures 4.6C-6D). Such findings attest the photothermal potential of the TPGS/nGO derivatives.

In general, TPGS/htGO generated a photoinduced heat 1.4 – 1.6 times higher than TPGS/bwGO (Figure 4.7). The enhanced photothermal conversion of TPGS/htGO is correlated with its higher NIR absorption and proves the utility of the hydrothermal treatment to improve the PTT capacity of nGO derivatives.

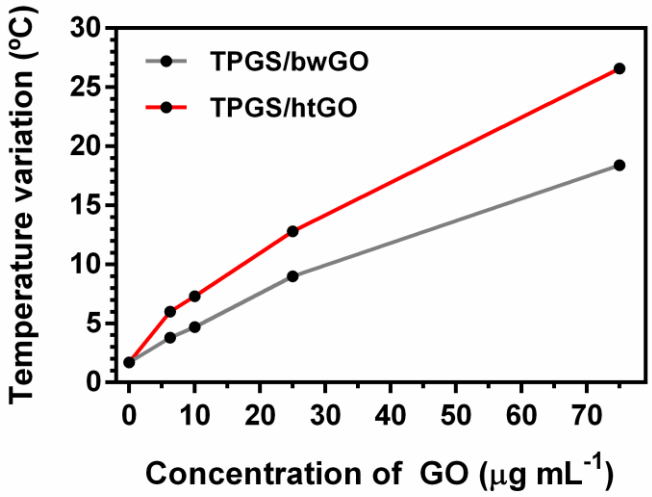

Figure 4.7. Temperature variation induced by different concentrations of TPGS/bwGO and TPGS/htGO, after 5 min of laser irradiation (808 nm, 1.7 W cm^{-2}).

Even though the applied hydrothermal treatment is not as effective as hydrazine hydrate-based treatments for obtaining nGO derivatives with an improved photothermal capacity, this method is a greener route since it does not employ hazardous and highly toxic chemicals [18]. Moreover, reductions based on hydrazine hydrate generally do not support one-pot approaches. As a consequence, first the nGO derivatives must be reduced and purified, followed by functionalization and new purification steps [18]. These facts emphasize the simplicity and convenience of the one-pot hydrothermal functionalization and reduction herein applied.

4.4.4. Evaluation of nGO derivatives' biocompatibility

Before assessing the biological performance of TPGS/nGO derivatives, the biocompatibility of the non-coated materials was evaluated by using NHDF and MCF-7 cells as healthy and breast cancer models, respectively. The results revealed that NHDF treated with bwGO and htGO up to 100 μg mL^{-1} display a viability superior to 92 % (Figures 4.8A-8B), which suggests the excellent biocompatibility of these materials within the tested concentration range (1 – 100 μg mL^{-1}) in healthy cells.

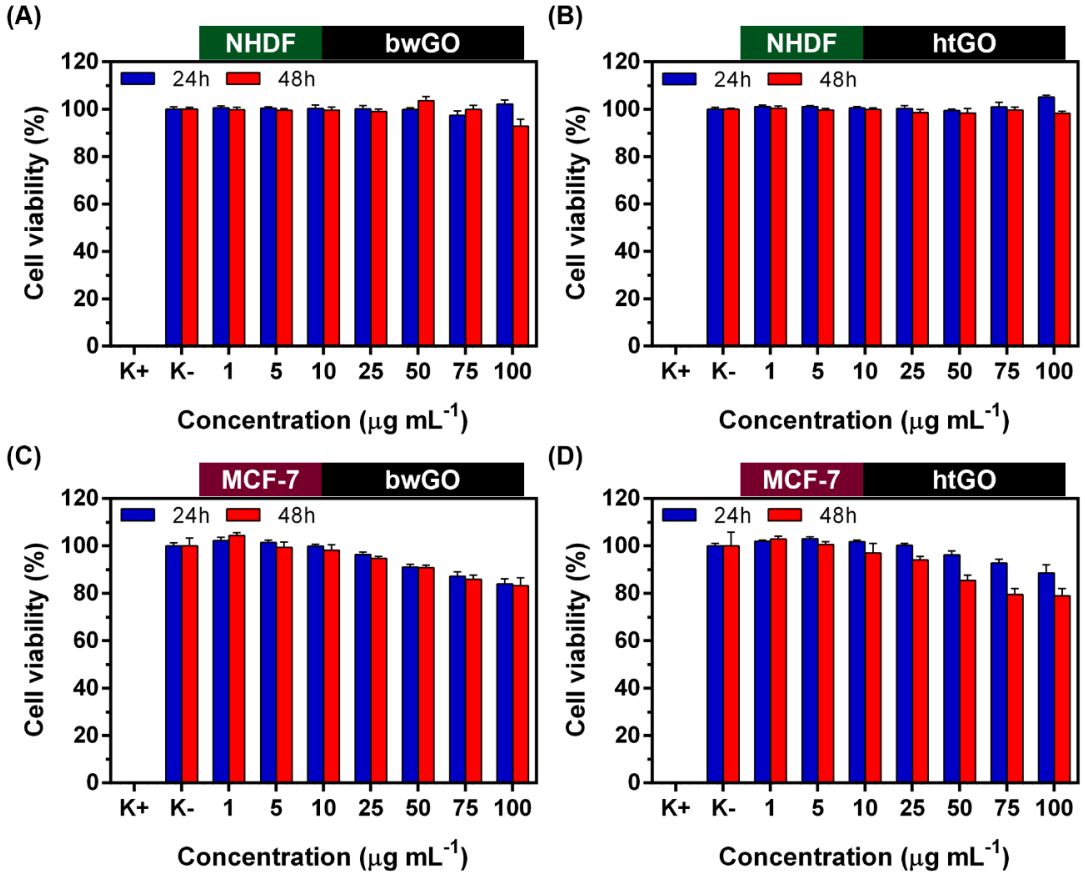

Figure 4.8. Evaluation of the biocompatible profile of bwGO (A) and htGO (B) at different concentrations and incubation periods in NHDF. The biocompatibility of bwGO (C) and htGO (D) in MCF-7 cells was also determined in the same experimental conditions. Data represent mean ± SD, n = 5. K^- and K^+ represent the negative and positive controls, respectively.

A dose-dependent variation in the viability of MCF-7 cells was noticed (Figures 4.8C-8D). Nevertheless, MCF-7 cells incubated with both materials up to 100 μg mL^{-1} demonstrated a viability above 78 %, which also indicates that these nanomaterials are biocompatible within the tested dose (Figures 4.8C-8D). Moreover, both materials did not induce modifications on

cells' morphology during the tested periods, thereby corroborating the cell viability results (Figure 4.9).

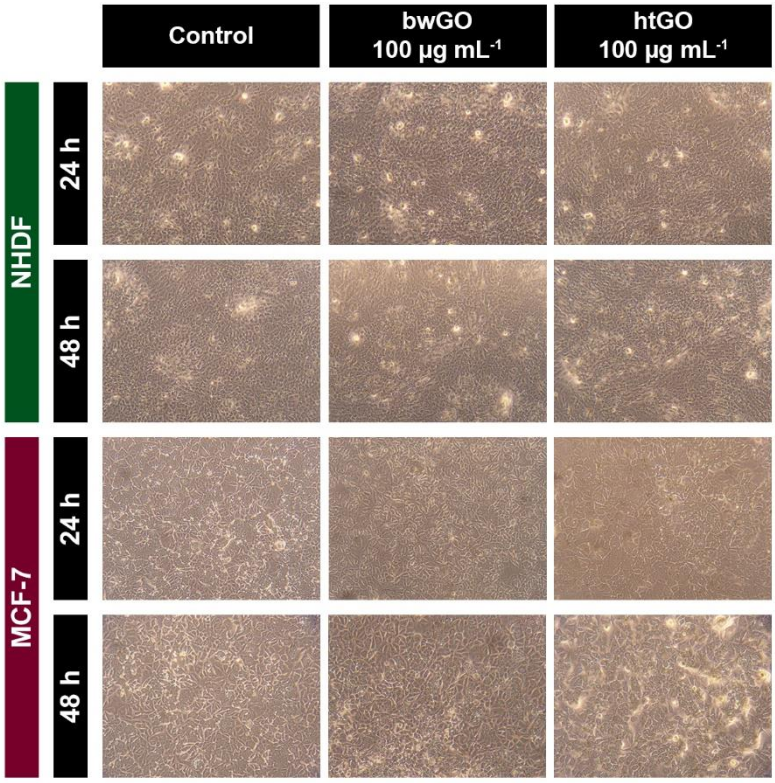

Figure 4.9. Optical microscopic images of NHDF and MCF-7 cells after different incubation periods (24 and 48 h) with bwGO and htGO (100 µg mL^{-1}). Non-treated cells were denoted as the control.

The potential biocompatibility or toxicity of GO-based materials depends strongly on the lateral dimensions, chemical composition and surface chemistry of the nanosheets [50-52]. Akhavan and co-workers demonstrated that ultra-small rGO-based materials (average lateral dimension of 11 nm) prepared using hydrazine hydrate induce a higher toxicity to human mesenchymal stem cells (hMSCs) than their equivalents with bigger dimensions [52]. In a different work, Zhang and co-workers verified that small sized GO (average lateral size of 34 nm and 147 nm), which has a similar size to that of bwGO and htGO, induces few alterations to human cervical cancer cells (HeLa) when compared to 206 nm sized GO [53]. Chang *et al*. demonstrated the biocompatible profile of GO with different lateral sizes in non-small cell lung cancer cells (A549) up to 100 µg mL^{-1} [54]. Recently, Pattammattel *et al*. reported that human embryonic kidney cells (HEK 293T) incubated with 75 and 100 µg mL^{-1} of bwGO for 24 h, display a viability of about 90 and 68 %, respectively, which is also in line with our results considering that the biocompatibility of GO-based materials depends on multiple factors [50, 55]. The slightly lower biocompatibility determined for htGO (in MCF-7 cells) is also in agreement with the results

available in literature since rGO-based materials (particularly those prepared using hydrazine hydrate) may display a weaker biocompatible profile [51, 56, 57].

4.4.5. Evaluation of TPGS/nGO derivatives' anticancer activity

After confirming the biocompatibility of the non-coated materials, the possible anticancer potential of the TPGS/nGO derivatives mediated by TPGS activity was also evaluated in NHDF and MCF-7 cells. As can be observed in Figures 4.10A-10B and 4.11, TPGS/bwGO and TPGS/htGO, at the tested concentrations (0.1 – 10 μg mL^{-1} of GO equivalents), did not induce any significant alterations in NHDF cellular viability and morphology after an incubation period of 24 or 48 h (viability > 88 %).

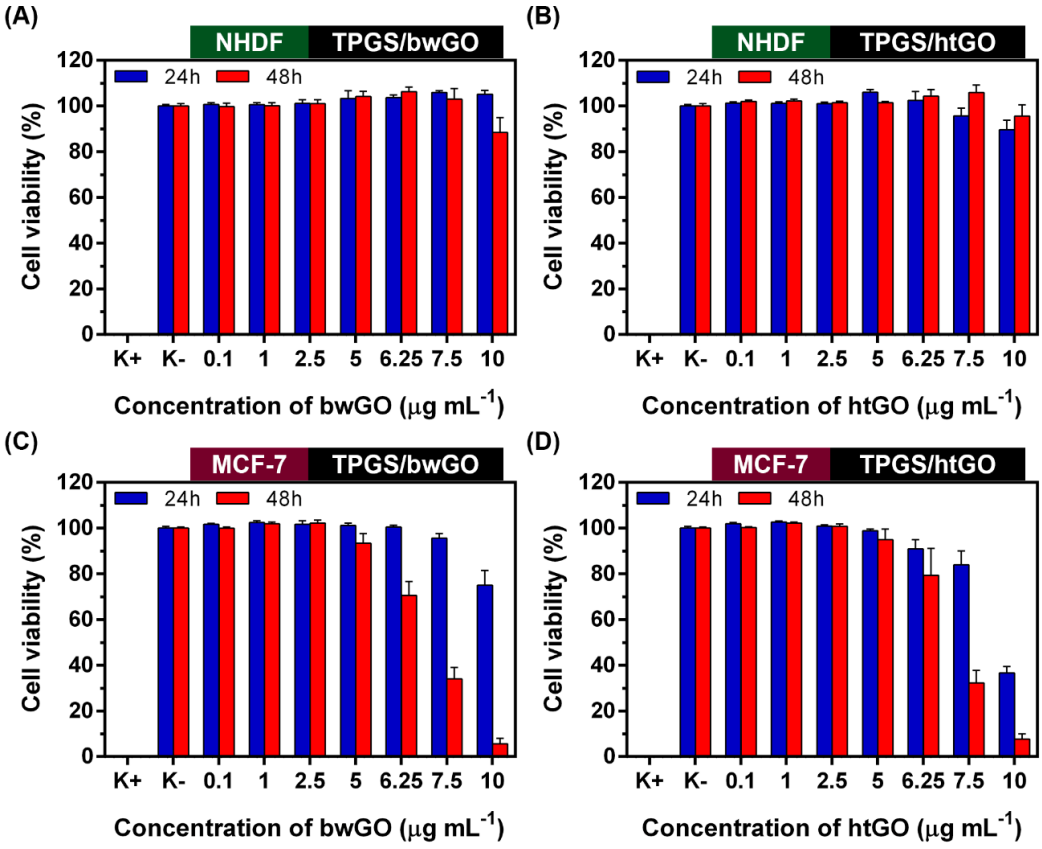

Figure 4.10. Evaluation of the cytotoxic profile of TPGS/bwGO (A) and TPGS/htGO (B) at different concentrations and incubation periods in NHDF. The cytotoxicity of TPGS/bwGO (C) and TPGS/htGO (D) in MCF-7 cells was also determined in the same experimental conditions. Data represent mean ± SD, n = 5. K^- and K^+ represent the negative and positive controls, respectively.

Interestingly, a reduction in MCF-7 cells' viability and modifications on cells' morphology were noticed for low concentrations of the produced materials (Figures 4.10C-10D and 4.11). After an incubation period of 24 h, TPGS/nGO derivatives induced cytotoxic effects for concentrations above 7.5 μg mL^{-1} (of GO equivalents). Moreover, after an incubation of 48 h these materials produced meaningful alterations in MCF-7 cells' viability for concentrations above 6.25 μg mL^{-1} (of GO equivalents) (Figures 4.10C-10D). In fact, after this period, TPGS/bwGO and TPGS/htGO at the concentration of 7.5 μg mL^{-1} (of GO equivalents) were able to reduce MCF-7 cells' viability up to 34 and 32 %, respectively.

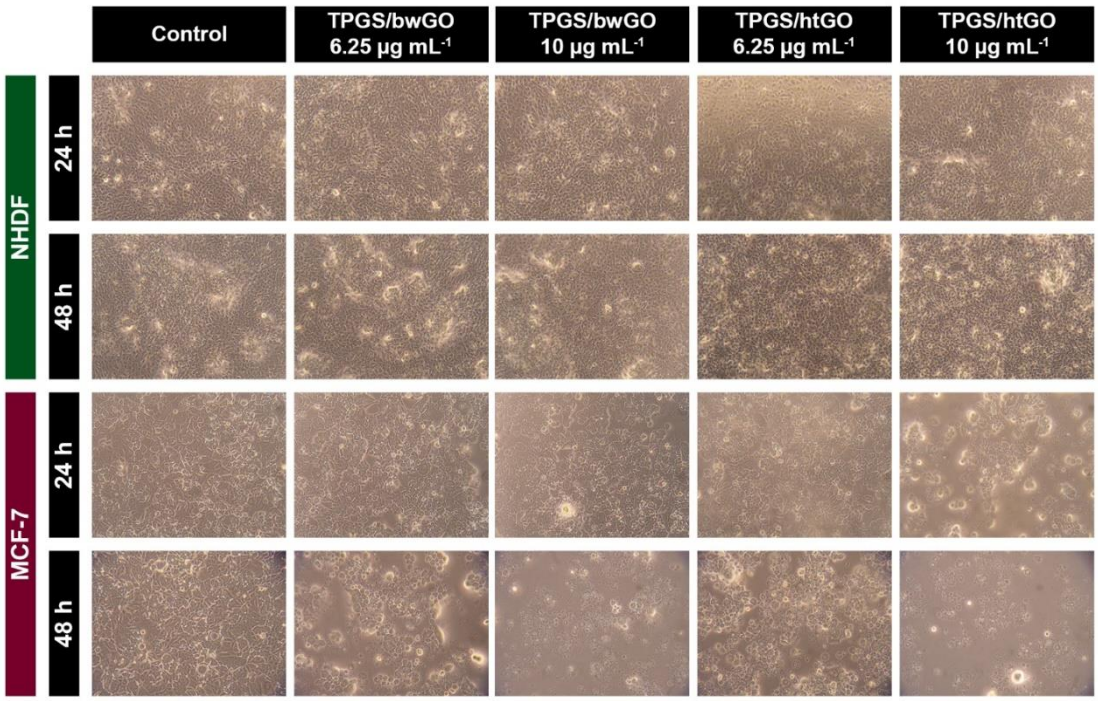

Figure 4.11. Optical microscopic images of NHDF and MCF-7 cells after different incubation periods (24 and 48 h) with TPGS/bwGO and TPGS/htGO (6.25 and 10 μg mL^{-1} of GO equivalents). Non-treated cells were denoted as control.

The differential effect of TPGS/nGO derivatives in NHDF and MCF-7 cells can be explained by the distinct sensitivity displayed by these cells to TPGS (Figure 4.12). In fact, TPGS produced a dose-dependent cytotoxic effect on MCF-7 cells, while NHDF incubated with this compound only display a decrease in their viability for higher concentrations and for long incubation periods (Figure 4.12). These results are in agreement with the findings previously reported by Neophytou *et al.*, which investigated the molecular mechanism of action of TPGS in different cell lines and also verified that breast cancer cells are sensitive to TPGS while healthy cells are

resistant to its effect [38]. In particular, authors verified that TPGS exerts its anticancer activity through inhibition of Protein Kinase B (PKB or Akt) phosphorylation [38]. In MCF-7 cells, this inhibition produces a decrease in the levels of BcL-2 and Survivin (which are overexpressed), leading to cell cycle arrest and caspase-dependent and -independent cell death [38]. In normal cells, authors verified that TPGS does not induce a cytotoxic effect since the targeted/affected signaling-cascade is not upregulated [38]. Due to these properties, TPGS was also combined with other materials and pro-drugs in order to explore and enhance its anticancer activity [58-61]. Therefore, the TPGS functionalization improves the stability of TPGS/bwGO and TPGS/htGO, and also endows these materials with a therapeutic effect preferential for breast cancer cells.

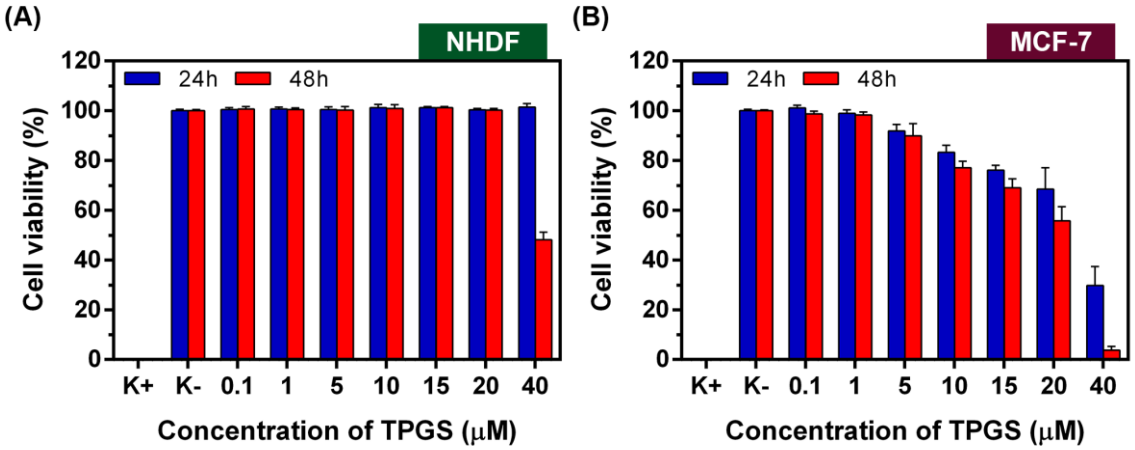

Figure 4.12. Evaluation of the cytotoxic profile of TPGS at different concentrations (0.1 – 40 μM) and incubation periods (24 and 48 h) in NHDF (A) and MCF-7 (B) cells. Data represent mean ± SD, n = 5. K^- and K^+ represent the negative and positive controls, respectively.

4.4.6. Evaluation of the phototherapeutic effect mediated by TPGS/nGO derivatives

After confirming the preferential therapeutic effect of TPGS/nGO derivatives in MCF-7 cells, the capacity of these materials to mediate an enhanced cytotoxic effect by combining their anticancer activity with photothermal capability was also evaluated. For this purpose, MCF-7 cells were incubated with TPGS/nGO derivatives for 24 h followed by their irradiation with NIR light (Figure 4.13A).

The combined application of TPGS/nGO derivatives and NIR light during 5 min produced a prominent reduction in MCF-7 cells viability (Figure 4.13B), which was superior to that mediated

by non-irradiated nanomaterials in the same experimental conditions (Figures 4.10C-10D). For instance, TPGS/bwGO, at the concentration of 6.25 μg mL^{-1} (of GO equivalents) and with an incubation time of 24 h, did not affect MCF-7 cells while its irradiation with NIR light decreased cells viability to about 35 % (Figures 4.10C and 4.13B). In equivalent experimental conditions (same concentration and incubation period), TPGS/htGO reduced slightly the viability of cancer cells (to approximately 91 %) and its combined application with NIR irradiation produced a decrease in cells viability to about 31 % (Figures 4.10D and 4.13B). The slightly better therapeutic effect mediated by TPGS/htGO under NIR laser irradiation may be a consequence of its improved photothermal capacity (Figure 4.6D) and slightly better anticancer activity (Figure 4.10D). Moreover, the sole application of the NIR light and its combination with non-coated materials (bwGO and htGO) did not induce any toxicity towards cancer cells (Figure 4.13B). These results imply that the temperature variation produced by TPGS/nGO derivatives under NIR laser irradiation sensitizes cancer cells to TPGS action, resulting in a synergistic therapeutic effect (Figure 4.13B).

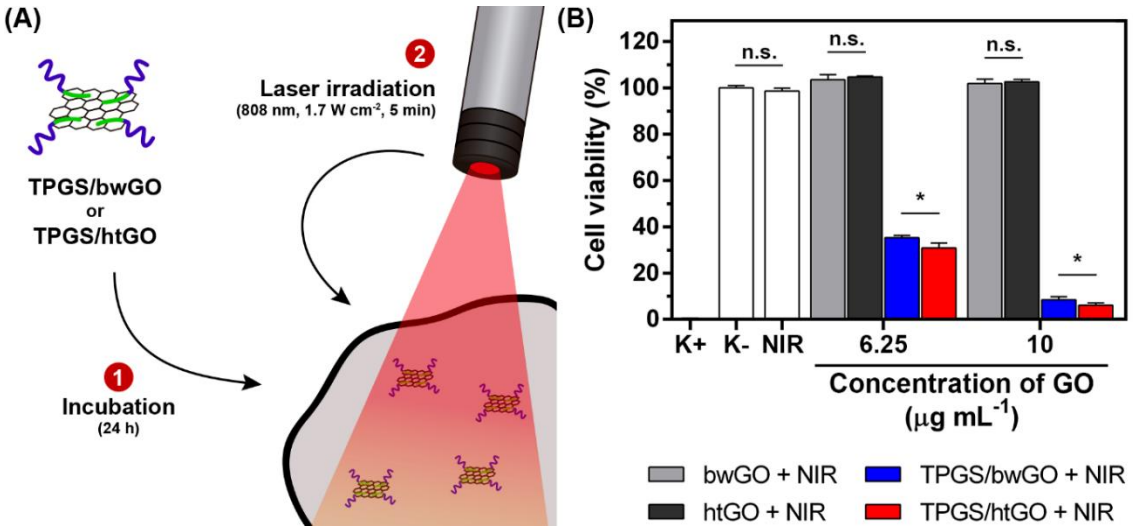

Figure 4.13. *In vitro* phototherapy using TPGS/nGO derivatives. Schematic representation of the phototherapy (A). Therapeutic effect mediated by bwGO, htGO, TPGS/bwGO and TPGS/htGO under NIR irradiation (808 nm, 1.7 W cm^{-2}, 5 min) towards MCF-7 cells (B). NIR represents cells solely irradiated with NIR light. K^- and K^+ represent the negative and positive controls, respectively. Data represent mean ± SD, n = 5, n.s. = non significant, $*p < 0.05$.

Trypan blue (stains cells that have a compromised membrane with blue color) and Calcein-AM (non-fluorescent dye that is converted to a fluorescent molecule by live cells) stainings were also used to provide a visual confirmation of TPGS/nGO derivatives phototherapeutic efficacy (Figure 4.14).

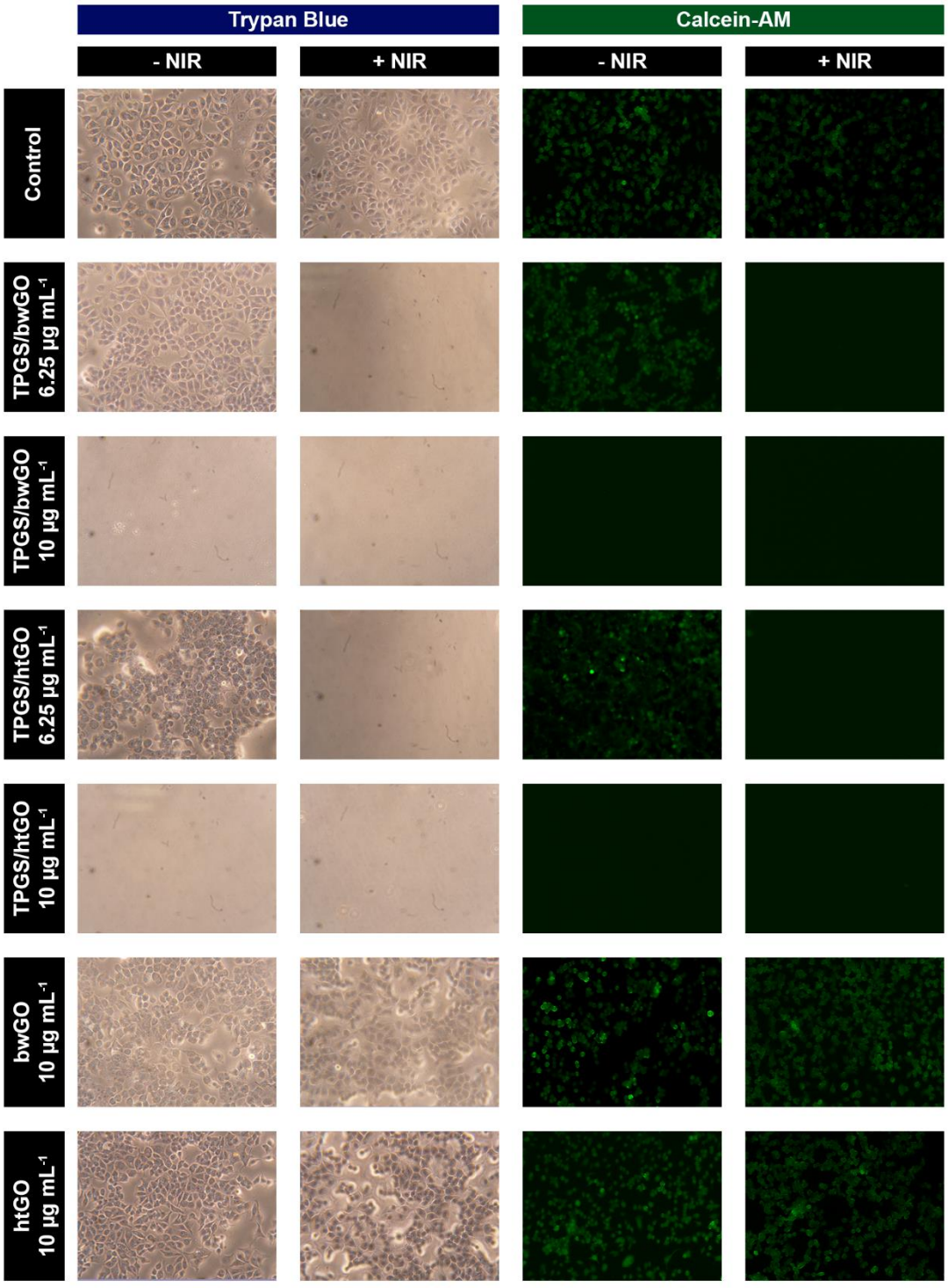

Figure 4.14. Trypan blue and Calcein-AM staining of MCF-7 cells after cells being incubated with different concentrations of nGO and TPGS/nGO derivatives (6.25 and 10 µg mL^{-1} of GO equivalents) during 24 h without (- NIR) or with (+ NIR) laser irradiation (808 nm, 1.7 W cm^{-2}, 5 min). Cells not treated with nanomaterials were used as controls.

Consistent with the previous findings, the sole application of non-functionalized nGO derivatives (bwGO and htGO) or their combination with NIR light did not affect MCF-7 cells

integrity (Figure 4.14). As expected, similar results were obtained for cells treated with TPGS/bwGO or TPGS/htGO at the concentration of 6.25 μg mL^{-1} (of GO equivalents) (Figure 4.14). However, the same materials in conjugation with NIR light produced a strong therapeutic effect since, after the treatment and staining protocol (comprises staining, fixing and washing steps), no intact cells remained in the well, thereby confirming that under these conditions MCF-7 cells are severely affected (Figure 4.14). TPGS/nGO derivatives at the concentration of 10 μg mL^{-1} (of GO equivalents) or in combination with NIR light produced a similar result, which is also in agreement with the previous results (Figure 4.10, 4.13 and 4.14).

So far, nGO derivatives have been: (i) functionalized with hydrophilic polymers to improve their stability and biocompatibility, (ii) reduced to enhance their photothermal capacity and (iii) decorated with targeting ligands to improve their selectivity. By combining these approaches, some materials were able to photoablate cancer cells/tumors, by using low concentrations and/or power density [18, 22, 24, 25]. In this work, TPGS/bwGO and TPGS/htGO preferentially diminished breast cancer cells' viability, displaying an insignificant effect on normal cells, an effect that can be attributed to TPGS intrinsic anticancer activity. This type of selectivity mediated by TPGS molecular action is advantageous since it may not be hindered by the formation of a protein corona on nanomaterials' surface as it has been reported for targeted nanomaterials [62]. Moreover, TPGS/nGO derivatives under NIR laser irradiation produced a synergistic therapeutic effect whose efficacy is comparable and, in some cases, superior to previously described materials by mediating cancer cells destruction at a relatively low concentration and power density [21, 22, 25, 42, 57, 63-69] (Table S.4.1 – supplementary information). Overall, the TPGS/bwGO and TPGS/htGO are promising agents for breast cancer phototherapy.

4.5. Conclusion

In the present study, TPGS/bwGO and TPGS/htGO nanomaterials were prepared through a simple sonication method and a one-pot hydrothermal treatment, respectively. The application of TPGS to coat nGO derivatives is herein reported for the first time and the results revealed that it was able to improve the stability of these nanomaterials. TPGS/htGO possessed about 1.9-fold higher NIR absorption than TPGS/bwGO, thus producing a 1.4 – 1.6 times superior temperature variation under NIR laser irradiation. *In vitro*, TPGS/bwGO and TPGS/htGO diminished breast cancer cells' viability and had an insignificant effect on healthy cells. This preferential effect towards breast cancer cells can be attributed to TPGS intrinsic anticancer activity. Moreover, at low doses, both TPGS/nGO derivatives mediated under NIR laser irradiation an improved cytotoxic effect towards cancer cells, and it was found that TPGS/htGO produced a slightly better therapeutic outcome. Overall, the results reveal that TPGS/bwGO and TPGS/htGO are promising agents for breast cancer therapy.

4.6. References

[1] L. Cheng, C. Wang, L. Feng, K. Yang, Z. Liu, Functional nanomaterials for phototherapies of cancer, Chemical Reviews, 114 (2014) 10869-10939.

[2] A. Vogel, V. Venugopalan, Mechanisms of pulsed laser ablation of biological tissues, Chemical Reviews, 103 (2003) 577-644.

[3] E.C. Dreaden, M.A. Mackey, X. Huang, B. Kang, M.A. El-Sayed, Beating cancer in multiple ways using nanogold, Chemical Society Reviews, 40 (2011) 3391-3404.

[4] L. Cheng, K. Yang, Q. Chen, Z. Liu, Organic stealth nanoparticles for highly effective in vivo near-infrared photothermal therapy of cancer, ACS Nano, 6 (2012) 5605-5613.

[5] Y. Wang, K.C. Black, H. Luehmann, W. Li, Y. Zhang, X. Cai, D. Wan, S.-Y. Liu, M. Li, P. Kim, Comparison study of gold nanohexapods, nanorods, and nanocages for photothermal cancer treatment, ACS Nano, 7 (2013) 2068-2077.

[6] B. Zhang, H. Wang, S. Shen, X. She, W. Shi, J. Chen, Q. Zhang, Y. Hu, Z. Pang, X. Jiang, Fibrin-targeting peptide CREKA-conjugated multi-walled carbon nanotubes for self-amplified photothermal therapy of tumor, Biomaterials, 79 (2016) 46-55.

[7] Z. Liu, J. Liu, R. Wang, Y. Du, J. Ren, X. Qu, An efficient nano-based theranostic system for multi-modal imaging-guided photothermal sterilization in gastrointestinal tract, Biomaterials, 56 (2015) 206-218.

[8] Z. Liu, X. Liu, X. Ran, E. Ju, J. Ren, X. Qu, Single-layer tungsten oxide as intelligent photo-responsive nanoagents for permanent male sterilization, Biomaterials, 69 (2015) 56-64.

[9] Z. Liu, X. Liu, Y. Du, J. Ren, X. Qu, Using Plasmonic Copper Sulfide Nanocrystals as Smart Light-Driven Sterilants, ACS Nano, 9 (2015) 10335-10346.

[10] C. Jang, J.H. Lee, A. Sahu, G. Tae, The synergistic effect of folate and RGD dual ligand of nanographene oxide on tumor targeting and photothermal therapy in vivo, Nanoscale, 7 (2015) 18584-18594.

[11] D.R. Dreyer, A.D. Todd, C.W. Bielawski, Harnessing the chemistry of graphene oxide, Chemical Society Reviews, 43 (2014) 5288-5301.

[12] Y. Fazaeli, O. Akhavan, R. Rahighi, M.R. Aboudzadeh, E. Karimi, H. Afarideh, In vivo SPECT imaging of tumors by 198,199Au-labeled graphene oxide nanostructures, Materials Science and Engineering: C, 45 (2014) 196-204.

[13] K. Yang, S. Zhang, G. Zhang, X. Sun, S.-T. Lee, Z. Liu, Graphene in mice: ultrahigh in vivo tumor uptake and efficient photothermal therapy, Nano Letters, 10 (2010) 3318-3323.

[14] D. Bitounis, H. Ali-Boucetta, B.H. Hong, D.H. Min, K. Kostarelos, Prospects and challenges of graphene in biomedical applications, Advanced Materials, 25 (2013) 2258-2268.

[15] X. Sun, Z. Liu, K. Welsher, J.T. Robinson, A. Goodwin, S. Zaric, H. Dai, Nano-graphene oxide for cellular imaging and drug delivery, Nano Research, 1 (2008) 203-212.

[16] H. Shen, M. Liu, H. He, L. Zhang, J. Huang, Y. Chong, J. Dai, Z. Zhang, PEGylated graphene oxide-mediated protein delivery for cell function regulation, ACS Applied Materials & Interfaces, 4 (2012) 6317-6323.

[17] K.V. Krishna, C. Ménard-Moyon, S. Verma, A. Bianco, Graphene-based nanomaterials for nanobiotechnology and biomedical applications, Nanomedicine, 8 (2013) 1669-1688.

[18] K. Yang, J. Wan, S. Zhang, B. Tian, Y. Zhang, Z. Liu, The influence of surface chemistry and size of nanoscale graphene oxide on photothermal therapy of cancer using ultra-low laser power, Biomaterials, 33 (2012) 2206-2214.

[19] H. Xu, M. Fan, A.M.A. Elhissi, Z. Zhang, K.-W. Wan, W. Ahmed, D.A. Phoenix, X. Sun, PEGylated graphene oxide for tumor-targeted delivery of paclitaxel, Nanomedicine, 10 (2015) 1247-1262.

[20] J.H. Lee, A. Sahu, C. Jang, G. Tae, The effect of ligand density on in vivo tumor targeting of nanographene oxide, Journal of Controlled Release, 209 (2015) 219-228.

[21] J.T. Robinson, S.M. Tabakman, Y. Liang, H. Wang, H. Sanchez Casalongue, D. Vinh, H. Dai, Ultrasmall reduced graphene oxide with high near-infrared absorbance for photothermal therapy, Journal of the American Chemical Society, 133 (2011) 6825-6831.

[22] O. Akhavan, E. Ghaderi, H. Emamy, Nontoxic concentrations of PEGylated graphene nanoribbons for selective cancer cell imaging and photothermal therapy, Journal of Materials Chemistry, 22 (2012) 20626-20633.

[23] L. Zhang, Z. Wang, Z. Lu, H. Shen, J. Huang, Q. Zhao, M. Liu, N. He, Z. Zhang, PEGylated reduced graphene oxide as a superior ssRNA delivery system, Journal of Materials Chemistry B, 1 (2013) 749-755.

[24] O. Akhavan, E. Ghaderi, Graphene nanomesh promises extremely efficient in vivo photothermal therapy, Small, 9 (2013) 3593-3601.

[25] O. Akhavan, A. Meidanchi, E. Ghaderi, S. Khoei, Zinc ferrite spinel-graphene in magneto-photothermal therapy of cancer, Journal of Materials Chemistry B, 2 (2014) 3306-3314.

[26] Z. Zhang, S. Tan, S.-S. Feng, Vitamin E TPGS as a molecular biomaterial for drug delivery, Biomaterials, 33 (2012) 4889-4906.

[27] D. Zhu, W. Tao, H. Zhang, G. Liu, T. Wang, L. Zhang, X. Zeng, L. Mei, Docetaxel (DTX)-loaded polydopamine-modified TPGS-PLA nanoparticles as a targeted drug delivery system for the treatment of liver cancer, Acta Biomaterialia, 30 (2016) 144-154.

[28] R.V. Kutty, S.L. Chia, M.I. Setyawati, M.S. Muthu, S.-S. Feng, D.T. Leong, In vivo and ex vivo proofs of concept that cetuximab conjugated vitamin E TPGS micelles increases efficacy of delivered docetaxel against triple negative breast cancer, Biomaterials, 63 (2015) 58-69.

[29] W. Tao, J. Zhang, X. Zeng, D. Liu, G. Liu, X. Zhu, Y. Liu, Q. Yu, L. Huang, L. Mei, Blended Nanoparticle System Based on Miscible Structurally Similar Polymers: A Safe, Simple, Targeted, and Surprisingly High Efficiency Vehicle for Cancer Therapy, Advanced Healthcare Materials, 4 (2015) 1203-1214.

[30] Y. Mi, J. Zhao, S.-S. Feng, Targeted co-delivery of docetaxel, cisplatin and herceptin by vitamin E TPGS-cisplatin prodrug nanoparticles for multimodality treatment of cancer, Journal of Controlled Release, 169 (2013) 185-192.

[31] J. Zhao, Y. Mi, S.-S. Feng, Targeted co-delivery of docetaxel and siPlk1 by herceptin-conjugated vitamin E TPGS based immunomicelles, Biomaterials, 34 (2013) 3411-3421.

[32] D. de Melo-Diogo, V.M. Gaspar, E.C. Costa, A.F. Moreira, D. Oppolzer, E. Gallardo, I.J. Correia, Combinatorial delivery of Crizotinib–Palbociclib–Sildenafil using TPGS-PLA micelles for

improved cancer treatment, European Journal of Pharmaceutics and Biopharmaceutics, 88 (2014) 718-729.

[33] M.S. Muthu, S. Avinash Kulkarni, Y. Liu, S.-S. Feng, Development of docetaxel-loaded vitamin E TPGS micelles: formulation optimization, effects on brain cancer cells and biodistribution in rats, Nanomedicine, 7 (2012) 353-364.

[34] V.M. Gaspar, A.F. Moreira, E.C. Costa, J.A. Queiroz, F. Sousa, C. Pichon, I.J. Correia, Gas-generating TPGS-PLGA microspheres loaded with nanoparticles (NIMPS) for co-delivery of minicircle DNA and anti-tumoral drugs, Colloids and Surfaces B: Biointerfaces, 134 (2015) 287-294.

[35] G. Tian, X. Zheng, X. Zhang, W. Yin, J. Yu, D. Wang, Z. Zhang, X. Yang, Z. Gu, Y. Zhao, TPGS-stabilized NaYbF4:Er upconversion nanoparticles for dual-modal fluorescent/CT imaging and anticancer drug delivery to overcome multi-drug resistance, Biomaterials, 40 (2015) 107-116.

[36] R.P. Singh, G. Sharma, S. Singh, M. Kumar, B.L. Pandey, B. Koch, M.S. Muthu, Vitamin E TPGS conjugated carbon nanotubes improved efficacy of docetaxel with safety for lung cancer treatment, Colloids and Surfaces B: Biointerfaces, 141 (2016) 429-442.

[37] N. Duhem, F. Danhier, V. Préat, Vitamin E-based nanomedicines for anti-cancer drug delivery, Journal of Controlled Release, 182 (2014) 33-44.

[38] C.M. Neophytou, C. Constantinou, P. Papageorgis, A.I. Constantinou, D-alpha-tocopheryl polyethylene glycol succinate (TPGS) induces cell cycle arrest and apoptosis selectively in Survivin-overexpressing breast cancer cells, Biochemical Pharmacology, 89 (2014) 31-42.

[39] N.M. Huang, H.N. Lim, C.H. Chia, M.A. Yarmo, M.R. Muhamad, Simple room-temperature preparation of high-yield large-area graphene oxide, International Journal of Nanomedicine, 6 (2011) 3443-3448.

[40] H.R. Thomas, S.P. Day, W.E. Woodruff, C. Vallés, R.J. Young, I.A. Kinloch, G.W. Morley, J.V. Hanna, N.R. Wilson, J.P. Rourke, Deoxygenation of graphene oxide: reduction or cleaning?, Chemistry of Materials, 25 (2013) 3580-3588.

[41] A.L. Antaris, J.T. Robinson, O.K. Yaghi, G. Hong, S. Diao, R. Luong, H. Dai, Ultra-low doses of chirality sorted (6, 5) carbon nanotubes for simultaneous tumor imaging and photothermal therapy, ACS Nano, 7 (2013) 3644-3652.

[42] J. Chen, X. Wang, T. Chen, Facile and green reduction of covalently PEGylated nanographene oxide via a 'water-only'route for high-efficiency photothermal therapy, Nanoscale Research Letters, 9 (2014) 86.

[43] V.M. Gaspar, P. Baril, E.C. Costa, D. de Melo-Diogo, F. Foucher, J.A. Queiroz, F. Sousa, C. Pichon, I.J. Correia, Bioreducible poly(2-ethyl-2-oxazoline)–PLA–PEI-SS triblock copolymer micelles for co-delivery of DNA minicircles and Doxorubicin, Journal of Controlled Release, 213 (2015) 175-191.

[44] V.M. Gaspar, C. Gonçalves, D. de Melo-Diogo, E.C. Costa, J.A. Queiroz, C. Pichon, F. Sousa, I.J. Correia, Poly (2-ethyl-2-oxazoline)–PLA-g–PEI amphiphilic triblock micelles for co-delivery of minicircle DNA and chemotherapeutics, Journal of Controlled Release, 189 (2014) 90-104.

[45] J. Mou, P. Li, C. Liu, H. Xu, L. Song, J. Wang, K. Zhang, Y. Chen, J. Shi, H. Chen, Ultrasmall Cu2-xS Nanodots for Highly Efficient Photoacoustic Imaging-Guided Photothermal Therapy, Small, 11 (2015) 2275-2283.

[46] V.R. Coluci, D.S.F.T. Martinez, J.G. Honório, A.I.F. de Faria, D.A. Morales, M.S. Skaf, O.L. Alves, G.A. Umbuzeiro, Noncovalent interaction with graphene oxide: the crucial role of oxidative debris, Journal of Physical Chemistry C, 118 (2014) 2187-2193.

[47] D. Ma, L. Dong, M. Zhou, L. Zhu, The influence of oxidation debris containing in graphene oxide on the adsorption and electrochemical properties of 1, 10-phenanthroline-5, 6-dione, Analyst, 141 (2016) 2761-2766.

[48] S.A. Kulkarni, S.-S. Feng, Effects of particle size and surface modification on cellular uptake and biodistribution of polymeric nanoparticles for drug delivery, Pharmaceutical Research, 30 (2013) 2512-2522.

[49] K.F. Chu, D.E. Dupuy, Thermal ablation of tumours: biological mechanisms and advances in therapy, Nature Reviews Cancer, 14 (2014) 199-208.

[50] S.F. Kiew, L.V. Kiew, H.B. Lee, T. Imae, L.Y. Chung, Assessing biocompatibility of graphene oxide-based nanocarriers: A review, Journal of Controlled Release, 226 (2016) 217-228.

[51] O. Akhavan, E. Ghaderi, H. Emamy, F. Akhavan, Genotoxicity of graphene nanoribbons in human mesenchymal stem cells, Carbon, 54 (2013) 419-431.

[52] O. Akhavan, E. Ghaderi, A. Akhavan, Size-dependent genotoxicity of graphene nanoplatelets in human stem cells, Biomaterials, 33 (2012) 8017-8025.

[53] H. Zhang, C. Peng, J. Yang, M. Lv, R. Liu, D. He, C. Fan, Q. Huang, Uniform ultrasmall graphene oxide nanosheets with low cytotoxicity and high cellular uptake, ACS Applied Materials & Interfaces, 5 (2013) 1761-1767.

[54] Y. Chang, S.-T. Yang, J.-H. Liu, E. Dong, Y. Wang, A. Cao, Y. Liu, H. Wang, In vitro toxicity evaluation of graphene oxide on A549 cells, Toxicology Letters, 200 (2011) 201-210.

[55] A. Pattammattel, C.L. Williams, P. Pande, W.G. Tsui, A.K. Basu, C.V. Kumar, Biological relevance of oxidative debris present in as-prepared graphene oxide, RSC Advances, 5 (2015) 59364-59372.

[56] C. Cheng, S. Nie, S. Li, H. Peng, H. Yang, L. Ma, S. Sun, C. Zhao, Biopolymer functionalized reduced graphene oxide with enhanced biocompatibility via mussel inspired coatings/anchors, Journal of Materials Chemistry B, 1 (2013) 265-275.

[57] O. Akhavan, E. Ghaderi, S. Aghayee, Y. Fereydooni, A. Talebi, The use of a glucose-reduced graphene oxide suspension for photothermal cancer therapy, Journal of Materials Chemistry, 22 (2012) 13773-13781.

[58] V. Khare, W.A. Sakarchi, P.N. Gupta, A.D. Curtis, C. Hoskins, Synthesis and characterization of TPGS–gemcitabine prodrug micelles for pancreatic cancer therapy, RSC Advances, 6 (2016) 60126-60137.

[59] P. Yu, H. Yu, C. Guo, Z. Cui, X. Chen, Q. Yin, P. Zhang, X. Yang, H. Cui, Y. Li, Reversal of doxorubicin resistance in breast cancer by mitochondria-targeted pH-responsive micelles, Acta Biomaterialia, 14 (2015) 115-124.

[60] E. Bernabeu, L. Gonzalez, M. Cagel, E.P. Gergic, M.A. Moretton, D.A. Chiappetta, Novel Soluplus®—TPGS mixed micelles for encapsulation of paclitaxel with enhanced in vitro cytotoxicity on breast and ovarian cancer cell lines, Colloids and Surfaces B: Biointerfaces, 140 (2016) 403-411.

[61] Y. Bao, M. Yin, X. Hu, X. Zhuang, Y. Sun, Y. Guo, S. Tan, Z. Zhang, A safe, simple and efficient doxorubicin prodrug hybrid micelle for overcoming tumor multidrug resistance and targeting delivery, Journal of Controlled Release, 235 (2016) 182-194.

[62] A. Salvati, A.S. Pitek, M.P. Monopoli, K. Prapainop, F.B. Bombelli, D.R. Hristov, P.M. Kelly, C. Åberg, E. Mahon, K.A. Dawson, Transferrin-functionalized nanoparticles lose their targeting capabilities when a biomolecule corona adsorbs on the surface, Nature Nanotechnology, 8 (2013) 137-143.

[63] F. Bani, M. Adeli, S. Movahedi, M. Sadeghizadeh, Graphene-Polyglycerol-Curcumin Hybrid as a Near-Infrared (NIR) Laser Stimuli-Responsive System for Chemo-Photothermal Cancer Therapy, RSC Advances, 6 (2016) 61141-61149.

[64] S.H. Kim, J.E. Lee, S.M. Sharker, J.H. Jeong, I. In, S.Y. Park, In vitro and in vivo tumor targeted photothermal cancer therapy using functionalized graphene nanoparticles, Biomacromolecules, 16 (2015) 3519-3529.

[65] T.H. Tran, H.T. Nguyen, T.T. Pham, J.Y. Choi, H.-G. Choi, C.S. Yong, J.O. Kim, Development of a graphene oxide nanocarrier for dual-drug chemo-phototherapy to overcome drug resistance in cancer, ACS Applied Materials & Interfaces, 7 (2015) 28647-28655.

[66] Z.M. Markovic, L.M. Harhaji-Trajkovic, B.M. Todorovic-Markovic, D.P. Kepić, K.M. Arsikin, S.P. Jovanović, A.C. Pantovic, M.D. Dramićanin, V.S. Trajkovic, In vitro comparison of the photothermal anticancer activity of graphene nanoparticles and carbon nanotubes, Biomaterials, 32 (2011) 1121-1129.

[67] X. Qin, Z. Guo, Z. Liu, W. Zhang, M. Wan, B. Yang, Folic acid-conjugated graphene oxide for cancer targeted chemo-photothermal therapy, Journal of Photochemistry and Photobiology B, 120 (2013) 156-162.

[68] W. Zhang, Z. Guo, D. Huang, Z. Liu, X. Guo, H. Zhong, Synergistic effect of chemo-photothermal therapy using PEGylated graphene oxide, Biomaterials, 32 (2011) 8555-8561.

[69] H.-W. Yang, Y.-J. Lu, K.-J. Lin, S.-C. Hsu, C.-Y. Huang, S.-H. She, H.-L. Liu, C.-W. Lin, M.-C. Xiao, S.-P. Wey, EGRF conjugated PEGylated nanographene oxide for targeted chemotherapy and photothermal therapy, Biomaterials, 34 (2013) 7204-7214.

4.7. Supplementary Information

Table S.4.1. *In vitro* performance of some nGO-based materials applied in cancer phototherapy.

Material	Concentration (μg mL^{-1})	Power density (W cm^{-2})	Irradiation time (min)	Cell type	Cancer cells' viability reduced to ≤ 10 %?	Ref.
Polyglicerol-reduced nGO loaded with Curcumin	30[a,b]	1	2	MCF-7	No	[1]
PEGylated and HA functionalized rGO loaded with IR825	1000	2	5	MDA-MB-231 and A549	No	[2]
Poloxamer 188-GO loaded with DOX[c] and Irinotecan	1[a]	3	5	SSC-7, MCF-7 and MDA-MB-231	No	[3]
DSPE-PEG-RGD functionalized reduced nGO	~ 6.6	15.3	8	U87MG	Yes	[4]
DSPE-PEG-RGD functionalized rGO nanoribbons	1 – 100	7.5	8	U87MG	Yes	[5]
$ZnFe_2O_4$–rGO hybrid nanostructures	10	7.5	4-12	LNCaP	Yes	[6]
Glucose rGO (prepared in the presence of Fe catalyst)	10-1000	7.5	0.5-12	LNCaP	Yes	[7]
PVP-graphene	5-10	2	5	U251	Yes	[8]
FA-PVP-nGO loaded with DOX	20[a]	2	5	HeLa	Yes	[9]
PEGylated nGO loaded with DOX	30[a]	2	3	EMT6	Yes	[10]
Cetuximab conjugated PEGylated nGO loaded with Epirubicin	5-25[a]	2	2	U87	Yes	[11]
PEGylated reduced nGO	6	0.6	5	A549	Yes	[12]
TPGS/nGO derivatives	10	1.7	5	MCF-7	Yes	This work

[a] Drug concentration; [b] value in μM; [c] Doxorubicin.

4.7.1. Supplementary References

[1] F. Bani, M. Adeli, S. Movahedi, M. Sadeghizadeh, Graphene-Polyglycerol-Curcumin Hybrid as a Near-Infrared (NIR) Laser Stimuli-Responsive System for Chemo-Photothermal Cancer Therapy, RSC Advances, 6 (2016) 61141-61149.

[2] S.H. Kim, J.E. Lee, S.M. Sharker, J.H. Jeong, I. In, S.Y. Park, In vitro and in vivo tumor targeted photothermal cancer therapy using functionalized graphene nanoparticles, Biomacromolecules, 16 (2015) 3519-3529.

[3] T.H. Tran, H.T. Nguyen, T.T. Pham, J.Y. Choi, H.-G. Choi, C.S. Yong, J.O. Kim, Development of a graphene oxide nanocarrier for dual-drug chemo-phototherapy to overcome drug resistance in cancer, ACS Applied Materials & Interfaces, 7 (2015) 28647-28655.

[4] J.T. Robinson, S.M. Tabakman, Y. Liang, H. Wang, H. Sanchez Casalongue, D. Vinh, H. Dai, Ultrasmall reduced graphene oxide with high near-infrared absorbance for photothermal therapy, Journal of the American Chemical Society, 133 (2011) 6825-6831.

[5] O. Akhavan, E. Ghaderi, H. Emamy, Nontoxic concentrations of PEGylated graphene nanoribbons for selective cancer cell imaging and photothermal therapy, Journal of Materials Chemistry, 22 (2012) 20626-20633.

[6] O. Akhavan, A. Meidanchi, E. Ghaderi, S. Khoei, Zinc ferrite spinel-graphene in magneto-photothermal therapy of cancer, Journal of Materials Chemistry B, 2 (2014) 3306-3314.

[7] O. Akhavan, E. Ghaderi, S. Aghayee, Y. Fereydooni, A. Talebi, The use of a glucose-reduced graphene oxide suspension for photothermal cancer therapy, Journal of Materials Chemistry, 22 (2012) 13773-13781.

[8] Z.M. Markovic, L.M. Harhaji-Trajkovic, B.M. Todorovic-Markovic, D.P. Kepić, K.M. Arsikin, S.P. Jovanović, A.C. Pantovic, M.D. Dramićanin, V.S. Trajkovic, In vitro comparison of the photothermal anticancer activity of graphene nanoparticles and carbon nanotubes, Biomaterials, 32 (2011) 1121-1129.

[9] X. Qin, Z. Guo, Z. Liu, W. Zhang, M. Wan, B. Yang, Folic acid-conjugated graphene oxide for cancer targeted chemo-photothermal therapy, Journal of Photochemistry and Photobiology B, 120 (2013) 156-162.

[10] W. Zhang, Z. Guo, D. Huang, Z. Liu, X. Guo, H. Zhong, Synergistic effect of chemo-photothermal therapy using PEGylated graphene oxide, Biomaterials, 32 (2011) 8555-8561.

[11] H.-W. Yang, Y.-J. Lu, K.-J. Lin, S.-C. Hsu, C.-Y. Huang, S.-H. She, H.-L. Liu, C.-W. Lin, M.-C. Xiao, S.-P. Wey, EGRF conjugated PEGylated nanographene oxide for targeted chemotherapy and photothermal therapy, Biomaterials, 34 (2013) 7204-7214.

[12] J. Chen, X. Wang, T. Chen, Facile and green reduction of covalently PEGylated nanographene oxide via a 'water-only'route for high-efficiency photothermal therapy, Nanoscale Research Letters, 9 (2014) 86.

Chapter 5

Research Work 2

POxylated Graphene Oxide Nanomaterials for Combination Chemo-Phototherapy of Breast Cancer Cells

This chapter is based on a manuscript submitted for publication entitled: POxylated Graphene Oxide Nanomaterials for Combination Chemo-Phototherapy of Breast Cancer Cells.

5.1. Abstract

PEGylated GO nanomaterials have been showing promising results in cancer therapy, due to their drug loading and photothermal capacities. However, the recent reports regarding the immunogenicity of PEG based coatings highlight the importance of investigating alternative materials to functionalize GO. Herein, GO derivatives were functionalized for the first time with an amphiphilic polymer based on poly(2-ethyl-2-oxazoline) and were co-loaded with doxorubicin (DOX) and D-α-Tocopherol succinate (TOS) to be applied in chemo-phototherapy of breast cancer cells. The results revealed that POxylated GO displays the required properties for application in cancer therapy. Moreover, the screening of different DOX:TOS combination ratios showed that the 1:3 DOX:TOS molar ratio produces an optimal synergistic therapeutic effect towards breast cancer cells. Furthermore, this drug ratio had a lower impact on normal cells. POxylated GO was then loaded with this drug combination in order to assess its chemo-phototherapeutic potential. The delivery of DOX:TOS by POxylated GO to cancer cells induced a stronger therapeutic effect than that attained with the free drug combination. Furthermore, an even greater cytotoxicity towards cancer cells was achieved by exposing DOX:TOS loaded POxylated GO to NIR radiation. Overall, POxylated GO is a promising drug delivery and phototherapeutic agent.

Keywords: cancer treatment; co-delivery; graphene oxide; photothermal therapy; POxylation.

5.2. Introduction

Combination chemotherapy is commonly applied to treat several types of cancers, including breast cancer. In this therapeutic approach, drug combinations (*e.g.* DOX + cyclophosphamide) are used to tackle cancer cells through different pathways, aiming to achieve additive or synergistic therapeutic effects, being the latter the most advantageous [1, 2]. However, the administration of multiple chemotherapeutics is challenging since an escalation of drugs' side-effects may occur [3, 4]. Furthermore, the distinct biodistribution and clearance profiles of the drugs may hamper the uptake of precise drug:drug combination ratios by cancer cells [5, 6].

To surpass these limitations, drug combinations can be loaded in nano-sized materials, allowing a ratiometric drug delivery to cancer cells [6]. In addition, the encapsulation of drugs in nanocarriers also improves their solubility and protects them from degradation or rapid clearance [7]. Among the different types of nanomaterials that have been explored for co-encapsulating drugs, nGO is a promising material since it has an excellent loading capacity and has the ability to encapsulate a wide variety of compounds through hydrophobic interactions and/or π-π stacking [8-10]. Moreover, the NIR absorption of GO based materials enables their application in cancer photothermal therapy [11, 12]. In this therapeutic approach, GO absorbs NIR radiation and converts it into heat, thus inducing cancer cells death and/or sensitization to the action of chemotherapeutics [13].

Despite the potential of GO based nanomaterials for use in combination chemo-photothermal therapy, these materials precipitate rapidly when in contact with biological fluids [14]. To overcome this limitation, GO is generally functionalized with PEG derivatives through covalent linkages or non-covalent interactions [11, 14]. The PEGylation of GO can also improve its blood circulation time, favoring its accumulation on the tumor zone [11, 14]. However, recently it was unveiled that PEGylated GO derivatives suffer from the accelerated blood clearance phenomenon [15], which may limit the repeated administration of these nanomaterials for cancer-related applications and highlights the importance of investigating PEG alternatives to functionalize GO.

In this work, GO derivatives were functionalized for the first time with an amphiphilic polymer based on poly(2-ethyl-2-oxazoline) (PEtOx) and were explored for combination chemo-phototherapy of breast cancer cells. PEtOx was selected due to its hydrophilic character and possible application as a PEG alternative [16-18]. PEtOx was grafted onto poly(maleic anhydride-*alt*-1-octadecene) (PMAO) since the hydrophobic blocks of the latter can efficiently adsorb to GO surface [14]. Furthermore, the DOX and TOS drug combination was selected to be loaded into GO since it was recently used with success in the treatment of gastric cancer cells [19]. Our results revealed that POxylated GO displays suitable physicochemical, colloidal, optical and biological properties for cancer therapy. Additionally, the screening of

different DOX:TOS combination ratios revealed that the 1:3 DOX:TOS molar ratio has an improved therapeutic potential since it has an optimal synergistic cytotoxic effect (low combination index across multiple fractions affected) towards breast cancer cells, while on normal cells it has a weaker effect. Therefore, POxylated GO was efficiently loaded with this drug combination in order to investigate its chemo-phototherapeutic performance. The delivery of DOX:TOS by POxylated GO to cancer cells produced a stronger therapeutic effect than that attained using the free drug combination. Furthermore, DOX:TOS loaded POxylated GO under NIR laser irradiation produced an even greater cytotoxicity towards cancer cells, thus confirming the therapeutic capacity of the ratiometric drug delivery and phototherapy mediated by POxylated GO.

5.3. Materials and Methods

5.3.1. Materials

DMEM-F-12, EDTA, PMAO (30000-50000 Da), resazurin, TOS and trypsin were purchased from Sigma–Aldrich (Sintra, Portugal). DOX was acquired from Carbosynth (Berkshire, UK). PEtOx (5000 Da) was obtained from Polysciences (Bergstrasse, Germany). MCF-7 cell line was acquired from ATCC (Middlesex, UK). NHDF were purchased from PromoCell (Heidelberg, Germany). FBS was obtained from Biochrom AG (Berlin, Germany). Cell culture plates and T-flasks were obtained from Thermo Fisher Scientific (Porto, Portugal). Water used in all assays was double deionized (0.22 μm filtered, 18.2 MΩ cm).

5.3.2. Methods

5.3.2.1. Synthesis of POx-*g*-PMAO

POx-*g*-PMAO was prepared according to a method previously described in the literature with slight modifications [20]. Briefly, PMAO (105 mg), PEtOx (510 mg) and a catalytic amount of concentrated H_2SO_4 (*i.e.*, several drops) were refluxed in chloroform at 70 °C for 12 h. Afterward, the solvent was removed through rotary-evaporation (Rotavap® R-215, Büchi, Switzerland). The obtained material was then dialyzed (14 kDa molecular-weight cutoff membrane) against water for 3 days and freeze-dried (ScanVac CoolSafe, LaboGene ApS, Denmark), yielding POx-*g*-PMAO.

5.3.2.2. Functionalization of GO derivatives

bwGO was produced as described in a previous publication of our group [21]. bwGO was then functionalized with POx-*g*-PMAO using a simple sonication method [21]. In brief, a mixture of bwGO (200 μg mL^{-1}; 1 mL) and POx-*g*-PMAO (500 μg) was sonicated for 60 min (Branson 5800, Branson Ultrasonics, CT, USA). Afterward, the solution was centrifuged (to remove any possible aggregates) and the supernatant was recovered, yielding POx-*g*-PMAO functionalized bwGO (POx-GO).

The absorption spectrum of POx-GO was used to determine the content of POx-*g*-PMAO incorporated on this nanomaterial, using the following equation:

$$Abs_{POx\text{-}GO\ at\ 206\ nm} = Abs_{bwGO\ at\ 206\ nm} + Abs_{POx\text{-}g\text{-}PMAO\ at\ 206\ nm}$$

To accomplish that, the absorption spectrum of POx-GO in water:methanol (1:1 (v/v)) was initially acquired. Afterward, the concentration of bwGO in the POx-GO solution was determined using a standard curve of bwGO at 808 nm (POx-*g*-PMAO does not display any absorbance at 808 nm in the concentration range used herein). Subsequently, $Abs_{bwGO\ at\ 206\ nm}$ (determined using a standard curve) was subtracted to the $Abs_{POx\text{-}GO\ at\ 206\ nm}$, rendering the $Abs_{POx\text{-}g\text{-}PMAO\ at\ 206\ nm}$. Finally, the concentration of POx-*g*-PMAO was determined using the $Abs_{POx\text{-}g\text{-}PMAO\ at\ 206\ nm}$ and a standard curve of POx-*g*-PMAO (at 206 nm). All the standard curves were prepared with the analytes dissolved in water:methanol (1:1 (v/v)).

5.3.2.3. Physicochemical characterization of POx-GO derivatives

The successful functionalization of bwGO with POx-*g*-PMAO was confirmed through FTIR using a Nicolet iS10 spectrometer (Thermo Scientific Inc., MA, USA) with a spectral width ranging from 4000 to 600 cm^{-1}. POx-GO size distribution and colloidal stability were confirmed by DLS using a Zetasizer Nano ZS (Malvern Instruments, Worcestershire, UK) at a scattering angle of 173°. UV-Vis absorption spectroscopy (Evolution 201 spectrophotometer, Thermo Scientific Inc.) was employed to confirm the NIR absorption of POx-GO. The photothermal capacity of POx-GO was confirmed by monitoring the temperature variations, using a thermocouple thermometer, upon irradiation of the nanostructures with NIR laser light over a period of 5 min (808 nm, 1.7 W cm^{-2}).

5.3.2.4. Evaluation of POx-GO cytocompatibility

The cytocompatibility of POx-GO to MCF-7 cells and NHDF was characterized using the resazurin method, as previously described by our group [22]. All cell lines were cultured in Dulbecco's Modified Eagle's Medium-F12 supplemented with 10 % (v/v) of FBS and 1 % (v/v) of penicillin/streptomycin in a humidified incubator (37 °C, 5 % CO_2). For the assay, MCF-7 cells and NHDF were seeded at a density of 1 x 10^4 cells/well in 96-well plates. After 24 h, the medium was removed, and cells were incubated with culture medium containing different doses of POx-GO (1 – 100 μg mL^{-1} of bwGO equivalents) for 24 or 48 h. Then, cells were incubated with culture medium containing resazurin (10 % (v/v)) in the dark for 4 h (37 °C, 5 % CO_2). Cells' viability was then determined by analyzing the fluorescence of resorufin (λ_{ex} = 560 nm; λ_{em} = 590 nm) in a Spectramax Gemini EM spectrofluorometer (Molecular Devices LLC, CA, USA). Negative (K-) and positive (K+) controls correspond to cells incubated solely with culture medium (without nanomaterials) and to cells treated with ethanol (70 % (v/v)), respectively.

5.3.2.5. Screening of DOX:TOS combinations

The concentration of DOX, TOS and DOX:TOS combinations (at different molar ratios ranging from 5:1 to 1:5) required to inhibit MCF-7 cells' viability by 20, 50 and 80 % (IC_{20}, IC_{50} and IC_{80}) were determined through the resazurin assay, as described above. In brief, MCF-7 cells were seeded at a density of 1 x 10^4 cells/well in 96-well plates. After 24 h, the medium was removed, and cells were incubated with culture medium containing different drug doses for 24 h. Then, cells were incubated with resazurin (10 % (v/v)) for 4 h in the dark (37 °C, 5 % CO_2) and their viability was determined as described in section 5.3.2.4. Subsequently, drugs' dose-response curves were traced to determine their IC_{20}, IC_{50} and IC_{80} (OriginPro, trial version, OriginLab Corporation, MA, USA). Finally, the Chou-Talalay method was employed to disclose the Combination Index (CI) of the different DOX:TOS combination ratios at inhibition levels of 20 (Fraction affected (Fa)=0.2), 50 (Fa=0.5) and 80 % (Fa=0.8) [23]. CI < 1 was considered to be a synergistic effect whereas CI > 1 was considered to be an antagonistic effect.

5.3.2.6. Preparation of DOX:TOS loaded POx-GO

DOX and TOS loaded POx-GO was prepared by using a simple sonication method. In brief, a solution containing bwGO and POx-*g*-PMAO was sonicated as described in section 5.3.2.2. Then, this solution was mixed with 20 μL of the dual drug combination mixture (DOX:TOS at 1:3 molar ratio in methanol), followed by sonication for 30 min. Subsequently, the solution was dialyzed (1000 Da molecular-weight cutoff membrane) against water for 90 min to remove non-loaded drugs and the methanol. Finally, the solution was centrifuged (to remove any possible

aggregates) and the supernatant was recovered, yielding DOX and TOS loaded POx-GO (DT loaded POx-GO).

The UV-Vis-NIR absorption spectrum of DT loaded POx-GO was used to determine the content of DOX and TOS on this nanomaterial, using the following equations:

$$Abs_{DT\ loaded\ POx\text{-}GO\ at\ 498\ nm} = Abs_{bwGO\ at\ 498\ nm} + Abs_{DOX\ at\ 498\ nm}$$

$$Abs_{DT\ loaded\ POx\text{-}GO\ at\ 284\ nm} = Abs_{bwGO\ at\ 284\ nm} + Abs_{DOX\ at\ 284\ nm} + Abs_{TOS\ at\ 284\ nm}$$

(please note that POx-*g*-PMAO does not display any absorbance at the above wavelengths in the concentration range used herein)

First, the absorption spectrum of DT loaded POx-GO in water:methanol (1:1 (v/v)) was acquired. Afterward, the concentration of bwGO in the DT loaded POx-GO solution was determined using a standard curve of bwGO at 808 nm (DOX and TOS do not display any absorbance at 808 nm in the concentration range used herein). Subsequently, $Abs_{bwGO\ at\ 498\ nm}$ (determined using a standard curve) was subtracted to the $Abs_{DT\ loaded\ POx\text{-}GO\ at\ 498\ nm}$, rendering the $Abs_{DOX\ at\ 498\ nm}$ (TOS does not display any absorbance at 498 nm in the concentration range used herein). The concentration of DOX was then determined using the $Abs_{DOX\ at\ 498\ nm}$ and a standard curve of DOX (at 498 nm).

Then, $Abs_{bwGO\ at\ 284\ nm}$ and $Abs_{DOX\ at\ 284\ nm}$ (determined using standard curves) were subtracted to the $Abs_{DT\ loaded\ POx\text{-}GO\ at\ 284\ nm}$, rendering the $Abs_{TOS\ at\ 284\ nm}$. The concentration of TOS was then determined using the $Abs_{TOS\ at\ 284\ nm}$ and a standard curve of TOS (at 284 nm). All the standard curves were prepared with the analytes dissolved in water:methanol (1:1 (v/v)).

5.3.2.7. Evaluation of DOX and TOS loaded POx-GO combination chemo-phototherapeutic effect

The combination chemo-phototherapeutic effect mediated by DT loaded POx-GO was determined as we previously described [21]. For such, MCF-7 cells were seeded in 96 well-plates as described above. After 24 h, cells were incubated with DT loaded POx-GO (20.5 μM of 1:3 DOX:TOS combination; 34.7 μg mL^{-1} of bwGO equivalents) or POx-GO (34.7 μg mL^{-1} of bwGO equivalents). After 4 h of incubation, cells were irradiated with NIR light (808 nm, 1.7 W cm^{-2}) during 5 min. Upon 24 h of incubation, cells were incubated with resazurin (10 % (v/v)) for 4 h in the dark (37 °C, 5 % CO_2) and their viability was determined as described in section 5.3.2.4.

5.3.2.8. Statistical analysis

ANOVA with the Student-Newman-Keuls test was applied for the comparison of multiple groups. A value of p lower than 0.05 ($p < 0.05$) was considered statistically significant. Data analysis was performed in GraphPad Prism v6.0 (Trial version, GraphPad Software, CA, USA).

5.4. Results and Discussion

5.4.1. Preparation and characterization of POx-GO

GrO was produced according to a previous publication of our group using a modified version of the improved Hummer's method [21]. Afterwards, this material was treated with sodium hydroxide and sonicated, yielding bwGO, whose characterization is reported elsewhere [21].

To prepare PEtOx-functionalized bwGO, we first conjugated bwGO with amine-terminated PEtOx using the EDC chemistry (data not shown). However, this material displayed an unsuitable colloidal stability since it promptly precipitated in saline solutions (data not shown). Considering that this type of functionalization relies on the carboxyl groups of bwGO that are available for conjugation, we hypothesized that the weak colloidal stability could be related with a scarce amount of PEtOx covalently bonded to bwGO.

In this way, we prepared a PEtOx-based amphiphilic polymer by grafting PEtOx into PMAO (POx-*g*-PMAO) by adapting a protocol described elsewhere [20]. In this case, the amount of PEtOx in the functionalized bwGO may be increased since the multiple PEtOx chains in POx-*g*-PMAO are used to functionalize bwGO through hydrophobic-hydrophobic interactions established between the nanomaterial and the hydrophobic regions of the amphiphilic polymer. The successful synthesis of POx-*g*-PMAO was confirmed by FTIR (Figure 5.1). In the FTIR spectrum of POx-*g*-PMAO, several peaks at 2853 cm^{-1} (C-H stretch) and 1779 cm^{-1} (C=O stretch from anhydrides) can be observed, which are also present in PMAO spectrum. Furthermore, the absence of the peak at 1856 cm^{-1} (C=O stretch from anhydrides) and the weak intensity of the one at 1779 cm^{-1} (C=O stretch from anhydrides) in POx-*g*-PMAO spectrum also corroborate the opening of the maleic anhydride ring and suggest the grafting of PEtOx into PMAO. Additionally, the peaks at 2976 cm^{-1} (C-H stretch), 1733 cm^{-1} (C=O stretch from carbonyls) and 1632 cm^{-1} (C=O stretch from amides) present in PEtOx spectrum are also present in POx-*g*-PMAO spectrum, which further corroborates the synthesis of the amphiphilic polymer.

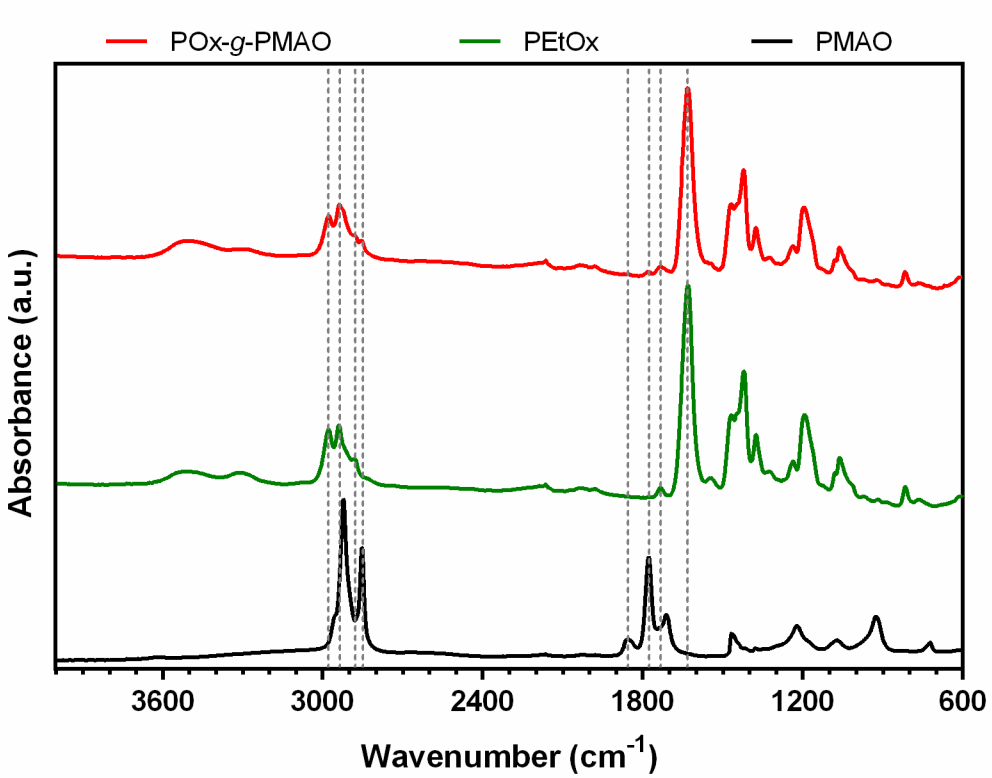

Figure 5.1. FTIR spectra of POx-*g*-PMAO, PEtOx and PMAO.

POx-*g*-PMAO was then employed to functionalized bwGO using a simple sonication method (for the sake of simplicity, POx-*g*-PMAO functionalized bwGO will be termed as POx-GO from here on) – Figure 5.2A [21]. The presence of POx-*g*-PMAO in POx-GO was confirmed by FTIR analysis (Figure 5.2B), which displays several peaks belonging to the amphiphilic polymer. POx-GO incorporated 1.76 ± 0.02 µg of POx-*g*-PMAO per µg of bwGO, which is fundamental to attain materials with improved colloidal stability. Furthermore, the DLS results confirmed that POx-GO maintained its size distribution upon incubation with PBS solution (Figure 5.2C). In fact, POx-GO remained stable as a colloid in saline solutions (Figure 5.2C), while bwGO precipitates in this type of solutions as we previously reported [21]. In this way, the functionalization of bwGO with POx-*g*-PMAO can address a major limitation of this GO derivative, thus ensuring its applicability in cancer therapy.

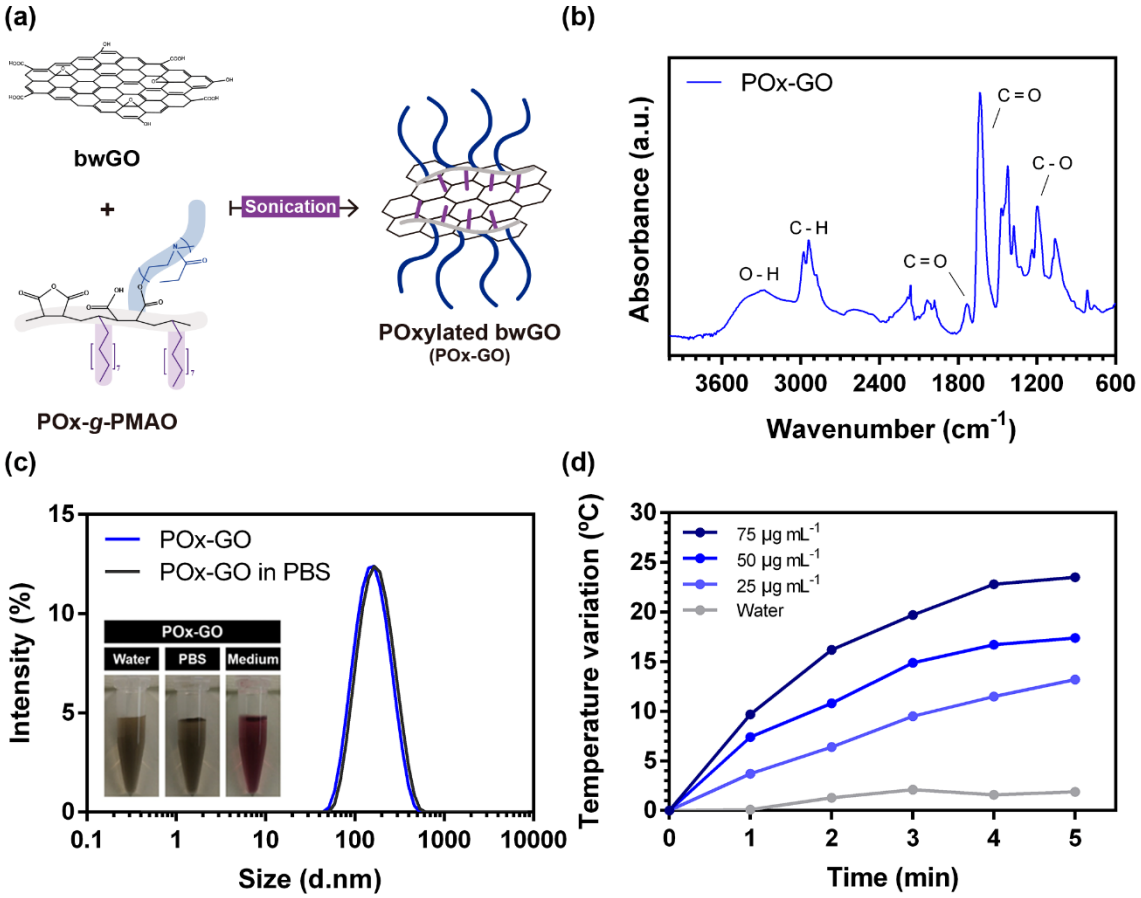

Figure 5.2. Preparation and characterization of POx-GO. Schematic illustration of the POx-GO preparation method (A). FTIR characterization of POx-GO (B). DLS size distribution of POx-GO and POx-GO in PBS (C). Macroscopic images of POx-GO in water, PBS and serum supplemented medium (DMEM-F12 supplemented with FBS (10 % (v/v)) (C inset). Temperature variation curves of POx-GO at different concentrations (of bwGO) during a 5 min NIR laser irradiation period (808 nm, 1.7 W cm^{-2}) (D).

Subsequently, we analyzed the UV-Vis-NIR absorption of POx-GO, which revealed that this nanomaterial possesses NIR absorption (Figure 5.3). The NIR absorption of POx-GO indicates that this material may be applied as a NIR-responsive photothermal agent. To confirm this hypothesis, the photothermal capacity of POx-GO was evaluated by exposing the nanomaterials to 808 nm laser radiation and recording the temperature variations attained (Figure 5.2D). After 5 min of NIR laser irradiation, POx-GO produced, at the highest concentration tested (75 µg mL^{-1} of bwGO equivalents), a temperature increase of ≈ 24 °C, which is sufficiently high to induce the death of cancer cells [13]. In turn, at the lower concentrations, a temperature variation of 13-17 °C was achieved upon irradiation of POx-GO (Figure 5.2D). Such raise in the temperature may still induce damage to cancer cells and/or sensitize them to the action of chemotherapeutic drugs (chemosensitization) [13]. As importantly, water irradiated with NIR light (control) only suffered a temperature variation of ≈ 2 °C (Figure 5.2D). These results

confirm that POx-GO can be employed in phototherapy applications since it elicits minimal off-target heating. When compared to a previous report, the photoinduced heat produced by POx-GO is superior to that of bwGO functionalized with PEGylated vitamin E [21], which can indicate that the surface coating conferred by POx-*g*-PMAO may be better for photothermal applications.

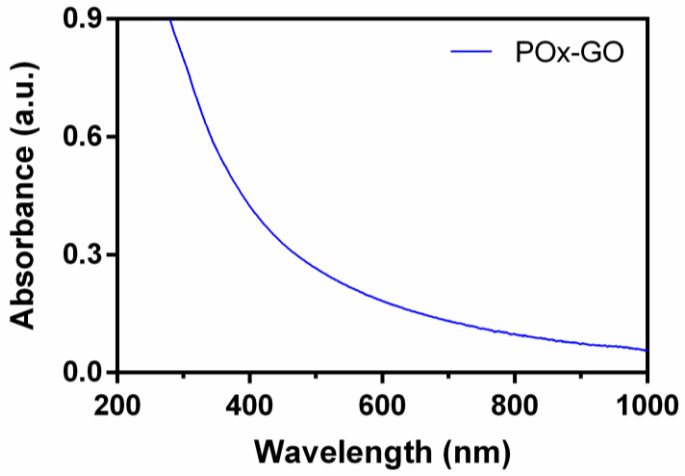

Figure 5.3. UV-Vis-NIR absorption spectrum of POx-GO.

Finally, the cytocompatibility of POx-GO towards MCF-7 cells (breast cancer cell model) and NHDF (normal cell model) was determined (Figure 5.4). At the highest concentration of POx-GO tested (100 μg mL^{-1} of bwGO equivalents), the functionalized materials did not affect meaningfully the viability of both cell lines (cellular viability > 88 %), which is fundamental for their use in biomedical applications (Figure 5.4). This data is in line with the good cytocompatibility reported for PEtOx-based nanomedicines [18, 24-26]. In fact, POx-GO revealed a similar cytocompatible profile to that of GO covalently conjugated with amine-terminated PEtOx reported by Wang *et al*. [26]. Moreover, when compared to PEGylated GO, POx-GO displayed an improved cytocompatibility towards MCF-7 cells, which is also a good indication of the safety profile of this nanomaterial [27].

Taken together, these results confirmed that POx-GO presents suitable physicochemical, colloidal, optical and biological properties to be explored as a nanoplatform for the delivery of the DOX-TOS combination to cancer cells and to be applied in photothermal therapy.

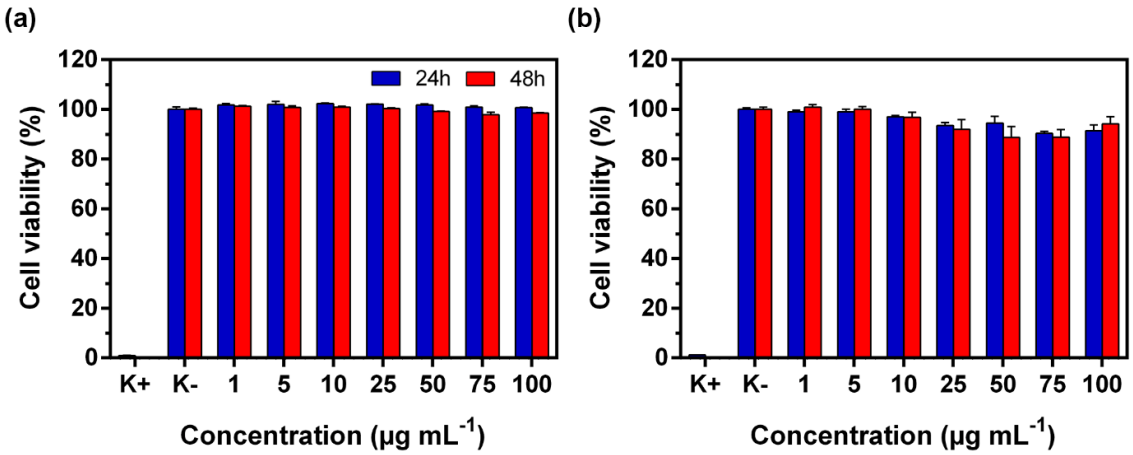

Figure 5.4. Evaluation of the cytocompatibility of POx-GO at different concentrations (of bwGO) and incubation times (24 and 48 h) towards MCF-7 cells (A) and NHDF (B). Data represent mean ± SD (n = 5).

5.4.2. Combinatorial drug screening

The administration of drug combination with synergistic activity to cancer cells can produce improved therapeutic outcomes. However, different drug:drug ratios may have distinct types of combinatorial effects depending on the Fa that is analyzed. Therefore, prior to the encapsulation of the DOX-TOS combination in POx-GO, we first determined the DOX:TOS molar ratio that presents optimal synergy across several Fa (Figure 5.5A). For this purpose, MCF-7 cells were incubated with DOX:TOS at different molar ratios (ranging from 5:1 to 1:5) and their IC_{20}, IC_{50} and IC_{80} were determined (Figure 5.5B and 5.6). Then, the CI at each Fa was calculated (Figure 5.5C).

In general, with the exception of the 1:2 DOX:TOS ratio (at Fa=0.2), all the tested combinations synergistically reduced MCF-7 cells' viability (Figure 5.5C). The DOX:TOS synergism is likely correlated to the fact that TOS, besides having the capacity to inhibit the proliferation and induce the apoptosis of MCF-7 cells [28], it can also increase the DOX influx and suppress its efflux from cancer cells [19], leading to an enhanced therapeutic effect.

Although the DOX:TOS ratios containing a higher DOX dose (5:1, 4:1, 3:1, 2:1) displayed a greater synergism (lower CI value) at Fa of 0.2 and 0.5 (*i.e.*, at inhibition levels of 20 and 50 %, respectively), those did not present the lowest CI value (*i.e.*, the highest synergism) at Fa=0.8 (at a inhibition level of 80 %). In this way, these drug ratios are not the most suited for breast cancer therapy since their synergy is weaker at higher inhibition levels. On the other hand, the 1:3 DOX:TOS ratio presented a CI ≈ 0.56 at all the Fa tested, and had a very low CI at Fa=0.8 (Figure 5.5C), thus displaying an optimal synergy. Furthermore, the use of DOX:TOS combinations with a greater content of TOS is appealing since this drug has a low effect on the viability of healthy cells [28, 29]. Therefore, the cytotoxicity of the 1:3 DOX:TOS combination

towards NHDF was also determined (Figure 5.5D). The IC_{20}, IC_{50} and IC_{80} of the 1:3 DOX:TOS combination towards NHDF were 39, 80 and 163 μM, respectively. Comparing the effect of this drug combination on NHDF and on MCF-7 cells, the 1:3 DOX:TOS combination displayed a 2 times weaker effect towards NHDF (Figure 5.5D).

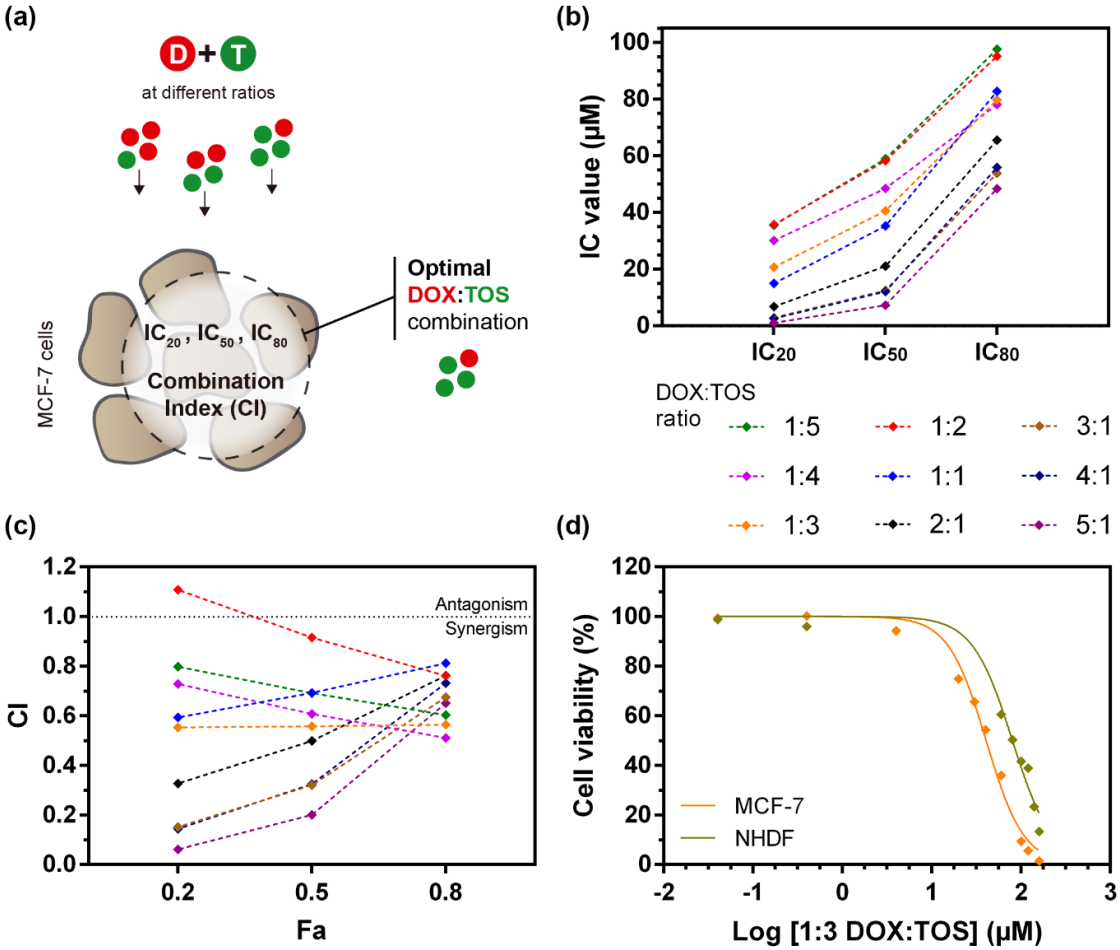

Figure 5.5. *In vitro* screening of the therapeutic potential of the DOX:TOS combinations. Schematic illustration of the parameters used to disclose the optimal DOX:TOS combination for MCF-7 cells treatment (A). IC_{20}, IC_{50} and IC_{80} of the different DOX:TOS combinations in MCF-7 cells (B). CI of the different DOX:TOS combinations at Fa=0.2, 0.5 and 0.8 in MCF-7 cells (C). Cell viability curves of MCF-7 cells and NHDF incubated with the 1:3 DOX:TOS combination (D). The points represent the mean of the experimental data (n = 5). The lines represent the determined dose-response curves.

Additionally, the therapeutic potential of the 1:3 DOX:TOS combination is also attested by the fact that this drug cocktail has a similar or greater synergy (CI ≈ 0.56) than other DOX-based drug combinations reported in the literature to treat MCF-7 cells (DOX:Resveratrol CI = 0.691 [30], DOX:Dihydroartemisinin CI = 0.50 [31], DOX:Fulvestrant CI = 0.71 [32], DOX:Tamoxifen

CI = 1.60 [32], DOX:4-Hydroxytamoxifen CI = 1.01 [32]). Therefore, the 1:3 DOX:TOS ratio was selected to be encapsulated in the POx-GO due to its optimal synergy in MCF-7 cells and weaker effect towards NHDF.

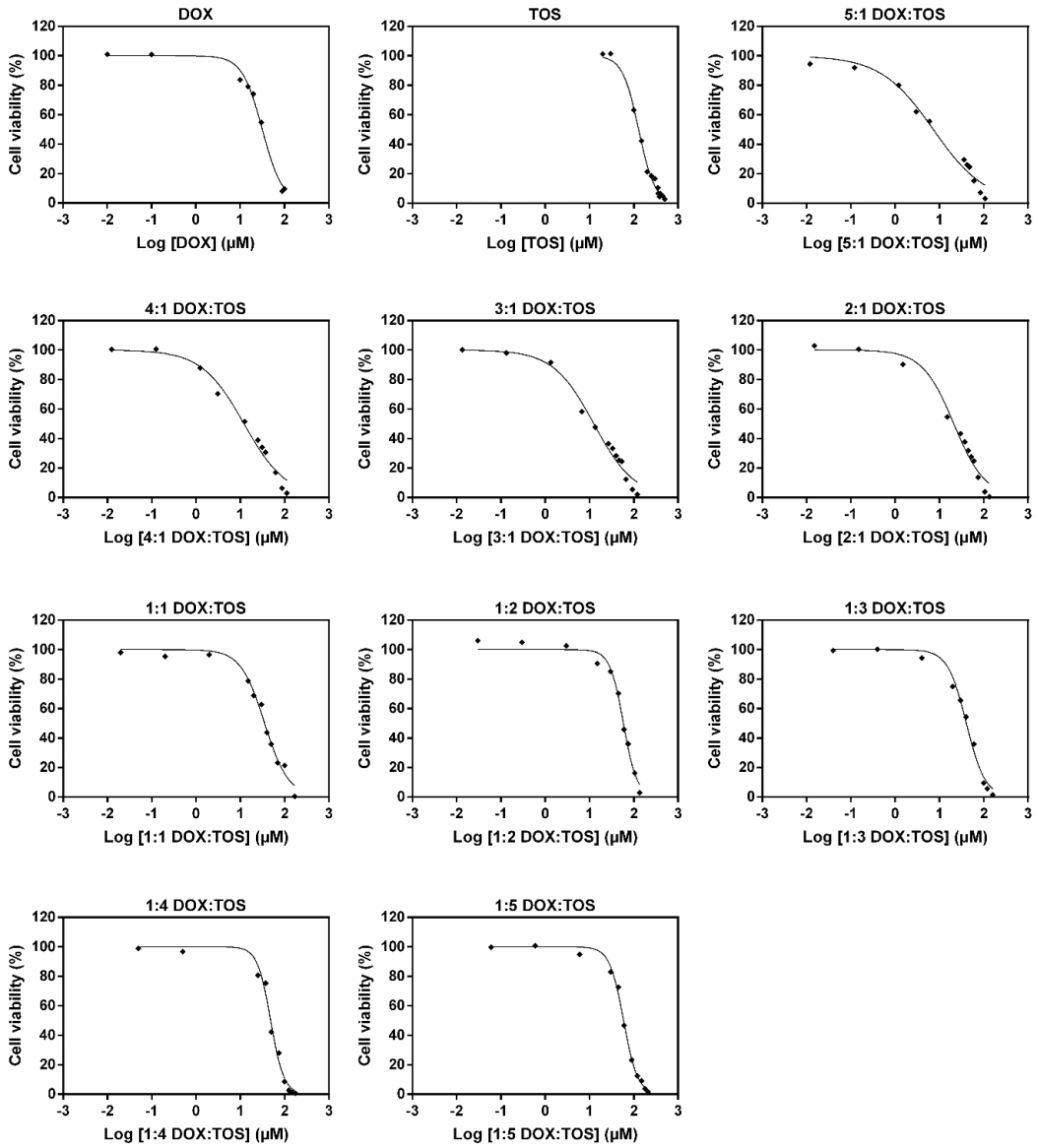

Figure 5.6. Cell viability curves of MCF-7 cells treated with different concentrations of DOX, TOS and DOX:TOS combinations (at different molar ratios). The points represent the mean of the experimental data (n = 5). The lines represent the determined dose-response curves.

5.4.3. Phototherapeutic capacity of DOX and TOS loaded POx-GO

The selected DOX:TOS combination ratio was encapsulated in POx-GO (termed DT loaded POx-GO from here on) through a simple sonication method since both drugs can be adsorbed on

GO based materials' surface through non-covalent interactions (Figure 5.7A). DT loaded POx-GO encapsulated 0.070 ± 0.012 µg of DOX per µg of bwGO and 0.205 ± 0.030 µg of TOS per µg of bwGO (n = 3). Besides showing a high loading capacity (a total of 0.275 ± 0.042 µg of drug per µg of bwGO), DT loaded POx-GO was able to encapsulate the DOX:TOS combination at the desired molar ratio, which is crucial for attaining an optimal synergistic effect. Furthermore, DT loaded POx-GO reveled a size distribution similar to that of POx-GO (Figure 5.7B), indicating that the loading of the drug combination is not detrimental to the nanomaterials' size. The zeta potential of DT loaded POx-GO (-34.2 ± 0.6 mV) and POx-GO (-37.2 ± 2.5 mV) were also similar, which also corroborates that the loading of the DOX:TOS combination occurs onto the aromatic matrix of POx-GO.

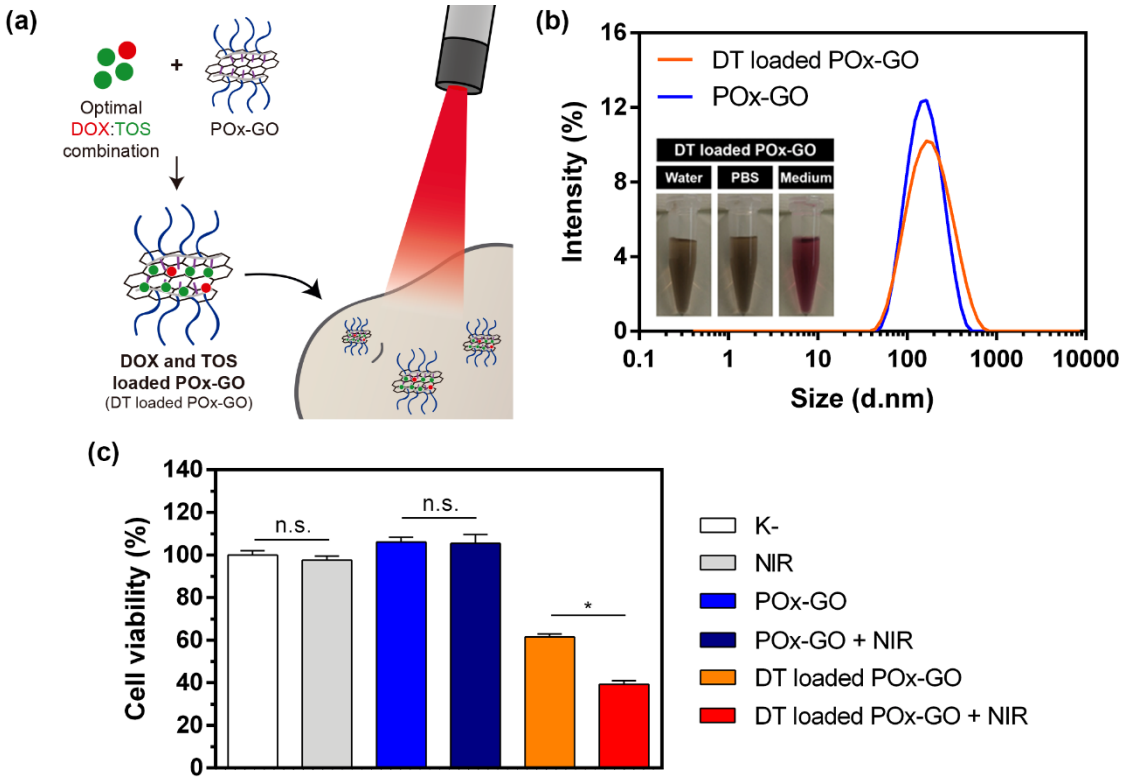

Figure 5.7. Preparation and characterization of DT loaded POx-GO. Schematic illustration of the phototherapy (A). DLS size distribution of POx-GO and DT loaded POx-GO (B). Macroscopic images of DT loaded POx-GO in water, PBS and serum supplemented medium (DMEM-F12 supplemented with FBS (10 % (v/v)) (B inset). Evaluation of the therapeutic capacity of POx-GO and DT loaded POx-GO without and with NIR irradiation (+ NIR; 808 nm, 1.7 W cm^{-2}, 5 min) towards MCF-7 cells (C). K- and NIR represent the negative control and cells solely treated with NIR light, respectively. Data represent mean ± SD (n = 5), *p < 0.0001, n.s. = non-significant.

Having confirmed the ability of POx-GO to load the DOX:TOS combination at its optimal molar ratio, then the efficacy of this formulation in decreasing MCF-7 cells' viability was assessed (Figure 5.7A). To clearly perceive the therapeutic potential of the DT loaded POx-GO, this nanomaterial was administered to cancer cells at a concentration that contains only half of the IC_{50} dose of the 1:3 DOX:TOS combination (20.5 μM) (Figure 5.7C). The results showed that the delivery of the DOX:TOS through POx-GO is efficient since cancer cells' viability was reduced to about 61 % (Figure 5.7C). In fact, drug loaded nanomaterials do not always outperform *in vitro* the therapeutic effect mediated by free drugs [33-35]. For instance, the delivery of Camptothecin+Methotrexate and DOX+Irinotecan combinations by GO based nanostructures to cancer cells did not result in a more effective therapy in comparison to the free drug combinations [33, 35]. Such may be related to the fact that, in *in vitro* assays, free drugs are not strongly impaired by clearance mechanisms or may present faster diffusion to the cells' cytoplasm. In this way, the improved therapeutic effect mediated by DT loaded POx-GO attests the drug delivery efficacy of this nanoformulation.

Furthermore, the combined application of DT loaded POx-GO and NIR radiation resulted in an even greater therapeutic effect, since it was able to further reduce MCF-7 cells' viability to ≈ 39 % (Figure 5.7C). As importantly, the sole application of NIR light did not induce a decrease on cancer cells' viability, which is in agreement with the low interaction of 808 nm radiation with biological components [13]. Moreover, POx-GO irradiated with NIR light did not induce cancer cells' death (Figure 5.7C). In this way, the enhanced chemo-phototherapeutic effect mediated by DT loaded POx-GO is likely to result from a chemosensitization effect induced by a local temperature increase produced by the nanomaterials under irradiation.

In the literature it is reported that Folate receptor targeted rGO loaded with Docetaxel and Irinotecan can produce a similar phototherapeutic effect towards MCF-7 cells, to that induced by DT loaded POx-GO, but requires a higher drug dose (50 *vs.* 20.5 μM) and a higher power density (3 *vs.* 1.7 W cm^{-2}) [36]. In another work, the exposure of PEGylated GO loaded with DOX+Irinotecan to NIR light (3 W cm^{-2}, 5 min) improved ≈ 1.13-times its therapeutic effect towards MCF-7 cells [35]. Herein, the NIR irradiation (1.7 W cm^{-2}, 5 min) of DT loaded POx-GO enhanced its therapeutic capacity by ≈ 1.56-fold. In this way, DT loaded POx-GO are promising materials for breast cancer therapy.

5.5. Conclusion

In the present study, the suitability of PEtOx based amphiphilic coatings to functionalize GO derivatives and the DOX:TOS combination ratio with optimal anticancer activity were investigated for the first time. POx-GO revealed suitable physicochemical, colloidal, optical and biological properties for application in cancer therapy. Furthermore, the 1:3 DOX:TOS

combination presented an optimal synergy for MCF-7 cells, and thus was efficiently loaded in POx-GO. The *in vitro* data revealed that the delivery of DOX:TOS by POx-GO to cancer cells produced a stronger therapeutic effect than that attained using the free drug combination. Furthermore, DT loaded POx-GO produced, under NIR laser irradiation, an even greater cytotoxicity towards cancer cells. Overall, POx-GO is a promising drug delivery and phototherapeutic agent. This study also paves the way for investigating PEtOx-based coatings in the functionalization of GO derivatives aimed for anti-cancer or other biomedical applications.

5.6. References

[1] R.B. Mokhtari, T.S. Homayouni, N. Baluch, E. Morgatskaya, S. Kumar, B. Das, H. Yeger, Combination therapy in combating cancer, Oncotarget, 8 (2017) 38022-38043.

[2] D. de Melo-Diogo, V.M. Gaspar, E.C. Costa, A.F. Moreira, D. Oppolzer, E. Gallardo, I.J. Correia, Combinatorial delivery of Crizotinib–Palbociclib–Sildenafil using TPGS-PLA micelles for improved cancer treatment, European Journal of Pharmaceutics and Biopharmaceutics, 88 (2014) 718-729.

[3] J.Y. Choi, R.K. Thapa, C.S. Yong, J.O. Kim, Nanoparticle-based combination drug delivery systems for synergistic cancer treatment, Journal of Pharmaceutical Investigation, 46 (2016) 325-339.

[4] D.R. Feldman, M.S. Ginsberg, M. Baum, C. Flombaum, H. Hassoun, S. Velasco, P. Fischer, N.M. Ishill, E.A. Ronnen, R.J. Motzer, Phase I trial of bevacizumab plus sunitinib in patients with metastatic renal cell carcinoma, Journal of Clinical Oncology, 26 (2008) 5100-5100.

[5] B.D. Liboiron, P.G. Tardi, T.O. Harasym, L.D. Mayer, Nanoscale delivery systems for combination chemotherapy, Drug Delivery in Oncology: From Basic Research to Cancer Therapy, (2012) 1013-1050.

[6] L.D. Mayer, A.S. Janoff, Optimizing combination chemotherapy by controlling drug ratios, Molecular Interventions, 7 (2007) 216-223.

[7] J.A. Kemp, M.S. Shim, C.Y. Heo, Y.J. Kwon, "Combo" nanomedicine: Co-delivery of multi-modal therapeutics for efficient, targeted, and safe cancer therapy, Advanced Drug Delivery Reviews, 98 (2016) 3-18.

[8] X. Sun, Z. Liu, K. Welsher, J.T. Robinson, A. Goodwin, S. Zaric, H. Dai, Nano-graphene oxide for cellular imaging and drug delivery, Nano Research, 1 (2008) 203-212.

[9] Z. Liu, J.T. Robinson, X. Sun, H. Dai, PEGylated nanographene oxide for delivery of water-insoluble cancer drugs, Journal of the American Chemical Society, 130 (2008) 10876-10877.

[10] B. Dimitrios, A.B. Hanene, H.B. Hee, M. Dal-Hee, K. Kostas, Prospects and Challenges of Graphene in Biomedical Applications, Advanced Materials, 25 (2013) 2258-2268.

[11] K. Yang, J. Wan, S. Zhang, Y. Zhang, S.-T. Lee, Z. Liu, In vivo pharmacokinetics, long-term biodistribution, and toxicology of PEGylated graphene in mice, ACS Nano, 5 (2010) 516-522.

[12] K. Yang, L. Feng, X. Shi, Z. Liu, Nano-graphene in biomedicine: theranostic applications, Chemical Society Reviews, 42 (2013) 530-547.

[13] D. de Melo-Diogo, C. Pais-Silva, D.R. Dias, A.F. Moreira, I.J. Correia, Strategies to improve cancer photothermal therapy mediated by nanomaterials, Advanced Healthcare Materials, 6 (2017) 1700073.

[14] K. Yang, J. Wan, S. Zhang, B. Tian, Y. Zhang, Z. Liu, The influence of surface chemistry and size of nanoscale graphene oxide on photothermal therapy of cancer using ultra-low laser power, Biomaterials, 33 (2012) 2206-2214.

[15] H.-J. Im, C.G. England, L. Feng, S.A. Graves, R. Hernandez, R.J. Nickles, Z. Liu, D.S. Lee, S.Y. Cho, W. Cai, Accelerated Blood Clearance Phenomenon Reduces the Passive Targeting of PEGylated Nanoparticles in Peripheral Arterial Disease, ACS Applied Materials & Interfaces, 8 (2016) 17955-17963.

[16] A. Mero, G. Pasut, L.D. Via, M.W.M. Fijten, U.S. Schubert, R. Hoogenboom, F.M. Veronese, Synthesis and characterization of poly(2-ethyl 2-oxazoline)-conjugates with proteins and drugs: Suitable alternatives to PEG-conjugates?, Journal of Controlled Release, 125 (2008) 87-95.

[17] M. Bauer, C. Lautenschlaeger, K. Kempe, L. Tauhardt, U.S. Schubert, D. Fischer, Poly(2-ethyl-2-oxazoline) as Alternative for the Stealth Polymer Poly(ethylene glycol): Comparison of in vitro Cytotoxicity and Hemocompatibility, Macromolecular Bioscience, 12 (2012) 986-998.

[18] V.M. Gaspar, C. Gonçalves, D. de Melo-Diogo, E.C. Costa, J.A. Queiroz, C. Pichon, F. Sousa, I.J. Correia, Poly (2-ethyl-2-oxazoline)–PLA-g–PEI amphiphilic triblock micelles for co-delivery of minicircle DNA and chemotherapeutics, Journal of Controlled Release, 189 (2014) 90-104.

[19] X. Zhang, X. Peng, W. Yu, S. Hou, Y. Zhao, Z. Zhang, X. Huang, K. Wu, Alpha-tocopheryl succinate enhances doxorubicin-induced apoptosis in human gastric cancer cells via promotion of doxorubicin influx and suppression of doxorubicin efflux, Cancer Letters, 307 (2011) 174-181.

[20] W.W. Yu, E. Chang, J.C. Falkner, J. Zhang, A.M. Al-Somali, C.M. Sayes, J. Johns, R. Drezek, V.L. Colvin, Forming Biocompatible and Nonaggregated Nanocrystals in Water Using Amphiphilic Polymers, Journal of the American Chemical Society, 129 (2007) 2871-2879.

[21] D. de Melo-Diogo, C. Pais-Silva, E.C. Costa, R.O. Louro, I.J. Correia, D-α-tocopheryl polyethylene glycol 1000 succinate functionalized nanographene oxide for cancer therapy, Nanomedicine, 12 (2017) 443-456.

[22] C. Pais-Silva, D. de Melo-Diogo, I.J. Correia, IR780-loaded TPGS-TOS micelles for breast cancer photodynamic therapy, European Journal of Pharmaceutics and Biopharmaceutics, 113 (2017) 108-117.

[23] T.-C. Chou, Drug combination studies and their synergy quantification using the Chou-Talalay method, Cancer Research, 70 (2010) 440-446.

[24] V.M. Gaspar, P. Baril, E.C. Costa, D. de Melo-Diogo, F. Foucher, J.A. Queiroz, F. Sousa, C. Pichon, I.J. Correia, Bioreducible poly (2-ethyl-2-oxazoline)–PLA–PEI-SS triblock copolymer micelles for co-delivery of DNA minicircles and Doxorubicin, Journal of Controlled Release, 213 (2015) 175-191.

[25] A.S. Silva, M.C. Silva, S.P. Miguel, V.D. Bonifácio, I.J. Correia, A. Aguiar-Ricardo, Nanogold Poxylation: Towards always-on fluorescent lung cancer targeting, RSC Advances, 6 (2016) 33631-33635.

[26] M. Wang, O.J.R. Gustafsson, G. Siddiqui, I. Javed, H.G. Kelly, T. Blin, H. Yin, S.J. Kent, D.J. Creek, K. Kempe, P.C. Ke, T.P. Davis, Human plasma proteome association and cytotoxicity of nano-graphene oxide grafted with stealth polyethylene glycol and poly(2-ethyl-2-oxazoline), Nanoscale, 10 (2018) 10863-10875.

[27] J.T. Robinson, S.M. Tabakman, Y. Liang, H. Wang, H.S. Casalongue, D. Vinh, H. Dai, Ultrasmall reduced graphene oxide with high near-infrared absorbance for photothermal therapy, Journal of the American Chemical Society, 133 (2011) 6825-6831.

[28] N. Duhem, F. Danhier, V. Préat, Vitamin E-based nanomedicines for anti-cancer drug delivery, Journal of Controlled Release, 182 (2014) 33-44.

[29] J. Neuzil, T. Weber, N. Gellert, C. Weber, Selective cancer cell killing by α-tocopheryl succinate, British Journal Of Cancer, 84 (2001) 87-89.

[30] G. Rai, S. Mishra, S. Suman, Y. Shukla, Resveratrol improves the anticancer effects of doxorubicin in vitro and in vivo models: A mechanistic insight, Phytomedicine, 23 (2016) 233-242.

[31] G.S. Wu, J.J. Lu, J.J. Guo, M.Q. Huang, L. Gan, X.P. Chen, Y.T. Wang, Synergistic anti-cancer activity of the combination of dihydroartemisinin and doxorubicin in breast cancer cells, Pharmacological Reports, 65 (2013) 453-459.

[32] H. Ikeda, N. Taira, T. Nogami, K. Shien, M. Okada, T. Shien, H. Doihara, S. Miyoshi, Combination treatment with fulvestrant and various cytotoxic agents (doxorubicin, paclitaxel, docetaxel, vinorelbine, and 5-fluorouracil) has a synergistic effect in estrogen receptor-positive breast cancer, Cancer Science, 102 (2011) 2038-2042.

[33] J.-M. Shen, F.-Y. Gao, L.-P. Guan, W. Su, Y.-J. Yang, Q.-R. Li, Z.-C. Jin, Graphene oxide-Fe3O4 nanocomposite for combination of dual-drug chemotherapy with photothermal therapy, RSC Advances, 4 (2014) 18473-18484.

[34] Z. Liming, X. Jingguang, Z. Qinghuan, L. Liwei, Z. Zhijun, Functional Graphene Oxide as a Nanocarrier for Controlled Loading and Targeted Delivery of Mixed Anticancer Drugs, Small, 6 (2010) 537-544.

[35] T.H. Tran, H.T. Nguyen, T.T. Pham, J.Y. Choi, H.G. Choi, C.S. Yong, J.O. Kim, Development of a Graphene Oxide Nanocarrier for Dual-Drug Chemo-phototherapy to Overcome Drug Resistance in Cancer, ACS Applied Materials & Interfaces, 7 (2015) 28647-28655.

[36] R.K. Thapa, Y. Choi, J.-H. Jeong, Y.S. Youn, H.-G. Choi, C.S. Yong, J.O. Kim, Folate-Mediated Targeted Delivery of Combination Chemotherapeutics Loaded Reduced Graphene Oxide for Synergistic Chemo-Photothermal Therapy of Cancers, Pharmaceutical Research, 33 (2016) 2815-2827.

Chapter 6

Concluding Remarks and Future Trends

Concluding Remarks and Future Trends

Nowadays, cancer continues to have a tremendous impact on the society. Despite all the efforts, cancer mortality rates remain very high. In fact, according to the World Health Organization, approximately 1 in 6 deaths are caused by cancer. The heterogenicity of this disease together with the core problems of the classic treatments (chemotherapy and radiotherapy) contribute for this scenario. The problems of the conventional therapies comprise a low therapeutic efficacy, that is further decreased by resistance mechanisms, and off-target toxicity, that can pose a threat to patients' life. Even though during the last decade new types of therapies have reached the clinic (targeted chemotherapy and immunotherapy), these are also overwhelmed by resistance mechanisms, and a have a remarkable higher cost to the health service providers.

To overcome these problems, PTT mediated by nanomaterials is currently under investigation. In particular, those based on GO have a tremendous potential for improving cancer treatment. In fact, the pre-clinical investigation performed so far highlights the excellent photothermal and drug delivery capacities of this nanomaterial. However, the direct use of GO in cancer-related applications is severely hindered by its weak colloidal stability, low tumor uptake and non-selectivity towards cancer cells.

The present research work aimed to address these problems and to implement novel strategies to improve cancer PTT mediated by GO-based materials. Such was pursued by i) employing coatings that can improve the biological performance of GO-based materials, ii) exploring preparation methods that can enhance GO photothermal capacity, and iii) encapsulating drug combinations with optimal synergistic anticancer activity on GO.

In the first experimental work presented here, GO derivatives were functionalized for the first time with TPGS, an FDA- and EMA-approved amphiphilic polymer. The TPGS functionalization successfully improved the colloidal stability of the GO-based nanomaterials. Particularly, the materials functionalized through the hydrothermal treatment revealed an enhanced stability and photothermal capacity. As importantly, the TPGS/GO derivatives retained the intrinsic anticancer activity of TPGS. Thus, in the *in vitro* studies, these nanodevices were able to induce cytotoxicity to breast cancer cells and minimal effects to healthy cells. Furthermore, the irradiation of TPGS/GO derivatives with NIR light induced an even greater reduction on the viability of breast cancer cells, thereby confirming their phototherapeutic potential.

The classic approach used in the literature to develop nanoformulations with a preferential effect towards cancer cells is the functionalization of nanomedicines' surface with targeting ligands [1]. Although some authors have applied this approach with success, the design of

targeting ligand-functionalized nanomaterials is challenging since i) the protein corona formed on nanomaterials' surface can cover the ligand, rendering an ineffective targeting, and ii) requires a fine-tuning of the ligand-density, which is problematic due to the disparities in nanomaterials' uptake found both in *in vitro* and *in vivo* assays [2, 3]. Furthermore, targeted nanomaterials have been showing disappointing results on clinical trials (*e.g.* BIND Therapeutics, Inc. Bind-014 – PSMA-targeted Nanoparticles loaded with Docetaxel) [4]. Due to these facts, nanostructures without surface passivation (*e.g.* DaunoXome® - Liposome loaded with Daunorubicin) or with PEG-passivation (*e.g.* DOXIL® – PEGylated Liposome loaded with DOX) are those that are still in use in the clinic [5]. In this way, achieving a preferential effect on cancer cells by coating GO derivatives with TPGS is promising since this type of selectivity is mediated by the TPGS molecular action (inhibition of Akt phosphorylation, leading to a decrease in the levels of BcL-2 and Survivin, which are overexpressed on breast cancer cells), and thus it is not likely to be affected by the problems described for targeting ligand-functionalized nanostructures.

In the second experimental study, GO-based materials aimed for cancer-therapy were functionalized for the first time with a POx-based amphiphilic polymer. The POxylated GO derivatives demonstrated suitable physicochemical, colloidal, optical and biological properties for application in cancer therapy. Parallelly, the therapeutic potential of the DOX:TOS combination was screened, demonstrating that the 1:3 DOX:TOS molar ratio produces an optimal synergistic therapeutic effect towards breast cancer cells (combination index of about 0.56 at different inhibition levels) and that it has a 2-times weaker effect on normal cells. POxylated GO derivatives were then loaded with the 1:3 DOX:TOS combination in order to evaluate its chemo-phototherapeutic potential. The *in vitro* studies revealed that the delivery of DOX:TOS by POxylated GO-based materials to cancer cells induced a stronger therapeutic effect than that attained with the free drug combination. Furthermore, an even greater cytotoxic effect towards cancer cells was achieved by exposing DOX:TOS loaded POxylated GO derivatives to NIR radiation, confirming the chemo-phototherapeutic potential of this nanoformulation.

During the course of this PhD thesis, it was revealed by Kataoka's research group that nanomaterials can accumulate in the tumor by extravasating through the dynamic vents that occur spontaneously in the tumor vasculature (also termed as eruptions) [6]. This finding completely shifts the paradigm by putting a high emphasis on enhancing the nanomaterials' blood circulation in order to improve their tumor uptake (prior to this study, the modulation of nanomaterials' size was excessively pursued with the intent of enhancing the tumor-homing capacity) [6]. Furthermore, the first case on the accelerated blood clearance of PEGylated GO-based materials was also reported [7]. In this regard, Cai's research group found that PEGylated GO derivatives can experience a rapid blood clearance mediated by anti-PEG antibodies, which will ultimately compromise their ability to reach the tumor [7]. Based on this

body of information, the POxylation of GO gives a major contribution to the pursuit of PEG-alternatives for coating GO-based nanomaterials. Furthermore, the discovery of the optimal DOX:TOS combination ratios for breast cancer treatment was also an important breakthrough. Besides having a greater synergism than other DOX-based combinatorial therapies reported in the literature, the selected DOX:TOS combination demonstrated a lower effect on healthy cells. In this way, the POxylation of GO derivatives and their ratiometric loading with the optimal DOX:TOS combination is an appealing strategy to produce nanoformulations that may achieve a high blood circulation time (and tumor uptake) and may induce a substantially higher therapeutic effect on the cancer cells.

Overall, the results obtained demonstrate that the applicability of GO-based materials in cancer therapy can be augmented by functionalizing them with amphiphilic polymers. Furthermore, the PTT potential of GO derivatives can be further enhanced by using coatings with intrinsic anticancer activity or by co-encapsulating drugs that display a higher effect on cancer cells. These novel strategies will further contribute for the translation of GO-based materials from the bench to the bedside.

In the future, three major topics should be investigated in order to further accelerate the translation of GO-based phototherapies:

1. *In vivo* validation of POx-based and zwitterionic-based amphiphilic coatings

In a near future, the validation of the *in vivo* biodistribution and biocompatibility of the POxylated GO materials will be crucial to fully disclose the potential of this coating as a PEG-alternative. Moreover, synthesizing a PEtOx-TOS conjugate (an analog of TPGS but with PEtOx instead of PEG as the hydrophilic segment) and exploring it in the functionalization of GO derivatives is also an appealing approach since such material may retain the long blood circulation properties of PEtOx and the intrinsic anticancer activity of Vitamin E derivatives. Furthermore, zwitterionic-based amphiphilic polymers also hold a great potential for improving the blood circulation time of GO-based materials, and hence their tumor accumulation. In this way, validating such materials in *in vitro* and *in vivo* assays can be of great interest.

2. Acceleration of GO biodegradation

The long-term body accumulation of inorganic nanomaterials constitutes a barrier for their clinical translation. In this regard, the body-clearance of functionalized GO can be accelerated by using detachable coatings (the detachment of the coating allows the degradation of GO through oxidative-biodegradation). This research topic is still poorly investigated, and the applicability of such phenomenon to rGO-based materials was not yet unveiled. In this way, the

evaluation of the *in vivo* behavior of GO/rGO functionalized with amphiphilic materials that are detached from nanomaterials' surface in response to tumor microenvironment (*e.g.* acidic pH or enzymatic degradation by MMP-2) or intracellular (*e.g.* reductive conditions) stimuli should be pursued.

3. Environmentally-friendly reduction of GO

As demonstrated herein, the hydrothermal-treatment improved the NIR absorption of GO (mass extinction coefficient = 5.64 L g^{-1} cm^{-1}, at 808 nm) and yield nanomaterials with good cytocompatibility. Nevertheless, rGO attained using hydrazine hydrate still has a higher NIR absorption (mass extinction coefficient = 24.6 L g^{-1} cm^{-1}, at 808 nm) than htGO. However, the latter is highly cytotoxic to cells, which is in part related to the toxicity of the hydrazine hydrate. Thus, evaluating the applicability of natural compounds in the reduction of GO is an area of great interest. In this regard, ongoing investigation has shown that Vitamin C can be used for the reduction of GO, yielding rGO with a high NIR absorption (mass extinction coefficient = 12.67 L g^{-1} cm^{-1}, at 808 nm), acceptable cytocompatibility and appropriate physicochemical properties for cancer-related applications. Further optimizations in the Vitamin C-mediated reduction protocols will surely enhance the PTT capacity of GO-based materials.

6.1. References

[1] D. de Melo-Diogo, C. Pais-Silva, D.R. Dias, A.F. Moreira, I.J. Correia, Strategies to Improve Cancer Photothermal Therapy Mediated by Nanomaterials, Advanced Healthcare Materials, 6 (2017) 1700073.

[2] A. Salvati, A.S. Pitek, M.P. Monopoli, K. Prapainop, F.B. Bombelli, D.R. Hristov, P.M. Kelly, C. Åberg, E. Mahon, K.A. Dawson, Transferrin-functionalized nanoparticles lose their targeting capabilities when a biomolecule corona adsorbs on the surface, Nature Nanotechnology, 8 (2013) 137-143.

[3] J.H. Lee, A. Sahu, C. Jang, G. Tae, The effect of ligand density on in vivo tumor targeting of nanographene oxide, Journal of Controlled Release, 209 (2015) 219-228.

[4] R. van der Meel, T. Lammers, W.E. Hennink, Cancer nanomedicines: oversold or underappreciated?, Expert Opinion on Drug Delivery, 14 (2017) 1-5.

[5] J.I. Hare, T. Lammers, M.B. Ashford, S. Puri, G. Storm, S.T. Barry, Challenges and strategies in anti-cancer nanomedicine development: An industry perspective, Advanced Drug Delivery Reviews, 108 (2017) 25-38.

[6] Y. Matsumoto, J.W. Nichols, K. Toh, T. Nomoto, H. Cabral, Y. Miura, R.J. Christie, N. Yamada, T. Ogura, M.R. Kano, Y. Matsumura, N. Nishiyama, T. Yamasoba, Y.H. Bae, K. Kataoka, Vascular bursts enhance permeability of tumour blood vessels and improve nanoparticle delivery, Nature Nanotechnology, 11 (2016) 533-538.

[7] H.-J. Im, C.G. England, L. Feng, S.A. Graves, R. Hernandez, R.J. Nickles, Z. Liu, D.S. Lee, S.Y. Cho, W. Cai, Accelerated Blood Clearance Phenomenon Reduces the Passive Targeting of PEGylated Nanoparticles in Peripheral Arterial Disease, ACS Applied Materials & Interfaces, 8 (2016) 17955-17963.